Technische Universität München
Lehrstuhl für Hochfrequenztechnik

Spectral Domain and FFT Accelerated Cavity Green's Function Boundary Element Methods for Numerical Modeling of Reverberation Chambers

Michael E. Gruber

Vollständiger Abdruck der von der Fakultät für Elektrotechnik und Informationstechnik der Technischen Universität München zur Erlangung des akademischen Grades eines

- Doktor-Ingenieurs -

genehmigten Dissertation.

Vorsitzender: Prof. Dr.rer.nat. Gerhard Wachutka
Prüfer der Dissertation: 1. Prof. Dr.-Ing. Thomas Eibert
2. Prof. Dr.rer.nat. Frank Gronwald

Die Dissertation wurde am 23.09.2015 bei der Technischen Universität München eingereicht und durch die Fakultät für Elektrotechnik und Informationstechnik am 29.01.2016 angenommen.

Acknowledgment

First and foremost, I would like to express my sincere gratitude and appreciation to my supervisor Prof. Dr.-Ing. Eibert. Without his advice, support, and funding, this work would not have been possible. In addition, I want to thank him for providing his finite element boundary integral algorithm which forms the basis for the algorithms in this work. I also want to thank Prof. Dr.rer.nat. Gronwald for fruitful discussions on numerous conferences and for agreeing to serve as second examiner.

I would like to thank my former colleagues for many fruitful discussions. My thanks go to, among other, Georg Schnattinger, Oliver Wiedenmann, Robert Brem, and Dennis Schobert. In particular, I want to thank Simon Adrian for his advice on programming, many discussions on scientific writing, and for proofreading numerous of my manuscripts.

Besides my colleagues, I want to thank the students who have contributed to this work. Christian Koenen did preliminary work on the Fast Fourier transform accelerated Ewald summation technique in his master's thesis. Lisa Broska, Thomas Dengler, Alexander Knaak, and Josef Knapp contributed to the practical, the reverberation chamber research part of this work. They analyzed and compared different stirring techniques, different stirrer geometries and sizes, and different measures to assess the performance of a reverberation chamber.

Last but not least, I want to express my gratitude to my wife, Kristin, and my two daughters, Emilia and Sophie for being an indispensable balance to academic work.

Abstract

A boundary element method (BEM) with the Green's function of the rectangular cavity is derived, analyzed, and employed for the numerical modeling of reverberation chambers. Different from previous work, two approaches, a fast group spectral domain approach (FGSDA) and a fast Fourier transform (FFT) accelerated Ewald summation technique, are presented which relieve the major shortcomings of the cavity Green's function (CGF) BEM: the large computational burden of the CGF in the high frequency regime and the computationally expensive filling of the system matrix.

The FGSDA is based on a hybrid Ewald-2D spectral representation of the CGF and a spectral domain factorization. In the hybrid representation, near interactions are calculated with the Ewald summation technique while far interactions are calculated with the 2D spectral representations. Combining the advantages of both representations, the hybrid representation reduces the frequency complexity of the CGF. To accelerate the filling of the system matrix, the interaction integrals are evaluated in the spectral instead of the spatial domain. In the spectral domain, the nested interaction integrals over the test and the source domain are decomposed into two non-nested integrals, one over the test and one over the source domain. Precomputing the non-nested integrals supersedes the double integration during the filling of the system matrix and leads to a significant acceleration.

The second approach is based on the Ewald summation technique, the FFT, and Lagrange interpolation. The Ewald summation is composed of a spatial and a spectral series. The computationally expensive spectral series is sampled and precomputed. The interaction integrals are calculated using the prestored values and Lagrange interpolation – the computationally expensive CGF does not have to be evaluated during the filling of the system matrix. To accelerate the sampling process, the spectral series is reformulated into a sum of eight plane waves which only depend on the relative position of observation and source point. Discretizing the reformulated series on a uniform grid, the computation of the sample values can be accelerated using the FFT.

Numerical results demonstrate the efficiency of the proposed approaches. In different scenarios, ranging from a reverberation chamber which contains a small-sized antenna to a reverberation chamber with a stirrer and a device under test, they outperform a multilevel fast multipole method (MLFMM) accelerated BEM and other state-of-the-art methods for the numerical modeling of reverberation chambers. Depending on the scenario, the simulation time is reduced by a factor of four to more than three orders of magnitude. The proposed methods are validated not only against the other numerical methods but also against measurements. An error analysis complements the validation and reveals the particular challenges in reverberation chamber simulation.

Besides, the proposed methods are applied to reverberation chamber research. First, the independent stirrer positions in reverberation chambers are considered in the framework of linear algebra. It is shown that the number of independent positions is limited by the number of measurement points in the test volume. Second, a dual rotation speed stirring mode is proposed and analyzed. Without reducing the available test volume as in the case of a second stirrer, the new stirring mode improves the chamber performance with respect to field homogeneity and independent stirrer positions.

Contents

List of Abbreviations

Acronym	Description
1D	one-dimensional
2D	two-dimensional
3D	three-dimensional
ACA	adaptive cross approximation
AIM	adaptive integral method
BEM	boundary element method
BI	boundary integral
CFIE	combined field integral equation
CGF	cavity Green's function
DSC	discrete singular convolution
DSC-MoM	discrete singular convolution method of moments
EFIE	electric field integral equation
EMC	electromagnetic compatibility
Ewd	Ewald
FDTD	finite difference time domain
FE	finite element
FEM	finite element method
FE/BI	finite element boundary integral
FT	Fourier transform
FFT	fast Fourier transform
FGF	free-space Green's function
FGSDA	fast group spectral domain approach
FMM	fast multipole method
GMRES	generalized minimal residual
GMRES-IO	inner-outer generalized minimal residual (GMRES)
IBC	impedance boundary condition
IEC	international electrotechnical commission

Continued …

Continued …

Acronym	Description
LUF	lowest usable frequency
MFIE	magnetic field integral equation
MIMO	multiple input multiple output
MLFMM	multilevel fast multipole method
MoM	method of moments
PEC	perfectly electrically conducting
PMC	perfectly magnetically conducting
RUDSC	recursive update discrete singular convolution
RWG	Rao-Wilton-Glisson
TE	transverse electric
TM	transverse magnetic
TLM	transmission line matrix

List of Symbols

Symbol	Unit	Description
Mathematics		
j		imaginary unit
x		scalar
$\boldsymbol{X}$		vector
$\overline{\boldsymbol{X}}$		dyad
$\boldsymbol{x}$		n-dimensional vector
$\boldsymbol{X}$		n-dimensional matrix
$\hat{x}$		unit vector in x-direction
$\overline{\boldsymbol{I}}$		unit dyad
$\mathcal{X}$		operator
$\boldsymbol{X} \cdot \boldsymbol{Y}$		scalar product
$\boldsymbol{X} \times \boldsymbol{Y}$		vector product
∇x		gradient of x
$\nabla \cdot \boldsymbol{X}$		divergence of $\boldsymbol{X}$
$\nabla \times \boldsymbol{X}$		curl of $\boldsymbol{X}$
$\widetilde{f}$		Fourier transform of f
O		Landau notation
$\langle \boldsymbol{x}, \boldsymbol{y} \rangle$		inner product
$\mathrm{Cov}\,(\boldsymbol{x}, \boldsymbol{y})$		covariance
$\mathrm{Var}\,\boldsymbol{x}$		variance
$\mathrm{erfc}\,(x)$		complementary error function
$\delta\left(\boldsymbol{r} - \boldsymbol{r}'\right)$		Dirac delta distribution
General Electromagnetics		
ε_0	$\mathrm{A\,s\,V^{-1}\,m^{-1}}$	vacuum permittivity
μ_0	$\mathrm{V\,s\,A^{-1}\,m^{-1}}$	vacuum permeability
c_0	$\mathrm{m\,s^{-1}}$	vacuum speed of light

Continued …

Continued …

Symbol	Unit	Description
$Z_{\mathrm{F},0}$	Ω	vacuum wave impedance
k_0	m^{-1}	vacuum wavenumber
$\boldsymbol{E}$	$\mathrm{V\,m}^{-1}$	electric field
$\boldsymbol{H}$	$\mathrm{A\,m}^{-1}$	magnetic field
$\boldsymbol{D}$	$\mathrm{A\,s\,m}^{-2}$	electric flux density
$\boldsymbol{B}$	$\mathrm{V\,s\,m}^{-2}$	magnetic flux density
$\boldsymbol{A}$	$\mathrm{V\,s\,m}^{-1}$	magnetic vector potential
$\boldsymbol{F}$	$\mathrm{A\,s\,m}^{-1}$	electric vector potential
ϕ_{e}	V	electric scalar potential
$\boldsymbol{J}$	$\mathrm{A\,m}^{-2}$	electric current density
$\boldsymbol{M}$	$\mathrm{V\,m}^{-2}$	magnetic current density
$\boldsymbol{\rho}$	$\mathrm{A\,s\,m}^{-3}$	electric charge density
$\boldsymbol{\rho}_{\mathrm{m}}$	$\mathrm{V\,s\,m}^{-3}$	magnetic charge density
$\boldsymbol{J}_{\mathrm{s}}$	$\mathrm{A\,m}^{-1}$	electric surface current density
$\boldsymbol{M}_{\mathrm{s}}$	$\mathrm{V\,m}^{-1}$	magnetic surface current density
$\boldsymbol{\rho}_{\mathrm{s}}$	$\mathrm{A\,s\,m}^{-2}$	electric surface charge density
$\boldsymbol{\rho}_{\mathrm{m,s}}$	$\mathrm{V\,s\,m}^{-2}$	magnetic surface charge density
ε	$\mathrm{A\,s\,V}^{-1}\,\mathrm{m}^{-1}$	permittivity
μ	$\mathrm{V\,s\,A}^{-1}\,\mathrm{m}^{-1}$	permeability
κ	$\mathrm{S\,m}^{-1}$	electric conductivity
κ_{m}	$\Omega\,\mathrm{m}^{-1}$	magnetic conductivity
Z_{F}	Ω	wave impedance
ω	s^{-1}	angular frequency
f	Hz	frequency
λ	m^{-1}	wavelength
k	m^{-1}	wavenumber
Cavity Green's Function Boundary Element Method		
a, b, c	m	length, width, height of the cavity
k_x, k_y, k_z	m^{-1}	wavenumber in x, y-, z-direction
k_{c}	m^{-1}	complex wavenumber

Continued …

Continued …

Symbol	Unit	Description
Q		quality factor
$\overline{W}_\mathrm{s}$	V A	time-averaged stored energy
$\overline{P}_\mathrm{l}$	W	average power loss
Z_s	Ω	surface impedance
μ_w	$\mathrm{V\,s\,A^{-1}\,m^{-1}}$	permeability of the cavity walls
$\mu_\mathrm{r,w}$		relative permeability of the cavity walls
κ_w	$\mathrm{S\,m^{-1}}$	conductivity of the cavity walls
δ_w	m	skin depth of the cavity walls
S_w	$\mathrm{m^2}$	surface area of the cavity
$\overline{\boldsymbol{G}}^\mathrm{A}$	$\mathrm{V\,s\,A^{-1}\,m^{-2}}$	cavity Green's function for the magnetic vector potential
$\overline{\boldsymbol{G}}^\mathrm{F}$	$\mathrm{A\,s\,V^{-1}\,m^{-2}}$	cavity Green's function for the electric vector potential
$\boldsymbol{r}, \boldsymbol{r}'$	m	observation and source point
$\mathcal{T}_\mathrm{w}, \mathcal{T}_\mathrm{h}$		weakly and hyper singular operator
$\mathcal{K}$		strong singular operator
$\tau_\mathrm{t}, \tau_\mathrm{r}$		tangential and rotated tangential trace operator
$\boldsymbol{\beta}_n$		Rao-Wilton-Glisson basis functions
$\boldsymbol{i}$	A	unknown current vector
$\boldsymbol{v}$	V	unknown voltage vector
$\boldsymbol{g}$	V	excitation vector, EFIE
$\boldsymbol{g}'$	A	excitation vector, MFIE
$\boldsymbol{A}, \boldsymbol{B}, \boldsymbol{C}, \boldsymbol{D}$		system matrices, EFIE
$\boldsymbol{A}', \boldsymbol{B}', \boldsymbol{C}', \boldsymbol{D}'$		system matrices, MFIE
N		number of unknowns of the objects within the cavity
N_tot		total number of unknowns of the objects within the cavity and the walls of the cavity
N_it		number of iterations

Continued …

Continued …

Symbol	Unit	Description
$\overline{\overline{G}}^{\mathrm{A}}_{\mathrm{spat}}$	$\mathrm{V\,s\,A^{-1}\,m^{-2}}$	spatial representation of the cavity Green's function
$\overline{\overline{G}}^{\mathrm{A}}_{\mathrm{spec}}$	$\mathrm{V\,s\,A^{-1}\,m^{-2}}$	spectral representation of the cavity Green's function
$\overline{\overline{G}}^{\mathrm{A}}_{x\text{-}2\mathrm{D}}$, $\overline{\overline{G}}^{\mathrm{A}}_{y\text{-}2\mathrm{D}}$, $\overline{\overline{G}}^{\mathrm{A}}_{z\text{-}2\mathrm{D}}$	$\mathrm{V\,s\,A^{-1}\,m^{-2}}$	2D spectral representations of the cavity Green's function
$\overline{\overline{G}}^{\mathrm{A}}_{\mathrm{Ewald}}$	$\mathrm{V\,s\,A^{-1}\,m^{-2}}$	Ewald representation of the cavity Green's function
$\overline{\overline{G}}^{\mathrm{A}}_{\mathrm{Ew\text{-}spat}}$, $\overline{\overline{G}}^{\mathrm{A}}_{\mathrm{Ew\text{-}spec}}$	$\mathrm{V\,s\,A^{-1}\,m^{-2}}$	spatial and spectral part of the Ewald representation
$\overline{\overline{G}}^{\mathrm{A}}_{\mathrm{hybrid}}$	$\mathrm{V\,s\,A^{-1}\,m^{-2}}$	hybrid Ewald-2D spectral representation of the cavity Green's function
$\phi_{x,mnp}$, $\phi_{y,mnp}$, $\phi_{z,mnp}$	$\mathrm{m^{-1.5}}$	eigenfunctions of the magnetic vector potential
$\psi_{x,mnp}$, $\psi_{y,mnp}$, $\psi_{z,mnp}$	$\mathrm{m^{-1.5}}$	eigenfunctions of the electric vector potential
$\xi_{x,mn}$, $\xi_{y,mn}$, $\xi_{z,mn}$	$\mathrm{m^{-1}}$	z-2D spectral functions of the magnetic vector potential
$\chi_{x,mn}$, $\chi_{y,mn}$, $\chi_{z,mn}$	$\mathrm{m^{-1}}$	z-2D spectral functions of the electric vector potential
r_0	m	radius of sphere in the spatial domain
$k_{r,0}$	$\mathrm{m^{-1}}$	radius of circle/sphere in the spectral domain
$N_{x\text{-}2\mathrm{D}}$, $N_{y\text{-}2\mathrm{D}}$, $N_{z\text{-}2\mathrm{D}}$		number of terms in the 2D spectral representations
$N_{\mathrm{Ew\text{-}spat}}$, $N_{\mathrm{Ew\text{-}spat}}$		number of terms in the spatial and the spectral series of the Ewald representation
E_{opt}, E_{hf}, E		optimum, high-frequency, and overall splitting parameter of the Ewald summation

Continued …

Continued …

Symbol	Unit	Description
Δx_{near}, Δy_{near}, Δz_{near}	m	length, width, height of the near region
$t_{\text{Ew-spec}}$, t_{2D}	s	computation time per mode of the spectral series of the Ewald representation and the 2D spectral representations
γ		ratio of computation times per mode between 2D spectral and Ewald representation
a_{g}, b_{g}, c_{g}	m	length, width, height of a group
$\boldsymbol{r}_{\text{c}}$	m	center of a group
T_{mn}		translation function between test and source group
$Q_{\alpha\beta\gamma}$		Q-array
h_{q}		sampling density of the Q-array
ℓ_u, ℓ_v, ℓ_w		Lagrange polynomials
N_{p}		order of Lagrange polynomials
N_{r}		number of measurement points
N_α		number of stirrer positions
$N_{\alpha,\text{ind}}$		number of independent stirrer positions
r_{ij}		Pearson correlation coefficient
r_{s}		correlation threshold
v_α		ratio of angle increments

1. Introduction

1.1. Introduction to Reverberation Chambers

An electromagnetic reverberation chamber is a facility for but not limited to electromagnetic compatibility (EMC) testing [Hol06]. The use of reverberation chambers for EMC testing was first proposed in 1968 [Hil09] and standardized in 2003 [IEC11]. A reverberation chamber is an electrically large cavity resonator with a high quality factor which contains one or several transmitting and receiving antennas, the device under test, and in most cases a mode stirrer [Hil09]. The cavity is usually rectangular in shape although other geometries have been proposed [Arn98; Hua99a; Hua99b].

Reverberation chambers are statistical facilities. Inside the test volume of the chamber, a normally distributed electromagnetic field is desired for EMC testing [Hil09]. To generate the statistics, the per se deterministic fields in the cavity need to be stirred. The most widespread stirring technique is mechanical stirring. An electrically large scatterer called mode stirrer or mode tuner is rotated to continuously change the resonance frequencies of the cavity modes. Other stirring techniques are wall [Hua92b], frequency [Hil94], source [Hua92a; Cer05; Mon08; Cer09], and platform stirring [Ros01; Che12].

Initially, reverberation chambers were used for EMC tests [Cor80; Cra86]. Nowadays, many other applications such as measuring the radiation efficiency, the free-space input impedance, and the effective diversity gain of antennas [Ros00; Ros01; Kil02a; Kil02b] exist. Reverberation chambers are used to determine the correlation and capacity of multiple input multiple output (MIMO) systems [Kil04; Ros05] and they are applied to characterize the shielding effectiveness of cables, connectors, materials, and enclosures (e.g., [Cra88; Wan04; Lou95; Fou96; Hol03; Hol08]). In addition to the classical high frequency applications, reverberation chambers are employed to study biological and biomedical effects [Jun08; Bia09; Fic12].

Besides the exploration of new application areas, more fundamental issues in reverberation chamber theory are researched. One example is the efficiency of the stirring process. Several methods exist to assess the effectiveness – all with their pros and cons with respect to simplicity, flexibility, and correctness [IEC11; Mad04; Kra05; Gra12; Pfe12; Esp13; Pfe13; Pfe14]. However, none of them combines all qualities. Another example is mechanical stirring. The effect of various parameters (e.g., the size, the shape, the position of the stirrer, and the number of stirrers) on the stirring performance has been studied [Wu89; Cle05; Arn06; Hua06; Wel07; Lun10; Mog10; Mog11; Mog12; Bos12; Pri14]. Yet, the construction guidelines given in the IEC standard are still rather basic (e.g., symmetries should be avoided or multiple stirrers can

improve the chamber performance) [IEC11]. A last example is the quality factor. It is known that too high or too low losses result in a poor reverberation chamber performance [Hol06]. However, the determination of the optimum quality factor is subject of ongoing research [Ada14].

1.2. Numerical Modeling of Reverberation Chambers

The numerical modeling of reverberation chambers is challenging as they are electrically large, highly resonant, and over-moded. The electrically large size yields a large number of unknowns. The resonant and over-moded nature impedes the convergence properties of iterative solvers in terms of iteration count and accuracy. As, for these reasons, standard solvers often fail to efficiently produce accurate results, many specialized techniques have been proposed in recent years.

For broadband analysis, time-domain methods, such as the finite difference time domain (FDTD) (see e.g., [Taf95; Pet98]) or the transmission line matrix (TLM) method (see e.g., [Chr95]), are advantageous. However, time-domain solvers convergence slowly in the case of resonating structures. Appropriate modifications of the numerical modeling process are necessary. In [Mog04], Moglie accelerated the convergence of an FDTD solver by artificially decreasing the conductivity of the cavity walls. He showed that the field distributions of the decreased conductivity and the original model are strongly correlated as long as the artificial conductivity of the cavity walls is greater than one hundredth of the real conductivity. In [Orj06], a post-processing of the time-domain signal was proposed to consider different quality factors of the cavity without repeating the simulation. With the post-processing technique, the simulation time could also be reduced.

In [Cle05], Clegg et al. tried to optimize stirrer designs with a genetic algorithm using the TLM method. Although they decreased the conductivity of the cavity walls, the optimization of the stirrer design inside the chamber was computationally not feasible. As a remedy, they optimized the stirrer design in a free-space model without the chamber. However, concerns about the validity of the free-space model were raised in [Wel07]. In [Coa07], the TLM method was validated against measurements. To reduce the simulation time, the solver was stopped long before the fields had been decayed. The agreement of measured and simulated data was not excellent but, according to [Coa07], satisfactory considering that the numerical model was rather simple.

When only a certain number of discrete frequencies is required, frequency domain methods, such as the finite element method (FEM) (see e.g., [Jin02]) and the boundary element method (BEM) (see e.g., [Jin10]), are favorable. As the FEM is a volume-discretizing method, the large space comprising air inside the cavity must be discretized. This drawback is often mitigated by restricting the numerical model to the two-dimensional (2D) case. In 1999, Bunting et al. compared mechanical and frequency stirring in a 2D reverberation chamber [Bun99]. As only the lower frequency range

was simulated, they could not reproduce a statistically uniform field in the case of mechanical stirring. In 2002, Bunting analyzed the max-to-average ratio, the normalized standard deviation, the stirring ratio, and the field uniformity in a 2D reverberation chamber [Bun02]. In [Bun01; Bun03], the shielding effectiveness of a 2D, electrically small box in a 2D reverberation chamber was investigated. In [Rau12], Raum et al. presented a preliminary study on the modeling of three-dimensional (3D) reverberation chambers using the FEM. However, the group has not published any further work until now.

The BEM, also referred to as method of moments (MoM), is a surface-discretizing method. The large empty space inside the cavity does not need to be discretized. The number of unknowns is considerably reduced in comparison to volume-discretizing methods, such as the FDTD, the TLM, or the FEM. However, the system matrix is dense. When a direct solver is used, the operation count grows with N^3 where N is the number of unknowns. Iterative solvers reduce the complexity to $\mathcal{O}\left(N^2\right)$, but they converge slowly because of the resonating and over-moded nature of reverberation chambers [Zha12a; Zha13]. In [Leu03a; Leu03b; Bru05], Bruns et al. simulated a medium-sized reverberation chamber using the BEM. Because of the high computational and memory complexity, the simulations were limited to lower frequencies (i.e., $f < 3f_{\mathrm{LUF}}$). The complexity of the BEM is improved by using fast multiplication methods, such as the adaptive cross approximation (ACA) (see e.g., [Jin10]) or the MLFMM (see e.g., [Che01; Jin10]). The matrix-vector equation is solved iteratively. By approximating the far interactions using the ACA or the MLFMM, the cost per matrix-vector product is reduced from N^2 to $N \log N$. Nevertheless, as in the case of the unaccelerated BEM, the iterative solver needs many iterations to converge [Zha12a; Zha13].

Besides the work on standard methods, non-standard approaches have been proposed in recent years. In 2011, Zhao and Shen presented a hybrid discrete singular convolution method of moments (DSC-MoM) [Zha11]. The large cavity is modeled by the discrete singular convolution (DSC) method which is advantageous for rectangular geometries: Maxwell's equations in differential form are approximated using Lagrange polynomials. Depending on the order of the polynomial interpolation, a discretization density of one third of the wavelength is sufficient. As the DSC method is less efficient for arbitrarily shaped geometries, objects inside the cavity are modeled by the more flexible MoM. Versus a commercial numerical solver, the DSC-MoM achieved a speed-up of one order of magnitude. However, because of the hybrid approach, the use of a direct solver is necessary which resulted in a large memory consumption. Using a recursive update discrete singular convolution (RUDSC) method, Zhao and Shen could reduce the memory demand of their algorithm, but at the expense of a larger computation time [Zha12b].

Another non-standard approach is the cavity Green's function (CGF) BEM. Instead of the free-space Green's function (FGF), the Green's function of the rectangular cavity is used in the boundary integral (BI) formulation. As the CGF incorporates the cavity

walls, they do not need to be discretized. Depending on the number and the size of objects within the cavity, the number of unknowns is significantly reduced. However, the CGF approach involves two challenges: 1) finding an efficient representation of the cavity Green's function, and 2) the quadratic complexity of the system matrix.

In 2004, Laermans et al. modeled a 2D cavity using a one-dimensional (1D) spectral representation of the CGF [Lae04]. The spectral representation only involves a simple series, although the problem is 2D. Yet, the convergence of the simple series deteriorates when the observation point approaches the source point. To accelerate the convergence, Learmans et al. used a Shanks transformation and the Veysoglu integral transform. In [Gro03; Gro05; Car05; Car06; Car09], 3D cavities were modeled using the Ewald summation technique [Ewa21] – a method which expresses the CGF as a sum of a spatial and a spectral series [Par98]. In 2006, the Green's function of the rectangular cavity was constructed combining image theory and the Green's function of 1D multilayer planar structures [Kar06]. Depending on the frequency, the proposed representation was slightly slower or faster than the Ewald representation in [Car05], but the computation times were in the same order of magnitude.

As the second limitation of the CGF BEM (i.e., the filling of the system matrix) was not addressed in [Gro03; Gro05; Car05; Kar06; Car06; Car09], the use of the CGF BEM was restricted to small, 1D objects. In [Gro03], the electromagnetic coupling of a dipole antenna to a rectangular cavity was investigated. In [Gro05], the mutual coupling of two dipole antennas was analyzed. Also using two dipoles, position and frequency stirring were investigated in [Car05; Car09]. In [Kar06], three z-directed wires were modeled.

In [Bor04; Yan14], both limitations of the CGF BEM were addressed. Borji and Safavi-Naeini approximated the CGF using Chebychev polynomials and the Ewald summation technique [Bor04]. The interactions integrals were evaluated using the cheap polynomial approximation. To generate the coefficients of the polynomials, the Ewald summation technique was employed in a preprocessing step. Although the approach does not reduce the complexity of the system matrix fill, it achieved a speed-up of more than one order of magnitude versus the ordinary Ewald summation technique in the lower frequency range.

In [Yan14], the CGF BEM was accelerated by Yang and Yilmaz using the Ewald summation technique together with the adaptive integral method (AIM), where only the parts of the spatial series (i.e., the source term and the immediate image term(s) when the source is located close to the boundary) are computed directly. The remainder of the spatial and the spectral series are computed on-the-fly using the adaptive integral method (AIM) during the iterative solution of the linear equation system. To achieve the shift invariance needed for the AIM, the modes in the spectral series are rewritten as a sum of eight plane waves. The algorithm achieved a significant speed-up for cavities containing large or multiple objects. However, for medium- or small-sized objects, the additional overhead introduced by the inter- and anterpolation steps of the AIM decelerated the algorithm.

1.3. Scope of this Thesis

In this thesis, two acceleration techniques for the CGF BEM are presented. Both approaches address the large computational burden of the CGF as well as the quadratic complexity of the system matrix.

The first approach uses a hybrid representation of the CGF and a fast group spectral domain approach (FGSDA). In most previous works, the Ewald summation technique was employed to evaluate the CGF [Gro03; Gro05; Car05; Car06; Car09]. The Ewald sum consists of two exponentially convergent series: the spatial and the spectral series [Ewa21]. Although the Ewald summation technique is optimal in the undermoded frequency regime, it suffers from a high-frequency breakdown in the overmoded range [Cap07]. The number of terms in the spectral series needs to be increased with f^3 where f is the frequency to avoid numerical overflow errors. Besides the Ewald representation, 2D spectral representations of the CGF exist [Tai76]. As they involve a double instead of a triple sum, the number of necessary terms grows with f^2 only. However, the convergence rates of the 2D spectral representations decrease when the observation point approaches the source. To combine the advantages of both representations, a hybridization of the Ewald and the 2D spectral representation is proposed herein. When observation and source point are close to one another, the Ewald summation technique is used. Otherwise, one of the 2D spectral representations is employed. The hybrid approach relieves the first shortcoming of the CGF BEM as it scales only with f^2. The second shortcoming, i.e., the computationally expensive filling of the system matrix is addressed by the FGSDA. Naturally, the interaction integrals are evaluated in the spatial domain. However, the interactions integrals can be evaluated in the spectral domain as well [Eib98; Eib00; Eib03]. The nested interaction integrals over test and source region are separated into two non-nested integrals, one over the test and one over the source domain. The non-nested integrals correspond to the representations of the basis functions in the spectral domain. Precomputing and storing the spectral representations, the integration over test and source domain in the evaluation of the interaction integrals is not needed anymore and the major computational load is reduced from complexity N^2 to N.

The second approach employs a fast Fourier transform (FFT) accelerated Ewald summation technique and Lagrange interpolation. The Ewald summation technique originated in electrostatics. In 1921, Ewald developed the method to calculate the interaction energy for a lattice of ions [Ewa21]. In electrostatics, the Ewald summation technique does not suffer from the high-frequency breakdown as it is used to solve the Laplace and not the Helmholtz equation. Nevertheless, there have been similar problems. The computational load scaled quadratically with the number of particles [Des98]. The breakthrough was the development of FFT accelerated Ewald techniques [Str92; Dar93; Ess95]. Appropriately discretizing the spectral part of the Ewald sum on an equispaced grid, the sum over the particle interactions becomes an FFT. When, in addition, the range of the spatial part is chosen small enough, the complex-

ity decreases to linearithmic [Des98]. In this thesis, the FFT acceleration is applied to the electromagnetic Green's function of the rectangular cavity. The spectral part of the Ewald summation, which naturally depends on observation and source point (i.e., it is a six-variable function), is reformulated as a sum of three-variable functions which only depend on the relative position of observation and source point. Discretizing the three-variable functions on an equispaced grid, they become an FFT. As the values on the grid are precomputed and stored, the interaction integrals are computed with little computational effort using the fast Lagrange interpolation.

1.4. Outline of this Thesis

This thesis is structured as follows. In the next chapter, the boundary value problem of the rectangular cavity is analyzed for perfectly and imperfectly conducting walls. The surface integral equations for the rectangular cavity Green's function and their discrete counterparts are derived. The modeling of perfectly conducting, well conducting, and dielectric objects is discussed. In Chapter 3, different representations of the Green's function of the rectangular cavity are introduced, derived, and discussed with respect to their convergence properties. The proposed acceleration techniques are presented in Chapter 4 and 5, respectively.

In Chapter 6, numerical results for reverberation chambers containing perfectly conducting, well conducting, and dielectric objects are presented. The proposed algorithms are validated against and compared with an MLFMM accelerated FGF BEM and other state-of-the-art methods for the numerical modeling of reverberation chambers. The particular challenges in reverberation chamber simulation are identified and numerical consistency checks are performed. The complexity of the proposed algorithms with regard to computation time and memory requirement is derived in Section 6.3. In the last section of Chapter 6, the proposed methods are validated against measurements. In Chapter 7, the presented algorithms are used to contribute to the answering of some questions raised in Section 1.1. The problem of the independent stirrer positions is considered in the framework of linear algebra and a new dual rotation speed stirring mode for reverberation chambers is proposed and analyzed.

2. Cavity Green's Function Boundary Element Method

2.1. Fundamental Concepts

2.1.1. Maxwell's Equations

James Clerk Maxwell discovered that electricity and magnetism are not two separate forces but are part of the same phenomena termed electromagnetism [Max65]. By inserting the displacement current into Ampère's law, he unified Gauss's law, Gauss's law for magnetism, Faraday's law, and Ampère's law into a single theory and laid the foundation for electromagnetic waves. About two decades after Maxwell's presentation on the theory of electromagnetism [Max65], Heinrich Hertz gave the first experimental verification of electromagnetic waves by transmitting and receiving an electromagnetic pulse [Her88] . Commonly, Maxwell's equations are written in the formalism of Heaviside [Hea93]. Assuming a time-harmonic dependence $\mathrm{e}^{\mathrm{j}\omega t}$, they are in differential form [Jin10]

$$\nabla \cdot \boldsymbol{D} = \rho, \tag{2.1}$$

$$\nabla \cdot \boldsymbol{B} = \rho_{\mathrm{m}}, \tag{2.2}$$

$$\nabla \times \boldsymbol{E} + \mathrm{j}\omega \boldsymbol{B} = -\boldsymbol{M}, \tag{2.3}$$

$$\nabla \times \boldsymbol{H} - \mathrm{j}\omega \boldsymbol{D} = \boldsymbol{J} \tag{2.4}$$

where $\boldsymbol{E}$ and $\boldsymbol{H}$ are the electric and the magnetic field, $\boldsymbol{D}$ and $\boldsymbol{B}$ are the electric and the magnetic flux density, $\boldsymbol{J}$ and $\boldsymbol{M}$ are the electric and the magnetic current density, and ρ and ρ_{m} are the electric and the magnetic charge density. Although magnetic charges and currents have not been found in normal matter[1] yet, they serve as a valuable tool in form of equivalent charges and currents for the solution of electromagnetic boundary value problems [Jin10].

The fields and currents in Maxwell's equations are related via the constitutive relations which specify the characteristics of the surrounding medium. Assuming a homogeneous, linear, isotropic, and non-dispersive medium, they are

$$\boldsymbol{D} = \varepsilon \boldsymbol{E}, \tag{2.5}$$

$$\boldsymbol{B} = \mu \boldsymbol{H}, \tag{2.6}$$

$$\boldsymbol{J} = \kappa \boldsymbol{E}, \tag{2.7}$$

$$\boldsymbol{M} = \kappa_{\mathrm{m}} \boldsymbol{H} \tag{2.8}$$

1 Recently, magnetic monopole quasi-particles have been observed in condensed matter systems [Cas08].

where ε is the permittivity, μ is the permeability, and κ and κ_m are the electric and the magnetic conductivity of the medium. In an inhomogeneous, non-linear, anisotropic, or dispersive medium, the material parameters would depend on the position, the electric or the magnetic field, the polarization, or the frequency, respectively. In the special case of a perfect electric conductor ($\kappa \to \infty$), the electric field is zero. Likewise, the magnetic field vanishes in a perfect magnetic conductor ($\kappa_\mathrm{m} \to \infty$).

From Maxwell's equations in integral form, boundary conditions at media interfaces can be derived [Jin10]. At the interface between a medium 1 and a medium 2, they are [Jin10]

$$\hat{n} \cdot (\boldsymbol{D}_2 - \boldsymbol{D}_1) = \rho_\mathrm{s}, \tag{2.9}$$

$$\hat{n} \cdot (\boldsymbol{B}_2 - \boldsymbol{B}_1) = \rho_\mathrm{m,s}, \tag{2.10}$$

$$\hat{n} \times (\boldsymbol{E}_2 - \boldsymbol{E}_1) = -\boldsymbol{M}_\mathrm{s}, \tag{2.11}$$

$$\hat{n} \times (\boldsymbol{H}_2 - \boldsymbol{H}_1) = \boldsymbol{J}_\mathrm{s} \tag{2.12}$$

where $\boldsymbol{J}_\mathrm{s}$ and $\boldsymbol{M}_\mathrm{s}$ are the impressed surface current densities, ρ_s and $\rho_{\mathrm{m},s}$ are the impressed surface charge densities, and $\hat{n}$ is the unit normal vector pointing from medium 1 to 2. If surface currents and charges are zero, (2.9) and (2.10) enforce the continuity of the normal components of electric and magnetic flux across an interface and (2.11) and (2.12) dictate the continuity of the tangential components of electric and magnetic field. If medium 1 is a perfect electric conductor, $\boldsymbol{E}_1 = 0$ and the tangential electric field $\hat{n} \times \boldsymbol{E}_2$ in medium 2 must vanish at the boundary. Likewise, if medium 1 is perfectly magnetically conducting (PMC), $\boldsymbol{H}_1 = 0$ and $\hat{n} \times \boldsymbol{H}_2 = 0$ at the media interface.

If the domain is unbounded (i.e., an open problem), the electric and the magnetic field satisfy the radiation conditions

$$\lim_{r\to\infty} r\,(\nabla \times \boldsymbol{E} + \mathrm{j}k\hat{r} \times \boldsymbol{E}) = 0, \tag{2.13}$$

$$\lim_{r\to\infty} r\,(\nabla \times \boldsymbol{H} + \mathrm{j}k\hat{r} \times \boldsymbol{H}) = 0. \tag{2.14}$$

The above equations have been first derived by Silver and Müller and are known as Silver-Müller radiation conditions [Sil49; Mül57]. They enforce that 1) waves propagate away from the source at infinity, 2) the ratio of the electric and the magnetic field is a fixed value (i.e., the wave impedance $Z_\mathrm{F} = \mu/\varepsilon$), and 3) electric field, magnetic field, and the propagation direction form a right-handed trihedron [Jin10].

Equations 2.1 – 2.4 are a coupled partial differential equation system. The decoupled curl curl equation for the electric field is derived by applying the curl to (2.3), substituting from (2.4) and using (2.5) and (2.6). Analogously, the curl curl equation for the magnetic field is derived by inserting (2.3) into the curl of (2.4) and using the constitutive relations. According to [Jin10], the curl curl equations are given by

$$\nabla \times \nabla \times \boldsymbol{E} - k^2 \boldsymbol{E} = -\mathrm{j}\omega\mu \boldsymbol{J} - \nabla \times \boldsymbol{M}, \tag{2.15}$$

$$\nabla \times \nabla \times \boldsymbol{H} - k^2 \boldsymbol{H} = -\mathrm{j}\omega\varepsilon \boldsymbol{M} + \nabla \times \boldsymbol{J} \tag{2.16}$$

where $k = \omega\sqrt{\mu\varepsilon}$ is the wavenumber.

2.1.2. Auxiliary Vector Potentials

An elegant way to solve Maxwell's equations are auxiliary scalar and vector potentials. Instead of a curl curl equation, they yield two vector Helmholtz equations. Following [Jin10], the electric and the magnetic field are decomposed into

$$\boldsymbol{E} = \boldsymbol{E}_\mathrm{e} + \boldsymbol{E}_\mathrm{m}\,, \tag{2.17}$$

$$\boldsymbol{H} = \boldsymbol{H}_\mathrm{e} + \boldsymbol{H}_\mathrm{m} \tag{2.18}$$

where $\boldsymbol{E}_\mathrm{e}$ and $\boldsymbol{H}_\mathrm{e}$ are due to electric sources and $\boldsymbol{E}_\mathrm{m}$ and $\boldsymbol{H}_\mathrm{m}$ are due to magnetic sources. Since the differential equation system in (2.1) – (2.4) is linear, it is decomposed into one system due to electric currents and charges and another one due to magnetic currents and charges.

In the case of electric sources, $\boldsymbol{B}_\mathrm{e} = \mu\boldsymbol{H}_\mathrm{e}$ is a solenoidal vector function as the divergence of $\mu\boldsymbol{H}_\mathrm{e}$ is zero. Introducing the magnetic vector potential $\boldsymbol{A}$ according to

$$\boldsymbol{H}_\mathrm{e} = \frac{1}{\mu}\nabla\times\boldsymbol{A} \tag{2.19}$$

the equation $\nabla\cdot\left(\mu\boldsymbol{H}_\mathrm{e}\right) = 0$ is satisfied by the definition of $\boldsymbol{A}$. Inserting (2.19) into Faraday's law from (2.3), the relation

$$\nabla\times\left(\boldsymbol{E}_\mathrm{e} + \mathrm{j}\omega\boldsymbol{A}\right) = 0 \tag{2.20}$$

applies which is satisfied by introducing the electric scalar potential ϕ_e according to

$$\boldsymbol{E}_\mathrm{e} + \mathrm{j}\omega\boldsymbol{A} = -\nabla\phi_\mathrm{e}\,. \tag{2.21}$$

Substituting (2.19) and (2.21) into Ampère's law from (2.4) and using that $\nabla\times\nabla\times\boldsymbol{A} = \nabla\left(\nabla\cdot\boldsymbol{A}\right) - \Delta\boldsymbol{A}$, the magnetic vector and the electric scalar potential satisfy the equation

$$\Delta\boldsymbol{A} + k^2\boldsymbol{A} = -\mu\boldsymbol{J} + \mathrm{j}\omega\varepsilon\mu\nabla\phi_\mathrm{e} + \nabla\nabla\cdot\boldsymbol{A}\,. \tag{2.22}$$

The magnetic vector potential is not uniquely defined. Only the curl of $\boldsymbol{A}$ is specified by (2.19), the choice of the divergence of $\boldsymbol{A}$ is free. In order to simplify (2.22), $\nabla\cdot\boldsymbol{A}$ is set to

$$\nabla\cdot\boldsymbol{A} = -\mathrm{j}\omega\mu\varepsilon\phi_\mathrm{e} \tag{2.23}$$

which is referred to as Lorenz gauge condition [Jin10]. Using (2.23), the electric field due to electric sources is derived as

$$\boldsymbol{E}_\mathrm{e} = -\mathrm{j}\omega\left(\boldsymbol{A} + \frac{1}{k^2}\nabla\nabla\cdot\boldsymbol{A}\right) \tag{2.24}$$

and (2.22) is simplified to

$$\Delta \boldsymbol{A} + k^2 \boldsymbol{A} = -\mu \boldsymbol{J} \,. \tag{2.25}$$

In the same manner, the introduction of the electric vector potential for magnetic sources yields

$$\boldsymbol{E}_{\mathrm{m}} = -\frac{1}{\varepsilon} \nabla \times \boldsymbol{F} \,, \tag{2.26}$$

$$\boldsymbol{H}_{\mathrm{m}} = -\mathrm{j}\omega \left(\boldsymbol{F} + \frac{1}{k^2} \nabla \nabla \cdot \boldsymbol{F} \right) \,, \tag{2.27}$$

and

$$\Delta \boldsymbol{F} + k^2 \boldsymbol{F} = -\varepsilon \boldsymbol{M} \,. \tag{2.28}$$

The introduction of scalar and vector potentials simplifies the solution of Maxwell's equations into solving two vector Helmholtz equations, one for the magnetic and one for the electric vector potential. The corresponding electric and magnetic fields are obtained via (2.19), (2.24), (2.26), and (2.27). In Cartesian coordinates, the auxiliary potentials are in particular advantageous as the vector Helmholtz equations in (2.25) and (2.28) decompose into three scalar Helmholtz equations, respectively.

2.2. Rectangular Cavity

2.2.1. Cavity Modes

Consider a source-free rectangular cavity with perfectly electrically conducting (PEC) walls and suppose the size of the cavity is $a \times b \times c$ (see Fig. 2.1). The interior V of the cavity is filled with a homogeneous, isotropic, linear, non-dispersive dielectric with the permittivity $\varepsilon \approx \varepsilon_0$ and the permeability $\mu \approx \mu_0$. According to (2.15) and (2.11), the electric field satisfies

$$\nabla \times \nabla \times \boldsymbol{E} - k^2 \boldsymbol{E} = \boldsymbol{0} \,, \quad \boldsymbol{r} \in V \tag{2.29}$$

together with the boundary condition

$$\hat{n} \times \boldsymbol{E} = \boldsymbol{0} \,, \quad \boldsymbol{r} \in \partial V \tag{2.30}$$

where $\hat{n}$ is the outward directed unit normal on ∂V.

The boundary value problem of the ideal rectangular cavity has a countably infinite number of solutions which are called eigenmodes. To derive the electric and magnetic fields of the eigenmodes, the auxiliary vector potentials introduced in Section 2.1 are used. Eigenmodes which are derived from the magnetic vector potential are called transverse magnetic (TM) modes. Eigenmodes which are derived from the electric vector potential are referred to as transverse electric (TE) modes. In contrast to waveguides, the rectangular cavity does not have a preferred direction. TM and TE modes

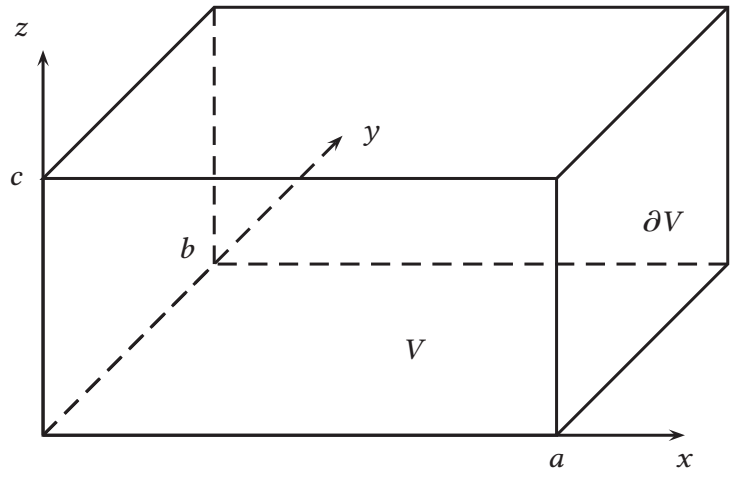

Fig. 2.1.: Source-free rectangular cavity of size $a \times b \times c$ with PEC walls.

can be constructed with respect to x-, y-, or z-direction. However, it is sufficient to select one component of the magnetic and the electric vector potential. The fields of the eigenmodes of the other two components are linearly dependent [Mor53, p. 1849 et sqq.]. In accordance with waveguide theory, the z-component is chosen in what follows.

Solving the homogeneous vector Helmholtz equation for $\boldsymbol{A} = A_z \hat{z}$, applying (2.24) and (2.19), and enforcing the boundary condition from (2.30), the electric and the magnetic field of TM modes become

$$\begin{aligned} \boldsymbol{E}^{\mathrm{TM}}_{mnp}(\boldsymbol{r}) = \mathrm{j}E_0 \frac{k_x k_z}{k_{xyz}^2} \phi_{x,mnp}(\boldsymbol{r})\, \hat{x} + \mathrm{j}E_0 \frac{k_y k_z}{k_{xyz}^2} \phi_{y,mnp}(\boldsymbol{r})\, \hat{y} \\ - \mathrm{j}E_0 \frac{k_x^2 + k_y^2}{k_{xyz}^2} \phi_{z,mnp}(\boldsymbol{r})\, \hat{z}\,, \end{aligned} \tag{2.31}$$

$$\boldsymbol{H}^{\mathrm{TM}}_{mnp}(\boldsymbol{r}) = H_0 \frac{k_y}{k_{xyz}} \psi_{x,mnp}(\boldsymbol{r})\, \hat{x} - H_0 \frac{k_x}{k_{xyz}} \psi_{y,mnp}(\boldsymbol{r})\, \hat{y}\,, \tag{2.32}$$

where m, n, and p are the non-negative indices of the respective mode, $k_x = m\pi/a$, $k_y = n\pi/b$, and $k_z = p\pi/c$ are the wavenumbers in x-, y-, and z-direction, $k_{xyz}^2 = k_x^2 + k_y^2 + k_z^2$, E_0 is the complex amplitude of the electric field, $H_0 = E_0/Z_{\mathrm{F}}$ where

$Z_\mathrm{F} = \sqrt{\mu/\varepsilon}$ is the wave impedance,

$$\phi_{x,mnp}(\boldsymbol{r}) = \sqrt{\frac{\tau_m\tau_n\tau_p}{abc}}\cos(k_x x)\,\sin(k_y y)\,\sin(k_z z)\,, \tag{2.33a}$$

$$\phi_{y,mnp}(\boldsymbol{r}) = \sqrt{\frac{\tau_m\tau_n\tau_p}{abc}}\sin(k_x x)\,\cos(k_y y)\,\sin(k_z z)\,, \tag{2.33b}$$

$$\phi_{z,mnp}(\boldsymbol{r}) = \sqrt{\frac{\tau_m\tau_n\tau_p}{abc}}\sin(k_x x)\,\sin(k_y y)\,\cos(k_z z)\,, \tag{2.33c}$$

where

$$\tau_i = \begin{cases} 2 & \text{if } i \neq 0, \\ 1 & \text{if } i = 0, \end{cases}$$

are the eigenfunctions of the magnetic vector potential, and

$$\psi_{x,mnp}(\boldsymbol{r}) = \sqrt{\frac{\tau_m\tau_n\tau_p}{abc}}\sin(k_x x)\,\cos(k_y y)\,\cos(k_z z)\,, \tag{2.34a}$$

$$\psi_{y,mnp}(\boldsymbol{r}) = \sqrt{\frac{\tau_m\tau_n\tau_p}{abc}}\cos(k_x x)\,\sin(k_y y)\,\cos(k_z z)\,, \tag{2.34b}$$

$$\psi_{z,mnp}(\boldsymbol{r}) = \sqrt{\frac{\tau_m\tau_n\tau_p}{abc}}\cos(k_x x)\,\cos(k_y y)\,\sin(k_z z)\,, \tag{2.34c}$$

are the eigenfunctions of the electric vector potential. In Fig. 2.2, the x-component of the electric and the magnetic field are exemplarily shown for the TM_{221} mode. Analogously, solving the homogeneous vector Helmholtz equation for $\boldsymbol{F} = F_z\hat{z}$, applying (2.26) and (2.27), and enforcing the boundary condition from (2.30), the electric and the magnetic field of the TE modes are derived as

$$\boldsymbol{E}^{\mathrm{TE}}_{mnp}(\boldsymbol{r}) = E_0\frac{k_y}{k_{xyz}}\phi_{x,mnp}(\boldsymbol{r})\,\hat{x} - E_0\frac{k_x}{k_{xyz}}\phi_{y,mnp}(\boldsymbol{r})\,\hat{y}\,, \tag{2.35}$$

$$\begin{aligned}\boldsymbol{H}^{\mathrm{TE}}_{mnp}(\boldsymbol{r}) = {}& \mathrm{j}H_0\frac{k_x k_z}{k_{xyz}^2}\psi_{x,mnp}(\boldsymbol{r})\,\hat{x} + \mathrm{j}H_0\frac{k_y k_z}{k_{xyz}^2}\psi_{y,mnp}(\boldsymbol{r})\,\hat{y} \\ & - \mathrm{j}H_0\frac{k_x^2 + k_y^2}{k_{xyz}^2}\psi_{z,mnp}(\boldsymbol{r})\,\hat{z}\,.\end{aligned} \tag{2.36}$$

For TM modes, the indices m and n must be greater than zero in order to obtain a non-trivial solution. In the case of TE modes, $p > 0$ and a non-zero m or n is sufficient.

The wavenumbers k_x, k_y, and k_z are related to the wavenumber k via the dispersion relation

$$k^2 = k_x^2 + k_y^2 + k_z^2\,. \tag{2.37}$$

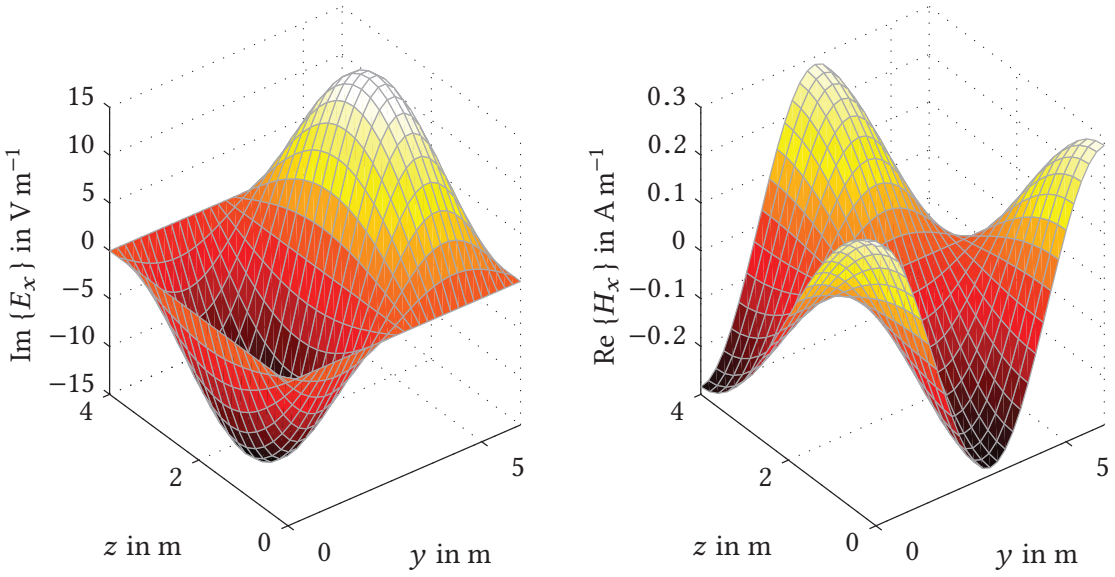

Fig. 2.2.: Im $\{E_x\}$ and Re $\{H_x\}$ of the TM_{221} mode in the plane $x = 4\,\mathrm{m}$ for $E_0 = 10^3\,\mathrm{V\,m^{-1}}$, $Z_\mathrm{F} = 120\pi\,\Omega$, and $a \times b \times c = 12\,\mathrm{m} \times 6\,\mathrm{m} \times 4\,\mathrm{m}$.

Using that $k = 2\pi f/c_0$, where f is the frequency and $c_0 = 1/\sqrt{\mu_0\varepsilon_0}$ is the vacuum speed of light , the resonance frequencies of the cavity are derived as

$$f_{mnp} = \frac{c_0}{2}\sqrt{\left(\frac{m}{a}\right)^2 + \left(\frac{n}{b}\right)^2 + \left(\frac{p}{c}\right)^2}\,. \tag{2.38}$$

In addition to the fields and the resonance frequencies of the eigenmodes, the mode distribution is of interest. Table 2.1 lists the first ten TM or TE modes and their resonant frequencies for a cavity of size $12\,\mathrm{m} \times 6\,\mathrm{m} \times 4\,\mathrm{m}$. Since modes number 4, 5, and 6; 7 and 8; and 9 and 10 have the same resonances frequencies, they are called degenerate modes. An estimation of the cumulated number of modes N_modes is given in [Liu83]. It is approximately

$$N_\mathrm{modes} \approx \frac{8\pi}{3}abc\left(\frac{f}{c_0}\right)^3 - (a+b+c)\,\frac{f}{c_0} + \frac{1}{2}\,. \tag{2.39}$$

The cumulated number of modes grows with f^3. Differentiating (2.39) with respect to frequency gives the mode density [Liu83]

$$\frac{\partial N_\mathrm{modes}}{\partial f} \approx 8\pi abc\left(\frac{f}{c_0}\right)^2 - (a+b+c)\,\frac{1}{c_0}\,. \tag{2.40}$$

The mode density increases with f^2. In Fig. 2.3, the cumulated number of modes and the estimated cumulated number of modes according to (2.39) are shown for a cubical

Number	Mode	f_{mnp} in MHz
1	TM_{110}	27.95
2	TM_{210}	35.36
3	TE_{101}	39.53
4	TE_{011}	45.07
5	TE_{201}	45.07
6	TM_{310}	45.07
7	TM_{111}	46.77
8	TE_{111}	46.77
9	TM_{120}	51.54
10	TM_{211}	51.54

Tab. 2.1.: First ten eigenmodes and their resonance frequencies for a cavity of size $12\,\mathrm{m} \times 6\,\mathrm{m} \times 4\,\mathrm{m}$.

and a cuboidal cavity. In both cases, (2.39) approximates the cumulated number of modes very well.

The cumulated number of modes and the mode density are important parameters for reverberation chambers. While microwave resonators are usually operated in the range of the fundamental resonance, reverberation chambers are operated in the over-moded frequency range of the cavity. The performance of reverberation chambers depends on the mode density. The higher the density of modes, the better is the performance of the chamber. Therefore, the lowest usable frequency of a reverberation chamber is often estimated using the cumulated number of modes or the mode density. It is defined by either the resonance frequency of the 60th eigenmode or a mode density which is greater than 1.5 modes/MHz. In the case of a cavity size of $12\,\mathrm{m} \times 6\,\mathrm{m} \times 4\,\mathrm{m}$, the resonance frequency of the 60th mode is 100.78 MHz and the mode density meets the requirement at about 75 MHz.

2.2.2. Wall Losses and Quality Factor

Real cavity walls are well but imperfectly conducting. The exact analytic solution of the boundary value problem of the imperfect cavity is difficult but an approximate solution is found using perturbation theory [Jin10]. The field distribution in the imperfect cavity is approximated by the field distribution of the corresponding perfect cavity. In contrast to the ideal cavity, the eigenmodes in the real cavity are damped. In frequency domain, a damped oscillation is usually modeled by a complex wavenumber according to [Hil94]

$$k_\mathrm{c} = k\left(1 - \frac{1}{2Q}\right) \tag{2.41}$$

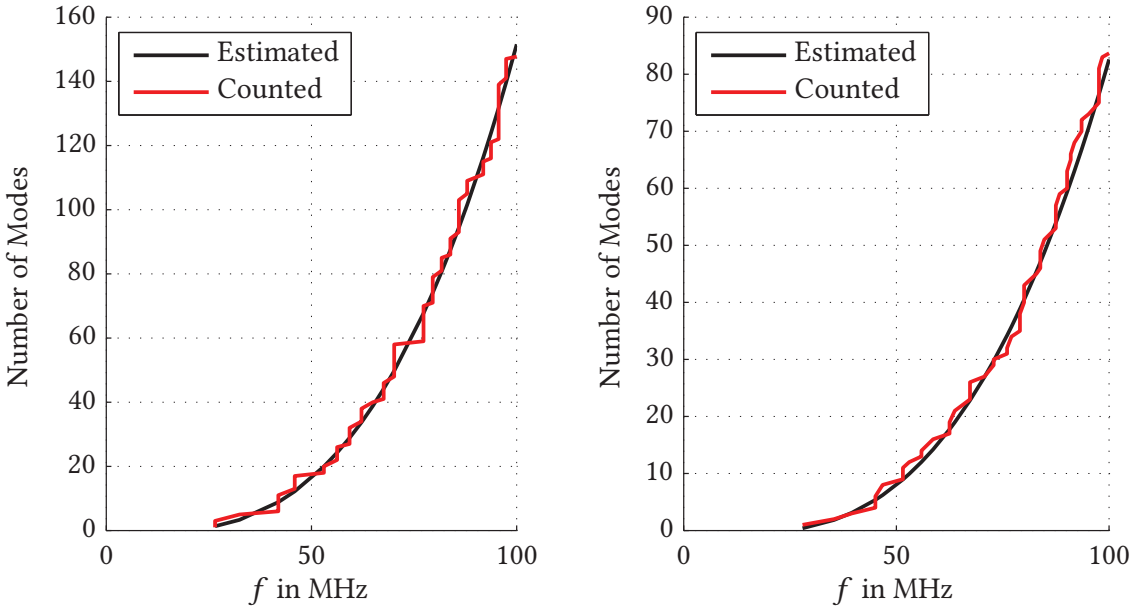

(a) Cavity size $a \times b \times c = 8\,\mathrm{m} \times 8\,\mathrm{m} \times 8\,\mathrm{m}$ *(b)* Cavity size $a \times b \times c = 12\,\mathrm{m} \times 6\,\mathrm{m} \times 4\,\mathrm{m}$

Fig. 2.3.: Counted cumulated number of modes and estimated cumulated number of modes according to (2.39).

where Q is the quality factor of the resonator. In general, the quality factor is defined as the ratio of the stored and the dissipated energy per period [Jac99]

$$Q = \omega \frac{\overline{W}_\mathrm{s}}{\overline{P}_\mathrm{l}} \tag{2.42}$$

where $\overline{W}_\mathrm{s}$ is the time-averaged stored energy and $\overline{P}_\mathrm{l}$ is the average power loss. In the case of the rectangular resonator, the quality factor of a mode mnp becomes [Hil09]

$$Q_{mnp} = \omega \frac{\mu \iiint_V \boldsymbol{H}_{mnp} \cdot \boldsymbol{H}^*_{mnp} \,\mathrm{d}v}{Z_\mathrm{s} \iint_S \boldsymbol{H}_{mnp} \cdot \boldsymbol{H}^*_{mnp} \,\mathrm{d}a} \tag{2.43}$$

where $\boldsymbol{H}_{mnp}$ is the magnetic field of the respective cavity mode,

$$Z_\mathrm{s} = \sqrt{\frac{\omega \mu_\mathrm{w}}{2\kappa_\mathrm{w}}} = \frac{1}{\kappa_\mathrm{w} \delta_\mathrm{w}} \tag{2.44}$$

is the surface impedance of the walls, μ_w is the wall permeability, κ_w is the wall conductivity, and δ_w is the skin depth of the walls. Inserting (2.32) and (2.36) respectively

into (2.43), the quality factors of TM and TE modes become

$$Q_{mnp}^{\mathrm{TM}} = \frac{\tau_p}{2\mu_{\mathrm{r,w}}\delta_{\mathrm{w}}} \frac{abc\,k_{xy}^2}{a\left(c\tau_p + b\right)k_y^2 + b\left(c\tau_p + a\right)k_x^2}, \tag{2.45}$$

$$Q_{mnp}^{\mathrm{TE}} = \frac{\tau_m\tau_n}{2\mu_{\mathrm{r,w}}\delta_{\mathrm{w}}} \frac{abc\,k^2k_{xy}^2}{bc\tau_n\left(k_{xy}^4 + k_z^2k_y^2\right) + ac\tau_m\left(k_{xy}^4 + k_z^2k_x^2\right) + ab\tau_m\tau_nk_{xy}^2k_z^2} \tag{2.46}$$

where $k_{xy}^2 = k_x^2 + k_y^2$ and $\mu_{\mathrm{r,w}}$ is the relative wall permeability.

A composite Q of TM and TE modes is calculated by averaging $1/Q$ over the individual modes. According to [Liu83], the composite Q of the rectangular cavity is given by

$$Q = \frac{1}{\left\langle \frac{1}{Q_{mnp}} \right\rangle} = \frac{3V}{2\mu_w S_{\mathrm{w}}\delta_{\mathrm{w}}} \frac{1}{1 + \frac{3\pi}{8k}\left(\frac{1}{a} + \frac{1}{b} + \frac{1}{c}\right)} \tag{2.47}$$

where V is the volume and S_{w} is the surface area of the cavity. For electrically large cavities (i.e., $ka \gg 1$, $kb \gg 1$, and $kc \gg 1$), (2.47) becomes

$$Q = \frac{3V}{2\mu_{\mathrm{w}}S_{\mathrm{w}}\delta_{\mathrm{w}}}. \tag{2.48}$$

In [Dun90], (2.47) and (2.48) were confirmed by using a local plane-wave method. It was shown that the additional terms in (2.47) originate from opposite walls in electrically short distance and from cavity edges. In Fig. 2.4a and 2.4b, the quality factors of the individual TM and TE modes and the composite Q's according to (2.47) and (2.48) are respectively shown for a cubical and an elongated cavity. Although the derivations in [Liu83] and [Dun90] are correct under the assumptions made, in the lower frequency range, (2.47) rather gives a lower bound for the individual quality factors than the average Q. The asymptotic composite Q from (2.48), on the other hand, provides a good estimate of the average Q at all frequencies.

2.2.3. Green's Functions

In the previous sections, the source-free cavity has been considered (i.e., the homogeneous boundary value problem). In this section, the inhomogeneous boundary value problem (e.g., an ideal cavity with an electric current source, see Fig. 2.5) is analyzed. Inhomogeneous boundary value problems can be solved using Green's functions. The Green's function of a boundary value problem is defined as its impulse response [Jac99]. Hence, using (2.15) together with (2.30), the Green's function of the rectangular cavity for the electric field due to electric currents satisfies

$$\nabla\times\nabla\times\overline{\boldsymbol{G}}_{\mathrm{J}}^{\mathrm{E}}\left(\boldsymbol{r},\boldsymbol{r}'\right) - k^2\overline{\boldsymbol{G}}_{\mathrm{J}}^{\mathrm{E}}\left(\boldsymbol{r},\boldsymbol{r}'\right) = -\mathrm{j}\omega\mu\,\overline{\boldsymbol{I}}\,\delta\left(\boldsymbol{r}-\boldsymbol{r}'\right), \quad \boldsymbol{r}\in V \tag{2.49}$$

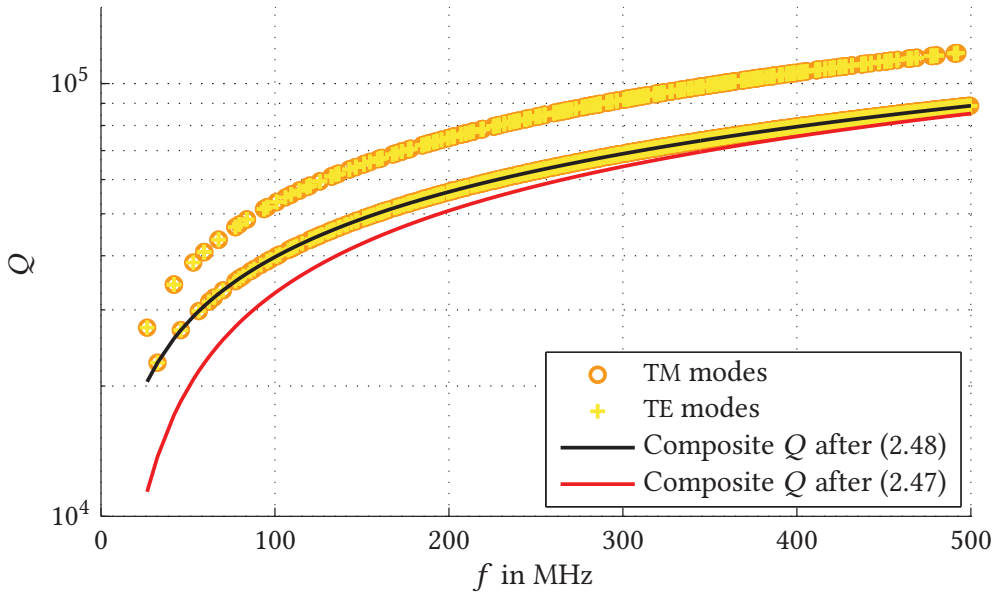

(a) Cavity size $a \times b \times c = 8\,\mathrm{m} \times 8\,\mathrm{m} \times 8\,\mathrm{m}$

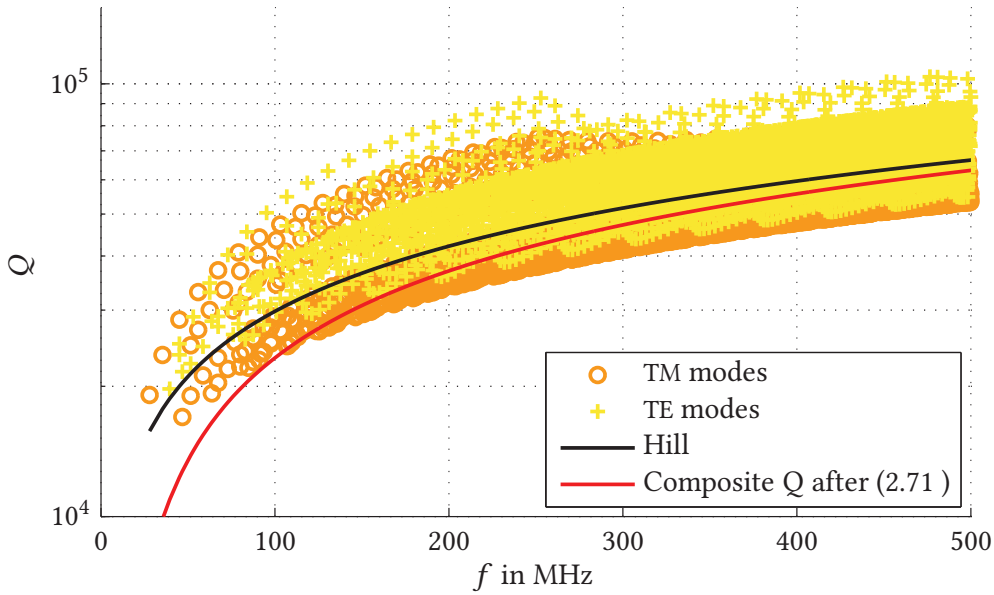

(b) Cavity size $a \times b \times c = 12\,\mathrm{m} \times 6\,\mathrm{m} \times 4\,\mathrm{m}$

Fig. 2.4.: Individual and composite quality factors for a wall conductivity of $\kappa_\mathrm{w} = 10^6\,\mathrm{S\,m^{-1}}$.

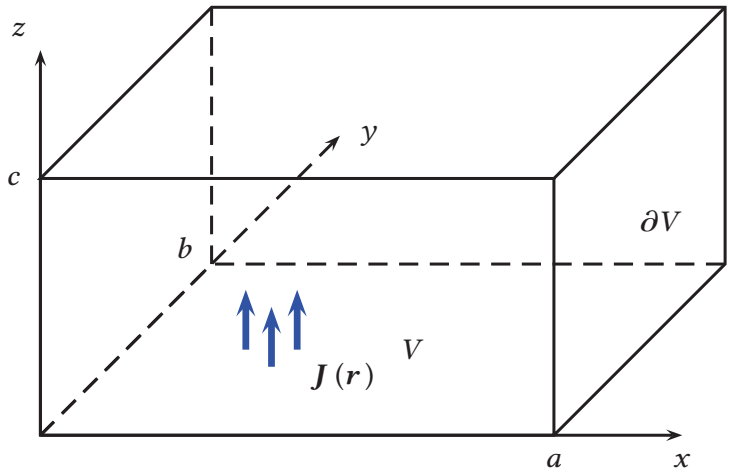

Fig. 2.5.: Ideal rectangular cavity with electric current density.

together with the boundary condition

$$\hat{n} \times \overline{G}_{\mathrm{J}}^{\mathrm{E}}\left(\boldsymbol{r}, \boldsymbol{r}'\right) = \mathbf{0}\,, \quad \boldsymbol{r} \in \partial V \tag{2.50}$$

where $\overline{\boldsymbol{I}}$ is the identity dyad[2] and $\delta\left(\boldsymbol{r} - \boldsymbol{r}'\right)$ is the Dirac delta distribution [Råd04]. In the same manner, the Green's function for the electric field due to magnetic currents and the Green's functions for the magnetic field are defined.

Following Section 2.1.2, auxiliary vector potentials are used to derive the Green's functions of the rectangular cavity for the electric and the magnetic field. According to (2.25), the Green's function for the magnetic vector potential $\overline{\boldsymbol{G}}^{\mathrm{A}}$ satisfies

$$\Delta \overline{\boldsymbol{G}}^{\mathrm{A}}\left(\boldsymbol{r}, \boldsymbol{r}'\right) + k^2 \overline{\boldsymbol{G}}^{\mathrm{A}}\left(\boldsymbol{r}, \boldsymbol{r}'\right) = -\mu\, \overline{\boldsymbol{I}}\, \delta\left(\boldsymbol{r} - \boldsymbol{r}'\right)\,, \quad \boldsymbol{r} \in V \tag{2.51}$$

together with the boundary condition

$$\hat{n} \times \left(\overline{\boldsymbol{I}} + \frac{1}{k^2} \nabla\nabla\right) \cdot \overline{\boldsymbol{G}}^{\mathrm{A}}\left(\boldsymbol{r}, \boldsymbol{r}'\right) = \mathbf{0}\,, \quad \boldsymbol{r} \in \partial V \tag{2.52}$$

where (2.24) and (2.50) have been used to derive (2.52). Using (2.28), the Green's function for the electric vector potential $\overline{\boldsymbol{G}}^{\mathrm{F}}$ satisfies

$$\Delta \overline{\boldsymbol{G}}^{\mathrm{F}}\left(\boldsymbol{r}, \boldsymbol{r}'\right) + k^2 \overline{\boldsymbol{G}}^{\mathrm{F}}\left(\boldsymbol{r}, \boldsymbol{r}'\right) = -\varepsilon\, \mathbf{I}\, \delta\left(\boldsymbol{r} - \boldsymbol{r}'\right)\,, \quad \boldsymbol{r} \in V \tag{2.53}$$

2 In Cartesian coordinates the identity dyad is given by $\overline{\boldsymbol{I}} = \hat{x}\hat{x} + \hat{y}\hat{y} + \hat{z}\hat{z}$.

together with the boundary condition

$$\hat{n} \times \nabla \times \overline{G}^{\mathrm{F}}\left(\boldsymbol{r}, \boldsymbol{r}'\right) = \mathbf{0}\,, \quad \boldsymbol{r} \in \partial V \tag{2.54}$$

where (2.26) and (2.50) have been used to derive (2.54). Different techniques are available to construct the Green's function of the rectangular cavity (e.g., the image principle and eigenfunction expansions). The different representations are introduced and analyzed in Chapter 3.

The solution of the inhomogeneous boundary value problem results as the convolution of the corresponding Green's function and the source distribution [Jac99]. Hence, the magnetic and the electric vector potential are calculated from an electric current density $\boldsymbol{J}$ and an magnetic current density $\boldsymbol{M}$ as

$$\boldsymbol{A}(\boldsymbol{r}) = \iiint_V \overline{G}^{\mathrm{A}}\left(\boldsymbol{r}, \boldsymbol{r}'\right) \cdot \boldsymbol{J}\left(\boldsymbol{r}'\right) \mathrm{d}v'\,, \tag{2.55}$$

$$\boldsymbol{F}(\boldsymbol{r}) = \iiint_V \overline{G}^{\mathrm{F}}\left(\boldsymbol{r}, \boldsymbol{r}'\right) \cdot \boldsymbol{M}\left(\boldsymbol{r}'\right) \mathrm{d}v'\,, \tag{2.56}$$

respectively. Using (2.19) – (2.27), the electric and magnetic field become

$$\begin{aligned} \boldsymbol{E}(\boldsymbol{r}) = {} & -\mathrm{j}\omega \iiint_V \left(\overline{I} + \frac{1}{k^2}\nabla\nabla\right) \cdot \overline{G}^{\mathrm{A}}\left(\boldsymbol{r}, \boldsymbol{r}'\right) \cdot \boldsymbol{J}\left(\boldsymbol{r}'\right) \mathrm{d}v' \\ & - \frac{1}{\varepsilon} \iiint_V \nabla \times \overline{G}^{\mathrm{F}}\left(\boldsymbol{r}, \boldsymbol{r}'\right) \cdot \boldsymbol{M}\left(\boldsymbol{r}'\right) \mathrm{d}v'\,, \qquad \boldsymbol{r} \in V, \end{aligned} \tag{2.57}$$

$$\begin{aligned} \boldsymbol{H}(\boldsymbol{r}) = {} & \frac{1}{\mu} \iiint_V \nabla \times \overline{G}^{\mathrm{A}}\left(\boldsymbol{r}, \boldsymbol{r}'\right) \cdot \boldsymbol{J}\left(\boldsymbol{r}'\right) \mathrm{d}v' \\ & - \mathrm{j}\omega \iiint_V \left(\overline{I} + \frac{1}{k^2}\nabla\nabla\right) \cdot \overline{G}^{\mathrm{F}}\left(\boldsymbol{r}, \boldsymbol{r}'\right) \cdot \boldsymbol{M}\left(\boldsymbol{r}'\right) \mathrm{d}v'\,, \qquad \boldsymbol{r} \in V, \end{aligned} \tag{2.58}$$

respectively.

The Helmholtz equations in (2.25) and (2.28) for the magnetic and the electric vector potential and (2.24) and (2.27) are derived under the assumption that the magnetic and the electric vector potential satisfy the Lorenz gauge condition [Jin10]. Accordingly, the Green's functions of the magnetic and the electric vector potential must meet the Lorenz gauge in order for (2.57) and (2.58) to be valid. In Appendix A.1, the validity of the Lorenz gauge for the Green's function of the rectangular cavity is shown.

2.3. Surface Integral Equations

In Section 2.2, the homogeneous and the inhomogeneous boundary value problem of the rectangular cavity have been considered for perfectly and imperfectly conducting cavity walls. In this section, arbitrarily shaped objects are placed in the cavity. The

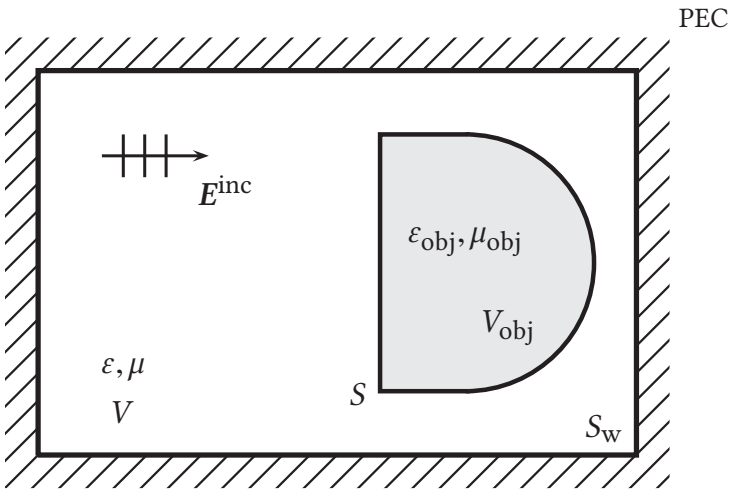

Fig. 2.6.: Rectangular cavity with arbitrarily shaped objects.

walls of the cavity are modeled as PEC and the cavity is excited by an incident electric field $\boldsymbol{E}_{\text{inc}}$. The material properties of the objects are described by the permittivity ε_{obj} and the permeability μ_{obj}. The interior of the objects is denoted by V_{obj}, the volume in the cavity is referred to as V, and S and S_{w} denote the surfaces of the objects and the cavity walls, respectively, see Fig. 2.6.

In general, the considered problem does not have an analytical solution and needs to be approximated using numerical techniques. While local techniques, such as finite difference and finite element methods, discretize the partial differential equations (i.e., Maxwell's equations), boundary element methods approximate the corresponding integral equations (i.e., the Stratton-Chu integral equations). In the following, the Stratton-Chu integral equations are derived but in contrast to the standard formulation, the Green's function of the rectangular cavity is used instead of the Green's function of free-space.

Using the surface equivalence principle [Jin10] with the CGF, the boundary value problem is converted into an equivalent empty cavity problem. The objects inside the cavity are replaced by equivalent electric and magnetic surface currents densities according to [Jin10]

$$\boldsymbol{J}_{\text{s}} = \hat{n} \times \boldsymbol{H}\big|_S, \tag{2.59}$$

$$\boldsymbol{M}_{\text{s}} = -\hat{n} \times \boldsymbol{E}\big|_S \tag{2.60}$$

where $\boldsymbol{E} = \boldsymbol{E}_{\text{inc}} + \boldsymbol{E}_{\text{sca}}$ and $\boldsymbol{H} = \boldsymbol{H}_{\text{inc}} + \boldsymbol{H}_{\text{sca}}$ are the total (incident and scattered) electric and magnetic field, respectively. The cavity walls do not need to be replaced by equivalent currents as they are incorporated into the CGF. The equivalent empty cavity problem is illustrated in Fig. 2.7.

In the volume V, the scattered fields are related to the equivalent currents via (2.57) and (2.58). On the boundary S, the integrals in (2.57) and (2.58) become singular. They

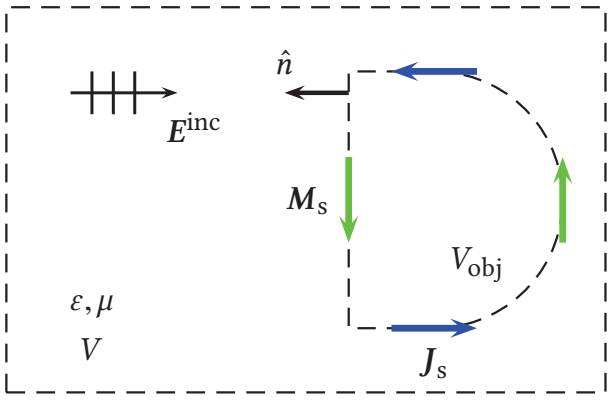

Fig. 2.7.: Equivalent empty-cavity problem.

are evaluated in a principle value sense, after the singularities have been extracted analytically [Mic14]. On locally smooth surfaces, the total fields satisfy [Ylä13]

$$\frac{1}{2}\boldsymbol{E}(\boldsymbol{r}) = -Z_{\text{F}}\mathcal{T}^{A}\left(\boldsymbol{J}_{\text{s}}\right) - \mathcal{K}^{F}\left(\boldsymbol{M}_{\text{s}}\right) + \boldsymbol{E}_{\text{inc}}(\boldsymbol{r}), \qquad \boldsymbol{r} \in S, \tag{2.61}$$

$$\frac{1}{2}\boldsymbol{H}(\boldsymbol{r}) = -\frac{1}{Z_{\text{F}}}\mathcal{T}^{F}\left(\boldsymbol{M}_{\text{s}}\right) + \mathcal{K}^{A}\left(\boldsymbol{J}_{\text{s}}\right) + \boldsymbol{H}_{\text{inc}}(\boldsymbol{r}), \qquad \boldsymbol{r} \in S \tag{2.62}$$

where $\mathcal{T}^{A/F} = \mathcal{T}_{\text{w}}^{A/F} + \mathcal{T}_{\text{h}}^{A/F}$, the weakly singular and the hypersingular operator[3] $\mathcal{T}_{\text{w}}^{A/F}$ and $\mathcal{T}_{\text{h}}^{A/F}$ are defined as

$$\mathcal{T}_{\text{w}}^{A/F}(\boldsymbol{X}) = \frac{\mathrm{j}k}{\mu/\varepsilon}\iint_{S}\overline{\boldsymbol{G}}^{A/F}\left(\boldsymbol{r},\boldsymbol{r}'\right)\cdot\boldsymbol{X}\left(\boldsymbol{r}'\right)\mathrm{d}s', \tag{2.63}$$

$$\mathcal{T}_{\text{h}}^{A/F}(\boldsymbol{X}) = \frac{\mathrm{j}k}{\mu/\varepsilon}\iint_{S}\frac{1}{k^2}\nabla\nabla\cdot\overline{\boldsymbol{G}}^{A/F}\left(\boldsymbol{r},\boldsymbol{r}'\right)\cdot\boldsymbol{X}\left(\boldsymbol{r}'\right)\mathrm{d}s', \tag{2.64}$$

and

$$\mathcal{K}^{A/F}(\boldsymbol{X}) = \frac{1}{\mu/\varepsilon}\iint_{S}\nabla\times\overline{\boldsymbol{G}}^{A/F}\left(\boldsymbol{r},\boldsymbol{r}'\right)\cdot\boldsymbol{X}\left(\boldsymbol{r}'\right)\mathrm{d}s' \tag{2.65}$$

is a strong singular operator.

The fields in (2.61) and (2.62) are related to the equivalent currents via (2.59) and (2.60) on the surface S. Following [Ylä13], the tangential trace operator τ_{t} and the

3 Herein, weakly, strong, and hypersingular operator refer to integral kernels which are proportional to $1/r$, $1/r^2$, and $1/r^3$, respectively where r is the distance between $\boldsymbol{r}$ and $\boldsymbol{r}'$

rotated tangential trace operator τ_r are defined as

$$\tau_\mathrm{t}\boldsymbol{X} := -\hat{n}\times\hat{n}\times\boldsymbol{X}\Big|_S\,, \tag{2.66}$$

$$\tau_\mathrm{r}\boldsymbol{X} := \quad \hat{n}\times\boldsymbol{X}\Big|_S\,. \tag{2.67}$$

Applying the tangential trace operator to (2.61) and using the boundary condition for the electric field according to (2.59) yields the electric field integral equation (EFIE)

$$\frac{1}{2}\hat{n}\times\boldsymbol{M}_\mathrm{s} - \hat{n}\times\hat{n}\times\left[Z_\mathrm{F}\mathcal{T}^A\left(\boldsymbol{J}_\mathrm{s}\right) + \mathcal{K}^F\left(\boldsymbol{M}_\mathrm{s}\right)\right] = -\hat{n}\times\hat{n}\times\boldsymbol{E}^\mathrm{inc}\left(\boldsymbol{r}\right). \tag{2.68}$$

Analogously, applying the rotated tangential trace operator to (2.62) and using the boundary condition for the magnetic field according to (2.60) gives the magnetic field integral equation (MFIE)

$$\frac{1}{2}\boldsymbol{J}_\mathrm{s} + \hat{n}\times\left[\frac{1}{Z_\mathrm{F}}\mathcal{T}^F\left(\boldsymbol{M}_\mathrm{s}\right) - \mathcal{K}^A\left(\boldsymbol{J}_\mathrm{s}\right)\right] = \hat{n}\times\boldsymbol{H}^\mathrm{inc}\left(\boldsymbol{r}\right). \tag{2.69}$$

Both the EFIE and the MFIE suffer from the internal resonance problem [Che01]. When the frequency of the incident wave is equal to an internal resonance frequency of a closed body, the solution is not unique [Che01]. The internal resonance problem can be overcome by using a combined field integral equation (CFIE) formulation. The CFIE is a linear combination of EFIE and MFIE according to

$$\mathrm{CFIE} = \alpha\,\mathrm{EFIE} + (1-\alpha)Z_\mathrm{F}\,\hat{n}\times\mathrm{MFIE} \tag{2.70}$$

where $0 \leq \alpha \leq 1$ is the combination coefficient. The CFIE is free from interior resonances as it shifts the internal resonance frequencies into the complex plane [Che01].

The discretization of the EFIE in (2.68) or the MFIE in (2.69) yields an underdetermined linear equation system. The unknown equivalent electric and magnetic current densities generate double the unknowns as equations. Additional constraints are necessary to solve the boundary value problem. As the integral equations in (2.68) and (2.69) only describe the field problem in V, the interior of the objects needs to be considered additionally. Setting up equations for the interior completes the system of equations. In the following, three cases are addressed: PEC, metallic, and dielectric objects.

On perfect electric conductors, the magnetic current density is zero. The number of unknowns is halved and the solution of the boundary value problem becomes unique. The EFIE and the MFIE from (2.68) and (2.69) simplify to

$$Z_\mathrm{F}\,\hat{n}\times\hat{n}\times\mathcal{T}^A\left(\boldsymbol{J}_\mathrm{s}\right) = \hat{n}\times\hat{n}\times\boldsymbol{E}^\mathrm{inc}\left(\boldsymbol{r}\right), \tag{2.71}$$

$$\frac{1}{2}\boldsymbol{J}_\mathrm{s} - \hat{n}\times\mathcal{K}^A\left(\boldsymbol{J}_\mathrm{s}\right) = \hat{n}\times\boldsymbol{H}^\mathrm{inc}\left(\boldsymbol{r}\right). \tag{2.72}$$

The EFIE in (2.71) is an integral equation of the first kind since the unknown quantity occurs only inside the integral. It is applicable to closed and open surfaces. In the

latter case, the surface current is the sum of the currents on both sides of the surface. The MFIE in (2.72) is an integral equation of the second kind as the unknown quantity occurs inside and outside the integral. In contrast to (2.71), it cannot be applied to open surfaces as the boundary condition for the magnetic field is not unique on an open PEC surface.

Good, but not perfect conductors actually belong to the class of penetrable objects. However, as the fields decay rapidly in the interior, they can be modeled using impedance boundary conditions (IBCs) [Sen95]. The most wide-spread IBC goes back to Leontovich. On a planar surface, the electric current density is related to the magnetic current density via

$$\boldsymbol{M}_\mathrm{s} = -Z_\mathrm{s}\hat{\boldsymbol{n}} \times \boldsymbol{J}_\mathrm{s} \tag{2.73}$$

where the characteristic surface impedance $Z_\mathrm{s} = \sqrt{\mu\omega/\kappa}$, μ is the permeability, and κ is the conductivity of the object. Impedance boundary conditions are applicable to solid objects (i.e., closed objects) only. Infinitesimally thin imperfectly conducting bodies can be modeled using resistive sheet boundary conditions [Med85].

In the case of dielectric bodies, the fields in the exterior and in the interior need to be considered. When the dielectric is homogeneous, a second set of integral equations can be formulated for the interior [Ylä13]. When the dielectric is inhomogeneous or anisotropic, surface integral equations are less appropriate [Ylä13] and hybrid methods, such as the finite element boundary integral (FE/BI) method, become favorable [Eib96; Eib99; Jin10]. The exterior is modeled in the integral equation while the interior is considered in the finite element (FE) formulation.

2.4. Method of Moments

The MoM is a general projection method: a linear integral (or differential) equation is approximated in a finite-dimensional space by a matrix-vector equation. Firstly, the unknown quantity is represented by a finite set of N basis functions. Secondly, the discretized quantity is inserted into the integral equation yielding an equation with N unknown coefficients. Lastly, to obtain a matrix-vector equation, the discretized integral equation is tested with so-called testing or weighting functions (i.e., the L^2-inner product of testing functions and the discretized integral equation is formed). A proper choice of the basis functions is crucial [Ylä13]. Appropriate basis functions should span the domain of the integral operator (i.e., the physical properties of the unknown quantity are represented well). When basis and testing functions are the same, the testing procedure is called a Galerkin method.

In the case of the EFIE and the MFIE, the unknown electric and magnetic current densities are elements of the Sobolev space $\mathcal{H}_\mathrm{div}^{-1/2}$ [Ylä13]. Basis functions in $\mathcal{H}_\mathrm{div}^{-1/2}$ are divergence-conforming (i.e., they are able to appropriately approximate the surface current and charge density). Non divergence-conforming basis functions would, for instance, allow unphysical line charges. The lowest order divergence-conforming func-

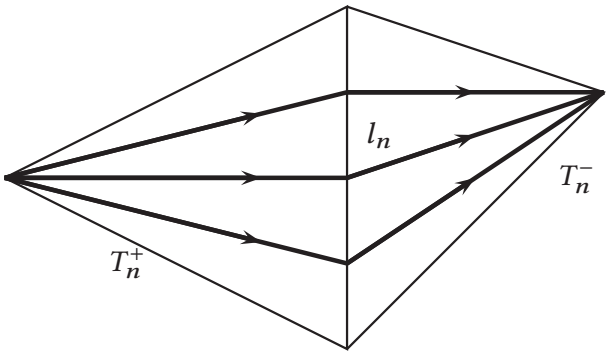

Fig. 2.8: RWG function on two adjacent triangles.

tions on a triangular mesh are the Rao-Wilton-Glisson (RWG) basis functions [Rao82]. RWG functions are local basis functions. They are defined on two adjacent triangles T_n^+ and T_n^- according to

$$\boldsymbol{\beta}_n(\boldsymbol{r}) = \begin{cases} \frac{l_n}{2A_n^\pm}\boldsymbol{\rho}_n^\pm, & \boldsymbol{r} \in T_n^\pm, \\ 0, & \text{otherwise} \end{cases} \tag{2.74}$$

where n is the index of the common edge of the triangles, l_n is the length of the common edge, $\boldsymbol{\rho}_n^\pm$ are the vectors connecting the free vertex of the triangle and the position vector $\boldsymbol{r}$ and vice versa, and $A_n^\pm$ is the surface area of the respective triangle (see Fig. 2.8). Expanding the unknown electric and magnetic surface current density into RWG basis functions gives

$$\boldsymbol{J}_\mathrm{s}(\boldsymbol{r}) \approx \sum_{n=1}^{N} I_n \boldsymbol{\beta}_n(\boldsymbol{r}), \tag{2.75}$$

$$\boldsymbol{M}_\mathrm{s}(\boldsymbol{r}) \approx \sum_{n=1}^{N} V_n \boldsymbol{\beta}_n(\boldsymbol{r}) \tag{2.76}$$

where I_n are the unknown current coefficients and V_n are the unknown voltage coefficients.

Inserting (2.75) and (2.76) in (2.68) yields the discretized EFIE. Following the classical approach [Rao82; Son97; Ism09], the discretized EFIE is tested with RWG functions. Using the identity[4] $\boldsymbol{\beta} \cdot (\hat{n} \times \hat{n} \times \boldsymbol{X}) = -\boldsymbol{\beta} \cdot \boldsymbol{X}$ yields a linear equation system in form of

$$\left(\frac{1}{2}\boldsymbol{A} + \frac{1}{\varepsilon}\boldsymbol{D}\right)\boldsymbol{v} + Z_\mathrm{F}\left(\frac{\mathrm{j}k}{\mu}\boldsymbol{B} + \frac{\mathrm{j}k}{\mu}\boldsymbol{C}\right)\boldsymbol{i} = \boldsymbol{g} \tag{2.77}$$

4 $\boldsymbol{\beta} \cdot (\hat{n} \times \hat{n} \times \boldsymbol{X}) = \boldsymbol{\beta} \cdot [(\hat{n} \cdot \boldsymbol{X})\,\hat{n} - (\hat{n} \cdot \hat{n})\,\boldsymbol{X}] = \boldsymbol{\beta} \cdot \hat{n}\,(\hat{n} \cdot \boldsymbol{X}) - \boldsymbol{\beta} \cdot \boldsymbol{X} = -\boldsymbol{\beta} \cdot \boldsymbol{X}$, as $\boldsymbol{\beta}$ is orthogonal to $\hat{n}$.

where the system matrices are

$$[\boldsymbol{A}]_{mn} = \iint_S \boldsymbol{\beta}_m(\boldsymbol{r}) \cdot \left[\hat{n} \times \boldsymbol{\beta}_n(\boldsymbol{r})\right] \mathrm{d}s\,, \tag{2.78a}$$

$$[\boldsymbol{B}]_{mn} = \iint_S \boldsymbol{\beta}_m(\boldsymbol{r}) \cdot \iint_S \overline{G}^{\mathrm{A}}\left(\boldsymbol{r},\boldsymbol{r}'\right) \cdot \boldsymbol{\beta}_n\left(\boldsymbol{r}'\right) \mathrm{d}s'\,\mathrm{d}s\,, \tag{2.78b}$$

$$[\boldsymbol{C}]_{mn} = \iint_S \boldsymbol{\beta}_m(\boldsymbol{r}) \cdot \iint_S \frac{1}{k^2}\nabla\nabla \cdot \overline{G}^{\mathrm{A}}\left(\boldsymbol{r},\boldsymbol{r}'\right) \cdot \boldsymbol{\beta}_n\left(\boldsymbol{r}'\right) \mathrm{d}s'\,\mathrm{d}s\,, \tag{2.78c}$$

$$[\boldsymbol{D}]_{mn} = \iint_S \boldsymbol{\beta}_m(\boldsymbol{r}) \cdot \iint_S \nabla \times \overline{G}^{\mathrm{F}}\left(\boldsymbol{r},\boldsymbol{r}'\right) \cdot \boldsymbol{\beta}_n\left(\boldsymbol{r}'\right) \mathrm{d}s'\,\mathrm{d}s\,, \tag{2.78d}$$

$m = 1,\ldots,N$, and the excitation vector is

$$[\boldsymbol{g}]_m = \iint_S \boldsymbol{\beta}_m(\boldsymbol{r}) \cdot \boldsymbol{E}_{\mathrm{inc}}(\boldsymbol{r})\,\mathrm{d}s\,. \tag{2.79}$$

Analogously, inserting (2.75) and (2.76) in $\hat{n}\times$(2.69) yields the discretized $\hat{n}\times$MFIE. Again, following the classical approach, the discretized $\hat{n}\times$MFIE is tested with $\hat{n}\times$RWG functions. Using the identity[5] $\left(\hat{n}\times\boldsymbol{\beta}\right)\cdot(\hat{n}\times\hat{n}\times\boldsymbol{X}) = -\left(\hat{n}\times\boldsymbol{\beta}\right)\cdot\boldsymbol{X}$ gives a linear equation system of the form

$$\frac{1}{Z_{\mathrm{F}}}\left(-\frac{1}{2}\boldsymbol{A}' - \frac{1}{\mu}\boldsymbol{D}'\right)\boldsymbol{v} + \left(\frac{\mathrm{j}k}{\varepsilon}\boldsymbol{B}' + \frac{\mathrm{j}k}{\varepsilon}\boldsymbol{C}'\right)\boldsymbol{i} = \boldsymbol{g}' \tag{2.80}$$

where the system matrices are

$$\left[\boldsymbol{A}'\right]_{mn} = \iint_S \left[\hat{n} \times \boldsymbol{\beta}_m(\boldsymbol{r})\right] \cdot \left[\hat{n} \times \boldsymbol{\beta}_n(\boldsymbol{r})\right] \mathrm{d}s\,, \tag{2.81a}$$

$$\left[\boldsymbol{B}'\right]_{mn} = \iint_S \left[\hat{n} \times \boldsymbol{\beta}_m(\boldsymbol{r})\right] \cdot \iint_S \overline{G}^{\mathrm{F}}\left(\boldsymbol{r},\boldsymbol{r}'\right) \cdot \boldsymbol{\beta}_n\left(\boldsymbol{r}'\right) \mathrm{d}s'\,\mathrm{d}s\,, \tag{2.81b}$$

$$\left[\boldsymbol{C}'\right]_{mn} = \iint_S \left[\hat{n} \times \boldsymbol{\beta}_m(\boldsymbol{r})\right] \cdot \iint_S \frac{1}{k^2}\nabla\nabla \cdot \overline{G}^{\mathrm{F}}\left(\boldsymbol{r},\boldsymbol{r}'\right) \cdot \boldsymbol{\beta}_n\left(\boldsymbol{r}'\right) \mathrm{d}s'\,\mathrm{d}s\,, \tag{2.81c}$$

$$\left[\boldsymbol{D}'\right]_{mn} = \iint_S \left[\hat{n} \times \boldsymbol{\beta}_m(\boldsymbol{r})\right] \cdot \iint_S \nabla \times \overline{G}^{\mathrm{A}}\left(\boldsymbol{r},\boldsymbol{r}'\right) \cdot \boldsymbol{\beta}_n\left(\boldsymbol{r}'\right) \mathrm{d}s'\,\mathrm{d}s\,, \tag{2.81d}$$

and the excitation vector is

$$\left[\boldsymbol{g}'\right]_m = \iint_S \left[\hat{n} \times \boldsymbol{\beta}_m(\boldsymbol{r})\right] \cdot \boldsymbol{H}_{\mathrm{inc}}(\boldsymbol{r})\,\mathrm{d}s\,. \tag{2.82}$$

The discretized EFIE and MFIE in (2.77) and (2.80) are underdetermined linear equation systems. There are twice as many unknowns (i.e., N discrete currents and N discrete

5 $\left(\hat{n}\times\boldsymbol{\beta}\right)\cdot(\hat{n}\times\hat{n}\times\boldsymbol{X}) = \left(\hat{n}\times\boldsymbol{\beta}\right)\cdot[(\hat{n}\cdot\boldsymbol{X})\,\hat{n} - (\hat{n}\cdot\hat{n})\,\boldsymbol{X}] = \left(\hat{n}\times\boldsymbol{\beta}\right)\cdot\hat{n}\,(\hat{n}\cdot\boldsymbol{X}) - \left(\hat{n}\times\boldsymbol{\beta}\right)\cdot\boldsymbol{X} = -\left(\hat{n}\times\boldsymbol{\beta}\right)\beta\cdot\boldsymbol{X}$, as $\left(\hat{n}\times\boldsymbol{\beta}\right)$ is orthogonal to $\hat{n}$.

voltages) as equations. To complete the equation systems, the interior of the objects needs to be considered. In the case of PEC objects, the unknown voltages are zero. For imperfectly conducting objects, the IBC from (2.73) yields a second system of equations in form of [Ism09]

$$\boldsymbol{A}'\boldsymbol{v} + Z_\mathrm{s}\boldsymbol{A}\boldsymbol{i} = 0. \tag{2.83}$$

In the case of dielectric objects, the discretization of the FE/BI approach results in a coupled system of equations according to [Jin10]

$$\begin{pmatrix} \boldsymbol{K}_{\mathrm{vv}} & \boldsymbol{K}_{\mathrm{vs}} & 0 \\ \boldsymbol{K}_{\mathrm{sv}} & \boldsymbol{K}_{\mathrm{ss}} & \boldsymbol{B} \\ 0 & \boldsymbol{P} & \boldsymbol{Q} \end{pmatrix} \begin{pmatrix} \boldsymbol{v}_\mathrm{v} \\ \boldsymbol{v}_\mathrm{s} \\ \boldsymbol{i}_\mathrm{s} \end{pmatrix} = \begin{pmatrix} 0 \\ 0 \\ \boldsymbol{b} \end{pmatrix} \tag{2.84}$$

where $\boldsymbol{v}_\mathrm{v}$ represents the discrete electric field inside the FE domain and $\boldsymbol{v}_\mathrm{s}$ and $\boldsymbol{i}_\mathrm{s}$ are the discrete electric and magnetic surface currents, respectively (cf. (2.75) and (2.76)). The blocks $\boldsymbol{K}_{\mathrm{vv}}$, $\boldsymbol{K}_{\mathrm{vs}}$, $\boldsymbol{K}_{\mathrm{sv}}$, $\boldsymbol{K}_{\mathrm{ss}}$, and $\boldsymbol{B}$ are the FE matrices and $\boldsymbol{P}$ and $\boldsymbol{Q}$ are the BI matrices. In the case of the EFIE, the matrix $\boldsymbol{P}$ is composed of the matrices $\boldsymbol{A}$ and $\boldsymbol{D}$ from (2.77) and the matrices $\boldsymbol{B}$ and $\boldsymbol{C}$ form the matrix $\boldsymbol{Q}$. In the case of the MFIE, $\boldsymbol{A}$, $\boldsymbol{B}$, $\boldsymbol{C}$, and $\boldsymbol{D}$ are replaced by their primed counterparts from (2.80).

The system matrices in (2.77) and (2.80) and the lower part of the system matrix in (2.84) are fully populated matrices. The computation of the coefficients of a dense matrix requires $O\left(N^2\right)$ operations. The solution of the linear equation system needs $O\left(N^3\right)$ operations when a direct solver is used and $O\left(N^2\right)$ operations per iteration when an iterative solver is employed. In contrast to the FGF BEM, the most computation time is needed by the interaction integrals in the CGF BI formulation as 1) the CGF is computationally considerably more expensive than the FGF and 2) the number of unknowns is significantly smaller since the cavity walls are not discretized. In the next chapter, different representations of the CGF are introduced. After that, two acceleration techniques for computing the system matrix are presented.

3. Representations of the Rectangular Cavity Green's Function

In the following, different representations of the rectangular cavity Green's function are presented and analyzed. The representations are introduced for the Green's function of the magnetic vector potential only as the analysis of the Green's function of the electric vector potential and the derivatives of the Green's functions is analogous. In brief, the representations of the other Green's functions are given in Appendix B.

3.1. Spatial Representation

The spatial representation of the Green's function of the rectangular cavity is constructed using the image principle [Mor53]. Starting from the boundary value problem of the rectangular cavity with an electric current element, the for example upper PEC boundary is replaced by an image current. Iteratively repeating the image principle in all directions moves the boundaries to infinity and results in the equivalent free-space problem, see Fig. 3.1.

Accordingly, the spatial representation of the CGF of the magnetic vector potential is given by [Ham70]

$$\overline{G}^{\mathrm{A}}_{\mathrm{spat}}\left(\boldsymbol{r},\boldsymbol{r}'\right) = \mu \sum_{m,n,p=-\infty}^{\infty} \sum_{q=0}^{7} \frac{\mathrm{e}^{-\mathrm{j}kr_{mnp,q}}}{4\pi r_{mnp,q}} \left(A_{x,q}\,\hat{x}\hat{x} + A_{y,q}\,\hat{y}\hat{y} + A_{z,q}\,\hat{z}\hat{z}\right) \tag{3.1}$$

where

$$r_{mnp,q} = \sqrt{\left(x_q - 2ma\right)^2 + \left(y_q - 2nb\right)^2 + \left(z_q - 2pc\right)^2} \tag{3.2}$$

is the distance between the observation point and the source or an image current. The distances x_q, y_q, and z_q are the Cartesian components of the distance vector between the observation point and the source or its seven immediate images. Likewise, the coefficients $A_{x,q}$, $A_{y,q}$, and $A_{z,q}$ correspond to the relative orientation of the source and its immediate images. The distances and the coefficients $A_{x,q}$, $A_{y,q}$, and $A_{z,q}$ are given in Tab. 3.1.

The spatial representation is conditionally convergent[6] as the number of terms in (3.1) grows cubically with $r_{mnp,q}$ but the terms decay only with $1/r_{mnp,q}$. While the singularity in the spatial domain (i.e., $\boldsymbol{r} = \boldsymbol{r}'$) is considered directly, the singularities in

6 A series $\sum_{n=0}^{\infty} a_n$ is conditionally convergent if $\lim_{N\to\infty} \sum_{n=0}^{N} a_n$ is a finite but $\sum_{n=0}^{\infty} |a_n| = \infty$ [Råd04].

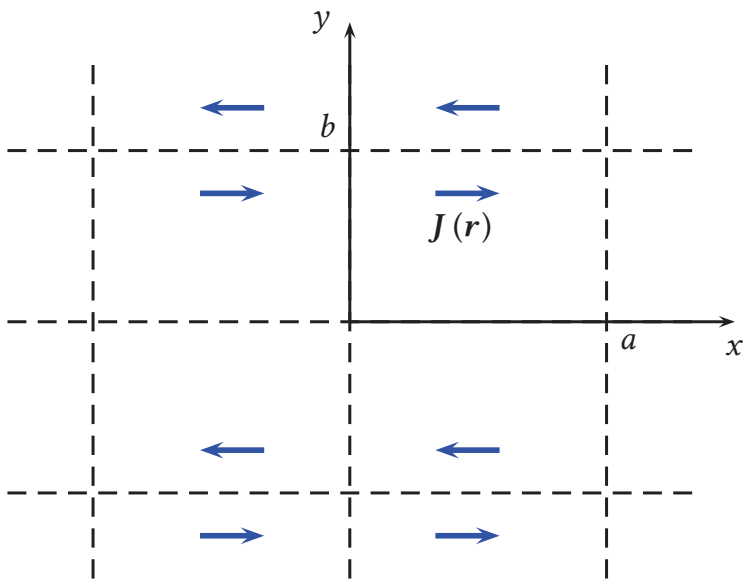

Fig. 3.1.: Image principle for the Green's function of the rectangular cavity.

q	x_q	y_q	z_q	$A_{x,q}$	$A_{y,q}$	$A_{z,q}$
0	$x - x'$	$y - y'$	$z - z'$	$+1$	$+1$	$+1$
1	$x + x'$	$y - y'$	$z - z'$	$+1$	-1	-1
2	$x + x'$	$y + y'$	$z - z'$	-1	-1	$+1$
3	$x - x'$	$y + y'$	$z - z'$	-1	$+1$	-1
4	$x - x'$	$y - y'$	$z + z'$	-1	-1	$+1$
5	$x + x'$	$y - y'$	$z + z'$	-1	$+1$	-1
6	$x + x'$	$y + y'$	$z + z'$	$+1$	$+1$	$+1$
7	$x - x'$	$y + y'$	$z + z'$	$+1$	-1	-1

Tab. 3.1.: Distances x_q, y_q, and z_q and coefficients $A_{x,q}$, $A_{y,q}$, and $A_{z,q}$.

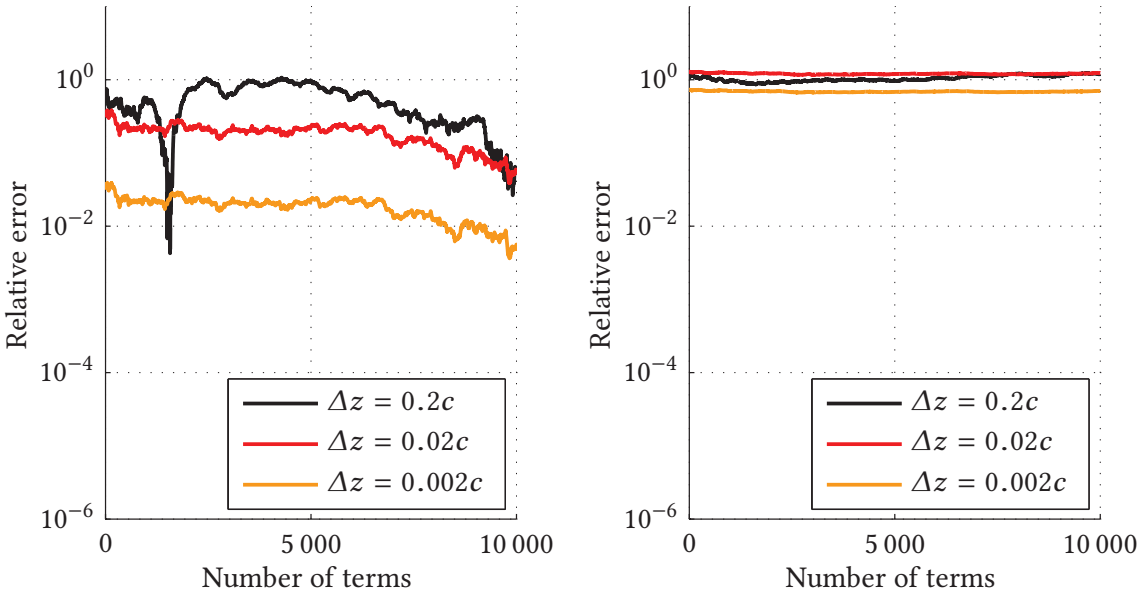

Fig. 3.2.: Relative error of the spatial representation at 200 MHz (left) and 400 MHz (right) for a cavity of size $a \times b \times c = 12\,\mathrm{m} \times 6\,\mathrm{m} \times 4\,\mathrm{m}$, $x = x' = a/2$, $y = y' = b/2$, and $z' = c/2$.

the spectral domain (i.e., the resonances of the cavity) are considered in the asymptotic limit only.

In Fig. 3.2, the convergence behavior of the series is illustrated for different distances between observation and source point and different frequencies. As the singularity in the spatial domain is modeled directly, the convergence of the series improves when the observation point approaches the source point. Still, the relative error is not monotonically decreasing. With increasing frequency the resonance density grows. As resonances are only considered in the asymptotic limit, the convergence is poor even when the distance between the observation and the source point is small. In conclusion, the spatial representation is not suited for numerical usage.

3.2. Spectral Representation

The dual representation to the spatial is the spectral representation. While the spatial representation is derived in the spatial domain by image theory, the spectral representation is constructed in the reciprocal spectral domain in terms of eigenfunctions which satisfy the boundary conditions of the field problem [Mor53]. For the magnetic

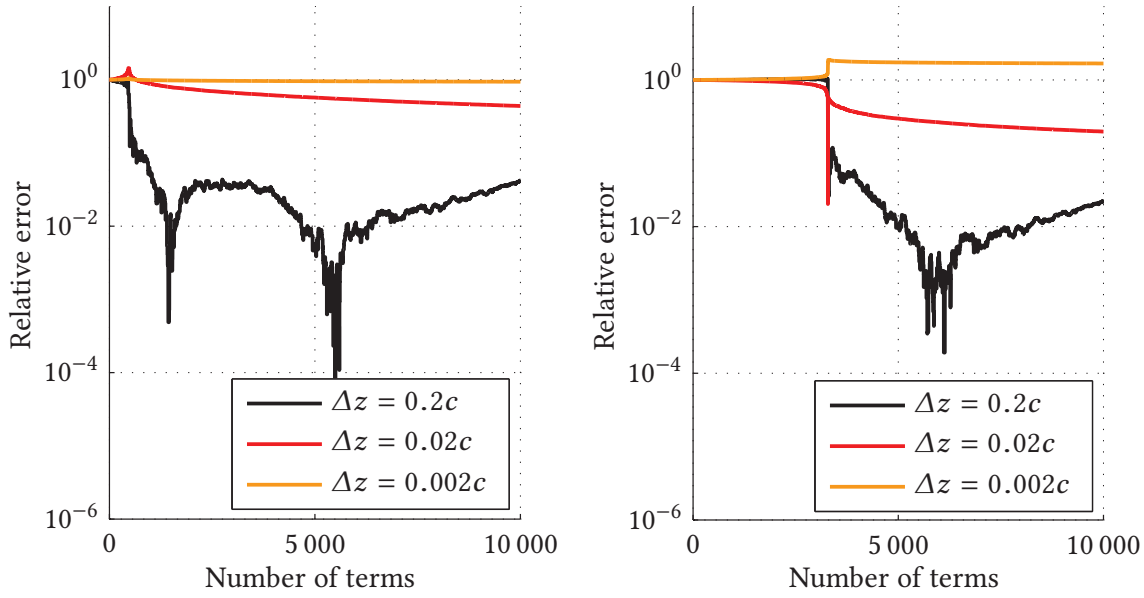

Fig. 3.3.: Relative error of the spectral representation at 200 MHz (left) and 400 MHz (right) for a cavity of size $a \times b \times c = 12\,\mathrm{m} \times 6\,\mathrm{m} \times 4\,\mathrm{m}$, $x = x' = a/2$, $y = y' = b/2$, and $z' = c/2$.

vector potential, the spectral representation is [Tai76]

$$\overline{G}^{\mathrm{A}}_{\mathrm{spec}}\left(\boldsymbol{r},\boldsymbol{r}'\right) = \mu \sum_{m,n,p=0}^{\infty} \frac{1}{k_{xyz}^2 - k^2} \Big[\phi_{x,mnp}\left(\boldsymbol{r}\right)\phi_{x,mnp}\left(\boldsymbol{r}'\right)\hat{x}\hat{x} + \phi_{y,mnp}\left(\boldsymbol{r}\right)\phi_{y,mnp}\left(\boldsymbol{r}'\right)\hat{y}\hat{y} + \phi_{z,mnp}\left(\boldsymbol{r}\right)\phi_{z,mnp}\left(\boldsymbol{r}'\right)\hat{z}\hat{z}\Big] \tag{3.3}$$

where $k_{xyz}^2 = k_x^2 + k_y^2 + k_z^2$ and $\phi_{x,mnp}\left(\boldsymbol{r}\right)$, $\phi_{y,mnp}\left(\boldsymbol{r}\right)$, and $\phi_{z,mnp}\left(\boldsymbol{r}\right)$ are the eigenfunctions of the magnetic vector potential as defined in Section 2.2.

The spectral representation is conditionally convergent because the number of terms in (3.3) grows with k_{xyz}^3 but the terms decay only with $1/k_{xyz}^2$. Vice versa to the spatial representation, the singularity in the spatial domain is considered only in the asymptotic limit while the resonances of the cavity are modeled directly.

In Figure 3.2, the convergence behavior of the spectral representation is illustrated. As the case $\boldsymbol{r} = \boldsymbol{r}'$ is only considered asymptotically in the spectral representation, the series decays either very slowly or not at all for small distances. When the distance increases, the convergence improves when the resonant modes (i.e., the modes whose resonance frequencies are in the range of the considered frequency) are added to the series. Yet, as the series is conditionally convergent, the error is not monotonously decreasing. In conclusion, the spectral representation is also not suitable for numerically usage.

3.3. 2D Spectral Representation

Another option to represent the cavity Green's function are the 2D spectral representations. In contrast to the spectral representation, only two of the three coordinates (e.g., the x- and the y-coordinate) are expanded into eigenfunctions. Inserting the eigenfunction expansion into the corresponding partial differential equation yields an ordinary differential equation for the remaining coordinate (e.g., the z-coordinate) [Col91]. The ordinary differential equation is solved piecewise for $z < z'$ and $z > z'$ first. Using that the derivative of the solution of the ordinary differential equation must undergo a unit step change at $z = z'$ to model the singularity in the spatial domain gives the remaining coefficient and yields the final solution for the Green's function.

Adapting the notation from Collin [Col91] where $z_>$ means the greater of z and z' and vice versa $z_<$ means the smaller of z and z', the z-2D spectral representation for the magnetic vector potential is written as [Tai76]

$$\overline{G}^{\mathrm{A}}_{\text{z-2D}}\left(\boldsymbol{r},\boldsymbol{r}'\right) = \mu \sum_{m,n=0}^{\infty} H_{mn}\left[\xi_{x,mn}\left(\boldsymbol{r}_>\right)\xi_{x,mn}\left(\boldsymbol{r}_<\right)\hat{x}\hat{x} + \xi_{y,mn}\left(\boldsymbol{r}_>\right)\xi_{y,mn}\left(\boldsymbol{r}_<\right)\hat{y}\hat{y} + \xi_{z,mn}\left(\boldsymbol{r}_>\right)\xi_{z,mn}\left(\boldsymbol{r}_<\right)\hat{z}\hat{z}\right] \tag{3.4}$$

where $\boldsymbol{r}_> = \left(x, y, c - z_>\right)$, $\boldsymbol{r}_< = \left(x', y', z_<\right)$,

$$H_{mn} = \frac{1}{\alpha_{mn}\sinh\left(\alpha_{mn}c\right)}, \tag{3.5}$$

and $\alpha_{mn} = \sqrt{k_x^2 + k_y^2 - k^2}$. The functions $\xi_{x,mn}$, $\xi_{y,mn}$, and $\xi_{z,mn}$ are defined as

$$\xi_{x,mn}\left(\boldsymbol{r}\right) = \sqrt{\frac{\tau_m\tau_n}{ab}}\cos\left(k_x x\right)\sin\left(k_y y\right)\sinh\left(\alpha_{mn}z\right), \tag{3.6a}$$

$$\xi_{y,mn}\left(\boldsymbol{r}\right) = \sqrt{\frac{\tau_m\tau_n}{ab}}\sin\left(k_x x\right)\cos\left(k_y y\right)\sinh\left(\alpha_{mn}z\right), \tag{3.6b}$$

$$\xi_{z,mn}\left(\boldsymbol{r}\right) = \sqrt{\frac{\tau_m\tau_n}{ab}}\sin\left(k_x x\right)\sin\left(k_y y\right)\cosh\left(\alpha_{mn}z\right) \tag{3.6c}$$

where

$$\tau_i = \begin{cases} 1 & \text{if } i = 0, \\ 2 & \text{if } i > 0. \end{cases}$$

In Fig. 3.4, the discontinuity of the individual terms in the 2D spectral representation at the z coordinate of the source point is illustrated.

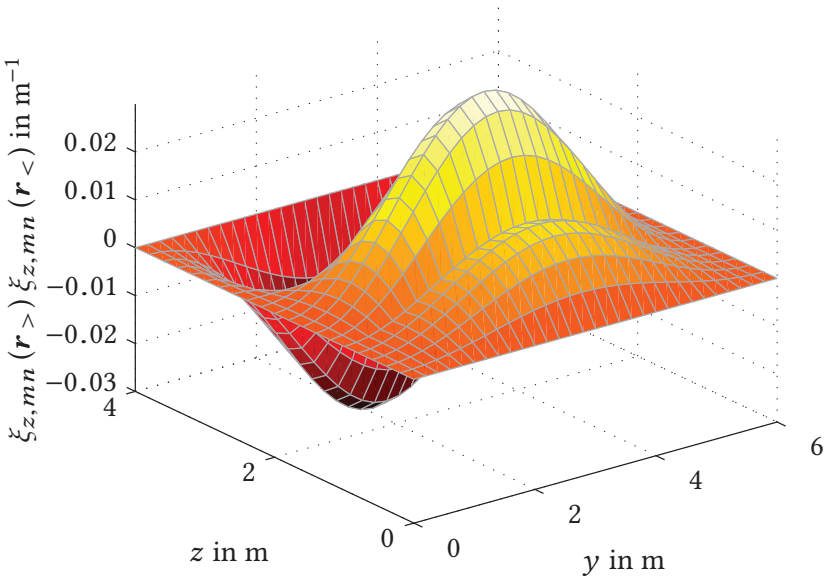

Fig. 3.4.: $\xi_{z,21}(\boldsymbol{r}_>)\,\xi_{z,21}(\boldsymbol{r}_<)$ in the plane $x = 4\,\mathrm{m}$ for $z' = 1\,\mathrm{m}$ and $a \times b \times c = 12\,\mathrm{m} \times 6\,\mathrm{m} \times 4\,\mathrm{m}$.

In the form of (3.4), the z-2D spectral representation is numerically unstable: the hyperbolic sine and the hyperbolic cosine functions in nominator and denominator cause numerical overflow errors for large α_{mn} . To remove the instability, the functions $\xi_{x,mn}(\boldsymbol{r})$, $\xi_{y,mn}(\boldsymbol{r})$, and $\xi_{z,mn}(\boldsymbol{r})$ are multiplied by $\mathrm{e}^{-\alpha_{mn}z}$. The modified functions $\xi'_{x,mn}(\boldsymbol{r})$, $\xi'_{y,mn}(\boldsymbol{r})$, and $\xi'_{z,mn}(\boldsymbol{r})$ become

$$\xi'_{x,mn}(\boldsymbol{r}) = \frac{1}{2}\sqrt{\frac{\tau_m\tau_n}{ab}}\cos(k_x x)\sin\left(k_y y\right)\left(1-\mathrm{e}^{-2\alpha_{mn}z}\right), \tag{3.7a}$$

$$\xi'_{y,mn}(\boldsymbol{r}) = \frac{1}{2}\sqrt{\frac{\tau_m\tau_n}{ab}}\sin(k_x x)\cos\left(k_y y\right)\left(1-\mathrm{e}^{-2\alpha_{mn}z}\right), \tag{3.7b}$$

$$\xi'_{z,mn}(\boldsymbol{r}) = \frac{1}{2}\sqrt{\frac{\tau_m\tau_n}{ab}}\sin(k_x x)\sin\left(k_y y\right)\left(1+\mathrm{e}^{-2\alpha_{mn}z}\right) \tag{3.7c}$$

and are bounded for large α_{mn}. Inserting the modified functions in (3.4), the z-2D spectral representation of the cavity Green's function is given by

$$\begin{aligned}\overline{G}^{\mathrm{A}}_{\text{z-2D}}\left(\boldsymbol{r},\boldsymbol{r}'\right) = \mu\sum_{m,n=0}^{\infty} H'_{mn}\Big[&\xi'_{x,mn}(\boldsymbol{r}_>)\,\xi'_{x,mn}(\boldsymbol{r}_<)\,\hat{x}\hat{x}\\ &+\xi'_{y,mn}(\boldsymbol{r}_>)\,\xi'_{y,mn}(\boldsymbol{r}_<)\,\hat{y}\hat{y}+\xi'_{z,mn}(\boldsymbol{r}_>)\,\xi'_{z,mn}(\boldsymbol{r}_<)\,\hat{z}\hat{z}\Big]\end{aligned} \tag{3.8}$$

where

$$H'_{mn} = \frac{\mathrm{e}^{\alpha_{mn}(c-z_>)}\mathrm{e}^{\alpha_{mn}z_<}}{\alpha_{mn}\sinh(\alpha_{mn}c)} = \frac{2\mathrm{e}^{\alpha_{mn}(c-z_>)}\mathrm{e}^{\alpha_{mn}z_<}}{\alpha_{mn}\left(\mathrm{e}^{\alpha_{mn}c}-\mathrm{e}^{-\alpha_{mn}c}\right)} = \frac{2\mathrm{e}^{-\alpha_{mn}\Delta z}}{\alpha_{mn}\left(1-\mathrm{e}^{-2\alpha_{mn}c}\right)}, \quad (3.9)$$

and $\Delta z = \left|z - z'\right| = z_> - z_<$. As the nominator of H'_{mn} goes to zero for large α_{mn} and the denominator goes to α_{mn}, (3.9) is also bounded and the z-2D spectral representation in the form of (3.8) is numerically stable.

Next, the convergence properties of the z-2D spectral representation are analyzed. In contrast to the spatial and the spectral representations, the z-2D spectral representation converges exponentially. For large α_{mn}, the terms in (3.8) are proportional to

$$\mathrm{e}^{-\alpha_{mn}\Delta z}. \quad (3.10)$$

In the following, the number of terms $N_{z\text{-2D}}$ in the z-2D spectral representation needed for an accuracy δ are determined. When the set of modes (m,n) with $k_x^2 + k_y^2 < k_{r,0}^2$ (i.e., the modes within a quarter circle of radius $k_{r,0}$, see Fig. 3.5) is considered in (3.8), the accuracy of the series is roughly given by[7]

$$\delta = \mathrm{e}^{-\sqrt{k_{r,0}^2 - k^2}\Delta z}. \quad (3.11)$$

Solving (3.11) for $k_{r,0}$ yields

$$k_{r,0} = \sqrt{k^2 + \left(\frac{\ln\delta}{\Delta z}\right)^2}. \quad (3.12)$$

The number of modes is approximately given by the area of the quarter circle with radius $k_{r,0}$ divided by the area of a single mode, see Fig. 3.5. Thus, the number of modes as a function of the radius $k_{r,0}$ becomes

$$N_{z\text{-2D}} = \frac{\frac{1}{4}\pi k_{r,0}^2}{\frac{\pi}{a}\frac{\pi}{b}} = \frac{abk_{r,0}^2}{4\pi}. \quad (3.13)$$

Inserting (3.12) in (3.13) gives the number of modes in dependence of the accuracy

$$N_{z\text{-2D}} = \frac{ab}{4\pi}\left[k^2 + \left(\frac{\ln\delta}{\Delta z}\right)^2\right]. \quad (3.14)$$

The convergence rate of the z-2D spectral representation depends on the distance Δz: the smaller the distance Δz, the slower is the convergence rate. Consequently, the number of necessary modes depends on the distance Δz: the smaller the distance Δz,

7 The remainder of an exponentially convergent series after n terms is less than the nth term. To proof this, the geometric series [Råd04] is used.

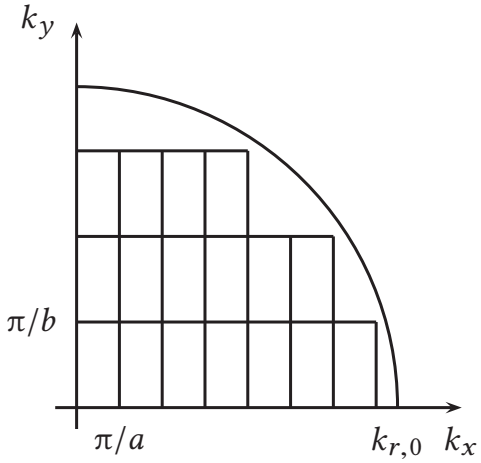

Fig. 3.5.: Number of modes within a circle of radius $k_{r,0}$.

the more modes are necessary to attain a desired accuracy. When $\Delta z = 0$ (i.e., $z = z'$), the series does not converge exponentially anymore. The number of necessary modes becomes infinite.

The x- and the y-2D spectral representations are derived in a similar manner. Analogous to the z-2D spectral representation, their convergence rates depend on the distances Δx and Δy and they do not converge when $\Delta x = 0$ and $\Delta y = 0$, respectively. The numbers of necessary modes are derived as

$$N_{x\text{-2D}} = \frac{bc}{4\pi}\left[k^2 + \left(\frac{\ln\delta}{\Delta x}\right)^2\right], \tag{3.15}$$

$$N_{y\text{-2D}} = \frac{ac}{4\pi}\left[k^2 + \left(\frac{\ln\delta}{\Delta y}\right)^2\right]. \tag{3.16}$$

The convergence rates of the 2D spectral representations do not only depend on the relative position of observation and source point but also depend on the frequency. For a given accuracy δ and given observation and source point, the number of modes in (3.15), (3.16), and (3.14) grows with f^2 for large frequencies. At low frequencies, the number of modes is approximately constant with respect to frequency. A possible definition for the transition range is to equate the summands in (3.15), (3.16), and (3.14), respectively. In Fig. 3.6, the numbers of necessary terms are shown for different distances Δz. The transition frequency is inversely proportional to the distance Δz. While it is at 220 MHz for $\Delta z = 0.5c$, the transition frequency for $\Delta z = 0.2c$ is at 550 MHz.

In Fig. 3.7, the convergence behavior of the z-2D spectral representation is illustrated for different distances Δz and frequencies. The numerical results confirm (3.14). One the on hand, the series decays the faster, the larger the distance Δz. On the other hand,

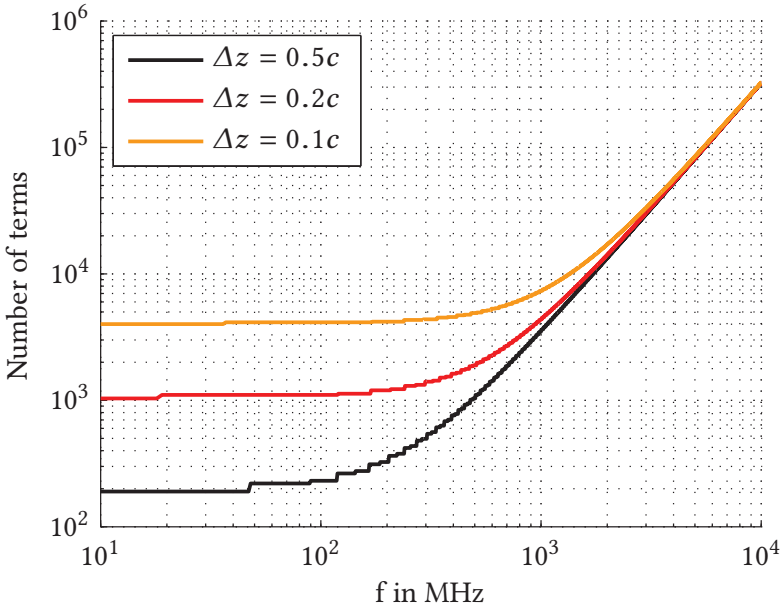

Fig. 3.6.: Number of necessary terms in the z-2D spectral representation for different distances Δz, an accuracy $\delta = 10^{-4}$, and a cavity of size 12 m × 6 m × 4 m.

the convergence rate hardly changes with frequency since the considered frequencies are smaller than the transition frequency.

3.4. Ewald Representation

Both the spatial and the spectral representation of the Green's function of the rectangular cavity are slowly and conditionally convergent series. The slow convergence of the spatial representation outside the source region originates from the singularities in the spectral domain (i.e., the resonances of the cavity). The poor convergence of the spectral representation in the source region is caused by the singularity in the spatial domain. Albeit, the convergence of the spatial and the spectral representations is improved in the source region and in the range of resonance frequencies, respectively. The advantage of the spatial representation is the drawback of the spectral representation and vice versa.

The Ewald summation technique [Ewa21] removes the shortcomings of the spatial and the spectral representations and combines their advantages. The transformation starts from the spatial representation using the identity

$$\frac{\mathrm{e}^{-\mathrm{j}kr_{mnp,q}}}{r_{mnp,q}} = \frac{2}{\sqrt{\pi}} \int_0^\infty \mathrm{e}^{-r_{mnp,q}^2 s^2 + \frac{k^2}{4s^2}} \, \mathrm{d}s \tag{3.17}$$

for a suitable path of integration in the complex plane [Jor86]. Splitting the path of integration at the so-called real-valued splitting parameter E [Val07] and inserting (3.17)

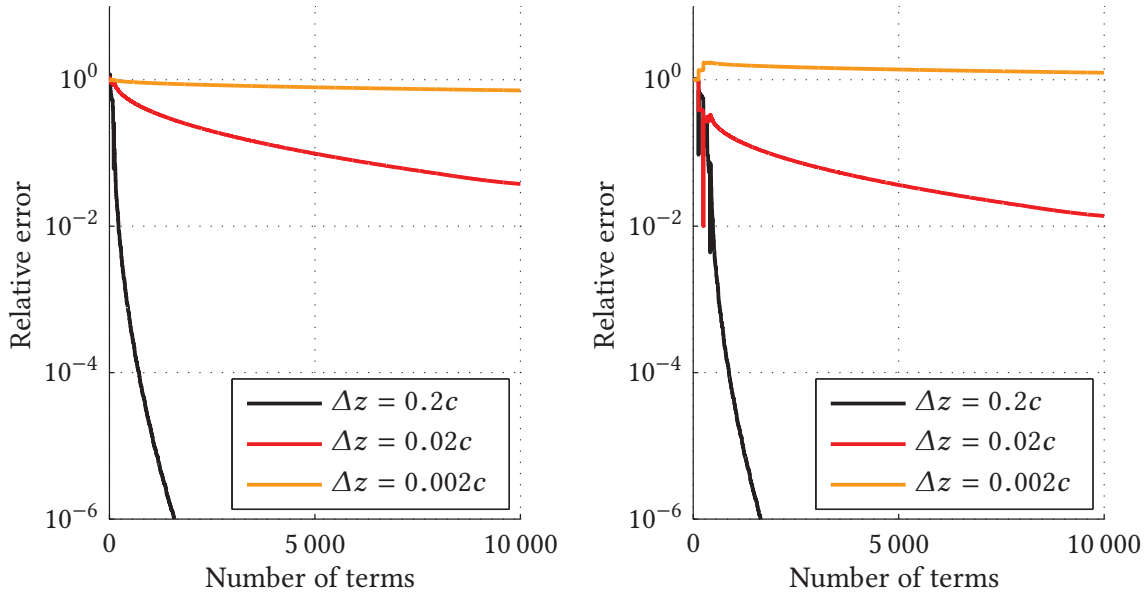

Fig. 3.7.: Relative error of the z-2D spectral representation at 200 MHz (left) and 400 MHz (right) for $a \times b \times c = 12\,\mathrm{m} \times 6\,\mathrm{m} \times 4\,\mathrm{m}$, $x = x' = a/2$, $y = y' = b/2$, and $z' = c/2$.

in (3.1), the Green's function of the rectangular cavity becomes a hybrid series of the form

$$\overline{G}^{\mathrm{A}}_{\mathrm{Ewald}}\left(\boldsymbol{r},\boldsymbol{r}'\right) = \overline{G}^{\mathrm{A}}_{\mathrm{Ew\text{-}spat}}\left(\boldsymbol{r},\boldsymbol{r}'\right) + \overline{G}^{\mathrm{A}}_{\mathrm{Ew\text{-}spec}}\left(\boldsymbol{r},\boldsymbol{r}'\right) \tag{3.18}$$

where

$$\overline{G}^{\mathrm{A}}_{\mathrm{Ew\text{-}spat}}\left(\boldsymbol{r},\boldsymbol{r}'\right) = \frac{2\mu}{4\pi\sqrt{\pi}} \sum_{m,n,p=-\infty}^{\infty} \sum_{q=0}^{7} \int_{E}^{\infty} \mathrm{e}^{-r^2_{mnp,q}s^2+\frac{k^2}{4s^2}}\,\mathrm{d}s \sum_{i=1}^{3} A_{i,q}\hat{x}_i\hat{x}_i \tag{3.19}$$

is referred to as the spatial series of the Ewald summation,

$$\overline{G}^{\mathrm{A}}_{\mathrm{Ew\text{-}spec}}\left(\boldsymbol{r},\boldsymbol{r}'\right) = \frac{2\mu}{4\pi\sqrt{\pi}} \sum_{m,n,p=-\infty}^{\infty} \sum_{q=0}^{7} \int_{0}^{E} \mathrm{e}^{-r^2_{mnp,q}s^2+\frac{k^2}{4s^2}}\,\mathrm{d}s \sum_{i=1}^{3} A_{i,q}\hat{x}_i\hat{x}_i \tag{3.20}$$

is denoted as the spectral series, and $\{x_1, x_2, x_3\} = \{x, y, z\}$. Following Ewald [Ewa21], the integral in (3.19) becomes

$$\frac{2}{\sqrt{\pi}} \int_{E}^{\infty} \mathrm{e}^{-r^2_{mnp,q}s^2+\frac{k^2}{4s^2}}\,\mathrm{d}s = \frac{1}{r_{mnp,q}} \mathrm{Re}\left\{\mathrm{e}^{+\mathrm{j}kr_{mnp,q}}\,\mathrm{erfc}\left(r_{mnp,q}E + \mathrm{j}\frac{k}{2E}\right)\right\} \tag{3.21}$$

where erfc is the complementary error function [Råd04]. Using this identity, the spatial series is given by [Par98; Gro05; Car05]

$$\overline{G}^{\mathrm{A}}_{\text{Ew-spat}}\left(\boldsymbol{r},\boldsymbol{r}'\right) = \mu \sum_{m,n,p=-\infty}^{\infty} \sum_{q=0}^{7} \frac{\operatorname{Re}\left\{\mathrm{e}^{+\mathrm{j}kr_{mnp,q}} \operatorname{erfc}\left(r_{mnp,q}E + \mathrm{j}\frac{k}{2E}\right)\right\}}{4\pi r_{mnp,q}} \cdot \left(A_{x,q}\,\hat{x}\hat{x} + A_{y,q}\,\hat{y}\hat{y} + A_{z,q}\,\hat{z}\hat{z}\right) \tag{3.22}$$

which is essentially an error function weighted spatial representation of the Green's function. The spectral series is more elaborate to derive as (3.20) needs to be transformed from the spatial to the spectral domain first. The Poisson summation formula [Råd04] relates an integrable function f with its Fourier transform $\widetilde{f}$ via

$$\sum_{m,n,p=-\infty}^{\infty} f\left(m,n,p\right) = \sum_{m,n,p=-\infty}^{\infty} \widetilde{f}\left(2m\pi, 2n\pi, 2p\pi\right) . \tag{3.23}$$

Scaling the arguments m, n, and p of the function f with $-2a$, $-2b$, and $-2c$, respectively and shifting the scaled arguments by x, y, and z, the Poisson summation formula from (3.23) becomes [Råd04]

$$\sum_{m,n,p=-\infty}^{\infty} f\left(x-2am, y-2bn, z-2cp\right) = \frac{1}{8abc} \sum_{m,n,p=-\infty}^{\infty} \widetilde{f}\left(-\frac{m\pi}{a}, -\frac{n\pi}{b}, -\frac{p\pi}{c},\right) \mathrm{e}^{\mathrm{j}\left(\frac{m\pi}{a}x + \frac{n\pi}{b}y + \frac{p\pi}{c}z\right)} . \tag{3.24}$$

Using (3.24) together with the 3D Fourier pair [Råd04]

$$f\left(\boldsymbol{x}\right) = \exp\left(-|\boldsymbol{x}|^2 s^2\right) \quad \circ\!\!-\!\!\bullet \quad \widetilde{f}\left(\boldsymbol{y}\right) = \frac{\pi^{1.5}}{s^3} \exp\left(-\frac{|\boldsymbol{y}|^2}{4s^2}\right), \tag{3.25}$$

the spectral series in (3.20) becomes

$$\overline{G}^{\mathrm{A}}_{\text{Ew-spec}}\left(\boldsymbol{r},\boldsymbol{r}'\right) = \frac{\mu}{16abc} \sum_{m,n,p=-\infty}^{\infty} \int_0^E \frac{1}{s^3} \exp\left(-\frac{k_{xyz}^2 - k^2}{4s^2}\right) \mathrm{d}s \cdot \sum_{q=0}^{7} \mathrm{e}^{\mathrm{j}\left(k_x x_q + k_y y_q + k_z z_q\right)} \sum_{i=1}^{3} A_{i,q}\hat{x}_i\hat{x}_i . \tag{3.26}$$

Evaluating the integral over s by substitution with $u = 1/s$ yields

$$\overline{G}^{\mathrm{A}}_{\text{Ew-spec}}\left(\boldsymbol{r},\boldsymbol{r}'\right) = \frac{\mu}{8abc}\sum_{m,n,p=-\infty}^{\infty} H_{mnp}\sum_{q=0}^{7}\mathrm{e}^{\mathrm{j}\left(k_x x_q + k_y y_q + k_z z_q\right)}\sum_{i=1}^{3} A_{i,q}\hat{x}_i\hat{x}_i \tag{3.27}$$

where

$$H_{mnp} = \frac{1}{k_{xyz}^2 - k^2}\exp\left(-\frac{k_{xyz}^2 - k^2}{4E^2}\right). \tag{3.28}$$

Now, using that[8]

$$\frac{1}{8abc}\sum_{m,n,p=-\infty}^{\infty} H_{mnp}\sum_{q=0}^{7} A_{i,q}\mathrm{e}^{\mathrm{j}\left(k_x x_q + k_y y_q + k_z z_q\right)} = \sum_{m,n,p=0}^{\infty} H_{mnp}\,\phi_{i,mnp}\left(\boldsymbol{r}\right)\phi_{i,mnp}\left(\boldsymbol{r}'\right) \tag{3.29}$$

gives the spectral series of the Ewald representation in its final form [Par98; Gro05; Car05]

$$\overline{G}^{\mathrm{A}}_{\text{Ew-spec}}\left(\boldsymbol{r},\boldsymbol{r}'\right) = \mu\sum_{m,n,p=0}^{\infty} H_{mnp}\left[\phi_{x,mnp}\left(\boldsymbol{r}\right)\phi_{x,mnp}\left(\boldsymbol{r}'\right)\hat{x}\hat{x} + \phi_{y,mnp}\left(\boldsymbol{r}\right)\phi_{y,mnp}\left(\boldsymbol{r}'\right)\hat{y}\hat{y} + \phi_{z,mnp}\left(\boldsymbol{r}\right)\phi_{z,mnp}\left(\boldsymbol{r}'\right)\hat{z}\hat{z}\right] \tag{3.30}$$

The spectral series is basically an exponential function weighted spectral representation of the Green's function. The principle of the Ewald summation technique is illustrated in Fig. 3.8. The singularity in the spatial domain is considered in the spatial part of the Ewald summation while the spectral part models the singularities in the spectral domain (i.e., the resonances of the cavity). The singularities in both domains are therefore modeled in the "correct" domain and hence, they do not impair the convergence of the series.

In the following, the convergence of the Ewald representation and the choice of the splitting parameter are analyzed. For large arguments, the complementary error function in the spatial series is approximated by its asymptotic expansion $\operatorname{erfc}(z) \approx \mathrm{e}^{-z^2}/\left(\sqrt{\pi}z\right)$ [Abr70]. Hence, the terms in (3.22) are proportional to

$$\exp\left(-r_{mnp,q}^2 E^2\right) \tag{3.31}$$

8 For a proof of (3.29), the interested reader is referred to Appendix A.2.

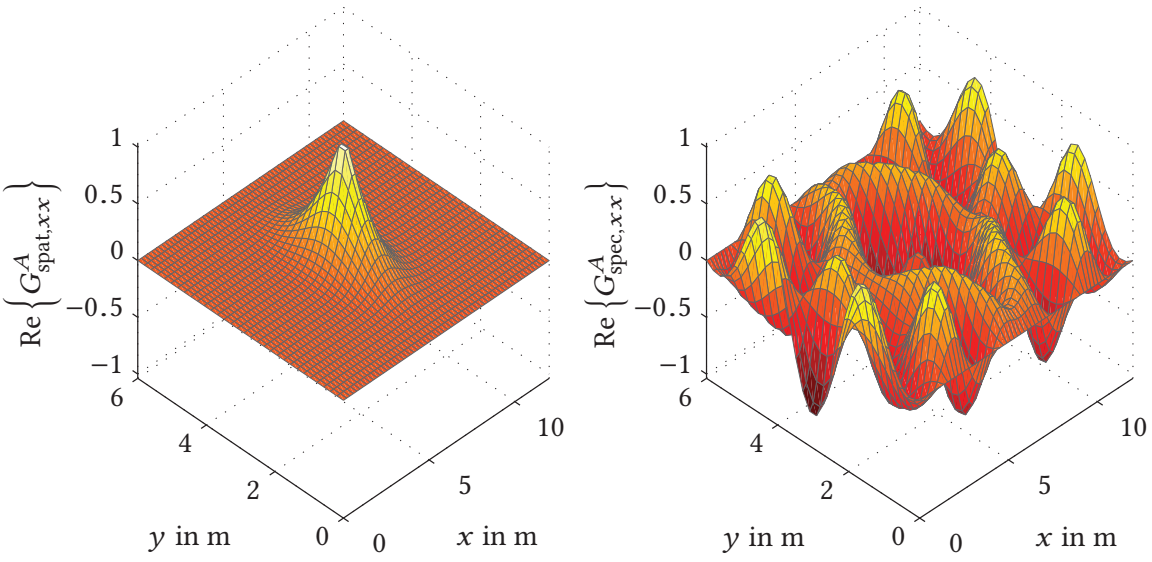

Fig. 3.8.: Spatial (left) and spectral (right) part of the cavity Green's function for the magnetic vector potential in the plane $z = c/2$ for $a \times b \times c = 12\,\text{m} \times 6\,\text{m} \times 4\,\text{m}$, $f = 150\,\text{MHz}$, $x' = a/2$, $y' = b/2$, and $z' = 0.55c$.

for large $r_{mnp,q}$. The asymptotic behavior of the spectral series is determined by H_{mnp} from (3.28) as the eigenfunctions in (3.30) are bounded. For large k_{xyz}, H_{mnp} is approximated as

$$\exp\left(-\frac{k_{xyz}^2 - k^2}{4E^2}\right). \tag{3.32}$$

Both the spatial and the spectral series exhibit exponential convergence. In the following, the number of necessary terms in the spatial and the spectral series are derived in dependence of the accuracy. When the source and the images within a sphere of radius r_0 (i.e., the set of currents (m,n,p,q) with $r_{mnp,q} < r_0$) are considered in (3.22), the accuracy δ of the spatial series is, according to (3.31), approximately given by

$$\delta = \exp\left(-r_0^2 E^2\right). \tag{3.33}$$

Given a desired accuracy, the radius of the sphere becomes

$$r_0 = \frac{\sqrt{-\ln \delta}}{E}. \tag{3.34}$$

The number of terms in a sphere of radius r_0 is approximately given by the volume of the sphere divided by the volume of a single cell, which is the volume of the cavity

in the case of the spatial series. Thus, the number of necessary terms $N_{\text{Ew-spat}}$ in the spatial series is

$$N_{\text{Ew-spat}} = \frac{\frac{4}{3}\pi r_0^3}{abc} = \frac{4\pi\left(-\ln\delta\right)^{3/2}}{3E^3abc}\,. \tag{3.35}$$

The accuracy of the spectral series is, according to (3.32), roughly given by

$$\delta = \exp\left(-\frac{k_{r,0}^2 - k^2}{4E^2}\right) \tag{3.36}$$

when the set of modes (m,n,p) with $k_x^2 + k_y^2 + k_z^2 < k_{r,0}^2$ is considered in (3.30). Given a desired accuracy, $k_{r,0}$ becomes

$$k_{r,0} = \sqrt{k^2 - 4E^2\ln\delta}\,. \tag{3.37}$$

In the case of the spectral series the number of terms $N_{\text{Ew-spec}}$ is approximately given by the volume of one eights of a sphere with radius $k_{r,0}$ divided by the volume of a single mode as only positive indices occur in (3.30). It is

$$N_{\text{Ew-spec}} = \frac{\frac{1}{8}\frac{4}{3}\pi k_{r,0}^3}{\frac{\pi}{a}\frac{\pi}{b}\frac{\pi}{c}} = \frac{abc\left(k^2 - 4E^2\ln\delta\right)^{3/2}}{6\pi^2}\,. \tag{3.38}$$

The splitting parameter E controls the convergence rate of the spatial and the spectral series. A larger splitting parameters results in a faster decaying spatial series and a slower decaying spectral series. Vice versa, a smaller splitting parameter accelerates the convergence of the spectral series while it decelerates the convergence of the spatial series. Consequently, the necessary terms in the spatial series decrease when the splitting parameter is increased (cf. (3.35)) while the necessary terms in the spectral series increase (cf. (3.38)). In general, the choice of the splitting parameter is arbitrary. It is chosen such that the total number of terms is minimized [Jor86; Cap07]. However, in the over-moded frequency range, the choice of the optimum splitting parameter results in numerical overflow errors [Cap07]. To avoid the so-called high frequency breakdown of the Ewald summation technique, a high frequency splitting parameter must be selected instead. Below, the choice of the splitting parameter and the consequences are analyzed for both low and high frequencies.

In the low frequency regime, the splitting parameter is chosen such that the total number of terms is minimized. As $k_{r,0} \gg k$ for low frequencies, the accuracy of the spectral series is approximately given by $\delta \approx \exp\left[-k_{r,0}^2/\left(4E^2\right)\right]$ and the number of spectral terms becomes

$$N_{\text{Ew-spec}} = \frac{4E^3abc\left(-\ln\delta\right)^{3/2}}{3\pi^2}\,. \tag{3.39}$$

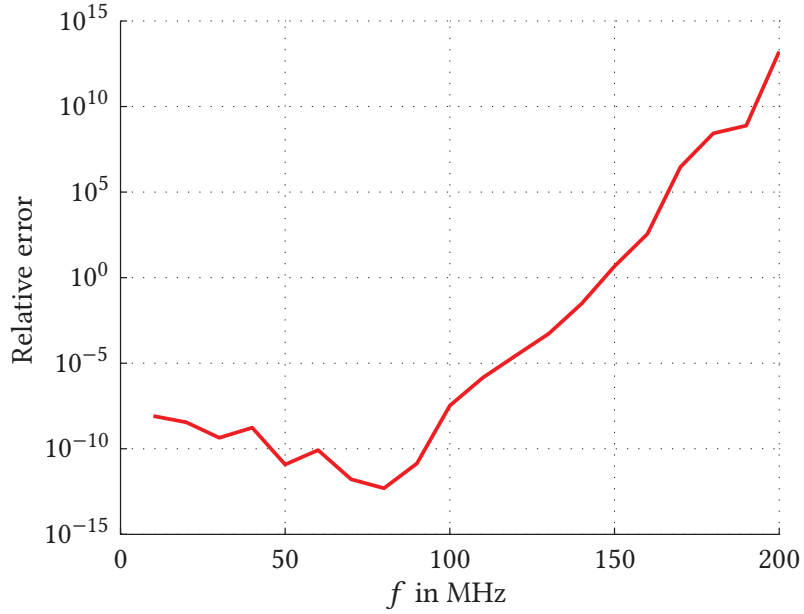

Fig. 3.9.: High-frequency breakdown of the Ewald summation technique: relative error of the cavity Green's function in the low- and the high-frequency regime for $E = E_{\text{opt}}$ and a cavity of size $a \times b \times c = 12\,\text{m} \times 6\,\text{m} \times 4\,\text{m}$. The threshold between low- and high-frequency regime is, according to (3.42), (3.43), and (3.44), at 51.26 MHz.

Minimizing the total number of terms with respect to the splitting parameter

$$\frac{\mathrm{d}}{\mathrm{d}E}\left(N_{\text{Ew-spat}} + N_{\text{Ew-spec}}\right) = 0\,, \tag{3.40}$$

$$-\frac{4\pi\,(-\ln\delta)^{3/2}}{E^4 abc} + \frac{4E^2 abc\,(-\ln\delta)^{3/2}}{\pi^2} = 0 \tag{3.41}$$

gives the optimum splitting parameter

$$E_{\text{opt}} = \frac{\sqrt{\pi}}{\sqrt[3]{abc}}\,. \tag{3.42}$$

With $E = E_{\text{opt}}$, the necessary terms in the spatial and the spectral series are constant.

In the high frequency regime, the terms in the spectral series grow exponentially with frequency for small m, n, and p when the optimum splitting parameter is selected. Although, the large terms in the spectral series cancel with large terms from the spatial series analytically, numerical overflow errors occur in practice as illustrated in Fig. 3.9. To avoid the so-called high-frequency breakdown of the Ewald summation technique, the splitting parameter is chosen as

$$E_{\text{hf}} = \frac{k}{4} \tag{3.43}$$

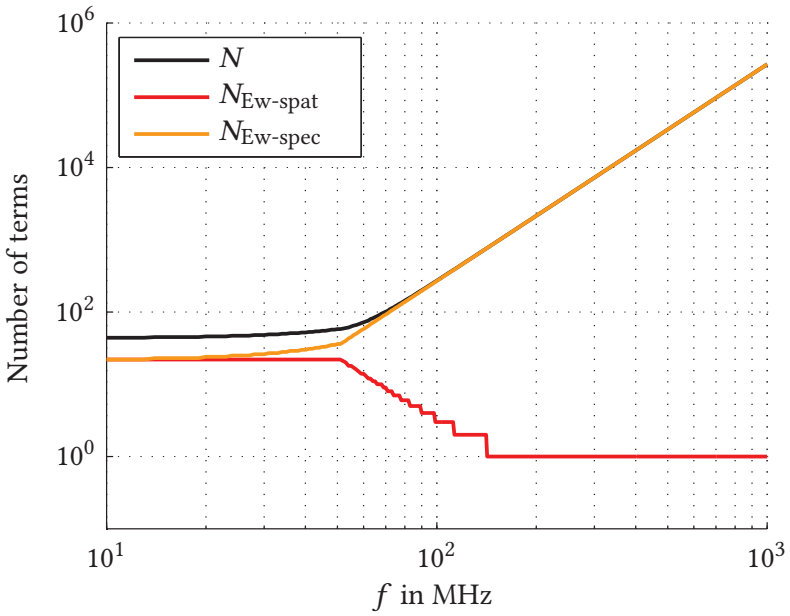

Fig. 3.10.: Number of necessary terms in the Ewald representation for an accuracy $\delta = 10^{-4}$, and a cavity size of 12 m × 6 m × 4 m. The threshold between low and high frequency regime is, according to (3.42), (3.43), and (3.44), at 51.26 MHz.

in the over-moded frequency range [Car05]. The overall splitting parameter is then chosen as

$$E = \max\left(E_{\text{opt}}, E_{\text{hf}}\right) . \tag{3.44}$$

The inevitable choice of the splitting parameter in the over-moded frequency range causes a major drawback of the Ewald summation technique. With $E_{\text{hf}} = k/4$, the number of necessary terms in the spectral series becomes

$$N_{\text{Ew-spec}} = \frac{abck^3\left(1 - \frac{1}{4}\ln\delta\right)^{3/2}}{6\pi^2}, \tag{3.45}$$

i.e., it grows with f^3. In Fig. 3.10, the number of necessary terms in the Ewald representation are shown as a function of frequency. While the total number of terms is approximately constant in the low frequency regime, it grows with f^3 in the over-moded regime. The threshold between low- and high-frequency regime is determined by equating E_{hf} and E_{opt}.

The convergence behavior of the Ewald representation is illustrated in Fig 3.11. In contrast to the 2D spectral representations (cf. 3.7), the Ewald representation converges exponentially independent from the relative position of observation and source point. Yet, because of the high frequency breakdown, the number of necessary terms grows with f^3 while the number of modes in the 2D spectral representations only grows with f^2. At 400 MHz, more than seven times as many terms as needed at 200 MHz are

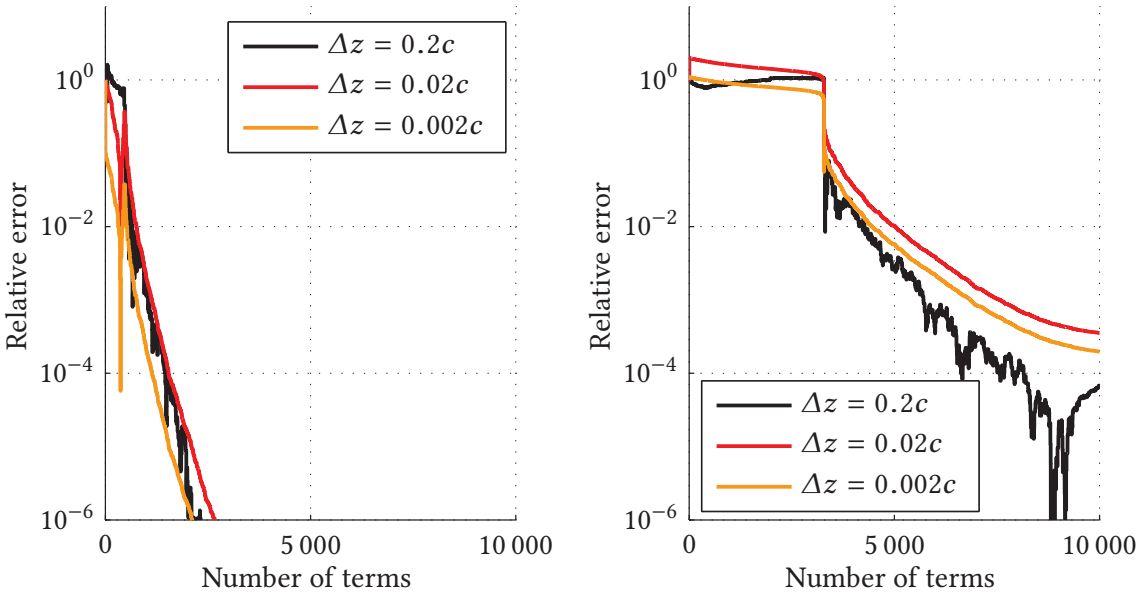

Fig. 3.11.: Relative error of the Ewald representation at 200 MHz (left) and 400 MHz (right) for $a \times b \times c = 12\,\mathrm{m} \times 6\,\mathrm{m} \times 4\,\mathrm{m}$, $x = x' = a/2$, $y = y' = b/2$, and $z' = c/2$.

necessary to achieve an accuracy of 10^{-4} and the series starts to decay only after the modes whose resonance frequencies are in the range of 400 MHz have been added (see steps of the curves in Fig. 3.11 (right) at roughly 3 300 terms).

4. Hybrid Fast Group Spectral Domain Approach

The CGF BEM has two shortcomings: the large computational burden of the CGF at high frequencies and the quadratic complexity of the system matrix. In this chapter, a hybrid representation of the CGF together with a FGSDA are proposed. The hybrid representation reduces the large computational effort of the CGF and is presented in Section 4.1. The FGSDA addresses the quadratic complexity in filling the system matrix and is described in Section 4.2.

4.1. Hybrid Ewald-2D Spectral Representation

4.1.1. Derivation

The advantage of the Ewald representation is the exponential convergence rate independent from the relative position of observation and source point. Its drawback is that the number of necessary terms increases with f^3 in the high frequency regime. In contrast, the number of necessary terms in the 2D spectral representations grows only with f^2 but at the expense of a slow convergence rate when the observation point is close to the source.

To combine the advantages of both representations and remove their limitations, a hybrid Ewald-2D Spectral representation is proposed in the following. When the observation point is near the source point, the Ewald representation is used. When observation and source point are well separated, one of the 2D spectral representations is employed. Let $\Delta x_{\text{near}} \times \Delta y_{\text{near}} \times \Delta z_{\text{near}}$ be the size of the near region, then the hybrid Ewald-2D Spectral representation is given by

$$\overline{G}^{\text{A}}_{\text{hybrid}} = \begin{cases} \overline{G}^{\text{A}}_{\text{Ewald}} & \text{if } \Delta x \leq \Delta x_{\text{near}}, \Delta y \leq \Delta y_{\text{near}}, \text{ and } \Delta z \leq \Delta z_{\text{near}}, \\ \overline{G}^{\text{A}}_{\text{2D}} & \text{else} \end{cases} \tag{4.1}$$

where $\overline{G}^{\text{A}}_{\text{2D}}$ refers to one of the 2D spectral representations. The convergence rates of the 2D spectral representations depend on the distances $\Delta x = x - x'$, $\Delta y = y - y'$, and $\Delta z = z - z'$, respectively. The larger the distance, the faster the respective series converges. Thus, the x-2D spectral representation is optimal when $\Delta x / \Delta x_{\text{near}}$ is maximal, the y−2D spectral representation is preferable when $\Delta y / \Delta y_{\text{near}}$ is maximal, and the z-2D spectral

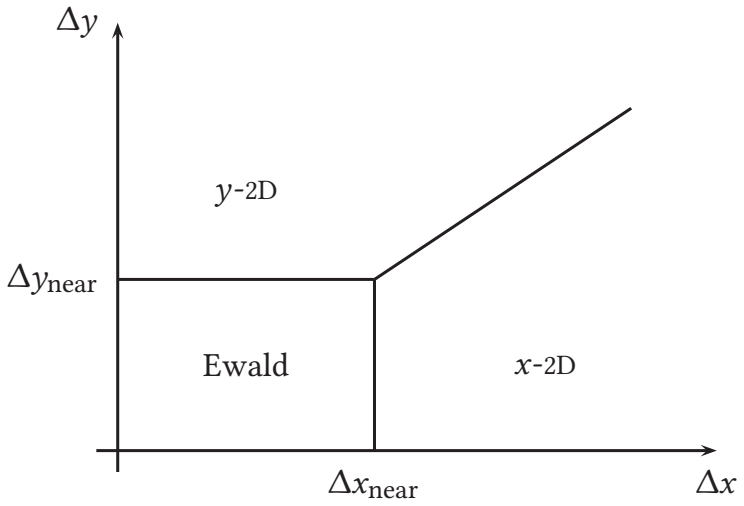

Fig. 4.1.: Coupling scheme of the hybrid Ewald-2D Spectral representation.

representation is the best choice when $\Delta z/\Delta z_{\text{near}}$ is maximal. Accordingly,

$$\overline{G}^{\text{A}}_{\text{2D}} = \begin{cases} \overline{G}^{\text{A}}_{x\text{-2D}} & \text{if } \Delta x/\Delta x_{\text{near}} \geq \Delta y/\Delta y_{\text{near}} \text{ and } \Delta x/\Delta x_{\text{near}} \geq \Delta z/\Delta z_{\text{near}}, \\ \overline{G}^{\text{A}}_{y\text{-2D}} & \text{if } \Delta y/\Delta y_{\text{near}} > \Delta x/\Delta x_{\text{near}} \text{ and } \Delta y/\Delta y_{\text{near}} \geq \Delta z/\Delta z_{\text{near}}, \\ \overline{G}^{\text{A}}_{z\text{-2D}} & \text{if } \Delta z/\Delta z_{\text{near}} > \Delta x/\Delta x_{\text{near}} \text{ and } \Delta z/\Delta z_{\text{near}} > \Delta y/\Delta y_{\text{near}}, \end{cases} \tag{4.2}$$

as illustrated in Fig. 4.1.

The size of the near region is chosen such that the Green's function is calculated with the representation which needs the least computation time. The computation time of the 2D spectral representations is given by the time per mode t_{2D} times the number of modes. As the spatial series is negligible in the over-moded frequency range, the computation time of the Ewald representation is approximately given by the spectral series, i.e., the computation time per mode $t_{\text{Ew-spec}}$ times the number of modes in the spectral series. Equating the computation times of the Ewald and the 2D spectral representations gives the optimum size of the near region. For the optimum length Δx_{near}, it follows

$$\begin{gathered} N_{\text{Ew-spec}}\, t_{\text{Ew-spec}} = N_{x\text{-2D}}\, t_{\text{2D}}\,, \\ \frac{abck^3 \left(1 - \frac{1}{4}\ln\delta\right)^{3/2}}{3\pi^2}\, t_{\text{Ew-spec}} = \frac{bc}{4\pi}\left[k^2 + \left(\frac{\ln\delta}{\Delta x}\right)^2\right] t_{\text{2D}}\,. \end{gathered} \tag{4.3}$$

Solving (4.3) for Δx gives the optimum length

$$\Delta x_{\text{near}} = \frac{1}{k}\frac{-\ln\delta}{\sqrt{\frac{2a}{3\pi\gamma}k\left(1 - \frac{1}{4}\ln\delta\right)^{1.5} - 1}} \tag{4.4}$$

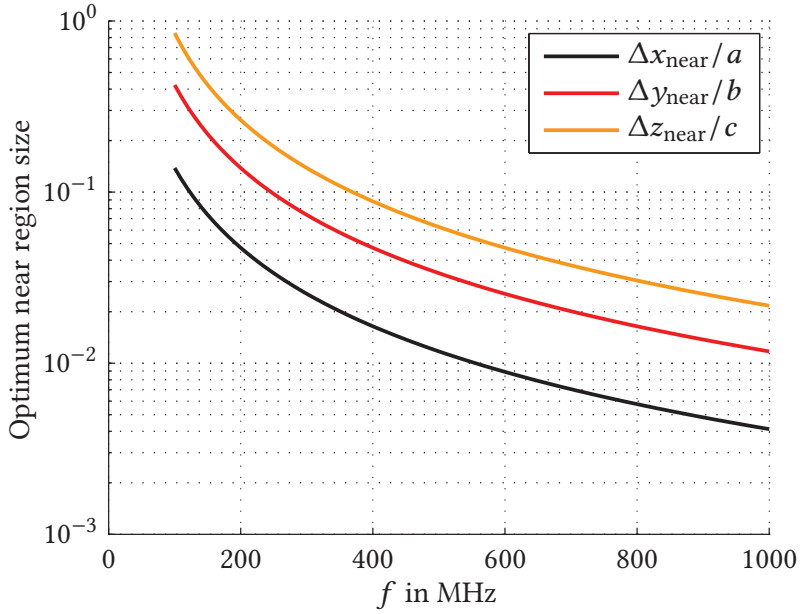

Fig. 4.2.: Normalized optimum length, width, and height of the near region for a cavity of size 12 m × 6 m × 4 m.

where $\gamma = t_{\text{2D}}/t_{\text{Ew-spec}}$ is the ratio of the computation times per mode between the 2D spectral representations and the Ewald representation. The ratio γ is around four as the 2D spectral representations mainly involve complex operations in contrast to the Ewald representation which mainly involves real operations. Likewise, the optimum width Δy_{near} and height Δz_{near} of the near region become

$$\Delta y_{\text{near}} = \frac{1}{k} \frac{-\ln \delta}{\sqrt{\frac{2b}{3\pi\gamma} k \left(1 - \frac{1}{4} \ln \delta\right)^{1.5} - 1}} \tag{4.5}$$

and

$$\Delta z_{\text{near}} = \frac{1}{k} \frac{-\ln \delta}{\sqrt{\frac{2c}{3\pi\gamma} k \left(1 - \frac{1}{4} \ln \delta\right)^{1.5} - 1}}, \tag{4.6}$$

respectively. As shown in Fig. 4.2, the optimum size of the near range decreases with frequency. In the over-moded frequency range, it is proportional to $1/f^{1.5}$. The optimum length, width, and height of the near region decrease when the respective dimensions of the cavity are increased. As the optimum size of the near region (i.e., the Ewald region) goes to zero in the asymptotic limit, the complexity of the hybrid representation with respect to frequency is inherited from the 2D spectral representations: the operation count scales with f^2.

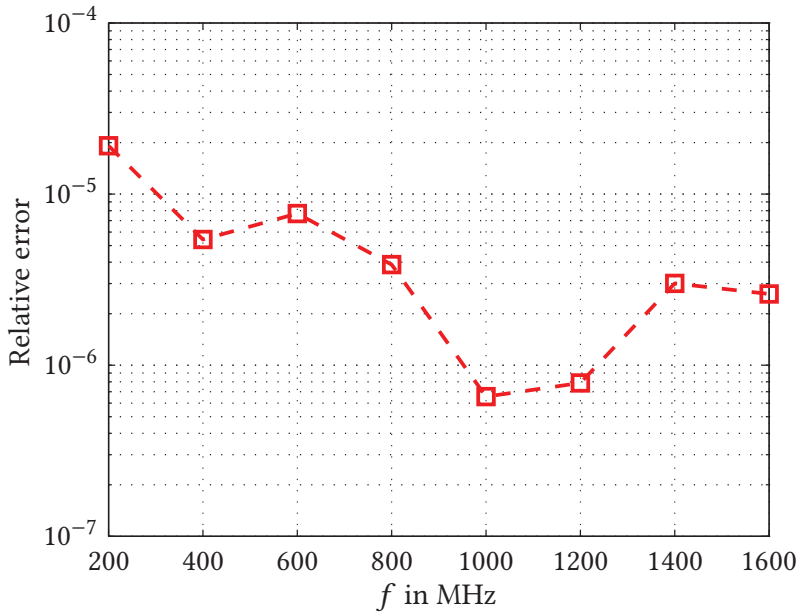

Fig. 4.3.: Relative error of the hybrid Ewald-2D Spectral representation averaged over 10^3 Green's function values.

4.1.2. Validation and Performance

The hybrid Ewald-2D Spectral representation is validated against and compared with the ordinary Ewald representation. The precision of the reference is set to 10^{-8} (i.e., single precision). The accuracy of the hybrid representation is set to 10^{-4} according to (3.11) and (3.36). A cavity of size $12\,\mathrm{m} \times 6\,\mathrm{m} \times 4\,\mathrm{m}$ is considered in the frequency range from 200 MHz to 1 600 MHz. The Green's function is evaluated at 1 000 randomly selected source and observation points.

In Figure 4.3, the average relative error of the hybrid Ewald-2D Spectral representation is plotted over the frequency. For all frequencies, the relative error is smaller than the preset value. In Table 4.1, the performance of the hybrid and the Ewald representation are compared. The hybrid representation outperforms the pure Ewald representation at all frequencies. At high frequencies, it is particularly advantageous. While the computation time of the ordinary Ewald summation scales with f^3, the computation time of the hybrid representation grows less than quadratically with frequency. The reasons for the less than quadratic growth are twofold. On the one hand, the size of the near region shrinks with frequency. Hence, more and more samples are calculated with the 2D spectral representations, see Table 4.1. On the other hand, the number of necessary modes in the 2D spectral representations grows with f^2 in the high frequency range only. In the lower frequency range, it is approximately constant, cf. Fig. 3.6.

	Ewald	Hybrid		
f in MHz	t_{Ewald} in s	t_{Hybrid} in s	N_{Ewald}	$N_{\text{2D spectral}}$
200	1.09	0.45	305	695
400	7.96	1.01	21	979
600	24.6	1.37	6	994
800	57.7	1.89	1	999
1 000	115.8	2.54	0	1 000
1 200	192.7	3.23	0	1 000
1 400	250.9	4.33	0	1 000
1 600	424.6	5.23	0	1 000

Tab. 4.1.: Computation times of the hybrid Ewald-2D Spectral and the ordinary Ewald representation for 10^3 values and number of samples calculated with the Ewald (N_{Ewald}) and the 2D spectral representations ($N_{\text{2D spectral}}$).

4.2. Fast Group Spectral Domain Approach

The Ewald-2D Spectral representation is a hybrid representation. Near couplings are calculated with the Ewald representation while far couplings are calculated with one of the 2D spectral representations. To transfer the hybrid scheme to the BI formulation, the domain (i.e., the cavity) is divided into groups of size $a_g \times b_g \times c_g$ and center $\boldsymbol{r}_c = \begin{pmatrix} x_c & y_c & z_c \end{pmatrix}$. The size of the groups is chosen as $a_g \approx \Delta x_{\text{near}}$ such that the a is an integer multiple of a_g, $b_g \approx \Delta y_{\text{near}}$ such that the b is an integer multiple of b_g, and so forth. Interactions within a group and between neighboring groups are calculated with the Ewald representation. Interactions between well separated groups are calculated with the x-, the y-, or the z-2D spectral representation. The x-2D spectral representation is employed when the relative distance $|(x_c - x_c')/a_g|$ in x-direction is maximal where the primed and the unprimed coordinate refer to test and group center, respectively. The y- and z-2D spectral representations are employed when the relative distances in y- and z-direction are maximal, respectively. The grouping scheme is illustrated in Fig. 4.4.

Accordingly, the system matrix is decomposed into near- and far-interaction components

$$\boldsymbol{B} = \boldsymbol{B}_{\text{near}} + \boldsymbol{B}_{\text{far}}. \tag{4.7}$$

Because the Ewald representation consists of a spatial and a spectral series, the near-interaction matrix is further decomposed into a spatial and a spectral part according to

$$\boldsymbol{B}_{\text{near}} = \boldsymbol{B}_{\text{spat}} + \boldsymbol{B}_{\text{spec}}. \tag{4.8}$$

In the over-moded frequency range, the operation count of the spatial part of the near-interaction matrix is negligible compared to the operation count of the spectral

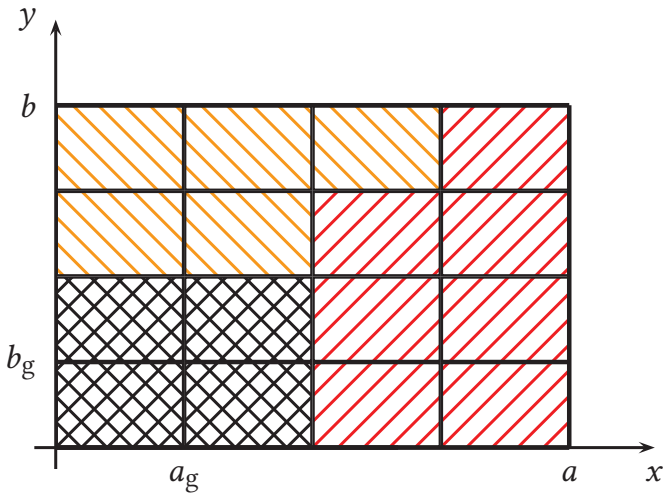

Fig. 4.4.: Grouping scheme of the hybrid approach for a source in the left lower group: Ewald representation (crosshatch), x-2D spectral representation (upward diagonal), y-2D spectral representation (downward diagonal)

part. It is evaluated in the spatial domain without any acceleration. The singular integrals originating from the singularity in the spatial domain are treated analogously to the singular integrals in FGF BI formulations. As the singular part of the spatial series has the same structure as the FGF, the hyper singularity is reduced to a weak singularity using the mixed potential formulation and the surface divergence theorem [Jin10]. The remaining weak singularities are integrated using singularity cancellation techniques (see e.g., [Kha05; Ism08; Li14]).

The spectral part of the near-interaction matrix causes the major operation count in the over-moded frequency. To accelerate the evaluation of the spectral part, a fast spectral domain approach (FSDA) is presented in the following. The approach is derived for the weakly singular system matrix $\boldsymbol{B}$ only. The other system matrices are treated analogously. Inserting (3.30) into (2.78b), the spectral part of the near-interaction matrix is

$$\left[\boldsymbol{B}_{\text{spec}}\right]_{kl} = \iint_S \iint_S \boldsymbol{\beta}_k(\boldsymbol{r}) \cdot \mu \sum_{m,n,p=0}^{\infty} H_{mnp} \sum_{i=1}^{3} \phi_{i,mnp}(\boldsymbol{r}) \, \phi_{i,mnp}\left(\boldsymbol{r}'\right) \hat{x}_i \hat{x}_i \cdot \boldsymbol{\beta}_l\left(\boldsymbol{r}'\right) \mathrm{d}s' \, \mathrm{d}s \tag{4.9}$$

where $\{x_1, x_2, x_3\} = \{x, y, z\}$. Interchanging the order of integration and summation

yields

$$\left[\boldsymbol{B}_{\text{spec}}\right]_{kl} = \mu \sum_{m,n,p=0}^{\infty} H_{mnp} \iint_S \iint_S \boldsymbol{\beta}_k(\boldsymbol{r}) \cdot \sum_{i=1}^{3} \phi_{i,mnp}(\boldsymbol{r}) \phi_{i,mnp}\left(\boldsymbol{r}'\right) \hat{x}_i \hat{x}_i \cdot \boldsymbol{\beta}_l\left(\boldsymbol{r}'\right) \mathrm{d}s' \, \mathrm{d}s \,. \tag{4.10}$$

Since the individual terms of the spectral series are factorizable with respect to observation and source point, the nested integration over test and source domain is split into two non-nested integrals according to

$$\left[\boldsymbol{B}_{\text{spec}}\right]_{kl} = \mu \sum_{m,n,p=0}^{\infty} H_{mnp} \sum_{i=1}^{3} \iint_S \phi_{i,mnp}(\boldsymbol{r}) \hat{x}_i \cdot \boldsymbol{\beta}_k(\boldsymbol{r}) \, \mathrm{d}s \iint_S \phi_{i,mnp}\left(\boldsymbol{r}'\right) \hat{x}_i \cdot \boldsymbol{\beta}_l\left(\boldsymbol{r}'\right) \mathrm{d}s' \,. \tag{4.11}$$

In compact form (4.11) reads

$$\left[\boldsymbol{B}_{\text{spec}}\right]_{kl} = \sum_{m,n,p=0}^{\infty} \widetilde{\boldsymbol{\beta}}_{k,mnp} \cdot \overline{\widetilde{\boldsymbol{G}}}^{A}_{\text{Ew-spec},mnp} \cdot \widetilde{\boldsymbol{\beta}}_{l,mnp} \,. \tag{4.12}$$

where

$$\widetilde{\boldsymbol{\beta}}_{k,mnp} = \sum_{i=1}^{3} \iint_S \phi_{i,mnp}(\boldsymbol{r}) \hat{x}_i \cdot \boldsymbol{\beta}_k(\boldsymbol{r}) \, \mathrm{d}s \tag{4.13}$$

turn out to be the representations of the basis functions in the spectral domain, and

$$\overline{\widetilde{\boldsymbol{G}}}^{A}_{\text{Ew-spec},mnp} = \mu H_{mnp} \sum_{i=1}^{3} \hat{x}_i \hat{x}_i \tag{4.14}$$

is the spectral representation of the spectral series of the Ewald summation. The FSDA significantly accelerates the evaluation of the near-interaction matrix as 1) the operation count of the spectral representations in (4.13) scales linearly with the number of unknowns when they are precomputed and stored and 2) the evaluation of (4.12) is significantly faster than the evaluation of (4.9) since the integration over test and source domain is not needed. A pseudo-code of the computation of the near interactions is sketched in Algorithm 4.1.

The far-interactions are calculated with one of the 2D-spectral representations. Accordingly, the far-interaction matrix is split into

$$\boldsymbol{B}_{\text{far}} = \boldsymbol{B}_{x\text{-far}} + \boldsymbol{B}_{y\text{-far}} + \boldsymbol{B}_{z\text{-far}}. \tag{4.15}$$

Algorithm 4.1 Fast group spectral domain approach

```
    % Near interactions
    % precompute and store spectral representations
 1: for k ← 1, N do        % loop basis functions
 2:     for i_mode ← 0, N_Ewald do        % loop modes
 3:         ...
 4:     end for
 5: end for

    % compute system matrix
 6: for k ← 1, N do        % loop test basis functions
 7:     for l ← 1, N do        % loop source basis functions
 8:         for i_mode ← 0, N_Ewald do        % loop modes
 9:             ...
10:         end for
11:     end for
12: end for
```

In the following, the spectral domain acceleration for $\boldsymbol{B}_{z\text{-far}}$ is presented. The other matrices are treated analogously. Although the z-2D spectral representation has a similar structure as the spectral series of the Ewald summation, the FSDA cannot be applied without modification. The key property of the spectral series is that its individual terms are factorizable with respect to observation and source point. Without this property the FSDA is not applicable. In (3.4), the individual terms of the 2D-spectral representation are factorizable but the series is numerically not stable. The series in (3.8) is numerically stable but the terms are no longer factorizable. To address this issue, a FGSDA inspired by the fast multipole method (FMM) [Jin10] is proposed. The functions $\xi_{i,mn}$ are shifted to the center of the corresponding group according to

$$\xi''_{i,mn}(\boldsymbol{r}_>) = \mathrm{e}^{-\alpha_{mn}\left(c - z_{\mathrm{c},>}\right)}\, \xi_{i,mn}(\boldsymbol{r}_>)\ , \tag{4.16a}$$

$$\xi''_{i,mn}(\boldsymbol{r}_<) = \mathrm{e}^{-\alpha_{mn} z_{\mathrm{c},<}}\, \xi_{i,mn}(\boldsymbol{r}_<)\ . \tag{4.16b}$$

The z-2D spectral representation becomes

$$\overline{\boldsymbol{G}}^{\mathrm{A}}_{\text{z-2D}}\left(\boldsymbol{r},\boldsymbol{r}'\right) = \mu \sum_{m,n=0}^{\infty} T_{mn} H_{mn} \sum_{i=1}^{3} \xi''_{i,mn}(\boldsymbol{r}_>)\, \xi''_{i,mn}(\boldsymbol{r}_<)\, \hat{x}_i \hat{x}_i \tag{4.17}$$

where

$$T_{mn} = \mathrm{e}^{-\alpha_{mn}\left(z_{\mathrm{c},>} - z_{\mathrm{c},<} - c\right)} \tag{4.18}$$

is the translation function between test and source group, $z_{\mathrm{c},>}$ means the greater of test and source group center, and vice versa $z_{\mathrm{c},<}$ means the lesser of test and source group

center. The z-2D spectral representation in the form of (4.17) meets both requirements. It is numerically stable for large α_{mn} as shown in Appendix A.3 and it preserves the factorizability of the individual terms as test and source group center do not depend on observation and source point. Following (4.9) to (4.12), the z-2D part of the far-interaction matrix becomes

$$[\boldsymbol{B}_{z\text{-far}}]_{kl} = \sum_{m,n=0}^{\infty} \widetilde{\boldsymbol{\beta}}_{k,mn,>} \cdot T_{mn} \overline{\widetilde{\boldsymbol{G}}}^{A}_{z\text{-2D},mn} \cdot \widetilde{\boldsymbol{\beta}}_{l,mn,<} \tag{4.19}$$

where

$$\widetilde{\boldsymbol{\beta}}_{k,mn,>/<} = \sum_{i=1}^{3} \iint_S \xi''_{i,mn}\left(\boldsymbol{r}_{>/<}\right) \hat{x}_i \cdot \boldsymbol{\beta}_k(\boldsymbol{r})\, \mathrm{d}s \tag{4.20}$$

are the shifted spectral representations of the basis functions and

$$\overline{\widetilde{\boldsymbol{G}}}^{A}_{z\text{-2D},mn} = \mu H_{mn} \sum_{i=1}^{3} \hat{x}_i \hat{x}_i \tag{4.21}$$

is the z-2D spectral representation in the spectral domain. The FGSDA needs only marginally more computation time per mode than the original FSDA. Both significantly accelerate the computation of the system matrix as the integration over test and source domain is not necessary. Only the translation function between test and source group must additionally be computed in the case of the FGSDA.

The implementation of the FGSDA as suggested in Fig. 4.1 requires a lot of memory at high frequencies. The spectral representations of the basis functions must be stored for each mode. As the number of modes grows with f^3, the memory demand of the algorithm would scale with f^3 as well. For a cavity of the size 12 m × 6 m × 4 m, roughly 10^5 modes (Ewald and 2D spectral representations) would have to be considered at 600 MHz (i.e., 2.9 MB memory are needed per basis function). However, it is not necessary to precompute all spectral representations of the basis functions at the same time. Instead, the interaction integrals are evaluated mode-wise: 1) the spectral representations of the first mode of the Ewald representation are precomputed and stored, 2) the contribution of the first mode to the interaction integrals is computed and added to the system matrix, and 3) the spectral representations of the first mode are deleted. Now, the steps are repeated for the second mode and so forth. After the near-zone part of the system matrix is complete, the far interactions are calculated in the same way. A pseudo-code of the mode-wise computation of the near interactions is sketched in Algorithm 4.2.

Algorithm 4.2 Mode-wise fast group spectral domain approach

```
    % Near interactions
 1: for i_mode ← 0, N_Ewald do        % loop modes
        % precompute and store spectral representations mode-wise
 2:     for k ← 1, N do        % loop basis functions
 3:         ...
 4:     end for

        % compute system matrix mode-wise
 5:     for k ← 1, N do        % loop test basis functions
 6:         for l ← 1, N do        % loop source basis functions
 7:             ...
 8:         end for
 9:     end for
10: end for
```

5. Fast Fourier Transform Approach

The CGF BEM suffers from two limitations: the computationally expensive CGF in the over-moded frequency range and the quadratic complexity in filling the system matrix. In this chapter, an FFT accelerated Ewald summation technique together with Lagrange polynomial interpolation is presented to address these limitations. The filling of the system matrix is accelerated by sampling the CGF in a pre-processing step and using Lagrange interpolation to evaluate the interaction integrals. To generate the required samples efficiently, the Ewald summation technique is accelerated using the FFT. In Section 5.1, the FFT accelerated Ewald summation technique is presented and analyzed. In Section 5.2, the computation of the interaction integrals is optimized.

5.1. Fast Fourier Transform Accelerated Ewald Summation Technique

5.1.1. Derivation

In the over-moded frequency range, the Ewald summation technique suffers from the high-frequency breakdown. The number of terms in the spectral series grows with f^3. To address this issue, an FFT accelerated spectral series is proposed in the following. For brevity, the FFT acceleration is only presented for the Green's function of the magnetic vector potential (i.e., the weakly singular integral kernel). The other Green's functions are treated similarly.

As the FFT is applicable to uniformly spaced data only, it is necessary to sample the spectral series. In the form of (3.30), the spectral series is a six-variable function as it depends on observation and source point. Sampling a six-variable function results in a prohibitively poor memory complexity. But the spectral series can be rewritten as a sum of eight three variable functions which only differ by their arguments. Using Euler's relations and changing the indices m, n, and p appropriately (see Appendix A.2), the spectral series becomes

$$\overline{G}^{A}_{\text{Ew-spec}}\left(\boldsymbol{r},\boldsymbol{r}'\right) = \frac{\mu}{8abc}\sum_{q=0}^{7} Q\left(x_q,y_q,z_q\right)\sum_{i=1}^{3} A_{i,q}\hat{x}_i\hat{x}_i \tag{5.1}$$

where

$$Q\left(x_q,y_q,z_q\right) = \sum_{m,n,p=-\infty}^{\infty} H_{mnp}\, \mathrm{e}^{\mathrm{j}k_x x_q}\mathrm{e}^{\mathrm{j}k_y y_q}\mathrm{e}^{\mathrm{j}k_z z_q}\,. \tag{5.2}$$

Sampling $Q\left(x_q, y_q, z_q\right)$ on an equispaced grid with $x_q = \alpha h_\mathrm{q}$, $y_q = \beta h_\mathrm{q}$, and $z_q = \gamma h_\mathrm{q}$, where h_q is the sampling density, the array $Q_{\alpha\beta\gamma}$ becomes the inverse Fourier transform (FT) of H_{mnp} according to

$$\begin{aligned} Q_{\alpha\beta\gamma} &= \sum_{m=-M+1}^{M} \sum_{n=-N+1}^{N} \sum_{p=-P+1}^{P} H_{mnp}\, \mathrm{e}^{\mathrm{j}\pi\alpha m/M} \mathrm{e}^{\mathrm{j}\pi\beta n/N} \mathrm{e}^{\mathrm{j}\pi\gamma p/P} \\ &= \mathrm{FT}^{-1}\left\{H_{mnp}\right\}. \end{aligned} \tag{5.3}$$

where $M = \lceil a/h_\mathrm{q} \rceil$, $N = \lceil b/h_\mathrm{q} \rceil$, and $P = \lceil c/h_\mathrm{q} \rceil$. Since $\alpha \in [-M+1; M]$, $\beta \in [-N+1; N]$, and $\gamma \in [-P+1; P]$, $-a < x_q \leq a$, $-b < y_q \leq b$, and $-c < z_q \leq c$, respectively. Values of x_q, y_q, and z_q outside these intervals[9] are obtained using the periodicity of the Q-array.

Values in between the grid are interpolated using Lagrange polynomials. The three-dimensional Lagrange interpolation of a function $f\left(x, y, z\right)$ is given by

$$f\left(x, y, z\right) \approx \sum_{u=1}^{N_\mathrm{p}+1} \sum_{v=1}^{N_\mathrm{p}+1} \sum_{w=1}^{N_\mathrm{p}+1} f\left(x_u, y_v, z_w\right) \ell_u\left(x\right) \ell_v\left(y\right) \ell_w\left(z\right), \tag{5.4}$$

where $\ell_u\left(x\right)$, $\ell_v\left(y\right)$, and $\ell_w\left(z\right)$ are the one-dimensional Lagrange polynomials [Abr70] in the respective dimension and N_p is the order of the Lagrange polynomials. Using the barycentric representation of the Lagrange polynomials, they are evaluated with linear instead of quadratic complexity [Str07] and the overall operation count of (5.4) scales only with N_p^3 instead of N_p^6. The interpolation nodes are chosen symmetrically around the interpolation point as the interpolation error is minimal at the center of the interpolation region. Using the Lagrange interpolation together with the Q-array, the spectral series of the Ewald summation is written as

$$\begin{aligned} \overline{G}^{A}_{\text{Ew-spec}}\left(\boldsymbol{r}, \boldsymbol{r}'\right) = \frac{\mu}{8abc} \sum_{q=0}^{7} \sum_{i=1}^{3} A_{i,q} \hat{x}_i \hat{x}_i \\ \sum_{u=1}^{N_p+1} \sum_{v=1}^{N_p+1} \sum_{w=1}^{N_p+1} Q_{\alpha_u \beta_v \gamma_w}\, \ell_u\left(x_q\right) \ell_v\left(y_q\right) \ell_w\left(z_q\right), \end{aligned} \tag{5.5}$$

where α_u, β_v, and γ_w are the indices of the symmetrically chosen interpolation nodes, see Fig. 5.1.

9 According to 3.1, x_q, y_q, and z_q are in the intervals $(-a; 2a)$, $(-b; 2b)$, and $(-c; 2c)$, respectively

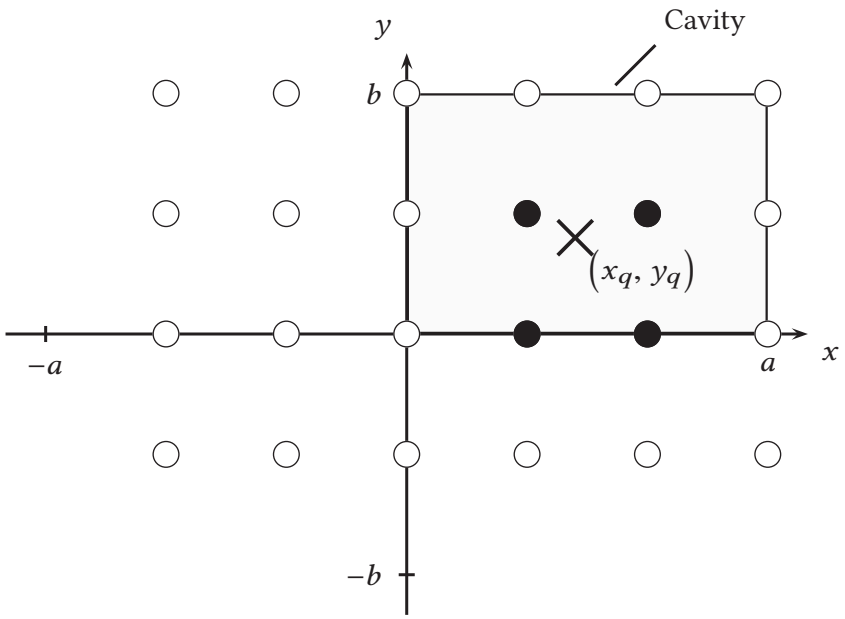

Fig. 5.1.: Choice of interpolation nodes for a Q-array of size 6×4 and a Lagrange polynomial order $N_\mathrm{p} = 1$. The indices α_u and β_v are $\alpha_1 = 1$, $\alpha_2 = 2$, $\beta_1 = 0$, and $\beta_1 = 1$.

5.1.2. Validation and Performance

In the following, the accuracy and the performance of the FFT accelerated Ewald summation technique are investigated. A cavity of size 12 m × 6 m × 4 m is considered. The ordinary Ewald summation technique with an accuracy of 10^{-8} (i.e., single precision) serves as reference. The Green's function is calculated at 1 000 points.

The accuracy of the proposed approach is influenced by the sampling density h_q of the Q-array and the Lagrange polynomial order N_p. In Fig. 5.2, the relative error is illustrated for different sampling densities and polynomial orders at 200 MHz. The FFT accelerated Ewald summation technique achieves an accuracy close to single precision for suitably chosen sampling densities and polynomial orders. With regard to efficiency, neither a combination of high sampling densities and low polynomial orders nor a combination of low sampling densities and high polynomial orders are advantageous. They lead to either high memory consumption or high computational effort. Combinations of medium sampling densities and medium polynomial orders are favorable as they balance memory demand and computational cost. A Lagrange polynomial order of $N_\mathrm{p} = 2$ would, for instance, require 40 samples per wavelength to attain an accuracy of 10^{-4}. When the polynomial order is doubled, however, 15 samples per wavelength (i.e., less than half) are sufficient.

The frequency may influence the accuracy of the proposed method. In Fig. 5.3, the relative error is shown for different frequencies. The sampling density is set to 15 samples per wavelength and the polynomial order is set to $N_\mathrm{p} = 4$. The relative error

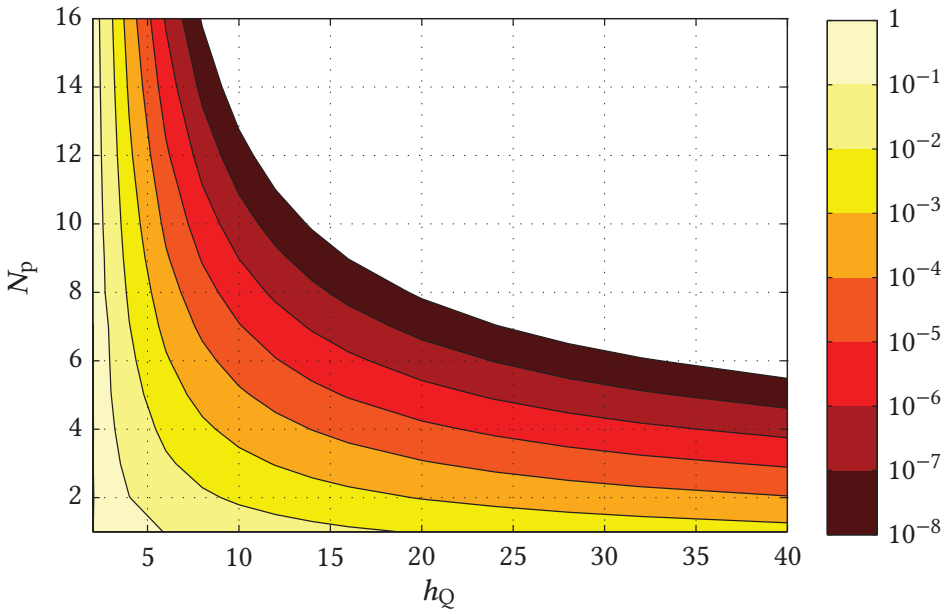

Fig. 5.2.: Relative error of FFT accelerated Ewald summation technique as a function of sampling density and polynomial order at 200 MHz.

varies little over frequency. It is constantly below 10^{-4}. Consequently, the accuracy of the FFT accelerated Ewald summation technique is not influenced by the frequency as long as the number of samples per wavelength is constant.

Next, the performance of the FFT accelerated Ewald summation technique is analyzed. The desired accuracy of the CGF is 10^{-4}. According to Fig. 5.2, a sampling density of 15 samples per wavelength and a polynomial order of $N_\mathrm{p} = 4$ achieve this precision. The computation times t_Ewald and t_Lagrange of the ordinary and the FFT accelerated Ewald summation are listed in Table 5.1 for different frequencies. The computation time of the ordinary Ewald summation scales approximately with f^3. While it needs 22.38 s at 600 MHz, 164.9 s are needed at twice the frequency. The FFT accelerated Ewald summation technique does, in contrast, barely depend on the frequency. The computation times are constant at lower frequencies. At higher frequencies, the computation times increase slightly since the memory access to the Q-array becomes more expensive. The constant computational time complexity comes at the expense of precomputing and storing the Q-array. The operation count of the Q-array scales with $f^3 \log f$ and its memory demand increases with f^3, see also Section 6.3. Yet, for several hundred million Green's function evaluations as needed in BEMs, the time of the Q-array is negligible. The next-to-last column in Table 5.1 shows the maximum speed-up (i.e., $t_{Q\text{-array}}$ is neglected) of the FFT accelerated versus the ordinary Ewald summation technique. The acceleration reaches up to four orders of magnitude.

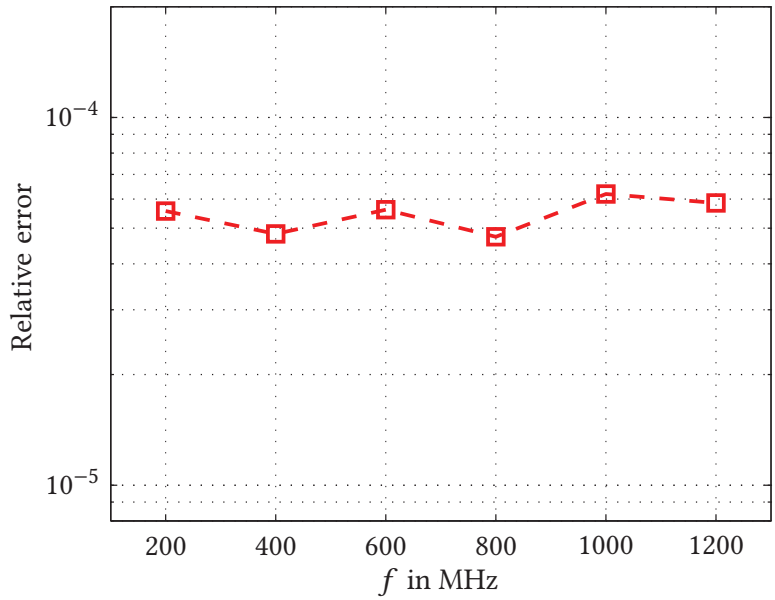

Fig. 5.3.: Relative error as a function of frequency for a sampling density of 15 samples per wavelength and a polynomial order of $N_\mathrm{p} = 4$.

	Ewald	FFT Ewald			
f in MHz	t_Ewald in s	t_Lagrange in s	$t_{Q\text{-array}}$ in s	memory in GB	maximum speed-up
200	0.951	$27.6 \cdot 10^{-3}$	0.476	0.018	34.5
400	7.261	$26.4 \cdot 10^{-3}$	3.981	0.147	275.0
600	22.38	$25.1 \cdot 10^{-3}$	13.30	0.498	891.6
800	50.91	$30.3 \cdot 10^{-3}$	34.03	1.180	1 680
1 000	103.3	$34.0 \cdot 10^{-3}$	68.00	2.304	3 038
1 200	164.9	$31.7 \cdot 10^{-3}$	109.9	3.981	5 202

Tab. 5.1.: Computation times of the FFT accelerated and of the ordinary Ewald summation technique for 10^3 Green's function values.

5.2. Accelerated System Matrix Fill

Inherited from the ordinary Ewald summation technique, the system matrix is decomposed into a spatial and a spectral part for the FFT accelerated technique according to

$$\boldsymbol{B} = \boldsymbol{B}_{\text{spat}} + \boldsymbol{B}_{\text{spec}}. \tag{5.6}$$

The spatial part is evaluated as described in Chapter 4. For the spectral part, the Q-array is computed and stored first. Then, the interaction integrals are evaluated using (2.78b) and (5.5) according to

$$\begin{aligned}\left[\boldsymbol{B}_{\text{spec}}\right]_{kl} = \frac{\mu}{8abc} \iint_S \iint_S \boldsymbol{\beta}_k(\boldsymbol{r}) \cdot \sum_{q=0}^{7} \sum_{i=1}^{3} A_{i,q} \hat{x}_i \hat{x}_i \\ \sum_{u=1}^{N_p+1} \sum_{v=1}^{N_p+1} \sum_{w=1}^{N_p+1} Q_{\alpha_u \beta_v \gamma_w} \ell_u\left(x_q\right) \ell_v\left(y_q\right) \ell_w\left(z_q\right) \cdot \boldsymbol{\beta}_l\left(\boldsymbol{r}'\right) \mathrm{d}s' \, \mathrm{d}s\end{aligned} \tag{5.7}$$

where α_u, β_v, and γ_w are the indices of the interpolation nodes which are chosen symmetrically around interpolation point. The computation of (5.7) is straightforward, however, the implementation is optimized as described in the following.

The integrals over test and source domain are evaluated using a Gaussian quadrature rule [Pre92]. The interpolation values are loaded from the memory for each quadrature point. In particular, when the Q-array is large, this is the most time-consuming step in the computation of the interaction integrals. As a remedy, the interpolation values are loaded only once per interaction integral. They are cached and used throughout the integration. The nodes are chosen on the basis of the centers of test and source triangles. As the distance between the triangle center and a quadrature point is, for reasonable discretization densities of the surfaces and sampling densities of the Q-array, considerably smaller than the size of the interpolation region, the accuracy of the Lagrange interpolation is maintained. In Fig. 5.4, the interpolation points and nodes are shown for an exemplary interaction integral.

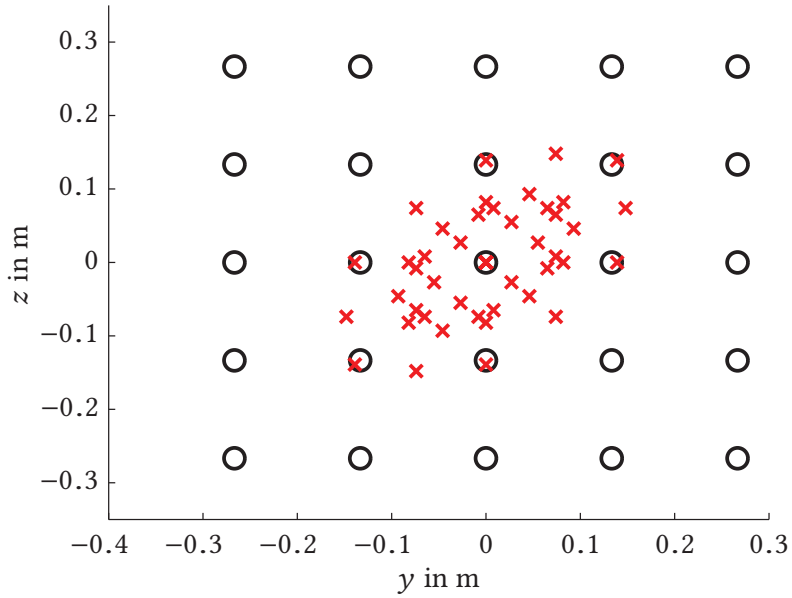

Fig. 5.4.: Interpolation points (crosses) and nodes (circles) for an exemplary interaction integral for $q = 0$, $N_\mathrm{p} = 4$, and a sampling density (Q-array) of $\lambda/15$. The discretization density is $\lambda/10$. The frequency is set to 150 MHz. Both the test and the source triangle are located in the yz-plane.

6. Numerical Results

In this chapter, numerical results are presented. In Section 6.1, the FGSDA and the FFT accelerated CGF BEM are validated against and compared with other state of the art algorithms. Examples of practical relevance which involve perfectly conducting, well conducting, and dielectric objects are presented. Standard simulation settings are used. In Section 6.2, the accuracy and the stability of the CGF BEM is further investigated. Among other consistency checks, the discretization density is refined. In Section 6.3, the complexities of the proposed algorithms are derived. The operation count and memory requirements of the FGSDA and FFT Ewald (Ewd) algorithm are analyzed in detail and discussed with respect to the complexity of the algorithms. Last but not least, the CGF BEM is validated against measurements in Section 6.4.

6.1. Validation and Comparison Against other Numerical Methods

The CGF BEM algorithms are validated against and compared with an MLFMM accelerated FGF BEM algorithm [Eib05] and two other recently proposed algorithms for the numerical modeling of reverberation chambers [Zha11; Yan14]. In the first part of the section, PEC objects are considered. In the second part, well but not perfectly conducting objects are modeled and dielectric objects are considered in the third part. In all cases, the EFIE is used. For well conducting objects, the IBC is added and for dielectric objects, the BI formulation is coupled to the FEM, see Section 2.3 and 2.4. In Sections 6.1.1 to 6.1.3, the walls of the cavity are modeled as perfect electric conductors. The validity of the CGF BEM for imperfectly conducting walls is investigated in Section 6.1.4.

6.1.1. Perfectly Conducting Objects

Firstly, the FGSDA and the FFT accelerated CGF BEM algorithms are compared with an MLFMM accelerated FGF BEM [Eib05]. The algorithms are referred to as FGSDA, FFT Ewd, and MLFMM, respectively. The linear equation system is solved with a GMRES solver in the case of the FGSDA and the FFT Ewd and with a flexible inner-outer GMRES (GMRES-IO) [Saa93] in the case of the MLFMM algorithm. Using the GMRES without inner loops would speed up the MLFMM algorithm, however, at the cost of a considerably increased memory demand. The exact trade-offs and limitations of the non inner-outer GMRES in the case of MLFMM accelerated BEM are not studied in here and remain for future work. The residual of the GMRES solver and the accuracy of the CGF are set to

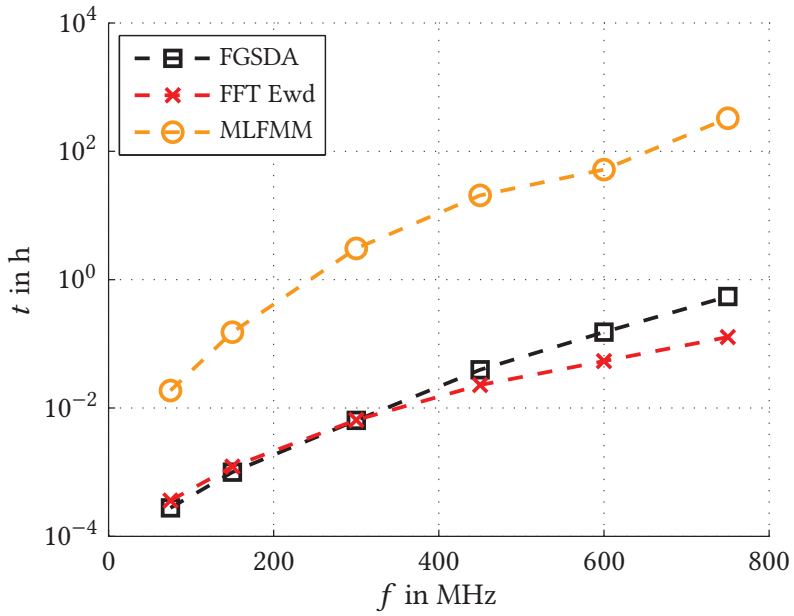

Fig. 6.1.: Computation times of the FGSDA, the FFT Ewd, and the MLFMM algorithm for the Vivaldi antenna.

10^{-4}. The discretization density is $\lambda/10$. A detailed list of all simulation parameters is given in Appendix C.

The size of the considered reverberation chamber is $12\,\mathrm{m} \times 6\,\mathrm{m} \times 4\,\mathrm{m}$. Its lowest usable frequency is around 75 MHz according to [IEC11]. Three different scenarios are considered in the frequency range from 75 MHz to 750 MHz: in the first scenario, a small object is placed in the reverberation chamber; in the second one, the chamber contains a medium-sized object; and a large and a mid-size object are considered in the third one.

In the first scenario, a Vivaldi antenna is considered. The shape of the Vivaldi antenna is adopted from [Mar13]. Its size is doubled as the considered reverberation chamber is approximately twice as large as the chamber in [Mar13]. The generator impedance Z_g is set to $50\,\Omega$. The computation times of the FGSDA, the FFT Ewd, and the MLFMM algorithm are compared in Figure 6.1. As the object in the cavity is small relative to the walls, the CGF BEM is in particular advantageous: the number of unknowns is reduced by more than two orders of magnitude. The speed-up of the FGSDA versus the MLFMM ranges from 67 at 75 MHz to 600 at 750 MHz. The FFT Ewd algorithm achieves an even higher speed-up in the upper frequency range. At 750 MHz, the gain versus the MLFMM algorithm is about 2 500. The normalized input impedance $Z_\mathrm{in}/Z_\mathrm{g}$ of the Vivaldi antenna is given in Table 6.1. At lower frequencies, the results are in good agreement: the relative difference at 75 MHz and 150 MHz is below 2%. With increasing frequency, the difference between the CGF BEM algorithms and the MLFMM algorithm increases: at 750 MHz, the relative deviation is about 17%.

f in MHz	$Z_{\text{in}}/Z_{\text{g}}$		
	MLFMM	FGSDA	FFT Ewd
75	0.00 − j0.48	0.00 − j0.49	0.00 − j0.49
150	0.00 + j3.58	0.00 + j3.61	0.00 + j3.61
300	0.02 + j0.00	0.00 + j1.25	0.00 + j1.25
450	0.00 + j0.46	0.00 + j0.69	0.00 + j0.69
600	0.01 + j2.16	0.00 + j2.18	0.00 + j2.18
750	0.08 + j2.52	0.00 + j3.08	0.00 + j3.08

Tab. 6.1.: Normalized input impedance $Z_{\text{in}}/Z_{\text{g}}$ of the Vivaldi antenna.

f in MHz	δ in %		
	FGSDA vs. MLFMM	FFT Ewd vs. MLFMM	FGSDA vs. FFT Ewd
75	0.79	0.79	0.00
150	1.88	1.89	0.01
300	20.03	20.07	0.07
450	22.27	22.42	0.14
600	212.2	201.2	10.29
750	161.0	164.5	80.30

Tab. 6.2.: Relative difference δ between the current densities on the stirrer.

As a mid-size object, a w-shaped two-plate stirrer inspired by [Wel07] is chosen. The surface area of the stirrer is 8.8 m. When it is rotated parallel to the z-axis around its center at (10.0 m, 3.0 m, 2.0 m), the stirred volume is about 8% of the cavity volume. The chamber is excited by an electrically small strip dipole of size 0.2 m × 0.05 m which is aligned to the z-axis. The generator impedance of the dipole is set to 50 Ω. The computation times of the CGF BEM algorithms and the MLFMM algorithm are shown in Fig. 6.2. The maximum speed-up of the FGSDA against the MLFMM is 37 at 300 MHz. With increasing frequency, the gain of the FGSDA compared to the MLFMM decreases slightly. In contrast, the speed-up of the FFT Ewd versus the MLFMM algorithm increases with frequency but the FFT Ewd algorithm is for $f < 750$ MHz slower than the FGSDA.

Table 6.2 shows the relative difference between the electric currents on the stirrer. Again, the difference is small at low frequencies and increases with frequency. In particular, the results of the CGF BEM algorithms deviate significantly from that of the MLFMM algorithm at high frequencies. The difference between the FGSDA and the FFT Ewd algorithm is generally low. Yet, there is also an increase at high frequencies.

In the last scenario, a car body is added to the w-shaped stirrer of the previous scenario. The center of the car bottom is at (5.5 m, 3.0 m, 0.3 m). As the reverberation

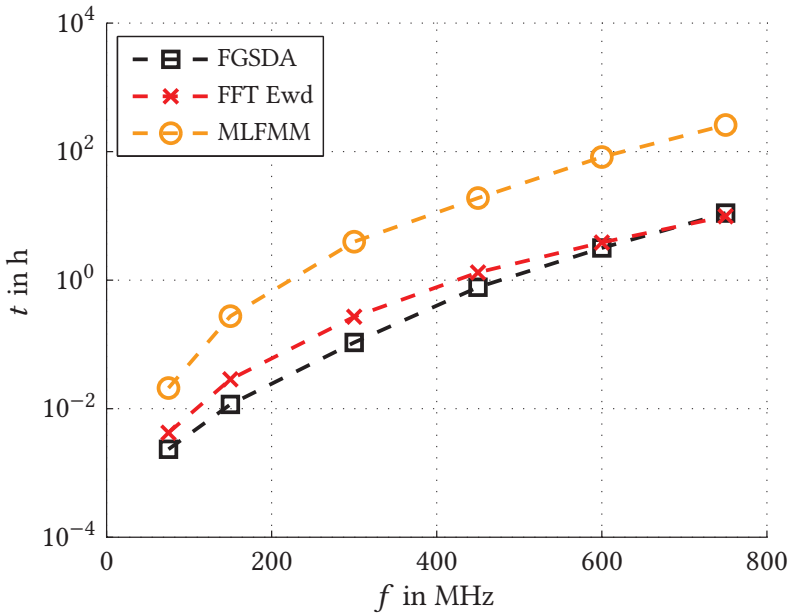

Fig. 6.2.: Computation times of the FGSDA, the FFT Ewd, and the MLFMM algorithm for the w-shaped two-plate stirrer.

chamber now contains a mid-size and a large object, the advantage of the CGF against the FGF BEM is reduced. The number of unknowns is only decreased by a factor of ten. At 750 MHz, the discretization of the cavity walls, the car body, and the stirrer create about 600 000 unknowns while only the car body and the stirrer generate about 60 000 unknowns. The computation times of the FGSDA, the FFT Ewd, and the MLFMM algorithm are shown in Fig. 6.3. At its best, the FFT Ewd algorithm outperforms the MLFMM by a factor of 2.4. The speed-up of the FGSDA versus the MLFMM ranges from 1.5 to 7.3. Except for 75 MHz, the FGSDA algorithm achieves an acceleration of at least 3.5.

In Fig. 6.4 and Fig. 6.5 the surface current densities computed by the FGSDA and the MLFMM algorithm are compared. The frequencies are 150 MHz and 450 MHz, respectively. Similar to the first and second scenario, the results are in good agreement at low frequencies and match less at high frequencies.

Lastly, the presented algorithms are compared with and validated against other state of the art methods for the numerical modeling of reverberation chambers, namely the DSC-MoM method [Zha11] and the AIM accelerated CGF BEM method [Yan14]. The considered cavity has the dimension 12.5 m × 8.5 m × 6 m. Its lowest usable frequency is approximately 50 MHz according [IEC11]. In [Zha11; Yan14], the cavity is excited by a Hertzian dipole at 82 MHz. As Hertzian dipoles are not implemented in our algorithm, the cavity is excited by an electrically short strip dipole herein. The dipole is oriented in $(-\hat{x} + \hat{y} + \hat{z})/\sqrt{3}$ direction. Its magnitude is $\sqrt{3}$ A m. A 8 m long and 0.8 m wide single plate stirrer is placed in the cavity. Its center is at (6.25 m, 6.6 m, 4.25 m).

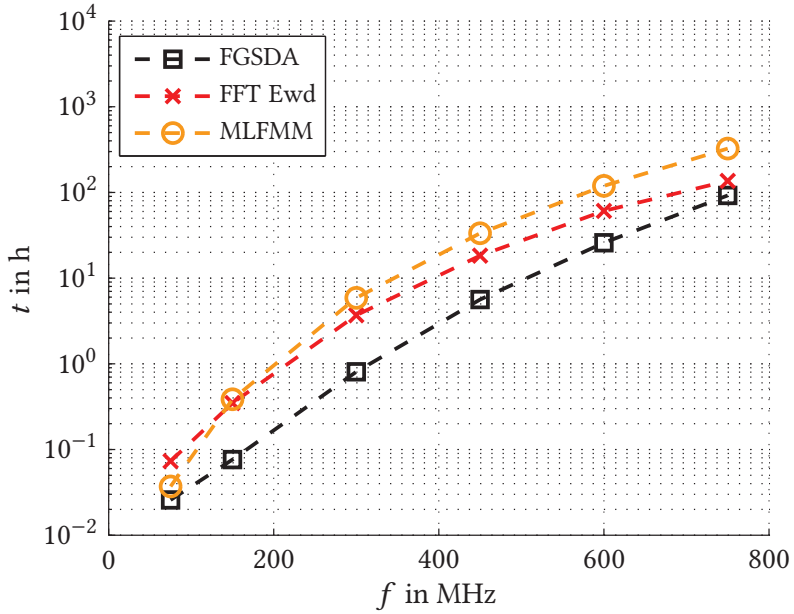

Fig. 6.3.: Computation times of the FGSDA, the FFT Ewd, and the MLFMM algorithm for the w-shaped two-plate stirrer and the car body.

Method	CPU time in s	Memory demand in MB
FGSDA	4.1	5
FFT Ewd	5.9	22
DSC-MoM	183	660
AIM	442.2	52
MLFMM	156.1	49

Tab. 6.3.: Computation times and memory requirements of the FGSDA, the FFT Ewd, the DSC-MoM, the AIM, and the MLFMM algorithm for the single plate stirrer

In Table 6.3, the timings and the memory requirements of the proposed algorithms (FGSDA and FFT Ewd), the algorithm of Zhao (DSC-MoM) [Zha11], and the algorithm of Yang (AIM) [Yan14] are shown. Additionally, the computational time and the memory demand of the MLFMM accelerated FGF BEM (MLFMM) [Eib05] are given. The computation times of the DSC-MoM and the AIM are taken from [Zha11] and [Yan14], respectively. In [Zha11], the results were computed on a personal computer with a 2.67 GHz CPU and 3.25 GB RAM. In [Yan14], the simulations were performed on the Lonestar Cluster where only one core of the multi-core processors was activated (see [Yan14] and references therein). Our simulations were performed on a personal computer with a 3.4 GHz CPU and 32 GB RAM. As the results were computed on different machines, a strict comparison of the timings is not possible. Yet, the advantage of the proposed algorithms against [Zha11] and [Yan14] is significantly more than one order of mag-

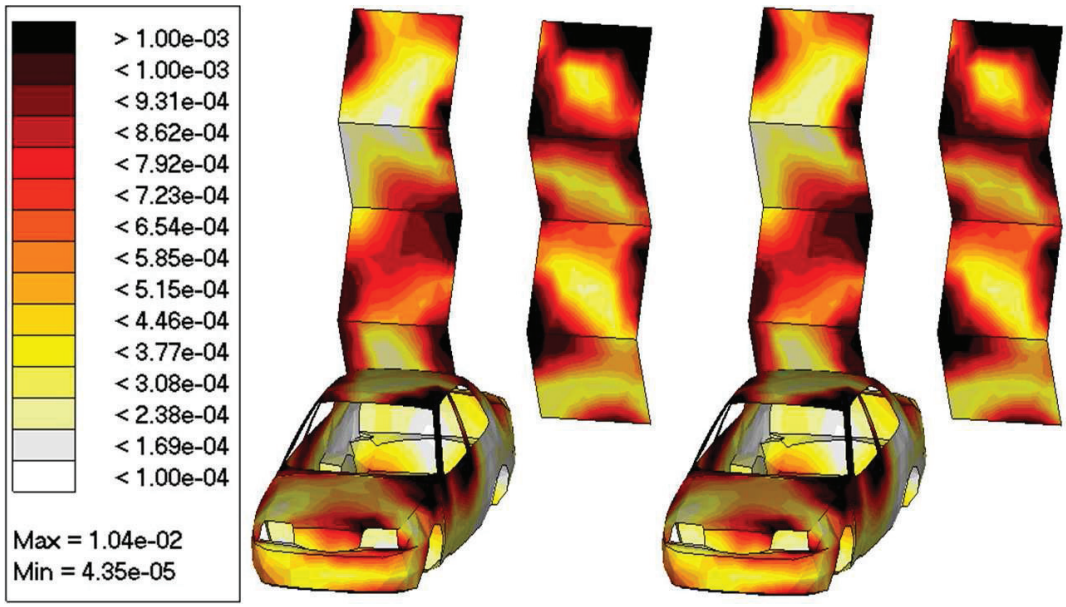

Fig. 6.4.: Surface current density in $\mathrm{A\,m^{-1}}$ at 150 MHz computed by the FGSDA (left) and the MLFMM (right) algorithm.

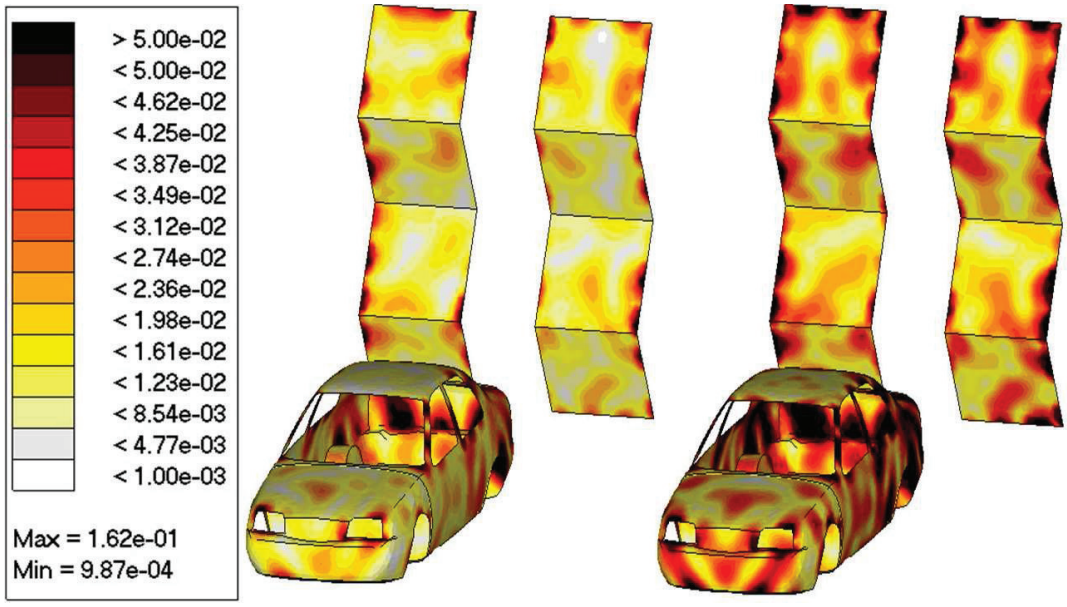

Fig. 6.5.: Surface current density in $\mathrm{A\,m^{-1}}$ at 450 MHz computed by the FGSDA (left) and the MLFMM (right) algorithm.

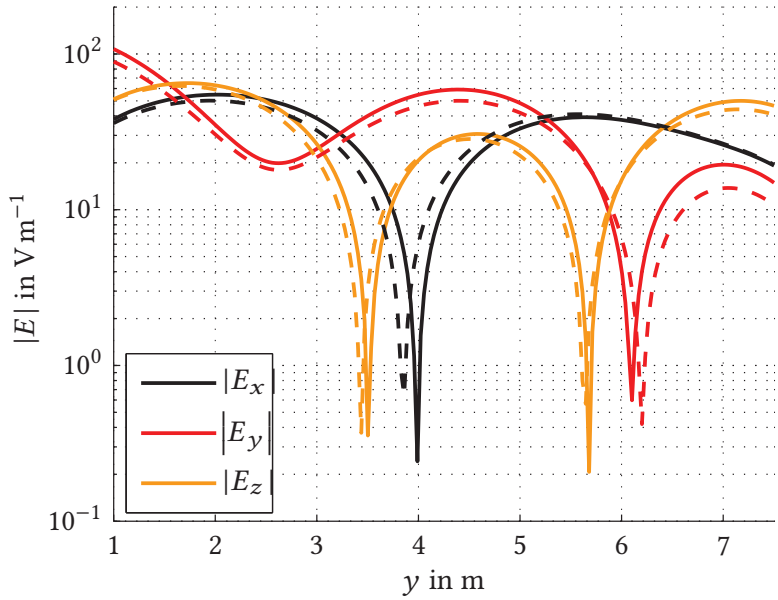

Fig. 6.6.: Magnitude of the electric field in V m^{-1} along a straight line from (2 m, 1 m, 3 m) to (2 m, 7.5 m, 3 m) computed by the FGSDA (-) and the AIM algorithm (- -).

nitude – a factor which cannot be caused by different hardware only. The major disadvantage of the DSC-MoM is its high memory consumption. It exceeds the demand of the FGSDA by roughly two orders of magnitude. Although the storage requirement of the AIM algorithm is not as high, the FGSDA outperforms it still by a factor of ten.

In Fig. 6.6, the magnitude of the components of the electric field along a straight line form (2 m, 1 m, 3 m) to (2 m, 7.5 m, 3 m). The results of the FGSDA agree well with that presented in [Yan14]. To compensate for the different excitations, the results of the FGSDA have been scaled by a constant factor.

Since the AIM accelerated CGF BEM is more efficient when large or multiple objects are in the cavity [Yan14], Yang and Yilmaz additionally consider a 6×3 array of stirrers with 1.2 m spacing in y- and z-direction. The cavity and the stirrers are of the same size as above. The center of the stirrer array is at (6.25 m, 4.25 m, 4 m) . The computational times and the memory requirements are displayed in Table 6.4.

Although the performance of the FGSDA and the FFT Ewd algorithm degrades, they still outperform the AIM accelerated CGF BEM in both computation time and memory demand. Considering the performance of the MLFMM accelerated FGF BEM, it is questionable whether the CGF BEM is the method of choice in this case. The ordinary BEM is only slightly slower than the FGSDA and considerably faster than the FFT Ewd and the AIM algorithm as the CGF loses its advantage over the FGF BEM when many objects are inside the cavity.

Method	CPU time in s	Memory demand in MB
FGSDA	190.4	67
FFT Ewd	947.6	80
AIM	4 600	342
MLFMM	353.0	63

Tab. 6.4: Computation times and memory requirements of the FGSDA, the FFT Ewd, the DSC-MoM, the AIM, and the MLFMM algorithm for the 6×3 array of plate stirrers.

6.1.2. Imperfectly Conducting Objects

Closed imperfectly conducting bodies are considered using the EFIE together with an IBC. In contrast to PEC surfaces, electric and magnetic currents exist on imperfectly conducting surfaces. As the FFT accelerated Ewald representations of the CGF for magnetic currents have not been implemented yet, the analysis is restricted to the FGSDA and the MLFMM algorithm. As in the previous section, the residual of the GMRES solver and the accuracy of the CGF are set to 10^{-4}, the discretization density is $\lambda/10$, and the remaining simulation parameters are set as in Appendix C.

A metallic cuboid with conductivity $\kappa = 10^6\,\mathrm{S\,m^{-1}}$ and relative permeability $\mu_\mathrm{r} = 1$ is placed in a chamber of the dimension $8\,\mathrm{m} \times 4.5\,\mathrm{m} \times 2.8\,\mathrm{m}$. The cuboid is centered at $(6\,\mathrm{m}, 2.25\,\mathrm{m}, 1.4\,\mathrm{m})$ and it is 0.8 m long, 1 m wide, and 0.6 m high. The loaded reverberation chamber is excited by an electrically small strip dipole in the frequency range from 100 MHz to 800 MHz. The lowest usable frequency of the reverberation chamber is around 130 MHz. At 100 MHz, the characteristic surface impedance Z_s of the metallic cuboid is calculated as 0.028 S.

The computation times of the FGSDA and the MLFMM algorithm are compared in Figure 6.7. The number of unknowns is reduced by a factor of 20. At 800 MHz, 16 500 unknowns are created in the case of the FGSDA while about 320 000 are needed by the MLFMM algorithm. The speed-up of the FGSDA versus the MLFMM algorithm ranges from 4 at 800 MHz to 11 at 200 MHz and decreases with frequency.

In Table 6.5, the relative deviations between the results (electric and magnetic currents on the strip dipole and the cuboid) of the FGSDA and the MLFMM algorithm are shown. As in the previous section, the results agree very well in the lower frequency range and differ more at high frequencies.

6.1.3. Dielectric Objects

For dielectric bodies, the CGF BEM is coupled to the FEM. Similar to metallic objects, dielectrics require the consideration of electric and magnetic currents in the BI formulation. Thus, again only the FGSDA is validated against and compared with the MLFMM algorithm.

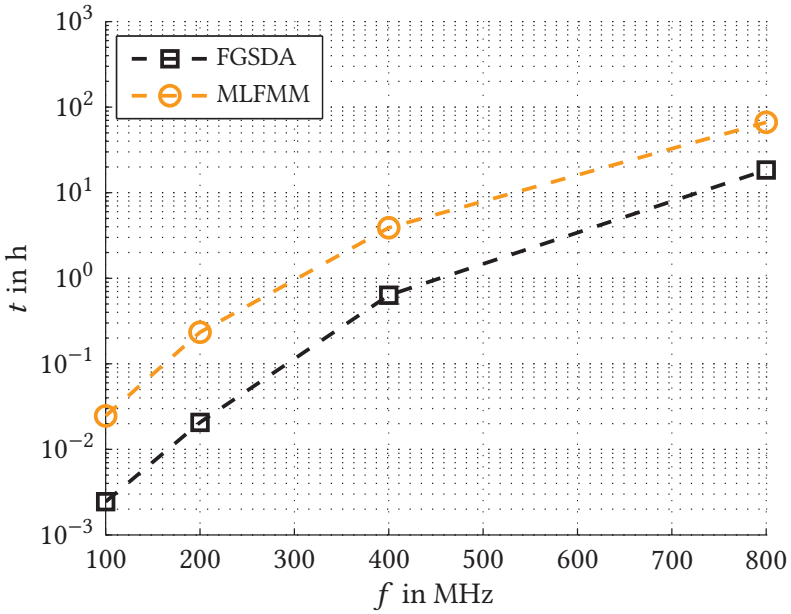

Fig. 6.7.: Computation times of the FGSDA and the MLFMM algorithm for the imperfectly conducting cuboid.

f in MHz	δ in %
100	0.7
200	1.7
400	2.1
800	18.3

Tab. 6.5.: Relative difference δ between the results of the FGSDA and the MLFMM algorithm.

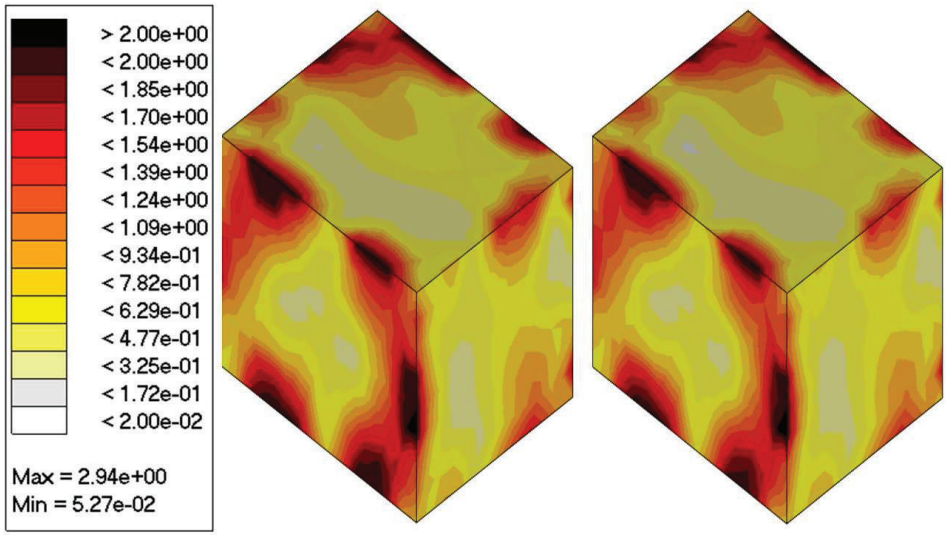

Fig. 6.8.: Magnetic surface current density on the dielectric cuboid in $\mathrm{V\,m^{-1}}$ at 400 MHz for the FGSDA (left) and the MLFMM algorithm (right).

The geometry from the previous section is considered except that a dielectric cuboid with permittivity $\varepsilon_\mathrm{r} = 4$ and permeability $\mu_\mathrm{r} = 1$ replaces the metallic one. The scenario is simulated at 400 MHz. The number of unknowns are $2\,017 + 8\,580 = 10\,687$ (BI + FE) for the CGF and $78\,121 + 8\,580 = 86\,701$ for the FGF BEM and the simulation times are 2 960.1 s and 23 389.2 s, respectively. In Fig. 6.8, the magnetic current density is shown on the cuboid. The visual agreement between the results of the FGSDA and the MLFMM algorithm is good. The relative deviation of electric and magnetic currents is calculated as 10.0 %.

6.1.4. Imperfectly Conducting Cavity Walls

The Green's function of the rectangular cavity is exact for perfectly conducting cavity walls only. Imperfectly conducting walls can be approximately handled by complexification of the wavenumber according to (2.41) [Gro05]. In the following, the validity of (2.41) in the CGF BI formulation is investigated.

Two 0.5 m long and 0.1 m wide strip dipoles are placed in a 12 m long, 6 m wide, and 4 m high cavity. The dipoles are aligned to the z-axis and are located at the points $(1\,\mathrm{m}, 3\,\mathrm{m}, 2\,\mathrm{m})$ and $(11\,\mathrm{m}, 3\,\mathrm{m}, 2\,\mathrm{m})$, respectively. The conductivity of the cavity walls is set to $10^6\,\mathrm{S\,m^{-1}}$. The transmission coefficient S_{21} between the two dipoles is computed in the range of the TM_{110} resonance using the FGSDA and the MLFMM accelerated FGF BEM as reference. In the CGF BI formulation, the lossy walls are considered using (2.41) together with the composite Q from (2.48) and the individual quality factor of the TM_{110} resonance, respectively. In the FGF BI formulation, the well conducting walls are modeled using the IBC as described in [Ism09]. In Fig. 6.9, the magnitude of the transmission coefficient is shown. Except in the immediate vicinity of the reso-

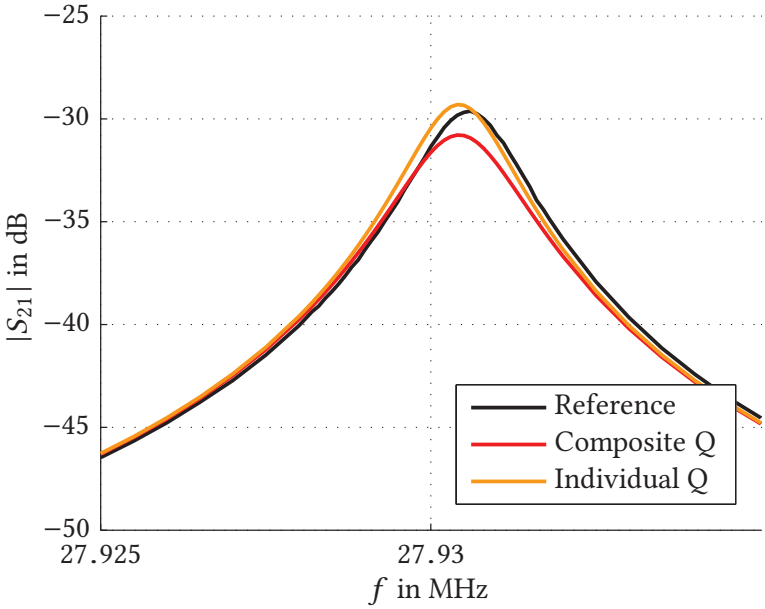

Fig. 6.9.: Magnitude of the transmission coefficient S_{21} in the range of the TM_{110} resonance for a wall conductivity of $\kappa = 10^6\,\mathrm{S\,m^{-1}}$.

nance frequency, the results agree perfectly. At the resonance frequency, the S_{21} of the composite Q is 1.5 dB smaller than the reference. However, the deviation is below 0.5 dB when the individual quality factor of the TM_{110} mode is used. Consequently, the approximate modeling of imperfectly conducting cavity walls is accurate when the correct quality factor is used.

However, the usage of the individual quality factors for each cavity mode in the CGF is difficult. In the spectral representation or the spectral part of the Ewald representation, the modeling of individual Q's is possible. Because the spectral representation is a sum over all modes, an individual wavenumber could be used for each mode. As the terms in the spatial representation and the 2D spectral representations do not correspond to the cavity modes, individual wavenumbers cannot be employed. As the FGSDA and the FFT Ewd algorithm involve at least one of the latter representations, the composite Q from (2.48) is used.

Although the composite Q is not as accurate as the individual Q's in the immediate vicinity of resonances, it is accurate elsewhere. Moreover, in the high frequency regime of the cavity, many modes contribute to the total fields. To estimate the average error which is introduced by the composite Q in the over-moded frequency range, the transmission coefficient of the two dipoles is computed at 100 arbitrary frequencies in the range from 100 MHz to 150 MHz. The results of the composite Q FGSDA algorithm are compared to the reference in Fig. 6.10. With the exception of a few frequencies, the results agree very well. The average relative error is below 10%. The maximum relative error is 27%.

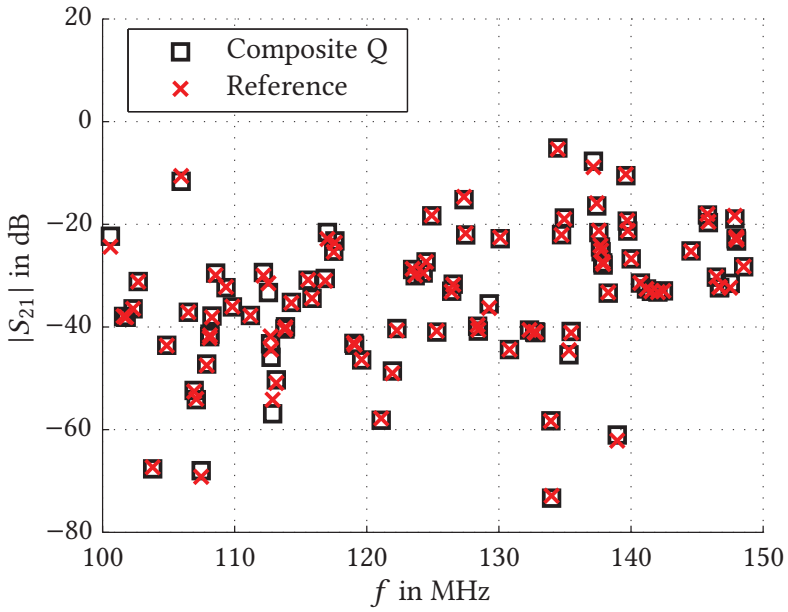

Fig. 6.10.: Transmission coefficient at 100 arbitrary frequencies for a wall conductivity of $\kappa = 10^6\,\mathrm{S\,m^{-1}}$.

6.2. Error Analysis

Common to all examples in Section 6.1.1 and 6.1.2 is the frequency dependence of the error. At low frequencies, the results of the different algorithms agree well while the agreement deteriorates with increasing frequency. This evokes two questions:

1. Why does the difference between the results tend to increase with frequency although the same accuracy settings are used?

2. Which method, the CGF or the FGF BEM, is more accurate?

The answer to the first question requires a closer look at over-moded cavities. The resonance density in a cavity grows with f^2, cf. Section 2.2. Consequently, the probability that a particular frequency is in the range of a resonance is larger at high than at low frequencies. As resonances deteriorate the conditioning of the system matrix, small differences in the input variables (i.e., the discretization of the cavity walls in contrast to the analytical modeling of the walls in the CGF) cause a large difference in the output variables (i.e., the surface current density or the electric field). Therefore, results tend to disagree more at high frequencies although the same accuracy settings are used.

The second question is more difficult to answer. A rigorous validation against analytical results is not possible as the boundary value problem of the rectangular cavity does, in the general case of arbitrarily shaped objects, not have a closed-form solu-

Q	Discretization	δ in %	
		MLFMM	FGSDA
10^3	$\lambda/10$ vs. $\lambda/20$	10.26	36.13
	$\lambda/15$ vs. $\lambda/20$	6.04	4.67
10^4	$\lambda/10$ vs. $\lambda/20$	15.76	48.25
	$\lambda/15$ vs. $\lambda/20$	7.54	7.77

Tab. 6.6.: Relative error δ in % between the electric fields of different discretization densities.

tion. Instead, three consistency checks are performed in the following. As recommended in [Jak14], the discretization is refined, the reciprocity condition is verified, and the power budget is checked. At first, the stability and the convergence of the results under mesh refinement are checked. The second scenario from Section 6.1.1 (i.e., the w-shaped stirrer) is considered. Because of the statistical nature of reverberation chambers, the results will be subject to statistical variation. To enhance the significance of the results, the chamber is simulated at twelve different stirrer angles $\alpha = 0°, 30°, \ldots, 330°$. The rotation axis is parallel to the z-axis and passes through the point $(10\,\text{m}, 3\,\text{m}, 2\,\text{m})$ (i.e., the center of the stirrer). The frequency is set to 100 MHz. Two different quality factors, $Q = 10^3$ and $Q = 10^4$, are considered, respectively. The magnitude of the electric field is computed at $5 \times 5 \times 3 = 75$ equispaced points within a cuboid volume of the size $4\,\text{m} \times 4\,\text{m} \times 2\,\text{m}$ for each stirrer position. Overall, $75 \cdot 12 = 900$ field values are computed. The stirrer and the cavity are discretized with an average edge length of $\lambda/10$, $\lambda/15$, and $\lambda/20$, respectively.

In Table 6.6, the relative error between the electric fields of different discretization densities is displayed. In addition, the magnitude of the electric field at the point $(4\,\text{m}, 1\,\text{m}, 3\,\text{m})$ is shown in Fig. 6.11 over the stirrer angle α for the different discretization densities and for $Q = 10^4$. The results in Table 6.6 show three developments: 1) the relative error goes up when the quality factor is increased, 2) the relative error becomes smaller with increasing discretization density, 3) both algorithms suffer roughly equally from the discretization error. The results in Fig. 6.11 show that the error is not evenly distributed over the stirrer angles. The relative error of the electric fields converges worse under mesh refinement for both algorithms when a resonance of the cavity is hit, for example, at $\alpha = 120°$ (FGSDA) and at $\alpha = 240°$ (MLFMM). Otherwise, both algorithms converge well.

Secondly, the reciprocity condition is checked. Two 0.5 m high and 0.1 m wide strip dipoles are placed in a cavity of the dimension $12\,\text{m} \times 6\,\text{m} \times 4\,\text{m}$. The dipoles are located at the points $(1\,\text{m}, 3\,\text{m}, 2\,\text{m})$ and $(11\,\text{m}, 3\,\text{m}, 2\,\text{m})$, respectively and are aligned to the z-axis. The walls of the cavity and the dipoles are modeled as PEC. Since the cavity does not contain any non-reciprocal materials, the problem is reciprocal.

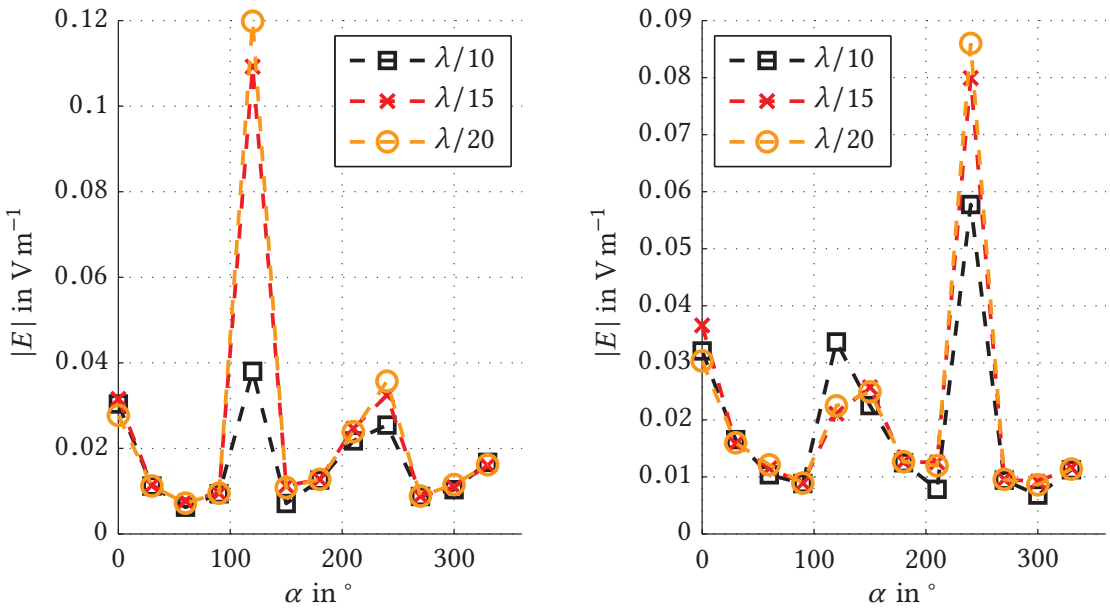

Fig. 6.11.: Magnitude of the electric field in $\mathrm{V\,m^{-1}}$ at the point $(4\,\mathrm{m}, 1\,\mathrm{m}, 3\,\mathrm{m})$ for different discretization densities and $Q = 10^4$ computed by the FGSDA (left) and the MLFMM (right) algorithm.

In Fig. 6.12, the difference $|S_{21} - S_{12}|$ of the forward and the reverse transmission coefficient is displayed for the FGF (MLFMM) and the CGF BEM (FGSDA). In Fig. 6.13, the absolute values $|S_{21}|$ of the forward transmission coefficient are shown. In addition, the five largest values of $|S_{21} - S_{12}|$ are displayed. The maximum deviation of the forward and the backward transmission coefficient is $1.82 \cdot 10^{-4}$ (MLFMM) and $0.41 \cdot 10^{-4}$ (FGSDA). The average deviations are $0.073 \cdot 10^{-4}$ and $0.059 \cdot 10^{-4}$, respectively. In the case of the MLFMM, the largest deviations occur in the immediate range of resonance frequencies, cf. black squares in Fig. 6.13. In the case of the FGSDA, the largest deviations are considerably lower and are not due to cavity resonances. The resonances are modeled more accurately as they are considered analytically within the CGF. In conclusion, the CGF BEM better reproduces the reciprocity condition since the FGF BEM is not as accurate in the range of resonances.

Lastly, the power budgets of the FGF and the CGF BEM are verified on the basis of the first scenario from Section 6.1 (Vivaldi antenna). As the cavity walls and the antenna are modeled as perfect conductors, the scenario is lossless and the power which is fed into the cavity should be zero. The input power is zero when the input impedance of the antenna has a zero real part. At low frequencies, both the FGF and the CGF BEM obtain input impedances with zero real part, see Table 6.1. However, at high frequencies, the FGF BEM fails to meet this condition while the values of the CGF algorithms remain purely imaginary.

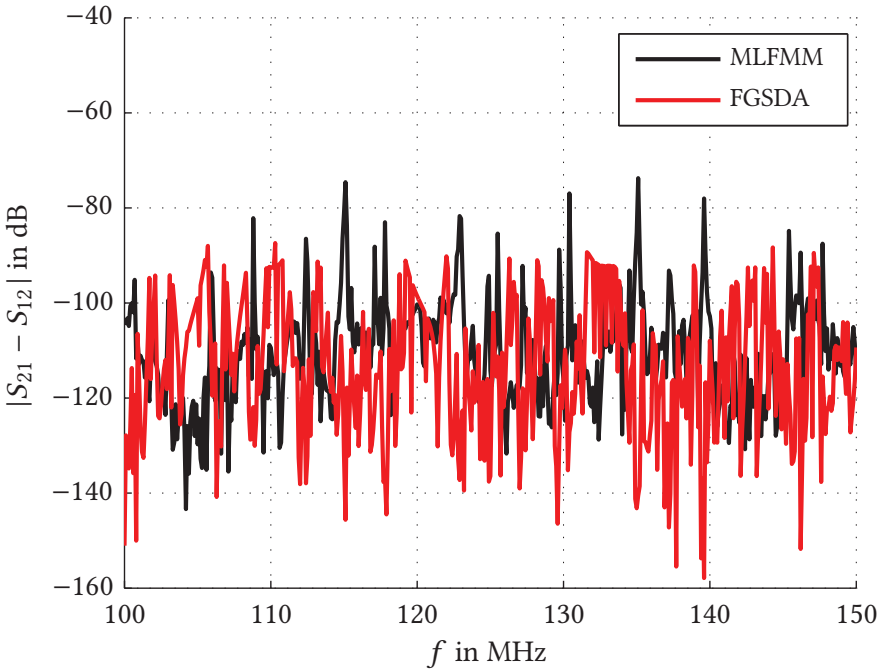

Fig. 6.12.: Deviation $|S_{21} - S_{12}|$ of the forward and the reverse transmission coefficient between two dipoles.

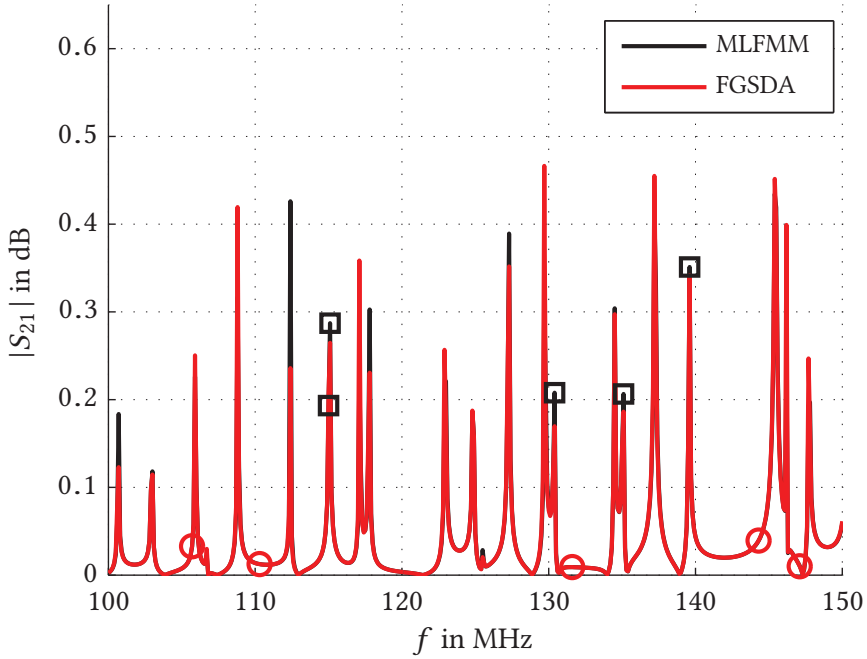

Fig. 6.13.: Absolute value $|S_{21}|$ of the forward transmission coefficient and five largest values of $|S_{21} - S_{12}|$ for the MLFMM (black squares) and the FGSDA (red circles).

ℓ_p in m	N	N_tot
1	1 550	155 528
2	3 087	157 065
3	4 624	158 602
4	6 161	160 139
5	7 698	161 676
6	9 235	163 213
7	10 772	164 750
8	12 309	166 287
9	13 841	167 819
10	15 383	169 361

Tab. 6.7.: Number of unknowns N of the plate and total number of unknowns N_tot of the plate and the cavity walls for the different plate lengths ℓ_p.

6.3. Complexity Analysis

The computational time and the memory complexity of the FGSDA and the FFT accelerated CGF BEMs are derived and analyzed. For comparison, the computational time and the memory complexity of the MLFMM accelerated FGF BEM are analyzed for reverberation chambers. Two cases are distinguished:

1. How do computation time and memory demand scale with the number of unknowns of the objects within the cavity assuming a constant frequency and discretization density?

2. How do computation time and memory demand scale with frequency assuming a constant geometry and discretization density per wavelength?

The first case is referred to as number of unknowns complexity (N-complexity) herein. For a fixed frequency, the number of unknowns is increased by either enlarging the objects within the cavity or by placing additional objects in the cavity but not by refining the discretization. The second case is referred to as frequency complexity (f-complexity) herein. In this case, the frequency is varied while the number of objects and the dimension of the objects are not changed. As the average cell size per wavelength is fixed, the number of unknowns increases with frequency squared.

If possible, the complexities are derived from theory. Simulated data serves to complete and supplement the analysis. For the N-complexity case, a rectangular plate is placed in a cavity of size $12\,\mathrm{m} \times 6\,\mathrm{m} \times 4\,\mathrm{m}$ in the plane $z = 2\,\mathrm{m}$. The length of the plate is varied from 1 m to 10 m while its width is 3 m. The plate and the cavity are discretized with an average edge length of $\lambda/10$ at 400 MHz. The number of unknowns N of the plate and the total number of unknowns N_tot of the plate and the cavity walls are displayed in Table 6.7. For the f-complexity case, a 10 m long and 2 m wide plate

f in MHz	N	N_{tot}
100	636	10 290
200	2 753	41 759
300	6 043	93 178
400	10 596	164 574
500	16 880	258 443
600	24 163	371 002
700	32 556	503 556

Tab. 6.8.: Number of unknowns N of the plate and total number of unknowns N_{tot} of the plate and the cavity walls for the different frequencies.

is placed in a cavity of the same size in the same plane. The plate and the cavity are discretized with an average edge length of $\lambda/10$. The frequency is varied from 100 MHz to 700 MHz. In Table 6.8, the number of unknowns and the total number of unknowns are displayed.

In the following sections, the complexities of the FGSDA, the FFT Ewd, and the MLFMM algorithm are derived and analyzed. As the complexity of the iterative solver cannot be derived from theory, it is analyzed in an additional section. Last but not least, the complexities of the algorithms are compared with one another and discussed.

6.3.1. Fast Group Spectral Domain Approach (CGF BEM)

The computational time and memory complexity of the FGSDA accelerated CGF BEM are derived and analyzed. The algorithm is subdivided into three parts: the computation of spectral representations of the basis functions (a), the computation of the system matrix (b), and the iterative solution of the linear equation system (c).

Number of Unknowns Complexity:

1a) As the spectral representations need to be computed only once per basis function, their computation time and their memory demand scale with N.

1b) The operation count and the memory demand of the system matrix grow with N^2 as the system matrix is fully populated.

1c) The solution of the matrix-vector equation needs N^2 operations per iteration. The number of iterations N_{it} increases roughly with N as the results in Section 6.3.4 indicate. Consequently, the time complexity is $O\left(N^3\right)$. The memory demand of the iterative solver is given by the product of the number of solution vectors and the length of the solution vectors. As the not-restarted GMRES is employed, cf. Section 6.3.4, the memory demand is proportional to $N_{\text{it}}N \propto N^2$.

Frequency Complexity:

2a) The operation count of the spectral representations depends on the number of unknowns and the number of modes in the respective representation of the CGF. The number of unknowns grows with f^2 as the cell size is proportional to the wavelength. The number of modes in the Ewald and the 2D spectral representations increase with f^3 and f^2, respectively. Thus, the computational time complexity of the spectral representations is $\mathcal{O}\left(f^5\right)$. The memory demand would scale with $Nf^3 \propto f^5$ if the spectral representation were computed and stored in advance for all modes, see Algorithm 4.1. However, when the interaction integrals are evaluated mode-wise, see Algorithm 4.2, the memory demand scales only with $N \propto f^2$.

2b) The system matrix is decomposed into near and far interaction components. The near interactions are calculated using the Ewald representation which scales with f^3. But, as the group size decreases with frequency, see Chapter 4, the number of near interactions grows only with N. The number of far interactions grows with N^2 but the number of modes scales only with f^2 as the far interactions are calculated with the 2D spectral representations. Thus, the operation counts of near and far interactions are proportional to $Nf^3 \propto f^5$ and $N^2f^2 \propto f^6$, respectively. Overall, the time complexity of the system matrix is $\mathcal{O}\left(f^6\right)$. The memory demand is proportional to $N^2 \propto f^4$.

In practice, however, it needs to be considered that the number of modes in the 2D spectral representations increases with f^2 in the high frequency range only. For low frequencies, the number of modes is constant, cf. Fig. 3.6. In Fig. 6.14, the computation time of the system matrix is displayed for the rectangular plate example. The data is fitted to polynomials of degree four, five, and six in the least square sense. In the considered frequency range, the polynomial of order five fits best. Hence, the operation count of the FGSDA grows rather with f^5 than f^6 in the low and mid frequency range. Compared to the CGF BEM with the standard Ewald representation, the FGSDA reduces the time complexity of the system matrix by two orders from $N^2f^3 \propto f^7$ to f^5.

2c) The solution of the linear system of equations requires N^2N_{it} operations. Since the number of iterations increases roughly with f^2 as indicated in Section 6.3.4, the time complexity becomes $\mathcal{O}\left(f^6\right)$. The memory demand of the iterative solution is proportional to $N^2 \propto f^4$.

The total number of unknowns complexity of the FGSDA is of the order N^3 with respect to operation count and of the order N^2 with respect to memory demand. The total frequency complexity is $\mathcal{O}\left(f^6\right)$ and $\mathcal{O}\left(f^4\right)$, respectively. The total time complexity is determined by the iterative solver. With regard to the memory demand, the system matrix and the iterative solver decide the total complexity.

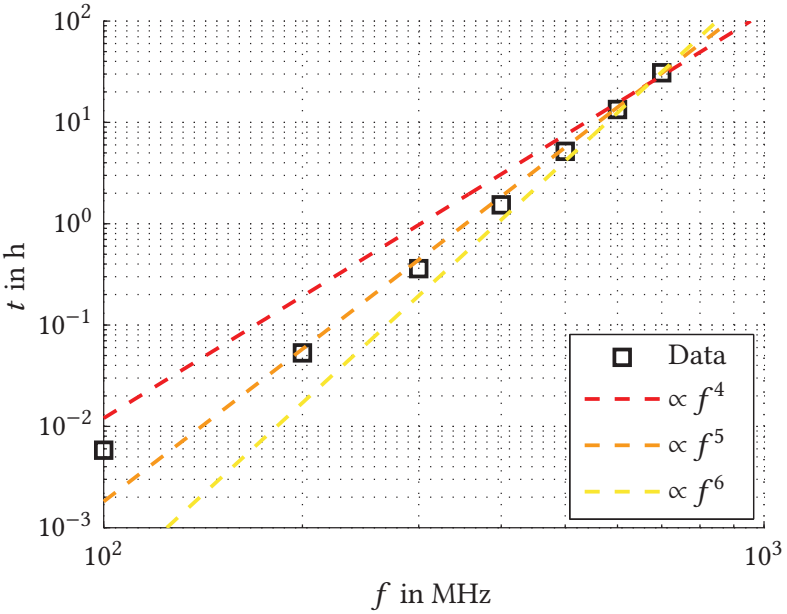

Fig. 6.14.: Computation time of the system matrix (FGSDA) for the rectangular plate example fitted to polynomials of degree four, five, and six in the least-square sense.

The complexity describes the performance of an algorithm except for a constant factor. While the constant factor is negligible in the asymptotic limit, it can be important for finite number of unknowns or frequencies: An algorithm with a higher complexity does not necessarily need more operations or more memory if the constant factor is considerably smaller. In Fig. 6.15 and 6.16, the percentages of the total computational time and the total memory demand of the single FGSDA subroutines are plotted over the number of unknowns and frequency, respectively for the rectangular plate examples. The percentage of the iterative solver with respect to computation time is very low despite its higher complexity. For the considered number of unknowns and frequency range, the computation of the spectral representations and particularly the system matrix are dominant. Consequently, the operation count of the FGSDA scales rather with N^2 than N^3 and is rather proportional to f^5 than f^6. Similar to the operation count, the memory demand of the iterative solver is very low while the storing of the system matrix needs the most memory. As both the iterative solver and the system matrix have the same memory complexity, the overall performance of the FGSDA with respect to memory does not change.

The theoretical considerations are confirmed by the simulated data from the rectangular plate examples. In Fig. 6.17, the total computation time is plotted versus the number of unknowns and the frequency, respectively and fitted to polynomials of different degrees in the least square sense. With respect to the number of unknowns, the total operation count scales even less than quadratically which can be explained as follows: With increasing length of the plate (i.e., with increasing number of unknowns),

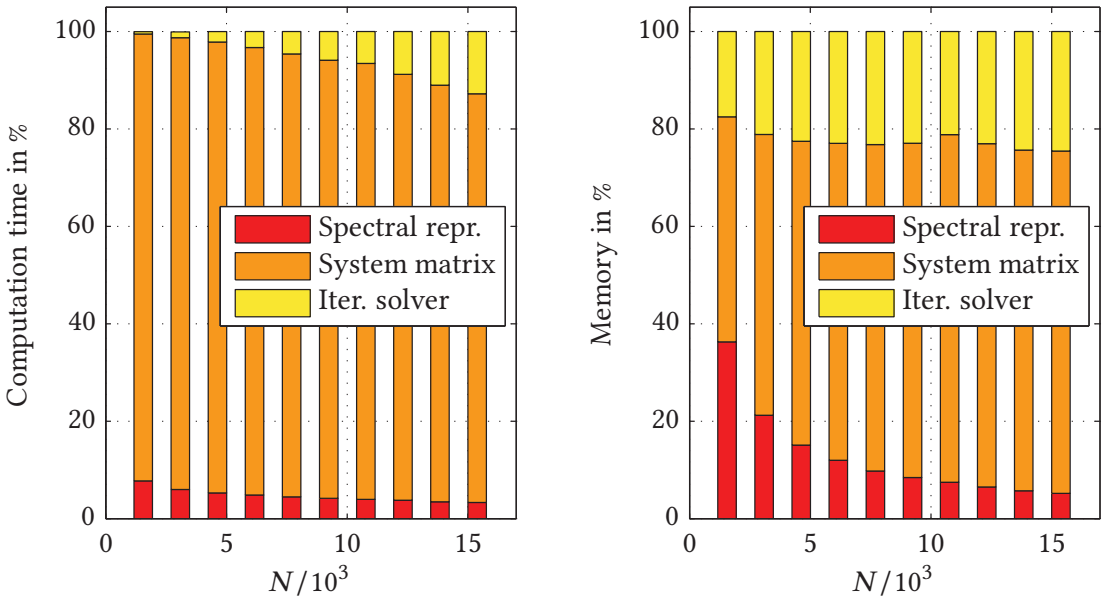

Fig. 6.15.: Percentage of the total computational time (left) and the total memory demand (right) of the single FGSDA subroutines versus the number of unknowns for the rectangular plate example.

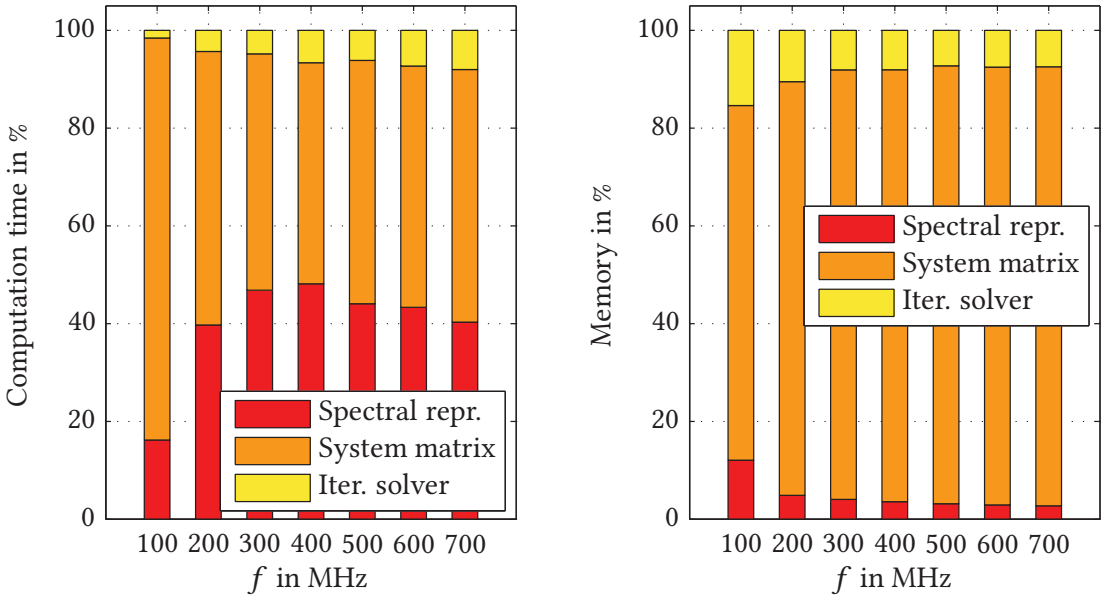

Fig. 6.16.: Percentage of the total computational time (left) and the total memory demand (right) of the single FGSDA subroutines versus frequency for the rectangular plate example.

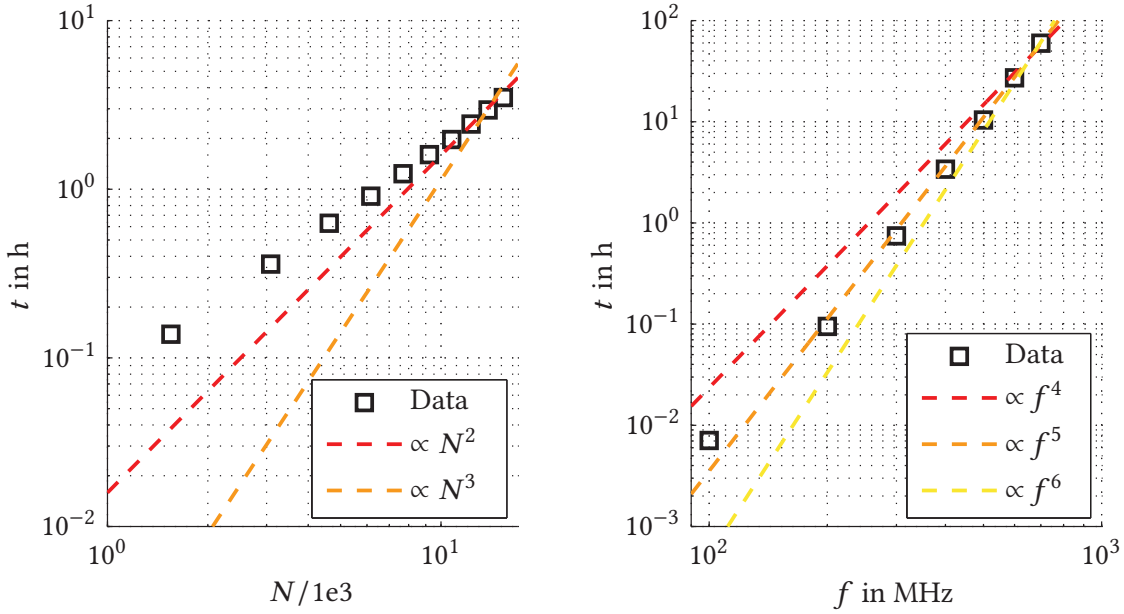

Fig. 6.17.: Total computation time of the FGSDA algorithm versus the number of unknowns (left) and frequency (right) for the rectangular plate examples.

the average distance between test and source edges grows. As the convergence rates of the 2D spectral representations improve with increasing distance between observation and source point, cf. Section 3.3, the evaluation of far interactions between more distant edges needs less computation time. With respect to frequency, the polynomial of order five fits best as derived.

6.3.2. Fast Fourier Transform Approach (CGF BEM)

The computational time and memory complexity of the FFT accelerated CGF BEM are derived. The algorithm consists of three parts: the computation of the Q-array (a), the computation of the interaction integrals (b), and the iterative solution of the linear system of equations (c).

Number of Unknowns Complexity:

1a) The operation count and the memory requirement of the Q-array depend on the number of samples only. As the sampling density of the Q-array is proportional to the wavelength but does not depend on the number of unknowns, the computational time and the memory complexity of the Q-array is constant with respect to the number of unknowns.

1b) As the system matrix is fully populated, the computation time and the memory demand of the system matrix increase with N^2.

1c) The iterative solution of the matrix-vector equation needs $\mathcal{O}\left(N^3\right)$ operations and the memory demand is proportional to N^2, see Section 6.3.1.

Frequency Complexity:

2a) The sampling density of the Q-array is set proportional to the wavelength. As the Q-array is a three dimensional object, the number of sampling points grows with f^3. The number of necessary terms in the Ewald summation technique is also proportional to f^3. Without FFT acceleration, this would yield an operation count proportional to f^6. With FFT acceleration, the computational time complexity of the sampling process is reduced to $\mathcal{O}\left(f^3 \log f\right)$. The memory requirement of the Q-array grows with f^3 as it is proportional to the number of sampling points.

2b) The operation count of the interaction integrals is determined by the number of unknowns and the order of the Lagrange polynomials. As the discretization density is proportional to the wavelength, the number of unknowns increases with f^2. The order of the Lagrange polynomials needs not to be increased with frequency because the sampling density of the Q-array is chosen proportional to the wavelength. Therefore, the time complexity of the system matrix is $\mathcal{O}\left(f^4\right)$. The memory demand of the system matrix is proportional to $N^2 \propto f^4$.

2c) The computational time and the memory complexity of the iterative solver are $\mathcal{O}\left(f^6\right)$ and $\mathcal{O}\left(f^4\right)$, respectively, cf. Section 6.3.1.

The total number of unknowns complexity of the FFT Ewd is of the order N^3 with respect to operation count and of the order N^2 with respect to memory demand. The total frequency complexity is $\mathcal{O}\left(f^6\right)$ and $\mathcal{O}\left(f^4\right)$, respectively. With regard to operation count, the iterative solver decides the total complexity. The total memory complexity is determined by the system matrix and the iterative solver.

As the complexity does not include the constant factor, the percentages of the single subroutines are, analog to the previous subsection, plotted versus the number of unknowns in Fig. 6.18 and versus frequency in Fig. 6.19. As in the case of the FGSDA, the operation count and the memory demand of the iterative solver are low compared to the time and memory requirements of the system matrix. The operation count of the Q-array is negligible. However, the memory demand of the Q-array is large for smaller numbers of unknowns and lower frequencies. With increasing number of unknowns and frequency, the memory requirement of the system matrix overshoots that of the Q-array because of the higher memory complexity of the system matrix. Overall, as a consequence of the low constant factor of the iterative solver, the total operation count of the FFT Ewd algorithm scales rather with N^2 or f^4 than with N^3 or f^6, respectively.

The theoretical considerations are confirmed by the simulated data from the rectangular plate examples. In Fig. 6.20, the total computation times are plotted versus the

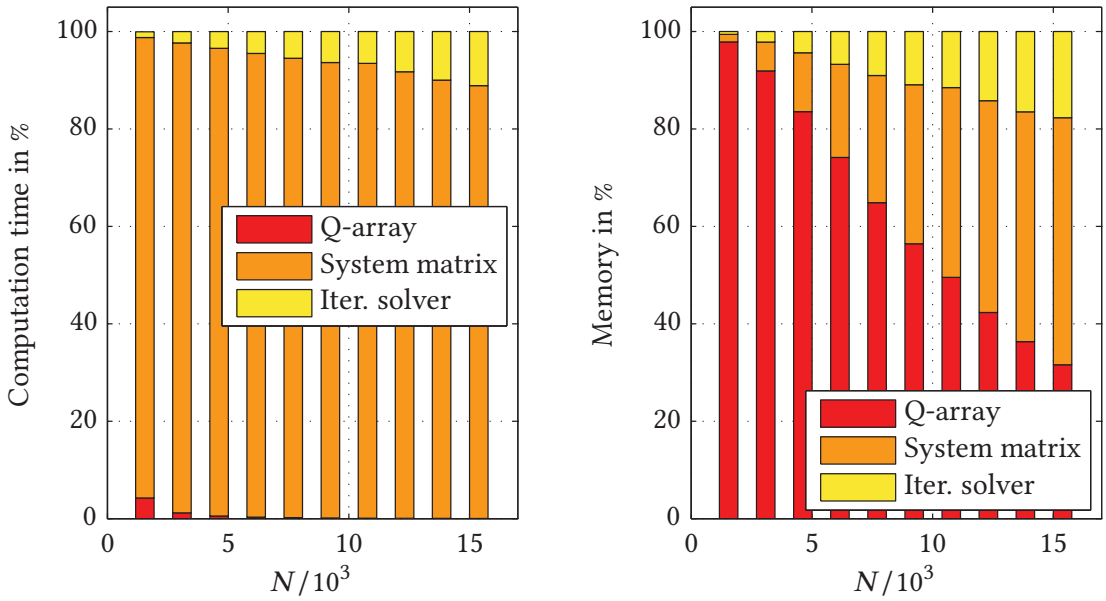

Fig. 6.18.: Percentage of the total computational time (left) and the total memory demand (right) of the single FFT Ewd subroutines versus the number of unknowns for the rectangular plate example.

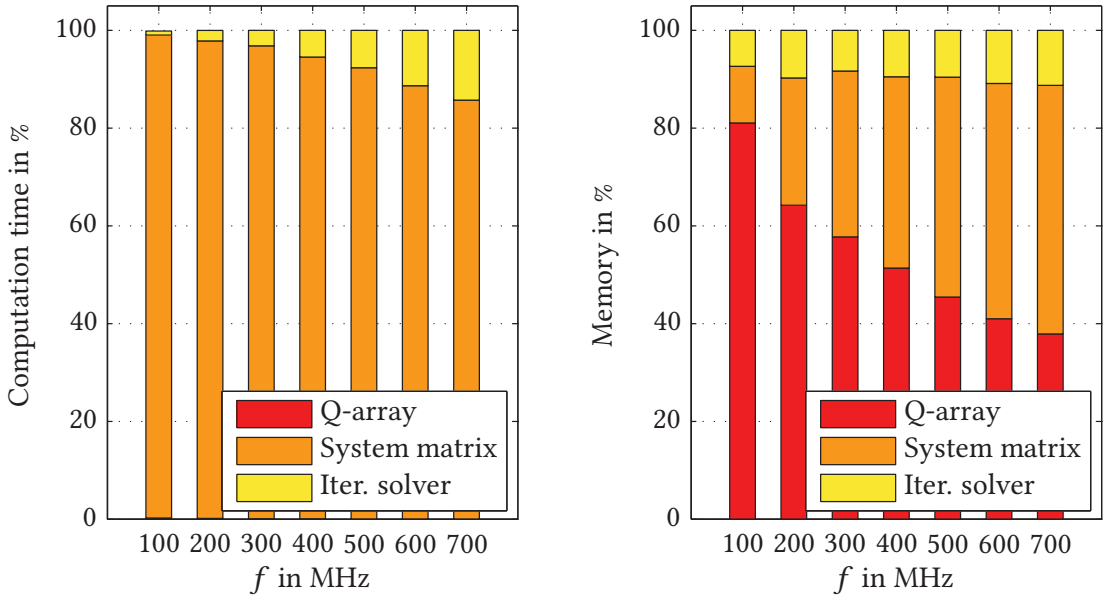

Fig. 6.19.: Percentage of the total computational time (left) and the total memory demand (right) of the single FFT Ewd subroutines versus frequency for the rectangular plate example.

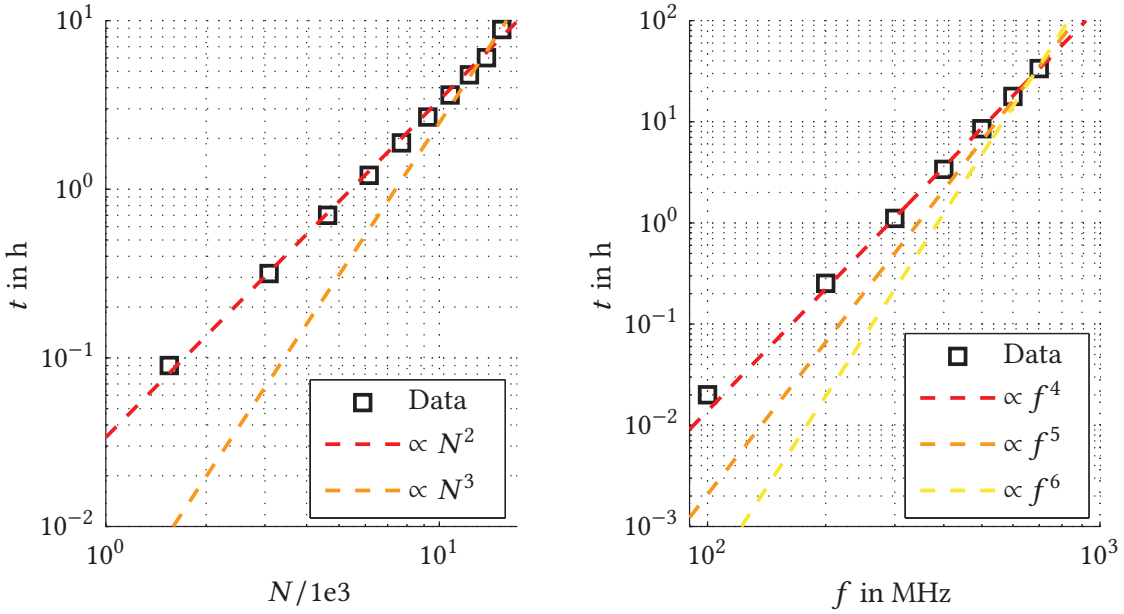

Fig. 6.20.: Total computation time of the FFT Ewd algorithm versus the number of unknowns (left) and frequency (right) for the rectangular plate examples.

number of unknowns and frequency, respectively. The computation times are fitted to polynomials of different degrees in the least square sense. As derived, the quadratic polynomials fits best for the number of unknowns and the polynomial of order four approximates the scaling with frequency best.

6.3.3. Multilevel Fast Multipole Method (FGF BEM)

The complexity of the MLFMM accelerated FGF BEM is analyzed for reverberation chambers. In contrast to the CGF BEM, the cavity walls have to be discretized in the FGF BI formulation. According to [Jin10], the time complexity of the MLFMM is $O\left(N_{\text{it}} N_{\text{tot}} \log N_{\text{tot}}\right)$ where N_{tot} is the total number of unknowns of the objects within the cavity and the cavity walls and N_{it} is the number of iterations. The memory complexity of the MLFMM is $O\left(N_{\text{tot}} \log N_{\text{tot}}\right)$ when the iterative solver is restarted after a fixed number of iterations [Jin10]. When the iterative solver is not restarted, the memory demand grows with $N_{\text{it}} N_{\text{tot}}$ as N_{it} solutions vectors of the length N_{tot} have to be stored during the iterative solution. In the following, N-complexity and f-complexity are again distinguished.

Number of Unknowns Complexity:

1. By their nature, most parts of reverberation chambers are filled with air. Hence, the unknowns of the objects inside the chamber is small compared with the

unknowns generated by the cavity walls and the total number of unknowns is hardly changed by adding objects or increasing the size of the objects (cf. also Table 6.7). Thus, the time and the memory N-complexity are approximately $O(1)$.

Frequency Complexity:

2. The total number of unknowns N_{tot} increases with f^2 as both the objects within the cavity and the cavity walls are discretized with a constant edge length per wavelength. The number of iterations grows approximately with f^2 as the results in Section 6.3.4 indicate. Consequently, the time complexity of the MLFMM is $O\left(f^4 \log f\right)$ for reverberation chambers. The memory demand grows with $N_{\text{it}} N_{\text{tot}} \propto f^4$ as the restarted iterative GMRES solver is not feasible for reverberation chambers, see Section 6.3.4.

6.3.4. Number of Iterations

The number of iterations plays a crucial role in determining the complexity of the algorithms. Since reverberation chambers are highly over-moded and resonant structures, the problem is ill-conditioned. The higher the resonance density (i.e., the higher the frequency) or the larger the number of unknowns, the larger is the number of iterations. This phenomenon is referred to as high-frequency breakdown of the EFIE [Bou14]. In contrast to the low-frequency and the dense-discretization breakdown [And10], the high-frequency breakdown has not been thoroughly described or cured for the general case yet. Only for convex geometries, it is addressed in [Bou14].

In order to still estimate the complexity of the algorithms, the convergence properties of the iterative solver are analyzed on the basis of the simulated data from the rectangular plate examples. In the case of the CGF BEM, an iterative GMRES solver is employed to solve the linear equation system. In the case of the MLFMM accelerated FGF BEM, a flexible GMRES-IO [Saa93; Eib07] is used and the near-zone matrix is preconditioned with a Gauss-Seidel and an iterative near-zone preconditioner in the innermost loop.

At first, the N-complexity is investigated. In Fig. 6.21, the number of iterations is plotted versus the number of unknowns generated by the objects inside the cavity. For the CGF BEM, the number of iterations increases approximately linearly with the number of unknowns. In the case of the MLFMM, the number of iterations is approximately constant since the total number of unknowns N_{tot} (i.e., the number of unknowns of the objects inside the cavity and the walls of the cavity) does hardly change when the size of the object inside the chamber is increased.

Secondly, the f-complexity is analyzed. In Fig. 6.22, the number of iterations is plotted versus frequency. In the case of the CGF BEM, the number of iterations grows

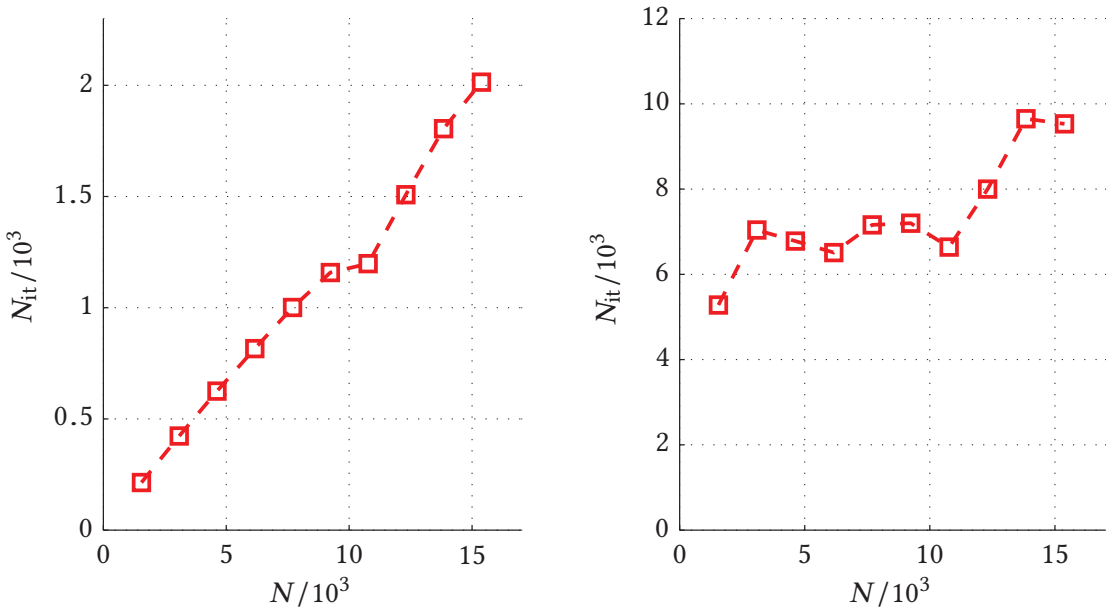

Fig. 6.21.: Number of iterations versus the number of unknowns for the CGF BEM (left) and the MLFMM accelerated FGF BEM (right).

approximately with f^2. Also, in the case of the ordinary BEM, quadratic growth can be observed although the curve shows stronger fluctuations.

To limit the memory consumption of the GMRES solver, it is usually restarted after a fixed number of iterations. However, the restarted GMRES does not necessarily converge. This is in particular the case when the problem is ill-conditioned. In Fig. 6.23, the convergence behavior of the restarted and the not-restarted GMRES are compared for the rectangular plate example at 400 MHz. In the case of the CGF BEM, the restarted solver does not converge. Although the restarted solver converges for the FGF BEM, the number of necessary iterations increases by a factor six versus the not-restarted GMRES.

6.3.5. Comparison and Discussion

The computational time and the memory complexities of the FGSDA accelerated CGF, the FFT accelerated CGF, and the MLFMM accelerated FGF BEM are summarized and compared in Table 6.9. The algorithms are referred to as FGSDA, FFT Ewd, and MLFMM, respectively.

In comparison with the MLFMM, the time complexities of the FGSDA and the FFT Ewd with respect to the number of unknowns are poor, i.e., $O(1)$ vs. $O\left(N^3\right)$. Although, according to Sections 6.3.1 and 6.3.2, the operation count of the proposed algorithms scales only with N^2 for the considered number of unknowns, quadratic growth is still poor compared to $O(1)$. Yet, as the cavity walls do not need to be discretized, the FGSDA

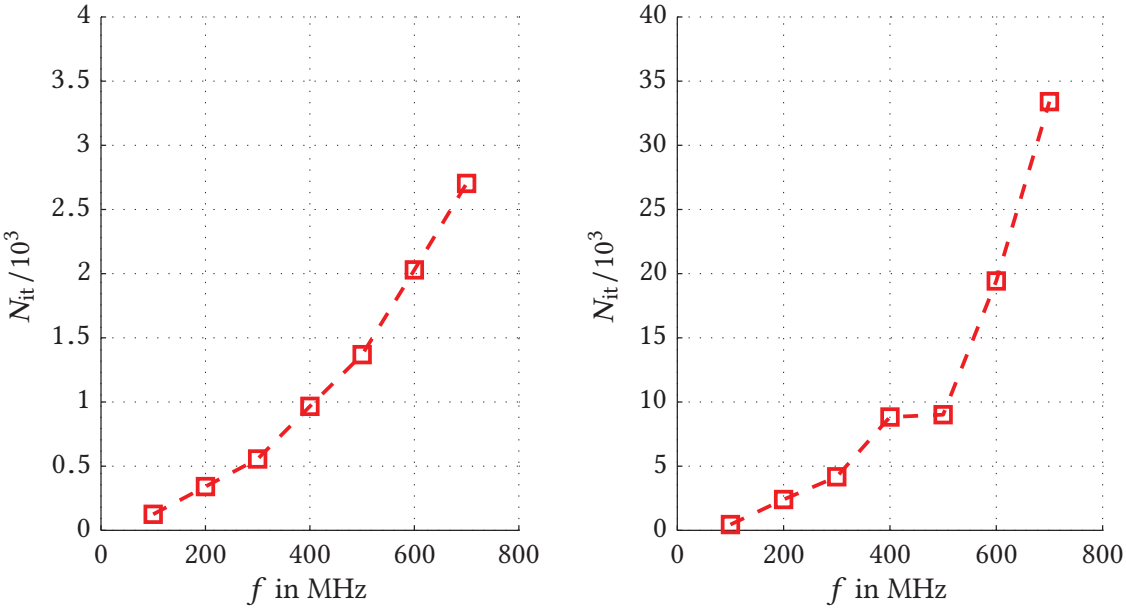

Fig. 6.22.: Number of iterations versus frequency for the CGF BEM (left) and the MLFMM accelerated FGF BEM (right).

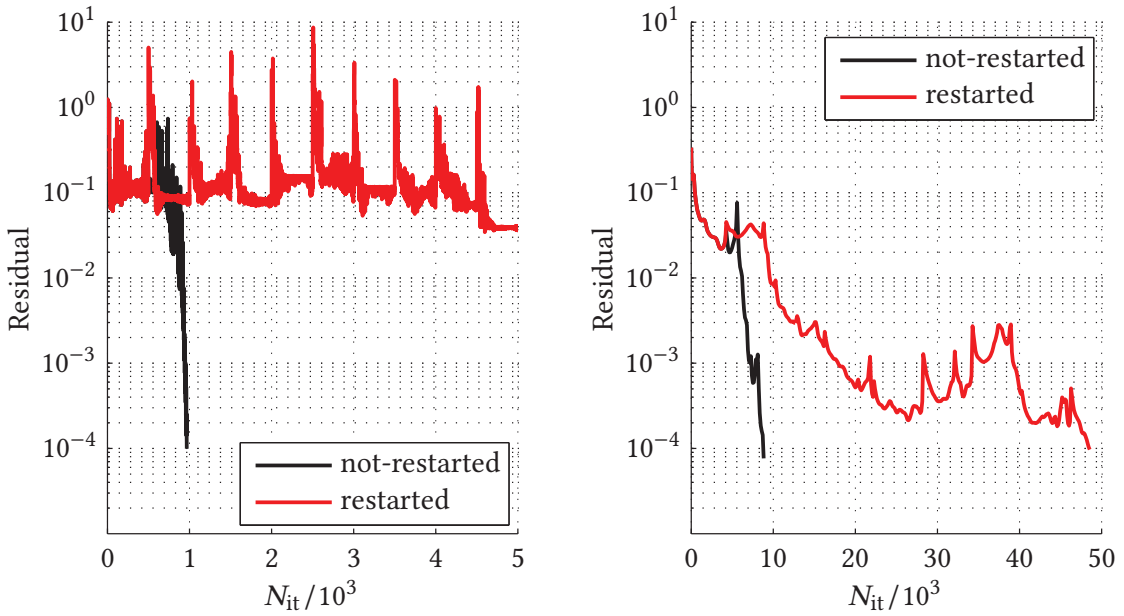

Fig. 6.23.: Convergence behavior of the restarted and the not-restarted GMRES for the CGF BEM (left) and the MLFMM accelerated FGF BEM (right) for the rectangular plate example at 400 MHz. For the CGF BEM, the number of iterations per restart was limited to 500. In the case of the MLFMM, the number of iterations per restart in the outer loop was limited to 50. In the second loop, the number of iterations was limited to 120.

Algorithm	N-complexity		f-complexity	
	CPU time	Memory	CPU time	Memory
FGSDA spec. repres.	$\mathcal{O}(N)$	$\mathcal{O}(N)$	$\mathcal{O}\left(f^5\right)$	$\mathcal{O}\left(f^2\right)$
FGSDA system matrix	$\mathcal{O}\left(N^2\right)$	$\mathcal{O}\left(N^2\right)$	$\mathcal{O}\left(f^6\right)$	$\mathcal{O}\left(f^4\right)$
FGSDA iter. solver	$\mathcal{O}\left(N^3\right)$	$\mathcal{O}\left(N^2\right)$	$\mathcal{O}\left(f^6\right)$	$\mathcal{O}\left(f^4\right)$
FGSDA overall	$\mathcal{O}\left(N^3\right)$	$\mathcal{O}\left(N^2\right)$	$\mathcal{O}\left(f^6\right)$	$\mathcal{O}\left(f^4\right)$
FFT Ewd Q-array	$\mathcal{O}(1)$	$\mathcal{O}(1)$	$\mathcal{O}\left(f^3 \log f\right)$	$\mathcal{O}\left(f^3\right)$
FFT Ewd system matrix	$\mathcal{O}\left(N^2\right)$	$\mathcal{O}\left(N^2\right)$	$\mathcal{O}\left(f^4\right)$	$\mathcal{O}\left(f^4\right)$
FFT Ewd iter. solver	$\mathcal{O}\left(N^3\right)$	$\mathcal{O}\left(N^2\right)$	$\mathcal{O}\left(f^6\right)$	$\mathcal{O}\left(f^4\right)$
FFT Ewd overall	$\mathcal{O}\left(N^3\right)$	$\mathcal{O}\left(N^2\right)$	$\mathcal{O}\left(f^6\right)$	$\mathcal{O}\left(f^4\right)$
MLFMM overall	$\mathcal{O}(1)$	$\mathcal{O}(1)$	$\mathcal{O}\left(f^4 \log f\right)$	$\mathcal{O}\left(f^4\right)$

Tab. 6.9.: Complexity of the FGSDA, the FFT Ewd, and the MLFMM algorithm for over-moded cavities versus frequency and number of unknowns.

and the FFT Ewd have significant advantages as long as the objects inside the cavity are small compared to the cavity itself. To quantify what "small" is, the timings of the FGSDA, FFT Ewd, and MLFMM from the rectangular plate example are plotted versus the ratio N/N_{tot} in Fig. 6.24. The timings of the FGSDA and FFT Ewd are fitted to quadratic polynomials in the least square sense and the timings of the MLFMM are fitted to a constant. Using the fitted polynomials, the break even points of the CGF BEMs versus the FGF BEM are estimated. In the case of the FGSDA, the MLFMM is less efficient as long as $N < N_{\text{tot}}/6$. The FFT Ewd approach is to prefer versus the MLFMM when $N < N_{\text{tot}}/8$.

The time complexity with respect to frequency of the FGSDA and the FFT Ewd is $\mathcal{O}\left(f^6\right)$ while the time complexity of the MLFMM is $\mathcal{O}\left(f^4 \log f\right)$. Yet, as it was discussed in Sections 6.3.1 and 6.3.2, the operation count of the iterative solver is small in scenarios of practical relevance and the time complexity of the CGF BEM algorithms is determined by the system matrix. For the FGSDA, the time complexity of the system matrix is $\mathcal{O}\left(f^6\right)$. For the FFT Ewd, it is $\mathcal{O}\left(f^4\right)$. As it was discussed in Section 6.3.1, the operation count of the FGSDA is proportional to f^5 and not f^6 in the frequency range of interest. Thus, the complexities of the CGF BEM algorithms and the MLFMM algorithm with respect to frequency are of similar order which is confirmed by the timings in Section 6.1.1.

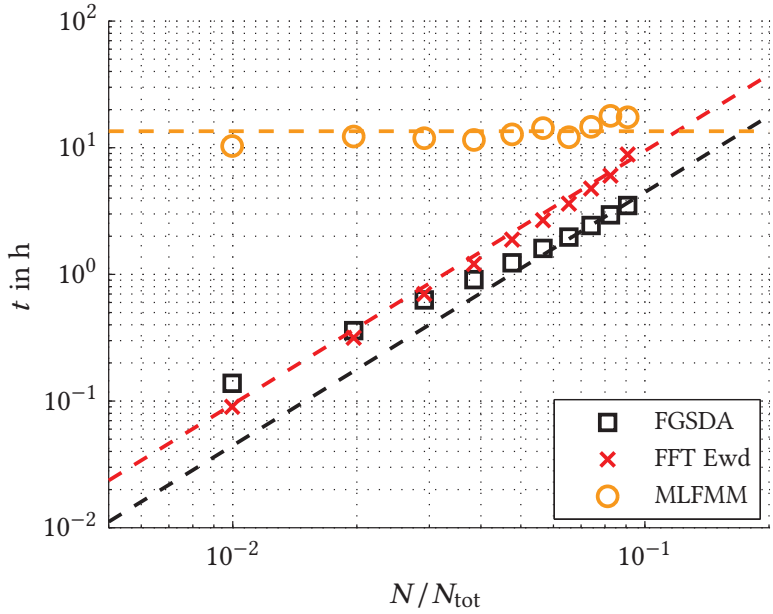

Fig. 6.24.: Computation times of the FGSDA, FFT Ewd, and MLFMM algorithm versus the number of unknowns ratio N/N_{tot} for the rectangular plate example.

6.4. Validation Against Measurements

The accurate numerical modeling of real reverberation chambers is a demanding and time-consuming process. As the problem is ill-conditioned, even fine geometrical details (e.g., cables, the stirrer axis, or chamber door) and fine modeling differences (e.g., discretization or analytic consideration of the cavity walls) have a non-negligible impact on the results (see e.g., [Leu03a; Bru05] and Section 6.2, respectively). However, in the majority of cases, deterministic quantities, such as the electric field, are of minor interest in reverberation chamber research and application. The important quantities are of statistical nature (e.g., the homogeneity of the field, the number of independent stirrer positions, or the field statistics). In the following, the reverberation chamber from the Technical University of Dresden is modeled using the FGSDA accelerated CGF BEM. The number of independent stirrer positions is determined according to the standard and the general method (see [IEC11] and [Pfe12], respectively). The simulated results are validated against the measured ones from [Pfe12].

The reverberation chamber at the TU Dresden is 5.3 m long, 3.7 m wide, and 3.0 m high. It is equipped with a z-shaped mode stirrer whose axis is defined by the points (4.3 m, 1.0 m, 0.0 m) and (4.3 m, 1.0 m, 3.0 m). Pictures of the stirrer and the antenna are displayed in Fig. 6.25. In [Pfe12], the stirrer was rotated clockwise in 1° steps. The chamber was excited by a log-per antenna at ten discrete frequencies in the frequency range from 150 MHz to 1 GHz. The magnitude of the electric field was measured in a cubic test volume with a side length of 1 m at $3\times3\times3 = 27$ equally spaced measurement

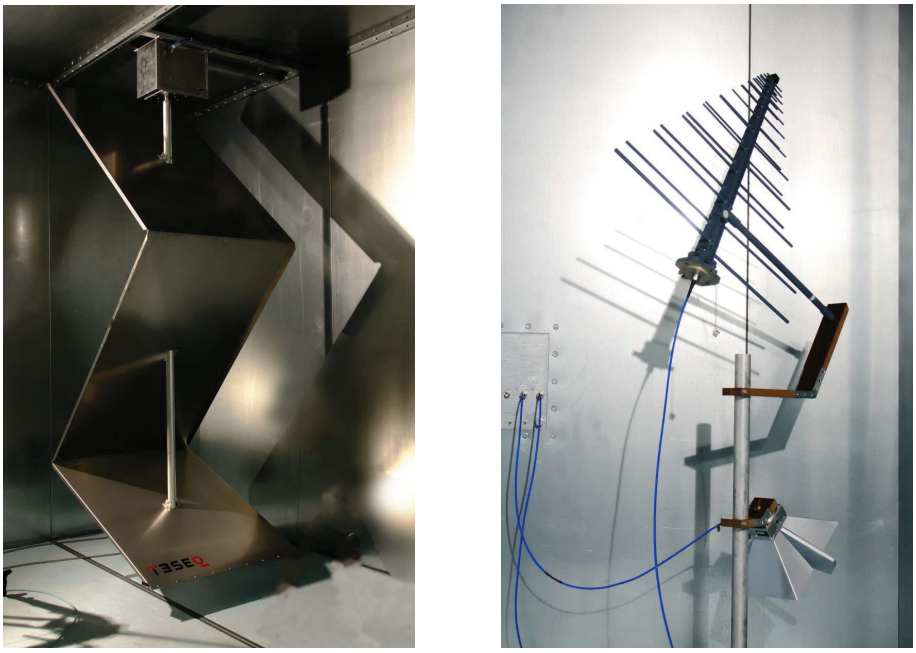

Fig. 6.25.: Picture of the mode stirrer (left) and the log-per antenna (right) in the reverberation chamber of the Technical University of Dresden by courtesy of the Chair of Electromagnetic Theory and Compatibility, TU Dresden, Germany.

points. The center of the test volume was at the point $(2.3\,\mathrm{m}, 2.0\,\mathrm{m}, 1.5\,\mathrm{m})$.

In the numerical model, fine geometrical details, such as the stirrer axis, cables, or field probes, are neglected. Instead of the geometrically complex log-per antenna, a strip dipole of the size $0.4\,\mathrm{m} \times 0.16\,\mathrm{m}$ is used. The dipole and the stirrer plates are discretized with an average edge length of $0.04\,\mathrm{m}$ or $\lambda/10$, respectively. The cavity walls do not need to be modeled since they are incorporated in the Green's function of the cavity. Although the CGF BEM is capable to consider metallic objects, the dipole and the stirrer plates are modeled as perfect electric conductors for simplicity. The losses are lumped together in the complex wavenumber according to (2.41). The quality factor of the reverberation chamber in use was measured in [Pfe15] and fitted to the model

$$Q = \frac{1}{\frac{1}{Q_\mathrm{a}} + \frac{1}{Q_\mathrm{w}}} \tag{6.1}$$

where

$$Q_\mathrm{a} = 16\pi^2 V \left(\frac{f}{c_0}\right)^3 \tag{6.2}$$

is the individual quality factor due to antenna losses and

$$Q_\mathrm{w} = \frac{3V}{2S_\mathrm{w}} \sqrt{\pi \mu_0 \kappa_\mathrm{w} f} \tag{6.3}$$

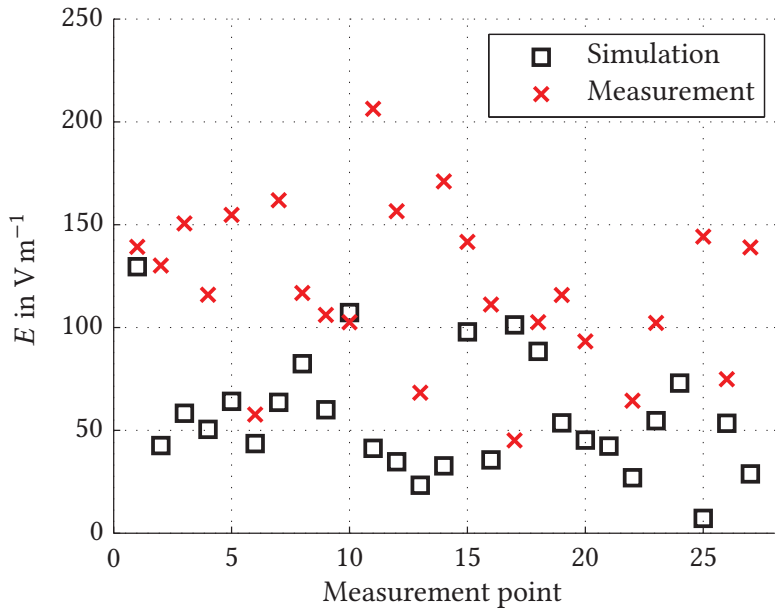

Fig. 6.26.: Magnitude of the electric field at the 27 measurement points within the test volume for the zeroth stirrer position at 250 MHz.

is the individual quality factor due to the wall losses. To include not only the wall but also the other losses in Q_w, an artificial wall conductivity of $\kappa_\mathrm{w} = 2 \cdot 10^4\,\mathrm{S\,m^{-1}}$ is used in accordance with [Pfe15].

In [Pfe12], the number of independent stirrer positions was estimated according to the standard [IEC11] and the general method [Pfe12]. The magnitude of the electric field was measured at $N_\mathrm{r} = 27$ points within the test volume for $N_\alpha = 360$ stirrer positions. In the case of the standard method, the average over the 27 measurement points was formed. Two positions were considered as independent when the correlation coefficient of the corresponding fields was less than the threshold $r_\mathrm{s} = 0.37$.

In Fig. 6.26, the magnitude of the electric field at the 27 measurement points for the zeroth stirrer position at 250 MHz. As expected, the measured and the simulated fields do not agree. Possible reasons are that 1) losses are modeled in an average quality factor but not individually for each stirrer position, 2) the log-per antenna is simplistically modeled as an electrically short dipole, 3) discretization errors, and 4) other fine geometrical details such as cables, the door, and the stirrer axis are not considered in the numerical model.

In Fig. 6.27 and 6.28, the number of independent stirrer positions $N_{\alpha,\mathrm{ind}}$ calculated according to the standard and the general method are shown, respectively. In the overmoded frequency range, the agreement between the simulated data agrees well with the measurements. The deviation is below 20% for frequencies greater than 250 MHz. In the transition range, the difference is larger. One possible reason for the deviation is the coarse modeling of the excitation antenna. While there is a direct path between

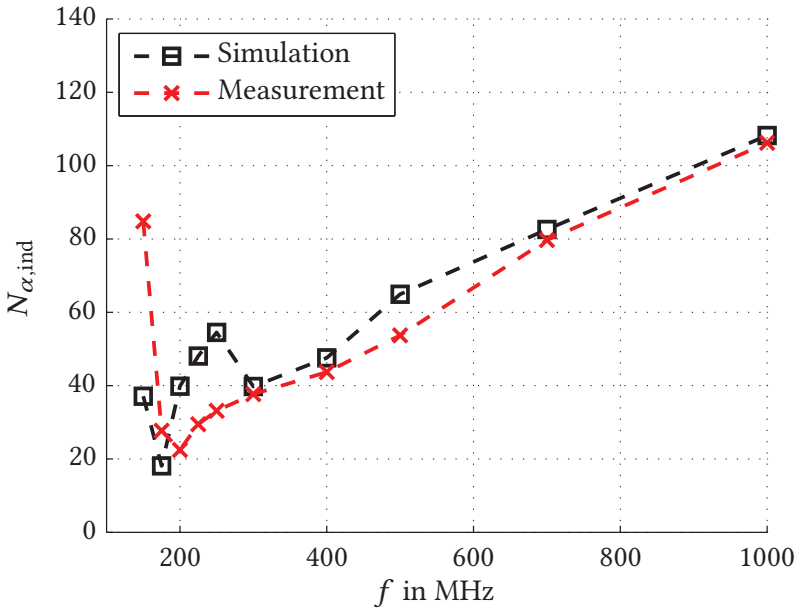

Fig. 6.27.: Number of independent stirrer positions $N_{\alpha,\mathrm{ind}}$ calculated according to the standard method [IEC11].

the test volume and the antenna in the numerical model, this is not the case in the real reverberation chamber. Another reason may be the modeling of the quality factor in (6.1). In the lower frequency range, the measured average quality factor showed strong deviations from the theoretical one [Pfe15].

In summary, the CGF BEM is able to reproduce statistical quantities such as the number of independent stirrer positions. Despite the coarseness of the numerical model, a good agreement was achieved in the over-moded frequency range. In the transition range of the reverberation chamber, a more detailed modeling of the antenna pattern and the quality factor may improve the accuracy of the numerical results. Deterministic quantities such as the electric field are difficult to reproduce. Although the resonances of the cavity are considered analytically in the Green's function of the rectangular cavity, the main error sources are discretization errors, the quality factor, and geometrical inaccuracies in the numerical modeling process.

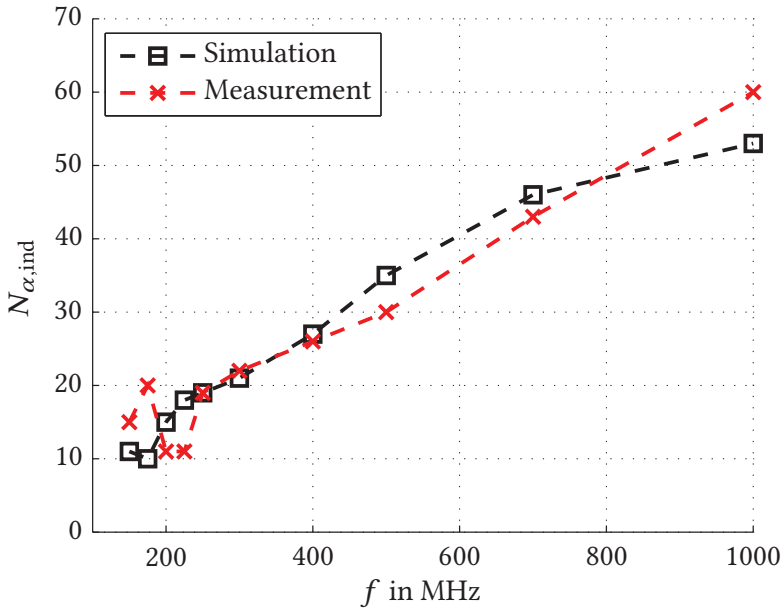

Fig. 6.28.: Number of independent stirrer positions $N_{\alpha,\mathrm{ind}}$ calculated according to the general method [Pfe12].

7. Application to Reverberation Chamber Research

7.1. The Number of Independent Stirrer Positions: An Inner Product Space Approach

Important measures for the performance of reverberation chambers are among others the field homogeneity, the statistically independent stirrer positions, the max-to-average ratio, and the field statistics [Mog10; Mog11]. While the definitions of the former and the latter two measures are non-controversial, there are several methods to estimate the number of independent stirrer positions [Pfe13]. The standard method [IEC11] is easy to perform but it is not applicable to multiple stirrers [Kra07; Mog10] and gives wrong results in the transition frequency range of a reverberation chamber [Pfe12].

In [Pfe12; Pfe13; Pfe14], a generalized method which does not have these shortcomings has been developed. The magnitude of the electric field is measured at N_r points within the test volume for each stirrer position $\alpha_0, \alpha_1, \ldots, \alpha_{N_\alpha}$. Two stirrer positions i_α and j_α are called independent when the Pearson correlation coefficient

$$r_{i_\alpha j_\alpha} = \frac{\mathrm{Cov}\left(\boldsymbol{x}_{i_\alpha}, \boldsymbol{x}_{j_\alpha}\right)}{\sqrt{\mathrm{Var}\,\boldsymbol{x}_{i_\alpha}\,\mathrm{Var}\,\boldsymbol{x}_{j_\alpha}}} \tag{7.1}$$

of the corresponding field distributions

$$\boldsymbol{x}_{i_\alpha} = \left(E_{i_\alpha 0}, E_{i_\alpha 1}, \ldots, E_{i_\alpha N_\mathrm{r}}\right), \tag{7.2}$$

$$\boldsymbol{x}_{j_\alpha} = \left(E_{j_\alpha 0}, E_{j_\alpha 1}, \ldots, E_{j_\alpha N_\mathrm{r}}\right) \tag{7.3}$$

is less than the correlation threshold r_s where $E_{i_\alpha i_r}$ is the magnitude of the electric field for the i_αth stirrer position at the i_rth measurement point, $i_\alpha, j_\alpha = 0, 1, \ldots, N_\alpha$, and $i_r = 0, 1, \ldots, N_r$. A set of independent stirrer positions is a set of stirrer positions which are mutually independent. The problem of finding the maximum set of independent stirrer positions is known from graph theory as the maximum clique problem and is illustrated in Fig. 7.1. The exact solution of the maximum clique problem is not possible in polynomial time, however, heuristic algorithms which achieve good results in reasonable time are available [Pul06]. Although the general method does not have the shortcomings of the standard method, Pfennig and Krauthäuser have not stated how many measurement points must be selected. In [Pfe12], the number of measurement points is set to 27. However, in [Pfe13], 63 measurement points result in a larger set of

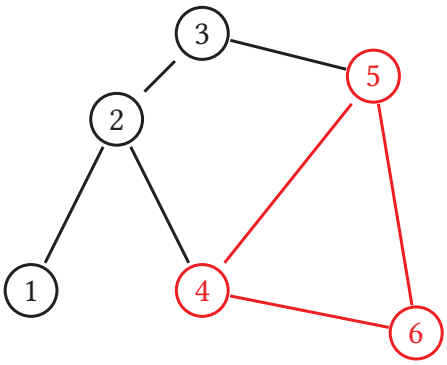

Fig. 7.1.: Number of independent stirrer positions as a maximum clique problem: the nodes correspond to the stirrer positions; two nodes are independent when they are connected; the maximum set of independent stirrer positions is colored in red.

independent stirrer positions and the question arises which number of measurement points yields the correct set.

Herein, the general method is considered in the framework of linear algebra. It is shown that the number of independent stirrer positions is bounded for a fixed correlation threshold and a fixed number of measurement points. As the correlation coefficient satisfies the axioms of an inner product (i.e., conjugate symmetry, linearity, and positive-definiteness [Råd04]), the field distributions $\boldsymbol{x}_i$ are elements of an N_r-dimensional inner product space. In this framework, the question

Problem 1. *How many independent stirrer positions exist given a correlation threshold r_s and a number of measurement points N_r?*

can be reformulated as

Problem 2. *How many vectors $\boldsymbol{x}_{i_\alpha}, \boldsymbol{x}_{j_\alpha}$ satisfying $\left\langle \boldsymbol{x}_{i_\alpha}, \boldsymbol{x}_{j_\alpha} \right\rangle < r_s$ exist in an N_r-dimensional vector space?*

The latter is known as the problem of spherical codes. A spherical code (n, N, r) is a set of N points on the unit hypersphere in n dimensions for which the scalar product of unit vectors from the origin to any two points is less than or equal to r (i.e., the minimum angle between two vectors is the inverse cosine of r) [Con99]. In Fig. 7.2, a spherical code on the ordinary sphere is illustrated. Unfortunately, the problem of spherical codes is unsolved in general. Solutions exist for a few special cases only (e.g., low dimensional spaces and symmetric configurations [Slo12]). Nevertheless, it has been shown that the number of points on a hypersphere is bounded for a given minimum angle between two points [Con99]. In the case of the independent stirrer positions problem, the points on the hypersphere correspond to the number of independent stirrer positions, the dimension of the hypersphere corresponds to the number of measurement points N_r, and r corresponds to the correlation threshold r_s. Accordingly,

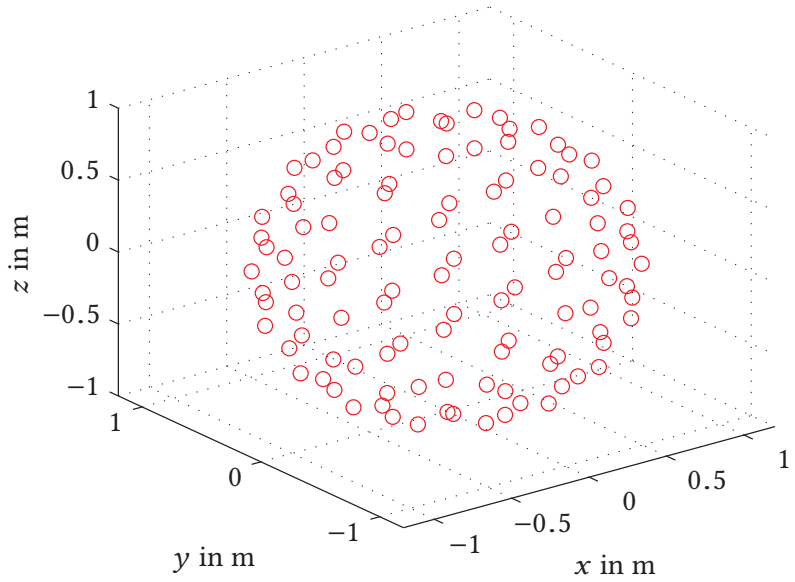

Fig. 7.2.: Spherical code on the ordinary sphere with $r = \cos 20^\circ \approx 0.9397$ and $N = 110$ [Slo12].

the number of independent stirrer positions is bounded given a correlation threshold and a number of measurement points.

In the following, a numerical example is shown. The w-shaped two plate stirrer scenario from Section 6.1 is considered. The quality factor of the reverberation chamber is set to 10^4. The stirrer is rotated parallel to the z-axis in 1° degree steps around its center. The magnitude of the electric field is computed at 120 equispaced points in a 7 m long, 4 m wide, and 2 m high test volume whose center is at $(4.5\,\mathrm{m}, 3\,\mathrm{m}, 2\,\mathrm{m})$. The maximum set of independent stirrer positions is searched using the algorithm from Pullan and Hoos [Pul06] for a correlation threshold of $r_\mathrm{s} = 0.37$. In Fig. 7.3, the number of independent stirrer positions $N_{\alpha,\mathrm{ind}}$ are shown in dependence of the number of measurement points for $f = 200\,\mathrm{MHz}$ and $f = 400\,\mathrm{MHz}$. In addition, the number of independent stirrer positions for an ideal reverberation chamber (i.e., the magnitude of the electric field is chi distributed with six degrees of freedom [Hil09].) is displayed. At 200 MHz, $N_{\alpha,\mathrm{ind}}$ saturates at $N_\mathrm{r} = 60$. At 400 MHz and in the case of the ideal reverberation chamber, about 100 measurement points are necessary to obtain the maximum number of independent stirrer positions. For 27 measurement points, only about 65% (200 MHz), 50% (400 MHz), and 30% (ideal reverberation chamber) of the maximum number of independent positions are found, respectively.

In summary, the number of measurement points limits the independent stirrer positions when insufficient measurement points are selected. In particular at high frequencies, the number of 27 measurement points, which was used in [Pfe12], leads to an underestimation of the independent positions.

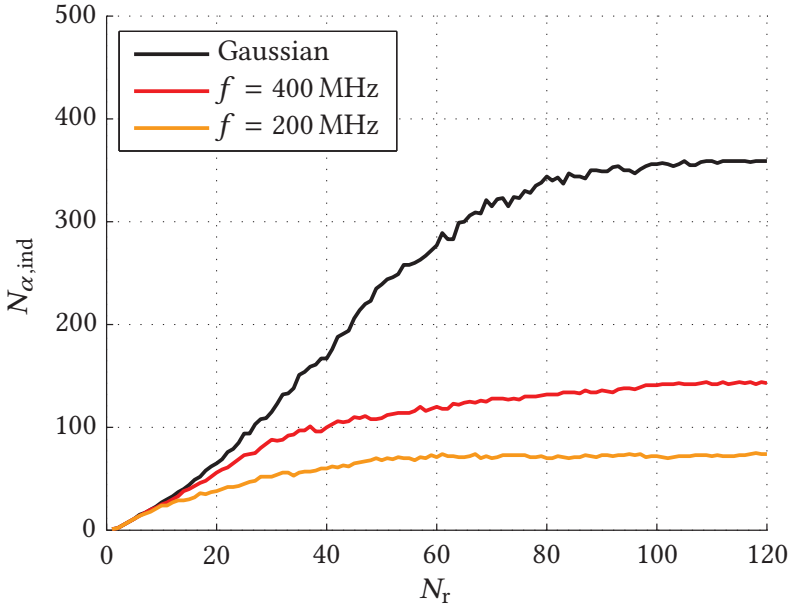

Fig. 7.3.: Number of independent stirrer positions $N_{\alpha,\mathrm{ind}}$ against the number of measurement points N_r for $f = 200\,\mathrm{MHz}$, $f = 400\,\mathrm{MHz}$, and an ideal reverberation chamber.

7.2. A Dual Rotation Speed Stirring Mode

7.2.1. Motivation

In the last decade, mechanical stirring played an important role in reverberation chamber research [Cle05; Arn06; Hua06; Wel07; Lun10; Mog10; Mog11; Mog12; Bos12; Pri14]. In [Wel07], the influence of the stirrer height and diameter on the homogeneity of the field was studied. In [Lun10], it was found that in particular the periphery of a stirrer contributes to the generation of the random process. Based on the results from [Lun10], Moglie and Primiani proposed a new location for the test volume within a carousel-like stirrer [Mog12]. The new location inside the tuner improves the chamber performance significantly. In contrast, the position of the stirrer hardly affects the quality of the stirring process [Pri14]. Another possibility to improve the performance of a reverberation chamber is adding a second stirrer [IEC11]. In [Mog10; Mog11], a reverberation chamber which contains two tuners was considered. The stirrers were operated in synchronized (i.e., the stirrers are rotated with the same speed) and in interleaved mode (i.e., the stirrer are rotated with different velocities). While the chamber performance only improved slightly in synchronized mode, a significant improvement was achieved in interleaved mode.

Although a second stirrer enhances the stirring process, there is a shortcoming: the space needed for the additional stirrer decreases the available test volume. Therefore, another approach is pursued herein. A reverberation chamber with a single tuner is

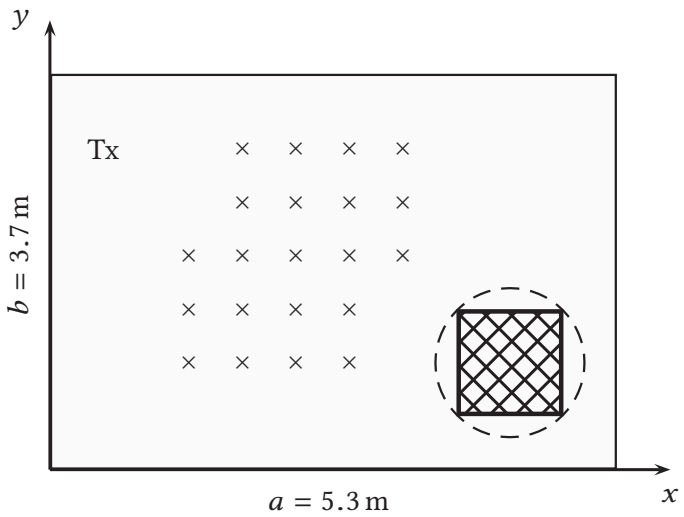

Fig. 7.4.: Geometry of the reverberation chamber and the test volume.

considered, but, in contrast to the standard case, not all parts of the stirrer are rotated by the same angular increment. The angle increment of the upper part of the stirrer is, for instance, five times the increment of the lower part. The efficiency of the proposed scheme is evaluated based on two criteria. The number of the independent stirrer positions is estimated according to the generalized method from [Pfe12; Pfe13; Pfe14] and the homogeneity of the field in the test volume is determined according to the international electrotechnical commission (IEC) standard [IEC11].

7.2.2. Geometry of the Analyzed Structure

The considered reverberation chamber is of the size $5.3\,\mathrm{m} \times 3.7\,\mathrm{m} \times 3\,\mathrm{m}$. A four-plate stirrer is located in the front right corner of the chamber. The stirrer is rotated parallel to the z-axis about its center at $(4.3, 1.0, 1.5)$. A $0.16\,\mathrm{m}$ long and $0.04\,\mathrm{m}$ wide strip dipole centered at the point $(0.5, 3.0, 1.5)$ is used as excitation. In the test volume, the magnitude of the electric field is determined at $N_\mathrm{r} = 63$ equally spaced points, see Fig. 7.4. The distance in x-, y-, or z-direction between any two points is $0.5\,\mathrm{m}$. The performance of the reverberation chamber is analyzed at six discrete frequencies in the frequency range from 150 MHz to 500 MHz.

In contrast to the standard mode, the plates of the stirrer are rotated with different speeds, e.g., the upper plates are rotated twice as fast as the lower ones. To investigate if the order of the rotation speeds influences the performance of the proposed stirring mode, two cases are considered. In case A, the upper plates are rotated by the angle $\Delta\alpha_1$ while the lower plates are rotated by the increment $\Delta\alpha_2$. In case B, the upper and the lower plate are rotated by the angle increment $\Delta\alpha_1$ while the two middle plates are

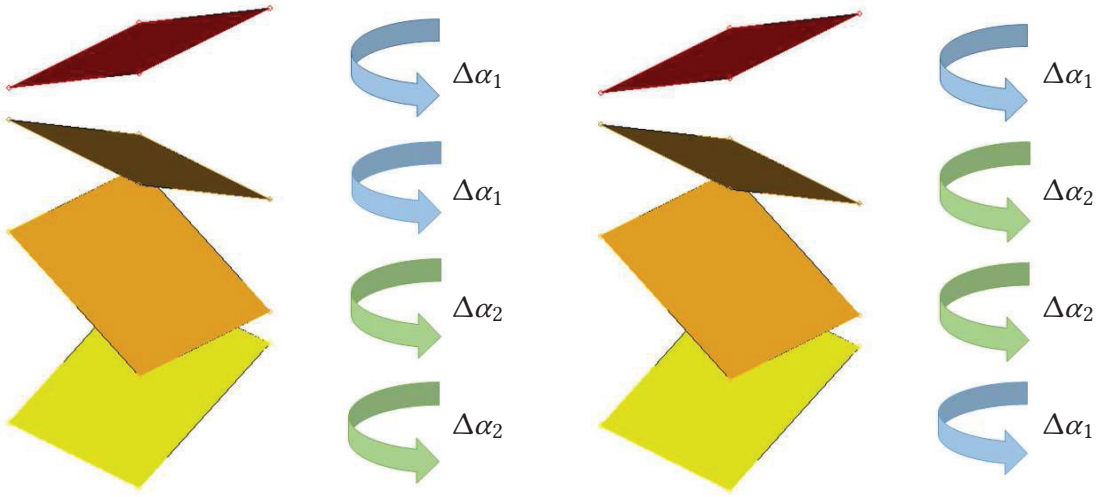

(a) Case A *(b)* Case B

Fig. 7.5.: Geometry of the four-plate stirrer and corresponding rotation speeds of the plates.

ν_α	$\Delta\alpha_1$	$\Delta\alpha_2$	Stirring Mode
1	1°	1°	standard
5	1°	5°	dual rotation speed
20	1°	20°	dual rotation speed
72	1°	72°	dual rotation speed

Tab. 7.1.: Ratios ν_α and angle increments for the considered stirring modes.

rotated by the increment $\Delta\alpha_2$, see Fig. 7.5. The ratio between the angle increments is denoted by $\nu_\alpha = \Delta\alpha_2/\Delta\alpha_1$. In Table 7.1, the considered ratios ν_α and the corresponding angle increments are listed. Overall, $N_\alpha = 360$ stirrer positions are considered.

7.2.3. Numerical Results

The reverberation chamber is simulated using the FGSDA accelerated CGF BEM algorithm. The excitation and the stirrer are modeled as PEC. They are discretized with an average edge length of 0.04 m and $\lambda/10$, respectively. Losses are introduced by complexification of the wavenumber according to (2.41). The quality factor of the chamber is adopted from Section 6.4.

The new stirring mode is evaluated based on the following criteria: the number of independent stirrer positions and the homogeneity of the electric field within the test volume. As the standard method [IEC11] for estimating the number of independent stirrer positions is restricted to one degree of freedom (i.e., one rotation speed

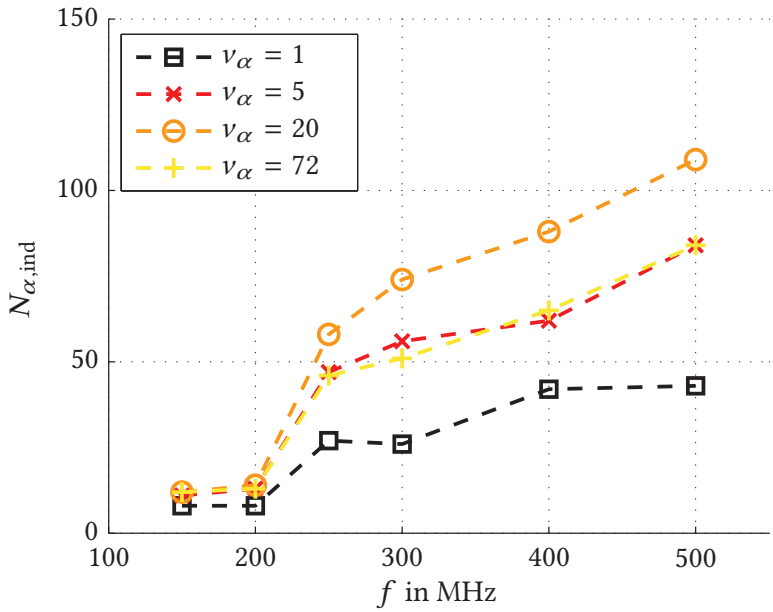

Fig. 7.6.: Number of independent stirrer positions for the standard ($\nu_\alpha = 1$) and the dual rotation speed ($\nu_\alpha = 5, 20, 72$) stirring modes (Case A).

in our case), it is not suited to assess the proposed stirring mode. Instead the general method [Pfe12], which does not suffer from this limitation, is employed. The threshold correlation for independence of two stirrer positions is set to

$$r_\mathrm{s} = \frac{1}{\mathrm{e}}\left(1 - \frac{7.22}{N_\alpha^{0.64}}\right) = \frac{1}{\mathrm{e}}\left(1 - \frac{7.22}{360^{0.64}}\right) = 0.3065 \tag{7.4}$$

in accordance with the IEC standard [IEC11]. The maximum set of independent stirrer positions is searched using the algorithm of Pullan and Hoos [Pul06].

In Fig. 7.6, the number of independent stirrer positions is displayed for the different ratios ν_α in case A. The dual rotation speed stirring modes outperform the standard mode. The modes $\nu_\alpha = 5$ and $\nu_\alpha = 72$ are similarly good. The mode $\nu_\alpha = 20$ performs best. In the over-moded frequency range ($f \geq 200\,\mathrm{MHz}$), it generates more than twice as many independent positions. In the under-moded range, it achieves an improvement of one and a half. In average over all frequencies, the number of independent stirrer positions is increased by a factor of 2.32. In Fig. 7.7, the number of independent stirrer positions is displayed in the case B. The results are similar to case A. In average, the number of independent stirrer positions is increased by a factor of 2.15.

As the second criteria, the homogeneity of the field is tested. In accordance with the IEC standard [IEC11], eight measurement points within the test volume and mutual distance of at least $\lambda/2$ are selected. The points are located at the vertices of a cubic volume with 1 m side length and center $(2.3, 2.0, 1.5)$. In order to obtain a single measure, we follow [Cle05]. The differences D_x, D_y, D_z, and D_tot of the standard

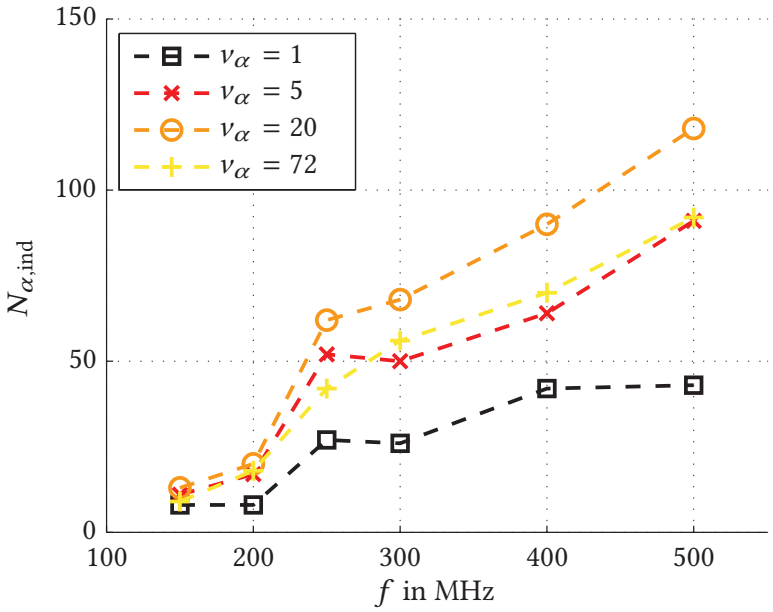

Fig. 7.7.: Number of independent stirrer positions for the standard ($\nu_\alpha = 1$) and the dual rotation speed ($\nu_\alpha = 5, 20, 72$) stirring modes (Case B).

deviations of E_x, E_y, E_z, and E_{tot} to the tolerance level specified in [IEC11] are calculated, respectively and added up to the total difference $D = D_x + D_y + D_z + D_{\mathrm{tot}}$. The greater the total difference, the more homogeneous is the field. When $D < 0$, at least one component does not meet the IEC criteria. In Fig. 7.8, the difference D is shown for the different ratios ν_α in case A. The dual rotation speed stirring modes generate a more homogeneous field than the standard mode although the improvement is not as significant as for the independent stirrer positions. In average, the mode $\nu_\alpha = 20$ achieves a 1 dB higher field homogeneity than the standard mode. The total difference of the modes $\nu_\alpha = 5$ and $\nu_\alpha = 72$ is, on average, about 0.5 dB larger than that of the standard mode. Again, the mode $\nu_\alpha = 20$ performs best. In Fig. 7.8, the difference D is shown for case B. The average improvement for the mode $\nu_\alpha = 20$ is 1.2 dB.

In summary, the dual rotation speed stirring mode improves the performance of reverberation chambers with respect to independent stirrer positions and field homogeneity. The order of the rotation speeds of the plates has a minor impact. The performance is best when the ratio of the rotation speeds is approximately the square root of the total number of tuner positions.

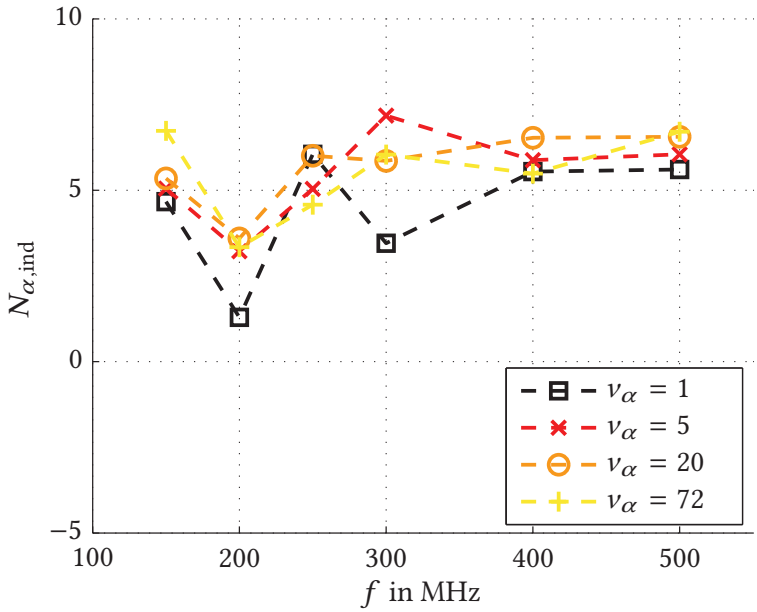

Fig. 7.8.: Homogeneity of the electric field for the standard ($\nu_\alpha = 1$) and the dual rotation speed ($\nu_\alpha = 5, 20, 72$) stirring modes (Case A).

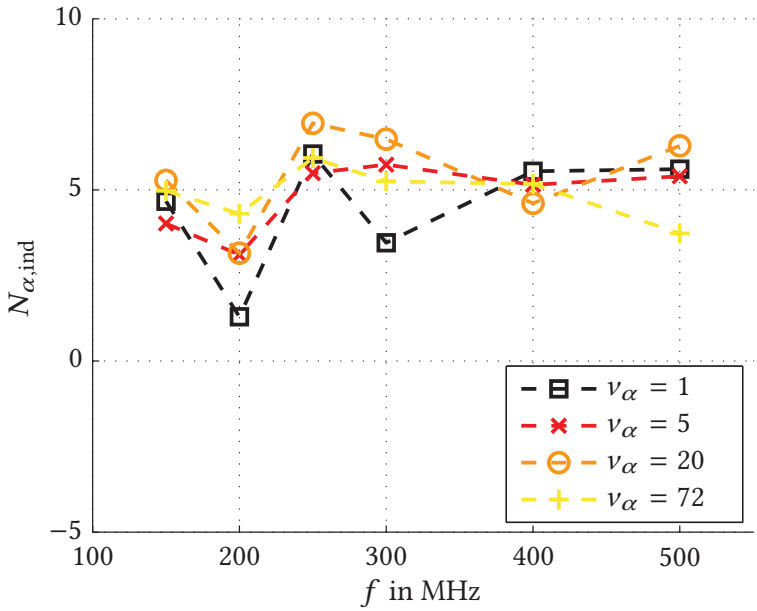

Fig. 7.9.: Homogeneity of the electric field for the standard ($\nu_\alpha = 1$) and the dual rotation speed ($\nu_\alpha = 5, 20, 72$) stirring modes (Case B).

8. Conclusion and Outlook

Two different acceleration techniques for the cavity Green's function (CGF) boundary element method (BEM), a fast group spectral domain approach (FGSDA) and a fast Fourier transform (FFT) accelerated Ewald summation technique, were presented. Both techniques address the major shortcomings of the unaccelerated CGF BEM. The complexity with respect to frequency is decreased by two, respectively, three orders. Although the complexity with respect to the number of unknowns is not reduced, the computationally most expensive part, the filling of the system matrix, is accelerated significantly.

The presented methods were compared with and validated against a multilevel fast multipole method (MLFMM) accelerated free-space Green's function (FGF) BEM over a wide frequency range for different scenarios. For a Vivaldi antenna, the FFT accelerated Ewald summation technique achieved a speed-up of more than three orders of magnitude. In the case of a mode stirrer, the simulation time was decreased by more than one order of magnitude using the FGSDA. Although the speed-up reduced for a car body, the simulation time was still decreased by at least a factor of four for frequencies greater than the lowest usable frequency of the chamber in the case of the FGSDA. The performances of the FGSDA and the FFT accelerated Ewald summation technique are similar. At high frequencies, the FFT accelerated Ewald summation is advantageous since the frequency complexity of the algorithm is lower. In the low and mid frequency range, the FGSDA is preferable. Also, for reverberation chambers with large or multiple objects, the FGSDA is favorably as the hybrid Ewald-2D Spectral representation of the CGF is the cheaper, the greater the distance between observation and source point. In addition, the CGF BEMs were compared with other state-of-the-art methods for reverberation chamber modeling, namely the discrete singular convolution method of moments (DSC-MoM) [Zha11] and the adaptive integral method (AIM) accelerated CGF BEM [Yan14]. In all scenarios, the proposed approaches outperformed the other methods by often more than one order of magnitude with respect to computation time and memory consumption.

The Vivaldi antenna, the mode stirrer, and the car body were modeled as perfect electric conductors using the electric field integral equation (EFIE). To model imperfectly electrically conducting and dielectric objects, the CGF boundary integral (BI) formulation was coupled to an impedance boundary condition (IBC) and the finite element method (FEM), respectively. An electrically well conducting and a dielectric cuboid were considered to validate the FGSDA. The speed-up versus the MLFMM accelerated FGF BEM decreased since well conducting and dielectric objects involve electric and magnetic currents. Still, an acceleration of up to a factor of ten was achieved.

The CGF BEM is valid for ideal cavity walls only. Well but not perfectly conducting cavity walls are usually approximated by complexification of the wavenumber using the quality factor of the cavity. In this work, the CGF BEM with the complex wavenumber approximation was validated against the FGF BEM where in the latter one, an IBC was used to model the well conducting walls. Using the individual quality factor of a cavity mode, the complex wavenumber approximation agreed very well with the reference. When the composite quality factor was used, the agreement deteriorated in the range of the cavity resonances. While the introduced error plays a minor role in the over-moded range of a reverberation chamber since in this range a large number of modes contributes to the field, it becomes important in the transition range of the chamber where only a few modes or a single mode contribute to the field. How to integrate the individual quality factors of the cavity modes into the representations of the CGF is a possible topic for future research.

As the walls and the resonances of the cavity are modeled analytically in the CGF, the CGF BEM is more accurate than the FGF BEM. The CGF BEM complies better with the reciprocity condition and satisfies the power budget not only at low but also at high frequencies. However, both the CGF and the FGF BEM suffer from the discretization errors in the range of the cavity resonances. In practice, the accuracy gain due to the analytical modeling of the cavity walls and resonances plays a minor role as the major challenges are the accurate modeling of the quality factor and small geometrical details.

Last but not least, the accelerated CGF BEM was applied to reverberation chamber research. The number of independent stirrer positions was considered in the framework of linear algebra and a new dual speed rotation stirring mode was proposed and analyzed. It was shown that the number of independent stirrer positions is limited by the number of measurement points in the test volume and that the new stirring mode improves the chamber performance although the available test volume is not reduced as in the case of a second stirrer. In this application area of mode stirrer analysis, the CGF BEM is particularly advantageous: on the one hand, the number of unknowns is reduced by one to two orders of magnitude versus the FGF BEM as only the chamber with the stirrer and not the chamber with the stirrer and the device under test is analyzed; on the other hand, stirrer analysis is easy to parallelize as each position of the stirrer is independent from the others.

In future work, the quadratic complexity of the FGSDA could be addressed. The FGSDA can, in principle, be applied on-the-fly during the iterative solution of the matrix-vector equation. This would reduce the complexity from quadratic to linear. However, the large number of iterations would degrade the efficiency of the iterative FGSDA. A possible remedy is proposed in [Eib06]. In [Eib00], a FSDA for the Green's function of double infinite periodic structures was presented. In [Eib06], the approach was extended to a multilevel FSDA. Using the multilevel approach, less modes must be stored on fine levels to represent the corresponding Green's function and the cost per matrix-vector product is reduced significantly.

A. Theorems and Proofs

A.1. Lorenz Gauge Condition

In the following, it is shown that the different representations of the CGF satisfy the Lorenz gauge condition. The Green's function of the rectangular cavity for the magnetic vector potential satisfies the Lorenz gauge

$$\nabla \cdot \boldsymbol{A} + \mathrm{j}\omega\mu\varepsilon\phi = 0 \tag{A.1}$$

if the equation

$$\nabla \cdot \overline{\boldsymbol{G}}^{\mathrm{A}} = -\mu\varepsilon\nabla' G^{\phi} \tag{A.2}$$

is fulfilled where ∇' denotes the nabla operator with respect to $\boldsymbol{r}'$, G^{ϕ} is the Green's function of the electric scalar potential [Mic90], and the dependence from observation and source point is suppressed for brevity. To prove that we start from the left-hand side of the Lorenz gauge

$$\begin{aligned}\nabla \cdot \boldsymbol{A} + \mathrm{j}\omega\mu\varepsilon\phi &= \nabla \cdot \iiint_V \overline{\boldsymbol{G}}^{\mathrm{A}} \cdot \boldsymbol{J}\,\mathrm{d}v' + \mathrm{j}\omega\mu\varepsilon \iiint_V G^{\phi}\rho\,\mathrm{d}v' ,\\ &= \iiint_V \left(\nabla \cdot \overline{\boldsymbol{G}}^{\mathrm{A}}\right) \cdot \boldsymbol{J}\,\mathrm{d}v' + \mathrm{j}\omega\mu\varepsilon \iiint_V G^{\phi}\rho\,\mathrm{d}v' .\end{aligned} \tag{A.3}$$

Using (A.2), the above equation becomes

$$= -\varepsilon\mu \iiint_V \nabla' G^{\phi} \cdot \boldsymbol{J}\,\mathrm{d}v' + \mathrm{j}\omega\mu\varepsilon \iiint_V G^{\phi}\rho\,\mathrm{d}v' . \tag{A.4}$$

Applying the divergence theorem [Råd04] to the first term gives

$$\begin{aligned}&= -\varepsilon\mu \left[\oiint_{\partial V} G^{\phi}\boldsymbol{J} \cdot \mathrm{d}\boldsymbol{a}' - \iiint_V G^{\phi}\nabla' \cdot \boldsymbol{J}\,\mathrm{d}v' \right]\\ &\quad + \mathrm{j}\omega\mu\varepsilon \iiint_V G^{\phi}\rho\,\mathrm{d}v',\\ &= -\varepsilon\mu \oiint_{\partial V} G^{\phi}\boldsymbol{J} \cdot \mathrm{d}\boldsymbol{a}' + \varepsilon\mu \iiint_V G^{\phi}\left(\nabla' \cdot \boldsymbol{J} + \mathrm{j}\omega\rho\right)\mathrm{d}v'\\ &= 0\end{aligned} \tag{A.5}$$

since $\boldsymbol{J}$ is orthogonal to $\mathrm{d}\boldsymbol{a}'$ on ∂V and $\nabla \cdot \boldsymbol{J} + \mathrm{j}\omega\rho = 0$ (continuity equation).

Now, (A.2) is shown for the spatial and the spectral representation of the CGF. The proofs for the 2D spectral and the Ewald representation are omitted as they are analogous to the spatial and the spectral representation. The divergence of the spatial representation of the CGF for the magnetic vector potential is

$$\nabla \cdot \overline{\boldsymbol{G}}^{\mathrm{A}}_{\mathrm{spat}}\left(\boldsymbol{r},\boldsymbol{r}'\right) = \mu \sum_{m,n,p=-\infty}^{\infty} \sum_{q=0}^{7} \nabla \cdot \left(\frac{\mathrm{e}^{-\mathrm{j}kr_{mnp,q}}}{4\pi r_{mnp,q}} \sum_i A_{i,q}\, \hat{x}_i \hat{x}_i \right),$$

$$= \mu \sum_{m,n,p=-\infty}^{\infty} \sum_{q=0}^{7} \frac{\mathrm{e}^{-\mathrm{j}kr_{mnp,q}}}{4\pi r_{mnp,q}} \left(-\frac{1}{r_{mnp,q}} - \mathrm{j}k \right) \Big[A_{x,q}\left(x_q - 2ma\right)\hat{x}$$

$$+ A_{y,q}\left(y_q - 2nb\right)\hat{y} + A_{z,q}\left(z_q - 2pc\right)\hat{z} \Big] . \quad \text{(A.6)}$$

The spatial representation of the CGF for the electric scalar potential reads

$$G^{\Phi}_{\mathrm{spat}}\left(\boldsymbol{r},\boldsymbol{r}'\right) = \frac{1}{\varepsilon} \sum_{m,n,p=-\infty}^{\infty} \sum_{q=0}^{7} \frac{\mathrm{e}^{-\mathrm{j}kr_{mnp,q}}}{4\pi r_{mnp,q}} A_q \quad \text{(A.7)}$$

where $A_q = 1$ for $q = 0,2,4,6$, $A_q = 0$ for $q = 1,3,5,7$ and $r_{mnp,q}$ is defined as in Chapter 3. Applying the gradient with respect to $\boldsymbol{r}'$ and multiplying (A.7) with $-\mu\varepsilon$ yields

$$-\mu\varepsilon\nabla' G^{\Phi}_{\mathrm{spat}}\left(\boldsymbol{r},\boldsymbol{r}'\right) = \mu \sum_{m,n,p=-\infty}^{\infty} \sum_{q=0}^{7} \frac{\mathrm{e}^{-\mathrm{j}kr_{mnp,q}}}{4\pi r_{mnp,q}} \left(-\frac{1}{r_{mnp,q}} - \mathrm{j}k \right)$$

$$\cdot \left[-\frac{\partial x_q}{\partial x'} A_q\left(x_q - 2ma\right)\hat{x} - \frac{\partial y_q}{\partial y'} A_q\left(y_q - 2nb\right)\hat{y} - \frac{\partial z_q}{\partial z'} A_q\left(z_q - 2pc\right)\hat{z} \right] . \quad \text{(A.8)}$$

Evaluating the partial derivatives of x_q, y_q, and z_q with respect to x', y', and z' by means of Table 3.1 gives (A.6).

The divergence of the spectral representation of the CGF for the magnetic vector potential is

$$\nabla \cdot \overline{\boldsymbol{G}}^{\mathrm{A}}_{\mathrm{spec}}\left(\boldsymbol{r},\boldsymbol{r}'\right) = \mu \sum_{m,n,p=0}^{\infty} \frac{1}{k^2_{xyz} - k^2} \nabla \cdot \sum_i \phi_{i,mnp}\left(\boldsymbol{r}\right) \phi_{i,mnp}\left(\boldsymbol{r}'\right) \hat{x}_i \hat{x}_i$$

$$= -\mu \sum_{m,n,p=0}^{\infty} \frac{1}{k^2_{xyz} - k^2} \sum_i k_i \phi_{mnp}\left(\boldsymbol{r}\right) \phi_{i,mnp}\left(\boldsymbol{r}'\right) \hat{x}_i \quad \text{(A.9)}$$

where

$$\phi_{mnp}\left(\boldsymbol{r}\right) = \sqrt{\frac{\tau_m \tau_n \tau_p}{abc}} \sin(k_x x)\, \sin(k_y y)\, \sin(k_z z) . \quad \text{(A.10)}$$

The spectral representation of the CGF for the electric scalar potential reads

$$G^{\Phi}_{\mathrm{spec}}\left(\boldsymbol{r},\boldsymbol{r}'\right) = \frac{1}{\varepsilon}\sum_{m,n,p=0}^{\infty}\frac{1}{k_{xyz}^2 - k^2}\phi_{mnp}\left(\boldsymbol{r}\right)\phi_{mnp}\left(\boldsymbol{r}'\right)\,. \tag{A.11}$$

Applying the gradient with respect to $\boldsymbol{r}'$ and multiplying (A.11) with $-\mu\varepsilon$ gives

$$-\mu\varepsilon\nabla' G^{\Phi}_{\mathrm{spec}}\left(\boldsymbol{r},\boldsymbol{r}'\right) = -\mu\sum_{m,n,p=0}^{\infty}\frac{1}{k_{xyz}^2 - k^2}\sum_{i}k_i\phi_{mnp}\left(\boldsymbol{r}\right)\phi_{i,mnp}\left(\boldsymbol{r}'\right)\hat{x}_i \tag{A.12}$$

which is equal to (A.9).

A.2. Spectral Series of the Ewald Summation Technique

For the derivation of the Ewald summation technique (cf. Section 3.4) and the FFT accelerated Ewald summation technique (cf. Section 5.1), the identity

$$\sum_{m,n,p=0}^{\infty}H_{mnp}\,\phi_{i,mnp}\left(\boldsymbol{r}\right)\phi_{i,mnp}\left(\boldsymbol{r}'\right) = \frac{1}{8}\sum_{m,n,p=-\infty}^{\infty}H_{mnp}\sum_{q=0}^{7}A_{q,i}\mathrm{e}^{\mathrm{j}\left(k_x x_q + k_y y + k_z z_q\right)} \tag{A.13}$$

is necessary. In the following, (A.13) is shown for the x-component. Inserting (2.33a), the x-component of the left-hand side of (A.13) is given by

$$\begin{aligned}\sum_{m,n,p=0}^{\infty}H_{mnp}\,\phi_{x,mnp}\left(\boldsymbol{r}\right)\phi_{x,mnp}\left(\boldsymbol{r}'\right) &= \sum_{m,n,p=0}^{\infty}H_{mnp}\frac{\tau_m\tau_n\tau_p}{abc}\\ &\quad\cdot\cos(k_x x)\cos(k_x x')\sin(k_y y)\sin(k_y y')\sin(k_z z)\sin(k_z z')\,.\end{aligned} \tag{A.14}$$

Using the exponential form of the sine and cosine function, it becomes

$$\begin{aligned}&= \sum_{m,n,p=0}^{\infty}H_{mnp}\frac{\tau_m\tau_n\tau_p}{64abc}\\ &\quad\cdot\left[+\mathrm{e}^{\mathrm{j}k_x(x+x')} + \mathrm{e}^{\mathrm{j}k_x(x-x')} + \mathrm{e}^{-\mathrm{j}k_x(x-x')} + \mathrm{e}^{-\mathrm{j}k_x(x+x')}\right]\\ &\quad\cdot\left[-\mathrm{e}^{\mathrm{j}k_y(y+y')} + \mathrm{e}^{\mathrm{j}k_y(y-y')} + \mathrm{e}^{-\mathrm{j}k_y(y-y')} - \mathrm{e}^{-\mathrm{j}k_y(y+y')}\right]\\ &\quad\cdot\left[-\mathrm{e}^{\mathrm{j}k_z(z+z')} + \mathrm{e}^{\mathrm{j}k_z(z-z')} + \mathrm{e}^{-\mathrm{j}k_z(z-z')} - \mathrm{e}^{-\mathrm{j}k_z(z+z')}\right].\end{aligned} \tag{A.15}$$

Observing that $H_{mnp} = H_{-m-n-p}$ and $\sum_{m=0}^{\infty} \tau_m \left(\mathrm{e}^{\mathrm{j}mx} + \mathrm{e}^{-\mathrm{j}mx}\right) = 2\sum_{m=-\infty}^{\infty} \mathrm{e}^{\mathrm{j}mx}$ reduces (A.15) to

$$= \frac{1}{8abc} \sum_{m,n,p=-\infty}^{\infty} H_{mnp} \left[\mathrm{e}^{\mathrm{j}k_x(x+x')} + \mathrm{e}^{\mathrm{j}k_x(x-x')}\right] \cdot \left[-\mathrm{e}^{\mathrm{j}k_y(y+y')} + \mathrm{e}^{\mathrm{j}k_y(y-y')}\right] \left[-\mathrm{e}^{\mathrm{j}k_z(z+z')} + \mathrm{e}^{\mathrm{j}k_z(z-z')}\right]. \quad \text{(A.16)}$$

Expanding the braces and using the relations from Tab. 3.1 yields

$$\begin{aligned} = \frac{1}{8abc} \sum_{m,n,p=-\infty}^{\infty} H_{mnp} \Big[& \mathrm{e}^{\mathrm{j}k_x(x+x')}\mathrm{e}^{\mathrm{j}k_y(y+y')}\mathrm{e}^{\mathrm{j}k_z(z+z')} \\ & - \mathrm{e}^{\mathrm{j}k_x(x+x')}\mathrm{e}^{\mathrm{j}k_y(y+y')}\mathrm{e}^{\mathrm{j}k_z(z-z')} - \mathrm{e}^{\mathrm{j}k_x(x+x')}\mathrm{e}^{\mathrm{j}k_y(y-y')}\mathrm{e}^{\mathrm{j}k_z(z+z')} \\ & + \mathrm{e}^{\mathrm{j}k_x(x+x')}\mathrm{e}^{\mathrm{j}k_y(y-y')}\mathrm{e}^{\mathrm{j}k_z(z-z')} + \mathrm{e}^{\mathrm{j}k_x(x-x')}\mathrm{e}^{\mathrm{j}k_y(y+y')}\mathrm{e}^{\mathrm{j}k_z(z+z')} \\ & - \mathrm{e}^{\mathrm{j}k_x(x-x')}\mathrm{e}^{\mathrm{j}k_y(y+y')}\mathrm{e}^{\mathrm{j}k_z(z-z')} - \mathrm{e}^{\mathrm{j}k_x(x-x')}\mathrm{e}^{\mathrm{j}k_y(y-y')}\mathrm{e}^{\mathrm{j}k_z(z+z')} \\ & + \mathrm{e}^{\mathrm{j}k_x(x-x')}\mathrm{e}^{\mathrm{j}k_y(y-y')}\mathrm{e}^{\mathrm{j}k_z(z-z')}\Big], \end{aligned} \quad \text{(A.17)}$$

$$= \frac{1}{8abc} \sum_{q=0}^{7} A_{q,x} \sum_{m,n,p=-\infty}^{\infty} H_{mnp}\, \mathrm{e}^{\mathrm{j}k_x x_q}\mathrm{e}^{\mathrm{j}k_y y_q}\mathrm{e}^{\mathrm{j}k_z z_q}. \quad \text{(A.18)}$$

The other components of (A.13) are shown in the same manner.

A.3. 2D Spectral Representation

In the derivation of the FGSDA, the functions $\xi_{i,mn}(\boldsymbol{r}_>)$ and $\xi_{i,mn}(\boldsymbol{r}_<)$ of the z-2D spectral representation are shifted to the center of the corresponding group to avoid numerical overflow errors and preserve the factorizability of the individual terms with respect to observation and source point.

In the following, it is shown that the shifted z-2D spectral representations in (4.17) are numerically stable, i.e., the shifted functions $\xi''_{i,mn}(\boldsymbol{r}_>)$ and $\xi''_{i,mn}(\boldsymbol{r}_<)$ are bounded for large α_{mn} and the product of the translation function and H_{mn} is bounded for large α_{mn}. The magnitudes of the shifted functions $\xi''_{i,mn}(\boldsymbol{r}_>)$ satisfy

$$\begin{aligned} \left|\xi''_{i,mn}(\boldsymbol{r}_>)\right| &= \left|\mathrm{e}^{-\alpha_{mn}(c-z_{\mathrm{c},>})}\, \xi_{i,mn}(\boldsymbol{r}_>)\right| \\ &\leq C\,\mathrm{e}^{-\alpha_{mn}(c-z_{\mathrm{c},>})}\left|\mathrm{e}^{\alpha_{mn}(c-z_>)} \pm \mathrm{e}^{-\alpha_{mn}(c-z_>)}\right| \\ &\leq C\left[\mathrm{e}^{-\alpha_{mn}(z_>-z_{\mathrm{c},>})} + \mathrm{e}^{-\alpha_{mn}(2c-z_>-z_{\mathrm{c},>})}\right] \end{aligned} \quad \text{(A.19)}$$

where the exponential notations of hyperbolic sine and hyperbolic cosine have been used and C is a real-valued constant. The first term in (A.19) is bounded: The distance between $z_>$ and $z_{\mathrm{c},>}$ is smaller than the group height c_g. As the z-2D spectral representation is used for far-interactions only, there is at least one group between test and source group. Because of this one group distance, $c_\mathrm{g} < \Delta z = \left|z - z'\right|$ and the relation

$$\mathrm{e}^{-\alpha_{mn}\left(z_> - z_{\mathrm{c},>}\right)} < \mathrm{e}^{-\alpha_{mn}\left|z_> - z_{\mathrm{c},>}\right|} < \mathrm{e}^{\alpha_{mn} c_\mathrm{g}} < \mathrm{e}^{\alpha_{mn}\Delta z} \tag{A.20}$$

holds. According to (3.11),

$$\alpha_{mn} = \sqrt{k_x^2 + k_y^2 - k^2} < \sqrt{k_0^2 - k^2} = -\frac{\ln \Delta}{\Delta z} \tag{A.21}$$

for an accuracy δ of the z-2D spectral representation. Inserting (A.21) into (A.20) shows

$$\mathrm{e}^{-\alpha_{mn}\left(z_> - z_{\mathrm{c},>}\right)} < \exp\left(-\frac{\ln \delta}{\Delta z}\Delta z\right) = \exp\left(\ln \frac{1}{\delta}\right) = \frac{1}{\delta}\,. \tag{A.22}$$

The second term in (A.19) is also bounded since $2c - z_> - z_\mathrm{c} > 0$.

The boundedness of the shifted functions $\xi''_{i,mn}\left(\boldsymbol{r}_<\right)$ is shown in a similar manner. Again using the exponential notation of hyperbolic and sine hyperbolic cosine, the magnitudes of the shifted functions $\xi''_{i,mn}\left(\boldsymbol{r}_<\right)$ satisfy

$$\begin{aligned}\left|\xi''_{i,mn}\left(\boldsymbol{r}_<\right)\right| &= \left|\mathrm{e}^{-\alpha_{mn} z_{\mathrm{c},<}}\, \xi_{i,mn}\left(\boldsymbol{r}_>\right)\right| \\ &< C\mathrm{e}^{-\alpha_{mn} z_{\mathrm{c},<}} \left|\left(\mathrm{e}^{\alpha_{mn} z_<} \pm \mathrm{e}^{-\alpha_{mn} z_<}\right)\right| \\ &= C\left|\mathrm{e}^{-\alpha_{mn}\left(z_{\mathrm{c},<} - z_<\right)} + \mathrm{e}^{-\alpha_{mn}\left(z_< + z_{\mathrm{c},<}\right)}\right|. \end{aligned} \tag{A.23}$$

As the distance between $z_{\mathrm{c},<}$ and $z_<$ is smaller than c_g, the first term in (A.23) is bounded by the aforementioned arguments. The second term is also bounded since $z_< + z_{\mathrm{c},<} > 0$.

The product of translation function and H_{mn} is given by

$$T_{mn} H_{mn} = \frac{\mathrm{e}^{-\alpha_{mn}\left(z_{\mathrm{c},>} - z_{\mathrm{c},<} - c\right)}}{\alpha_{mn} \sinh\left(\alpha_{mn} c\right)} < \frac{\mathrm{e}^{\alpha_{mn}\left(z_{\mathrm{c},>} - z_{\mathrm{c},<} - c\right)}}{\sinh\left(\alpha_{mn} c\right)} \tag{A.24}$$

for large α_{mn}. Writing the hyperbolic sine in exponential notation and expanding the fraction by $\mathrm{e}^{-\alpha_{mn} c}$ gives

$$T_{mn} H_{mn} < \frac{\mathrm{e}^{-\alpha_{mn}\left(z_{\mathrm{c},>} - z_{\mathrm{c},<}\right)}}{1 - \mathrm{e}^{-2\alpha_{mn} c}}\,. \tag{A.25}$$

In the asymptotic limit the denominator goes to one and the nominator goes to zero as $z_{\mathrm{c},>} - z_{\mathrm{c},<} > 0$. Therefore, the product of translation function and H_{mn} is bounded.

A.4. Dyadic Analysis

In this section, some expressions which are required in Appendix B are derived. Let $\overline{\boldsymbol{A}} = A_{xx}\hat{x}\hat{x} + A_{yy}\hat{y}\hat{y} + A_{zz}\hat{z}\hat{z} = \sum_{i=1}^{3} A_{ii}\hat{x}_i\hat{x}_i$ be a dyadic field, δ_{ij} is the Kronecker symbol, and ϵ_{ijk} be the Levi-Civita symbol [Its07]. Then, the curl of the dyadic field $\overline{\boldsymbol{A}}$ is given by

$$\begin{aligned}\nabla \times \overline{\boldsymbol{A}} &= \sum_{i=1}^{3} \frac{\partial}{\partial x_i}\hat{x}_i \times \left(\sum_{j=1}^{3} A_{jj}\hat{x}_j\hat{x}_j\right) = \sum_{i,j=1}^{3} \frac{\partial}{\partial x_i} A_{jj}\left(\hat{x}_i \times \hat{x}_j\right)\hat{x}_j\,, \\ &= \sum_{i,j,k=1}^{3} \epsilon_{ijk}\frac{\partial}{\partial x_j} A_{kk}\hat{x}_i\hat{x}_k\,. \end{aligned} \tag{A.26}$$

The gradient of the divergence of the dyadic field is

$$\begin{aligned}\nabla\nabla \cdot \overline{\boldsymbol{A}} &= \sum_{i=1}^{3} \frac{\partial}{\partial x_i}\hat{x}_i \left[\sum_{j=1}^{3} \frac{\partial}{\partial x_j}\hat{x}_j \cdot \left(\sum_{k=1}^{3} A_{kk}\hat{x}_k\hat{x}_k\right)\right], \\ &= \sum_{i,j,k=1}^{3} \frac{\partial}{\partial x_i}\frac{\partial}{\partial x_j} A_{kk}\left[\hat{x}_i\left(\hat{x}_j \cdot \hat{x}_k\right)\right]\hat{x}_k\,, \\ &= \sum_{i,j,k=1}^{3} \frac{\partial}{\partial x_i}\frac{\partial}{\partial x_j}\delta_{jk} A_{kk}\hat{x}_i\hat{x}_k\,, \\ &= \sum_{i,j=1}^{3} \frac{\partial}{\partial x_i}\frac{\partial}{\partial x_j} A_{jj}\hat{x}_i\hat{x}_j\,. \end{aligned} \tag{A.27}$$

B. Representations of the Rectangular Cavity Green's Functions for the Magnetic Vector Potential and the Derivatives

In Chapter 3, the different representations of the rectangular cavity Green's function for the magnetic vector potential are derived and analyzed. As the Green's function for the electric vector potential and the curl and the gradient of the divergence of the Green's functions are also needed to evaluate the interaction integrals in Chapter 2, they are introduced in the following.

B.1. Spatial Representation

The spatial representation of the Green's function of the rectangular cavity for the electric vector potential is given by

$$\overline{G}^{\mathrm{F}}_{\mathrm{spat}}\left(\boldsymbol{r},\boldsymbol{r}'\right) = \varepsilon \sum_{m,n,p=-\infty}^{\infty} \sum_{q=0}^{7} \frac{\mathrm{e}^{-\mathrm{j}kr_{mnp,q}}}{4\pi r_{mnp,q}} \left(F_{x,q}\,\hat{x}\hat{x} + F_{y,q}\,\hat{y}\hat{y} + F_{z,q}\,\hat{z}\hat{z}\right) \tag{B.1}$$

where $r_{mnp,q}$ is the distance between the observation point and the source or an image current as defined in Chapter 3. The coefficients $F_{x,q}$, $F_{y,q}$, and $F_{z,q}$ correspond to the relative orientation of the magnetic source and its immediate images and are given in Table B.1.

Using (A.26), the curl of the Green's function of the rectangular cavity for the mag-

q	$F_{x,q}$	$F_{y,q}$	$F_{z,q}$
0	+1	+1	+1
1	−1	+1	+1
2	−1	−1	+1
3	+1	−1	+1
4	+1	+1	−1
5	−1	+1	−1
6	−1	−1	−1
7	+1	−1	−1

Tab. B.1.: Coefficients $F_{x,q}$, $F_{y,q}$, and $F_{z,q}$.

netic vector potential is

$$\nabla \times \overline{G}^{\mathrm{A}}_{\mathrm{spat}}\left(\boldsymbol{r},\boldsymbol{r}'\right) = \mu \sum_{m,n,p=0}^{\infty} \sum_{i,j,k=1}^{3} \epsilon_{ijk} \frac{\partial G_0}{\partial r_{mnp,q}} \frac{\partial r_{mnp,q}}{\partial x_j} A_{k,q}\, \hat{x}_i \hat{x}_k \tag{B.2}$$

and the curl of the CGF for the electric vector potential becomes

$$\nabla \times \overline{G}^{\mathrm{F}}_{\mathrm{spat}}\left(\boldsymbol{r},\boldsymbol{r}'\right) = \varepsilon \sum_{m,n,p=0}^{\infty} \sum_{i,j,k=1}^{3} \epsilon_{ijk} \frac{\partial G_0}{\partial r_{mnp,q}} \frac{\partial r_{mnp,q}}{\partial x_j} F_{k,q}\, \hat{x}_i \hat{x}_k \tag{B.3}$$

where

$$G_0 = \frac{\mathrm{e}^{-\mathrm{j}kr_{mnp,q}}}{4\pi r_{mnp,q}} \tag{B.4}$$

and the partial derivative of G_0 with respect to $r_{mnp,q}$ is

$$\frac{\partial G_0}{\partial r_{mnp,q}} = \left(-\frac{1}{r_{mnp,q}} - \mathrm{j}k\right) G_0\,. \tag{B.5}$$

The partial derivatives of $r_{mnp,q}$ with respect to x, y, and z are trivial and are for brevity not given herein.

Using (A.27), the gradient of the divergence of the CGF for the magnetic vector potential is

$$\nabla\nabla \cdot \overline{G}^{\mathrm{A}}_{\mathrm{spat}}\left(\boldsymbol{r},\boldsymbol{r}'\right) = \mu \sum_{m,n,p=0}^{\infty} \sum_{q=0}^{7} \sum_{i,j=1}^{3} \left(\frac{\partial^2 G_0}{\partial r_{mnp,q}^2} \frac{\partial r_{mnp,q}}{\partial x_i} \frac{\partial r_{mnp,q}}{\partial x_j} + \frac{\partial G_0}{\partial r_{mnp,q}} \frac{\partial r_{mnp,q}^2}{\partial x_i \partial x_j} \right) A_{j,q}\, \hat{x}_i \hat{x}_j \tag{B.6}$$

and the gradient of the divergence of the CGF for the electric vector potential becomes

$$\nabla\nabla \cdot \overline{G}^{\mathrm{F}}_{\mathrm{spat}}\left(\boldsymbol{r},\boldsymbol{r}'\right) = \varepsilon \sum_{m,n,p=0}^{\infty} \sum_{q=0}^{7} \sum_{i,j=1}^{3} \left(\frac{\partial^2 G_0}{\partial r_{mnp,q}^2} \frac{\partial r_{mnp,q}}{\partial x_i} \frac{\partial r_{mnp,q}}{\partial x_j} + \frac{\partial G_0}{\partial r_{mnp,q}} \frac{\partial r_{mnp,q}^2}{\partial x_i \partial x_j} \right) F_{j,q}\, \hat{x}_i \hat{x}_j \tag{B.7}$$

where the second derivative of G_0 with respect to $r_{mnp,q}$ is

$$\frac{\partial^2 G_0}{\partial r_{mnp,q}^2} = \left(\frac{2}{r^2} + \frac{2\mathrm{j}k}{r} - k^2\right) G_0\,. \tag{B.8}$$

B.2. Spectral Representation

The spectral representation of the Green's function of the rectangular cavity for the electric vector potential is derived as

$$\overline{G}^{\mathrm{F}}_{\mathrm{spec}}\left(\boldsymbol{r},\boldsymbol{r}'\right) = \varepsilon \sum_{m,n,p=0}^{\infty} \frac{1}{k_{xyz}^2 - k^2} \Big(\psi_{x,mnp}\left(\boldsymbol{r}\right) \psi_{x,mnp}\left(\boldsymbol{r}'\right) \hat{x}\hat{x} + \psi_{y,mnp}\left(\boldsymbol{r}\right) \psi_{y,mnp}\left(\boldsymbol{r}'\right) \hat{y}\hat{y} + \psi_{z,mnp}\left(\boldsymbol{r}\right) \psi_{z,mnp}\left(\boldsymbol{r}'\right) \hat{z}\hat{z} \Big) \tag{B.9}$$

where k_{xyz}^2 is defined as in Chapter 3 and $\psi_{x,mnp}\left(\boldsymbol{r}\right)$, $\psi_{y,mnp}\left(\boldsymbol{r}\right)$, and $\psi_{z,mnp}\left(\boldsymbol{r}\right)$ are the eigenfunctions of the electric vector potential as given in Section 2.2.

Using (A.26), the curl of the Green's function of the rectangular cavity for the magnetic vector potential becomes

$$\nabla \times \overline{G}^{\mathrm{A}}_{\mathrm{spec}}\left(\boldsymbol{r},\boldsymbol{r}'\right) = \mu \sum_{m,n,p=0}^{\infty} \frac{1}{k_{xyz}^2 - k^2} \cdot \sum_{i,j,k=1}^{3} \epsilon_{ijk} k_j \psi_{i,mnp}\left(\boldsymbol{r}\right) \phi_{k,mnp}\left(\boldsymbol{r}'\right) \hat{x}_i \hat{x}_k \,. \tag{B.10}$$

Analogously, the curl of the CGF for the electric vector potential is

$$\nabla \times \overline{G}^{\mathrm{F}}_{\mathrm{spec}}\left(\boldsymbol{r},\boldsymbol{r}'\right) = -\varepsilon \sum_{m,n,p=0}^{\infty} \frac{1}{k_{xyz}^2 - k^2} \cdot \sum_{i,j,k=1}^{3} \epsilon_{ijk} k_j \phi_{i,mnp}\left(\boldsymbol{r}\right) \psi_{k,mnp}\left(\boldsymbol{r}'\right) \hat{x}_i \hat{x}_k \tag{B.11}$$

Using (A.27), the gradient of the divergence of the CGF for the magnetic vector potential is

$$\nabla\nabla \cdot \overline{G}^{\mathrm{A}}_{\mathrm{spec}}\left(\boldsymbol{r},\boldsymbol{r}'\right) = -\mu \sum_{m,n,p=0}^{\infty} \frac{1}{k_{xyz}^2 - k^2} \cdot \sum_{i,j=1}^{3} \frac{k_i k_j}{k^2} \phi_{i,mnp}\left(\boldsymbol{r}\right) \phi_{j,mnp}\left(\boldsymbol{r}'\right) \hat{x}_i \hat{x}_j \tag{B.12}$$

and the gradient of the divergence of the CGF for the electric vector potential becomes

$$\nabla\nabla\cdot\overline{G}^{\mathrm{F}}_{\mathrm{spec}}\left(\boldsymbol{r},\boldsymbol{r}'\right)=-\varepsilon\sum_{m,n,p=0}^{\infty}\frac{1}{k_{xyz}^2-k^2}\cdot\sum_{i,j=1}^{3}\frac{k_ik_j}{k^2}\psi_{i,mnp}\left(\boldsymbol{r}\right)\psi_{j,mnp}\left(\boldsymbol{r}'\right)\hat{x}_i\hat{x}_j\,. \tag{B.13}$$

B.3. 2D Spectral Representation

The z-2D spectral representation of the Green's function of the rectangular cavity for the electric vector potential is derived as

$$\overline{G}^{\mathrm{F}}_{\text{z-2D}}\left(\boldsymbol{r},\boldsymbol{r}'\right)=\varepsilon\sum_{m,n=0}^{\infty}H_{mn}\left[\chi_{x,mn}\left(\boldsymbol{r}_>\right)\chi_{x,mn}\left(\boldsymbol{r}_<\right)\hat{x}\hat{x}+\chi_{y,mn}\left(\boldsymbol{r}_>\right)\chi_{y,mn}\left(\boldsymbol{r}_<\right)\hat{y}\hat{y}+\chi_{z,mn}\left(\boldsymbol{r}_>\right)\chi_{z,mn}\left(\boldsymbol{r}_<\right)\hat{z}\hat{z}\right] \tag{B.14}$$

where

$$\chi_{x,mn}\left(\boldsymbol{r}\right)=\sqrt{\frac{\tau_m\tau_n}{ab}}\sin\left(k_xx\right)\cos\left(k_yy\right)\cosh\left(\alpha_{mn}z\right), \tag{B.15a}$$

$$\chi_{y,mn}\left(\boldsymbol{r}\right)=\sqrt{\frac{\tau_m\tau_n}{ab}}\cos\left(k_xx\right)\sin\left(k_yy\right)\cosh\left(\alpha_{mn}z\right), \tag{B.15b}$$

$$\chi_{z,mn}\left(\boldsymbol{r}\right)=\sqrt{\frac{\tau_m\tau_n}{ab}}\cos\left(k_xx\right)\cos\left(k_yy\right)\sinh\left(\alpha_{mn}z\right), \tag{B.15c}$$

and $\boldsymbol{r}_>$, $\boldsymbol{r}_<$, τ_m, τ_n, α_{mn}, and H_{mn} are defined as in Chapter 3.

Using (A.26), the curl of the Green's function of the rectangular cavity for the magnetic vector potential becomes

$$\nabla\times\overline{G}^{\mathrm{A}}_{\text{z-2D}}\left(\boldsymbol{r},\boldsymbol{r}'\right)=\mu\sum_{m,n=0}^{\infty}\sum_{i,j,k=1}^{3}\epsilon_{ijk}H^{\nabla\times}_{mn,ij}\hat{x}_i\hat{x}_k\cdot\begin{cases}\chi_{i,mn}\left(x,y,c-z\right)\xi_{k,mn}\left(x',y',z'\right), & \text{if } z\geq z',\\ \chi_{i,mn}\left(x,y,z\right)\xi_{k,mn}\left(x',y',c-z'\right), & \text{if } z<z'\end{cases} \tag{B.16}$$

and the curl of the CGF for the electric vector potential is

$$\nabla \times \overline{G}^{\mathrm{F}}_{\text{z-2D}}\left(\boldsymbol{r},\boldsymbol{r}'\right) = -\varepsilon \sum_{m,n=0}^{\infty} \sum_{i,j,k=1}^{3} \epsilon_{ijk} H^{\nabla\times}_{mn,ij} \hat{x}_i \hat{x}_k \cdot \begin{cases} \xi_{i,mn}\left(x,y,c-z\right) \chi_{k,mn}\left(x',y',z'\right), & \text{if } z \geq z', \\ \xi_{i,mn}\left(x,y,z\right) \chi_{k,mn}\left(x',y',c-z'\right), & \text{if } z < z' \end{cases} \tag{B.17}$$

where

$$\boldsymbol{H}^{\nabla\times}_{mn} = H_{mn} \begin{pmatrix} 0 & -\sigma_{zz'}\alpha_{mn} & k_y \\ \sigma_{zz'}\alpha_{mn} & 0 & -k_x \\ -k_y & k_x & 0 \end{pmatrix} \tag{B.18}$$

and $\sigma_{zz'} = 1$ if $z \geq z'$ and $\sigma_{zz'} = -1$ if $z < z'$.

Using (A.27), the gradient of the divergence of the CGF for the magnetic vector potential is

$$\nabla\nabla\cdot \overline{G}^{\mathrm{A}}_{\text{z-2D}}\left(\boldsymbol{r},\boldsymbol{r}'\right) = -\frac{\mu}{k^2} \sum_{m,n=0}^{\infty} \sum_{i,j=1}^{3} H^{\nabla\nabla\cdot}_{mn,ij}\, \xi_{i,mn}\left(\boldsymbol{r}_>\right) \xi_{j,mn}\left(\boldsymbol{r}_<\right) \hat{x}_i \hat{x}_j \tag{B.19}$$

and the gradient of the divergence of the CGF for the electric vector potential becomes

$$\nabla\nabla\cdot \overline{G}^{\mathrm{F}}_{\text{z-2D}}\left(\boldsymbol{r},\boldsymbol{r}'\right) = -\frac{\varepsilon}{k^2} \sum_{m,n=0}^{\infty} \sum_{i,j=1}^{3} H^{\nabla\nabla\cdot}_{mn,ij}\, \chi_{i,mn}\left(\boldsymbol{r}_>\right) \chi_{j,mn}\left(\boldsymbol{r}_<\right) \hat{x}_i \hat{x}_j \tag{B.20}$$

where

$$\boldsymbol{H}^{\nabla\nabla\cdot}_{mn} = H_{mn} \begin{pmatrix} k_x^2 & k_x k_y & k_x \sigma_{zz'}\alpha_{mn} \\ k_x k_y & k_y^2 & k_y \sigma_{zz'}\alpha_{mn} \\ -k_x \sigma_{zz'}\alpha_{mn} & -k_y \sigma_{zz'}\alpha_{mn} & -k_x^2 + k_y^2 \end{pmatrix}. \tag{B.21}$$

B.4. Ewald Representation

The Ewald representations of the Green's function of the rectangular cavity for the electric vector potential and the derivatives of the Green's functions are derived using the results from Section B.1 and B.2. The spatial parts of the Ewald representations have the same form as (B.1) – (B.3), (B.6), and (B.7), respectively, except that G_0 is replaced by

$$G_{\text{Ew-0}} = \frac{\mathrm{Re}\left\{ \mathrm{e}^{\mathrm{j}kr_{mnp,q}} \operatorname{erfc}\left(r_{mnp,q}E + \mathrm{j}\frac{k}{2E}\right)\right\}}{4\pi r_{mnp,q}}. \tag{B.22}$$

Introducing $f = e^{+\mathrm{j}kr_{mnp,q}}\,\mathrm{erfc}\left(r_{mnp,q}E + \mathrm{j}\frac{k}{2E}\right)$ and $g = \mathrm{e}^{-r_{mnp,q}^2E^2+\frac{k^2}{4E^2}}$, the first and the second derivative of $G_{\text{Ew-0}}$ with respect to $r_{mnp,q}$ are derived as

$$\begin{aligned}\frac{\partial G_{\text{Ew-0}}}{\partial r_{mnp,q}} &= -\frac{\mathrm{Re}\left\{f\right\}}{4\pi r_{mnp,q}^2} + \frac{1}{4\pi r_{mnp,q}}\,\mathrm{Re}\left\{\frac{\partial f}{\partial r_{mnp,q}}\right\}\\ &= -\frac{\mathrm{Re}\left\{f\right\}}{4\pi r_{mnp,q}^2} + \frac{\mathrm{Re}\left\{\mathrm{j}kf\right\}}{4\pi r_{mnp,q}} - \frac{\mathrm{Re}\left\{g\right\}}{4\pi r_{mnp,q}}\,\frac{2E}{\sqrt{\pi}}\end{aligned} \tag{B.23}$$

$$\begin{aligned}\frac{\partial^2 G_{\text{Ew-0}}}{\partial r_{mnp,q}^2} &= \frac{2\,\mathrm{Re}\left\{f\right\}}{4\pi r_{mnp,q}^3} - \frac{2}{4\pi r_{mnp,q}^2}\,\mathrm{Re}\left\{\frac{\partial f}{\partial r_{mnp,q}}\right\} + \frac{1}{4\pi r_{mnp,q}}\,\mathrm{Re}\left\{\frac{\partial^2 f}{\partial r_{mnp,q}^2}\right\}\\ &= \frac{\mathrm{Re}\left\{f\right\}}{4\pi r_{mnp,q}^3} - \frac{2\,\mathrm{Re}\left\{\mathrm{j}kf\right\}}{4\pi r_{mnp,q}^2} + \frac{4E\,\mathrm{Re}\left\{g\right\}}{4\pi r_{mnp,q}^2\sqrt{\pi}} - \frac{\mathrm{Re}\left\{k^2 f\right\}}{4\pi r_{mnp,q}}\\ &\quad - \frac{2E\,\mathrm{Re}\left\{\mathrm{j}kg\right\}}{4\pi r_{mnp,q}\sqrt{\pi}} + \frac{4E^3\,\mathrm{Re}\left\{g\right\}}{4\pi\sqrt{\pi}}\end{aligned} \tag{B.24}$$

The spectral parts of the Ewald representations have the same form as (B.9) – (B.13), respectively except that $1/(k_{xyz}^2 - k^2)$ is replaced by H_{mnp}.

C. Simulation Parameters

The simulation parameters of the CGF BEM algorithms and the MLFMM algorithm are listed in Table C.1 and C.2, respectively.

Parameter	Value	
	FGSDA	FFT
Cavity Green's function		
Accuracy of cavity Green's function	10^{-4}	10^{-4}
CPU time ratio of 2D-spectral and Ewald representation	4	
Lagrange polynomial order		4
Sampling density of Q-array		$\lambda/15$
GMRES		
Residual GMRES	10^{-4}	10^{-4}

Tab. C.1.: Simulation parameters of the FGSDA and the FFT algorithm.

Parameter	Value
MLFMM	
Group size	$\lambda/4$
Number of spherical harmonics	4
Accuracy d_0 of Green's function series	3
Lagrange polynomial order	12
GMRES	
Solver	Flexible GMRES-IO with 2 inner loops
Preconditioner 1st inner loop	Full system matrix (MLFMM)
Preconditioner 2nd inner loop	Full near-zone matrix (non-MLFMM contributions)
Preconditioner on top of everything	Gauss-Seidel
Number of iterations in the 1st inner loop	120
Residual	10^{-4}

Tab. C.2.: Simulation parameters of the MLFMM algorithm.

Bibliography

[Abr70] M. Abramowitz and I. Stegun. *Handbook of Mathematical Functions*. Dover books on mathematics. New York: Dover Publications, 1970 (cit. on pp. 38, 56).

[Ada14] A. Adardour, G. Andrieu, and A. Reineix. "On the low-frequency optimization of reverberation chambers". In: *IEEE Transactions on Electromagnetic Compatibility* 56.2 (2014), pp. 266–275 (cit. on p. 2).

[And10] F. P. Andriulli, A. Tabacco, and G. Vecchi. "Solving the EFIE at low frequencies with a conditioning that grows only logarithmically with the number of unknowns". In: *IEEE Transactions on Antennas and Propagation* 58.5 (2010), pp. 1614–1624 (cit. on p. 87).

[Arn06] L. R. Arnaut. "Effect of size, orientation, and eccentricity of mode stirrers on their performance in reverberation chambers". In: *IEEE Transactions on Electromagnetic Compatibility* 48.3 (2006), pp. 600–602 (cit. on pp. 1, 100).

[Arn98] L. R. Arnaut and P. D. West. "Evaluation of the NPL untuned stadium reverberation chamber using mechanical and electronic stirring techniques". In: *NPL, CEM 11* (1998) (cit. on p. 1).

[Bia09] P. F. Biagi, L. Castellana, T. Maggipinto, G. Maggipinto, T. Ligonzo, L. Schiavulli, D. Loiacono, A. Ermini, M. Lasalvia, G. Perna, and V. Capozzi. "A reverberation chamber to investigate the possible effects of in vivo exposure of rats to 1.8 GHz electromagnetic fields: a preliminary study". In: *Progress In Electromagnetics Research* 94 (2009), pp. 133–152 (cit. on p. 1).

[Bor04] A. Borji and S. Safavi-Naeini. "Rapid calculation of the Green's function in a rectangular enclosure with application to conductor loaded cavity resonators". In: *IEEE Transactions on Microwave Theory and Techniques* 52.7 (2004), pp. 1724–1731 (cit. on p. 4).

[Bos12] G. Bosco, C. Picciani, V. M. Primiani, and F. Moglie. "Numerical and experimental analysis of the performance of a reduced surface stirrer for reverberation chambers". In: *IEEE International Symposium on Electromagnetic Compatibility - EMC*. Pittsburgh, USA, 2012, pp. 156–161 (cit. on pp. 1, 100).

[Bou14] Y. Boubendir and C. Turc. *Well-conditioned boundary integral equation formulations for the solution of high-frequency electromagnetic scattering problems*. 2014. URL: `http://arxiv.org/abs/1310.1406` (cit. on p. 87).

[Bru05] C. Bruns and R. Vahldieck. “A closer look at reverberation chambers – 3-D simulation and experimental verification”. In: *IEEE Transactions on Electromagnetic Compatibility* 47.3 (2005), pp. 612–626 (cit. on pp. 3, 91).

[Bun01] C. F. Bunting. “Shielding effectiveness in a reverberation chamber using finite element techniques”. In: *IEEE International Symposium on Electromagnetic Compatibility - EMC*. Montreal, Canada, 2001, pp. 740–745 (cit. on p. 3).

[Bun02] C. F. Bunting. “Statistical characterization and the simulation of a reverberation chamber using finite-element techniques”. In: *IEEE Transactions on Electromagnetic Compatibility* 44.1 (2002), pp. 214–221 (cit. on p. 3).

[Bun03] C. F. Bunting. “Shielding effectiveness in a two-dimensional reverberation chamber using finite-element techniques”. In: *IEEE Transactions on Electromagnetic Compatibility* 45.3 (2003), pp. 548–552 (cit. on p. 3).

[Bun99] C. F. Bunting, K. J. Moeller, C. J. Reddy, and S. A. Scearce. “A two dimensional finite-element analysis of reverberation chambers”. In: *IEEE Transactions on Electromagnetic Compatibility* 41.4 (1999), pp. 280–289 (cit. on p. 2).

[Cap07] F. Capolino, D. Wilton, and W. Johnson. “Efficient computation of the 3D Green’s function for the Helmholtz operator for a linear array of point sources using the Ewald method”. In: *Journal of Computational Physics* 223.1 (2007), pp. 250–261 (cit. on pp. 5, 40).

[Car05] U. Carlberg, P.-S. Kildal, and J. Carlsson. “Study of antennas in reverberation chamber using method of moments with cavity Green’s function calculated by Ewald summation”. In: *IEEE Transactions on Electromagnetic Compatibility* 47.4 (2005), pp. 805–814 (cit. on pp. 4, 5, 37, 38, 42).

[Car06] U. Carlberg, P.-S. Kildal, and A. A. Kishk. “Fast numerical model of reverberation chambers with metal stirrers using moment method and cavity Green’s function calculated by Ewald summation”. In: *IEEE Antennas and Propagation Society International Symposium*. Albuquerque, USA, 2006, pp. 2827–2830 (cit. on pp. 4, 5).

[Car09] U. Carlberg, P.-S. Kildal, and J. Carlsson. “Numerical study of position stirring and frequency stirring in a loaded reverberation chamber”. In: *IEEE Transactions on Electromagnetic Compatibility* 51.1 (2009), pp. 12–17 (cit. on pp. 4, 5).

[Cas08] C. Castelnovo, R. Moessner, and S. L. Sondhi. “Magnetic monopoles in spin ice”. In: *Nature* 451.7174 (2008), pp. 42–45 (cit. on p. 7).

[Cer05] G. Cerri, V. M. Primiani, S. Pennesi, and P. Russo. “Source stirring mode for reverberation chambers”. In: *IEEE Transactions on Electromagnetic Compatibility* 47.4 (2005), pp. 815–823 (cit. on p. 1).

[Cer09] G. Cerri, V. M. Primiani, C. Monteverde, and P. Russo. “A theoretical feasibility study of a source stirring reverberation chamber”. In: *IEEE Transactions on Electromagnetic Compatibility* 51.1 (2009), pp. 3–11 (cit. on p. 1).

[Che01] W. C. Chew. *Fast and Efficient Algorithms in Computational Electromagnetics*. Boston: Artech House, 2001 (cit. on pp. 3, 22).

[Che12] X. Chen. “On independent platform sample number for reverberation chamber measurements”. In: *IEEE Transactions on Electromagnetic Compatibility* 54.6 (2012), pp. 1306–1309 (cit. on p. 1).

[Chr95] C. Christopoulos. *The Transmission-Line Modeling Method: TLM*. New York: Inst. of Electrical and Electronics Engineers, 1995 (cit. on p. 2).

[Cle05] J. Clegg, A. Marvin, J. Dawson, and S. Porter. “Optimization of stirrer designs in a reverberation chamber”. In: *IEEE Transactions on Electromagnetic Compatibility* 47.4 (2005), pp. 824–832 (cit. on pp. 1, 2, 100, 103).

[Coa07] A. Coates, H. G. Sasse, D. E. Coleby, A. P. Duffy, and A. Orlandi. “Validation of a three-dimensional transmission line matrix (TLM) model implementation of a mode-stirred reverberation chamber”. In: *IEEE Transactions on Electromagnetic Compatibility* 49.4 (2007), pp. 734–744 (cit. on p. 2).

[Col91] R. E. Collin. *Field Theory of Guided Waves*. 2nd ed. New York: IEEE Press, 1991 (cit. on p. 31).

[Con99] J. H. Conway and Sloane, N. J. A. *Sphere Packings, Lattices, and Groups*. 3rd ed. New York: Springer, 1999 (cit. on p. 98).

[Cor80] P. Corona, G. Latmiral, and E. Paolini. “Performance and analysis of a reverberating enclosure with variable geometry”. In: *IEEE Transactions on Electromagnetic Compatibility* 22.1 (1980), pp. 2–5 (cit. on p. 1).

[Cra86] M. L. Crawford and G. H. Koepke. *Design, evaluation, and use of a reverberation chamber for performing electromagnetic susceptibility/vulnerability measurements*. National Bureau of Standards, 1986 (cit. on p. 1).

[Cra88] M. L. Crawford and J. M. Ladbury. “Mode-stirred chamber for measuring shielding effectiveness of cables and connectors: an assessment of MIL-STD-1344A method 3008”. In: *IEEE International Symposium on Electromagnetic Compatibility - EMC*. Seattle, USA, 1988, pp. 30–36 (cit. on p. 1).

[Dar93] T. Darden, D. York, and L. Pedersen. “Particle mesh Ewald: An N log N method for Ewald sums in large systems”. In: *The Journal of chemical physics* 98.12 (1993), pp. 10089–10092 (cit. on p. 5).

[Des98] M. Deserno and C. Holm. “How to mesh up Ewald sums. I. A theoretical and numerical comparison of various particle mesh routines”. In: *The Journal of chemical physics* 109.18 (1998), pp. 7678–7693 (cit. on pp. 5, 6).

[Dun90] J. M. Dunn. “Local, high-frequency analysis of the fields in a mode-stirred chamber”. In: *IEEE Transactions on Electromagnetic Compatibility* 32.1 (1990), pp. 53–58 (cit. on p. 16).

[Eib00] T. Eibert and J. Volakis. “Fast spectral domain algorithm for hybrid finite element/boundary integral modelling of doubly periodic structures”. In: *IEE Proceedings - Microwaves, Antennas and Propagation* 147.5 (2000), pp. 329–334 (cit. on pp. 5, 108).

[Eib03] T. F. Eibert, Y. E. Erdemli, and J. L. Volakis. “Hybrid finite element-fast spectral domain multilayer boundary integral modeling of doubly periodic structures”. In: *IEEE Transactions on Antennas and Propagation* 51.9 (2003), pp. 2517–2520 (cit. on p. 5).

[Eib05] T. Eibert. “A diagonalized multilevel fast multipole method with spherical harmonics expansion of the k-space integrals”. In: *IEEE Transactions on Antennas and Propagation* 53.2 (2005), pp. 814–817 (cit. on pp. 63, 67).

[Eib06] T. F. Eibert. “A multilevel fast spectral domain algorithm for electromagnetic analysis of infinite periodic arrays with large unit cells”. In: *Advances in Radio Science* 4 (2006), pp. 41–47 (cit. on p. 108).

[Eib07] T. F. Eibert. “Some scattering results computed by surface-integral-equation and hybrid finite-element-boundary-integral techniques, accelerated by the multilevel fast multipole method”. In: *IEEE Antennas and Propagation Magazine* 49.2 (2007), pp. 61–69 (cit. on p. 87).

[Eib96] T. Eibert and V. Hansen. “Calculation of unbounded field problems in free space by a 3D FEM/BEM-hybrid approach”. In: *Journal of Electromagnetic Waves and Applications* 10.1 (1996), pp. 61–78 (cit. on p. 23).

[Eib98] T. F. Eibert and J. L. Volakis. “Fast spectral domain algorithm for rapid solution of integral equations”. In: *Electronics Letters* 34.13 (1998), pp. 1297–1299 (cit. on p. 5).

[Eib99] T. Eibert, J. Volakis, D. Wilton, and D. Jackson. “Hybrid FE/BI modeling of 3-D doubly periodic structures utilizing triangular prismatic elements and an MPIE formulation accelerated by the Ewald transformation”. In: *IEEE Transactions on Antennas and Propagation* 47.5 (1999), pp. 843–850 (cit. on p. 23).

[Esp13] G. Esposito, G. Gradoni, F. Moglie, and V. Mariani Primiani. “Stirrer performance of reverberation chambers evaluated by time domain fidelity”. In: *IEEE International Symposium on Electromagnetic Compatibility - EMC*. Denver, USA, Aug. 2013, pp. 207–212 (cit. on p. 1).

[Ess95] U. Essmann, L. Perera, M. L. Berkowitz, T. Darden, H. Lee, and L. G. Pedersen. “A smooth particle mesh Ewald method”. In: *The Journal of chemical physics* 103.19 (1995), pp. 8577–8593 (cit. on p. 5).

[Ewa21] P. P. Ewald. “Die Berechnung optischer und elektrostatischer Gitterpotentiale”. In: *Annalen der Physik* 369.3 (1921), pp. 253–287 (cit. on pp. 4, 5, 35, 36).

[Fic12] L. O. Fichte, K. Grutza, and M. Stiemer. “Feldexpositionsmessungen an biologischem Gewebe unter Nutzung von Modenverwirblungskammern”. In: *Kleinheubacher Tagung*. Miltenberg, Germany, Sept. 2012 (cit. on p. 1).

[Fou96] B. Foulonneau, F. Gaudaire, and Y. Gabillet. “Measurement method of electromagnetic transmission loss of building components using two reverberation chambers”. In: *Electronics Letters* 32.23 (1996), pp. 2130–2131 (cit. on p. 1).

[Gra12] G. Gradoni, V. M. Primiani, and F. Moglie. “Reverberation chamber as a statistical relaxation process: Entropy analysis and fast time domain simulations”. In: *IEEE International Symposium on Electromagnetic Compatibility - EMC Europe*. Rome, Italy, 2012, pp. 1–6 (cit. on p. 1).

[Gro03] F. Gronwald. “Method of moment analysis of a dipole antenna within a rectangular cavity”. In: *IEEE International Symposium on Electromagnetic Compatibility - EMC*. Vol. 2. 2003, pp. 1144–1147 (cit. on pp. 4, 5).

[Gro05] F. Gronwald. “Calculation of mutual antenna coupling within rectangular enclosures”. In: *IEEE Transactions on Electromagnetic Compatibility* 47.4 (2005), pp. 1021–1025 (cit. on pp. 4, 5, 37, 38, 72).

[Ham70] M. Hamid and W. Johnson. “Ray-optical solution for the dyadic Green’s function in a rectangular cavity”. In: *Electronics Letters* 6.10 (1970), pp. 317–319 (cit. on p. 27).

[Hea93] O. Heaviside. *Electromagnetic Theory*. London: Printing and Publishing Company, 1893 (cit. on p. 7).

[Her88] H. Hertz. *Untersuchungen über die Ausbreitung der elektrischen Kraft*. 2. Aufl., Unveränd. Neudr. der Ausg. Leipzig, Barth, 1894. Vol. / von Heinrich Hertz ; Bd. 2. Gesammelte Werke. Vaduz: Sändig-Reprint-Verl, 1988 (cit. on p. 7).

[Hil09] D. A. Hill. *Electromagnetic Fields in Cavities: Deterministic and Statistical Theories*. Hoboken: Wiley and IEEE Press, 2009 (cit. on pp. 1, 15, 99).

[Hil94] D. A. Hill. “Electronic mode stirring for reverberation chambers”. In: *IEEE Transactions on Electromagnetic Compatibility* 36.4 (1994), pp. 294–299 (cit. on pp. 1, 14).

[Hol03] C. L. Holloway, D. A. Hill, J. Ladbury, G. Koepke, and R. Garzia. “Shielding effectiveness measurements of materials using nested reverberation chambers”. In: *IEEE Transactions on Electromagnetic Compatibility* 45.2 (2003), pp. 350–356 (cit. on p. 1).

[Hol06] C. L. Holloway, D. A. Hill, J. M. Ladbury, and G. Koepke. "Requirements for an effective reverberation chamber: unloaded or loaded". In: *IEEE Transactions on Electromagnetic Compatibility* 48.1 (2006), pp. 187–194 (cit. on pp. 1, 2).

[Hol08] C. L. Holloway, D. A. Hill, M. Sandroni, J. M. Ladbury, J. Coder, G. Koepke, A. C. Marvin, and Yuhui H. "Use of reverberation chambers to determine the shielding effectiveness of physically small, electrically large enclosures and cavities". In: *IEEE Transactions on Electromagnetic Compatibility* 50.4 (2008), pp. 770–782 (cit. on p. 1).

[Hua06] Y. Huang, N. Abumustafa, Q. Wang, and X. Zhu. "Comparison of two stirrer designs for a new reverberation chamber". In: *The 4th Asia-Pacific Conference on Environmental Electromagnetics*. Dalian, 2006, pp. 450–453 (cit. on pp. 1, 100).

[Hua92a] Y. Huang and D. J. Edwards. "A novel reverberating chamber: the source-stirred chamber". In: *Eighth International Conference on Electromagnetic Compatibility*. Edinburgh, UK, Sept. 1992, pp. 120–124 (cit. on p. 1).

[Hua92b] Y. Huang and D. J. Edwards. "An investigation of electromagnetic field inside a moving wall mode-stirred chamber". In: *Eighth International Conference on Electromagnetic Compatibility*. Edinburgh, UK, Sept. 1992, pp. 115–119 (cit. on p. 1).

[Hua99a] Y. Huang. "Asymmetric reverberation chambers for EMC measurements". In: *International Conference and Exhibition on Electromagnetic Compatibility - EMC York*. York, UK, 1999, pp. 65–69 (cit. on p. 1).

[Hua99b] Y. Huang. "Conducting triangular chambers for EMC measurements". In: *Measurement Science and Technology* 10.3 (1999), pp. L21–L24 (cit. on p. 1).

[IEC11] IEC 61000-4-21. *Electromagnetic Compatibility (EMC) - Part 4-21: Testing and Measurement Techniques - Reverberation Chamber Test Methods*. Geneva, 2011 (cit. on pp. 1, 2, 64, 66, 91, 93, 94, 97, 100–104).

[Ism08] Ismatullah and T. Eibert. "Adaptive singularity cancellation for efficient treatment of near-singular and near-hypersingular integrals in surface integral equation formulations". In: *IEEE Transactions on Antennas and Propagation* 56.1 (2008), pp. 274–278 (cit. on p. 50).

[Ism09] Ismatullah and T. Eibert. "Surface integral equation solutions by hierarchical vector basis functions and spherical harmonics based multilevel fast multipole method". In: *IEEE Transactions on Antennas and Propagation* 57.7 (2009), pp. 2084–2093 (cit. on pp. 24, 26, 72).

[Its07] M. Itskov. *Tensor Algebra and Tensor Analysis for Engineers*. Berlin and New York: Springer, 2007 (cit. on p. 114).

[Jac99] J. D. Jackson. *Classical Electrodynamics*. 3rd ed. New York and Chichester: Wiley, 1999 (cit. on pp. 15, 16, 19).

[Jak14] U. Jakobus, R. G. Marchand, and D. J. Ludick. "Aspects of and insights into the rigorous validation, verification, and testing processes for a commercial electromagnetic field solver package". In: *IEEE Transactions on Electromagnetic Compatibility* 56.4 (2014), pp. 759–770 (cit. on p. 75).

[Jin02] J.-M. Jin. *The Finite Element Method in Electromagnetics*. 2nd ed. Hoboken: Wiley, 2002 (cit. on p. 2).

[Jin10] J.-M. Jin. *Theory and Computation of Electromagnetic Fields*. Hoboken: IEEE Press, 2010 (cit. on pp. 2, 3, 7–9, 14, 19, 20, 23, 26, 50, 52, 86).

[Jor86] K. E. Jordan, G. R. Richter, and P. Sheng. "An efficient numerical evaluation of the Green's function for the Helmholtz operator on periodic structures". In: *Journal of Computational Physics* 63.1 (1986), pp. 222–235 (cit. on pp. 35, 40).

[Jun08] K. B. Jung, T. H. Kim, J. L. Kim, H. J. Doh, Y. C. Chung, J. H. Choi, and J. K. Pack. "Development and validation of reverberation-chamber type whole-body exposure system for mobile-phone frequency". In: *Electromagnetic biology and medicine* 27.1 (2008), pp. 73–82 (cit. on p. 1).

[Kar06] K. Karlsson, J. Carlsson, and P.-S. Kildal. "Reverberation chamber for antenna measurements: modeling using method of moments, spectral domain techniques, and asymptote extraction". In: *IEEE Transactions on Antennas and Propagation* 54.11 (2006), pp. 3106–3113 (cit. on p. 4).

[Kha05] M. A. Khayat and D. R. Wilton. "Numerical evaluation of singular and near-singular potential Integrals". In: *IEEE Transactions on Antennas and Propagation* 53.10 (2005), pp. 3180–3190 (cit. on p. 50).

[Kil02a] P.-S. Kildal, C. Carlsson, and J. Yang. "Measurement of free-space impedances of small antennas in reverberation chambers". In: *Microwave and Optical Technology Letters* 32.2 (2002), pp. 112–115 (cit. on p. 1).

[Kil02b] P.-S. Kildal, K. Rosengren, J. Byun, and J. Lee. "Definition of effective diversity gain and how to measure it in a reverberation chamber". In: *Microwave and Optical Technology Letters* 34.1 (2002), pp. 56–59 (cit. on p. 1).

[Kil04] P.-S. Kildal and K. Rosengren. "Correlation and capacity of MIMO systems and mutual coupling, radiation efficiency, and diversity gain of their antennas: simulations and measurements in a reverberation chamber". In: *IEEE Communications Magazine* 42.12 (2004), pp. 104–112 (cit. on p. 1).

[Kra05] H. G. Krauthäuser, T. Winzerling, J. Nitsch, N. Eulig, and A. Enders. "Statistical interpretation of autocorrelation coefficients for fields in mode-stirred chambers". In: *IEEE International Symposium on Electromagnetic Compatibility - EMC*. Chicago, USA, 2005, pp. 550–555 (cit. on p. 1).

[Kra07] H. G. Krauthäuser. "Grundlagen und Anwendungen von Modenverwirbelungskammern". Habilitation. Magdeburg: Otto-von-Guericke-Universität Magdeburg, 2007 (cit. on p. 97).

[Lae04] E. Laermans, L. Knockaert, and D. de Zutter. "Two-dimensional method of moments modelling of lossless overmoded transverse magnetic cavities". In: *Journal of Computational Physics* 198.1 (2004), pp. 326–348 (cit. on p. 4).

[Leu03a] P. Leuchtmann, C. Bruns, and R. Vahldieck. "Broadband method of moment simulation and measurement of a medium-sized reverberation chamber". In: *International Symposium on Electromagnetic Compatibility - EMC*. Boston, USA, 2003, pp. 844–849 (cit. on pp. 3, 91).

[Leu03b] P. Leuchtmann, C. Bruns, and R. Vahldieck. "On the validation of simulated fields in a reverberation chamber". In: *33rd European Microwave Conference*. Munich, Germany, 2003, pp. 1035–1038 (cit. on p. 3).

[Li14] L. Li, K. Wang, and T. F. Eibert. "A projection height independent adaptive radial-angular-R^2 transformation for singular integrals". In: *IEEE Transactions on Antennas and Propagation* 62.10 (2014), pp. 5381–5386 (cit. on p. 50).

[Liu83] B.-H. Liu, D. C. Chang, and M. T. Ma. "Eigenmodes and the composite quality factor of a reverberating chamber". In: *National Bureau of Standards Technical Note* 1066 (1983) (cit. on pp. 13, 16).

[Lou95] T. A. Loughry and S. H. Gurbaxani. "The effects of intrinsic test fixture isolation on material shielding effectiveness measurements using nested mode-stirred chambers". In: *IEEE Transactions on Electromagnetic Compatibility* 37.3 (1995), pp. 449–452 (cit. on p. 1).

[Lun10] O. Lunden, N. Wellander, and M. Backstrom. "Stirrer blade separation experiment in reverberation chambers". In: *IEEE International Symposium on Electromagnetic Compatibility - EMC*. Fort Lauderdale, USA, 2010, pp. 526–529 (cit. on pp. 1, 100).

[Mad04] K. Madsen, P. Hallbjorner, and C. Orlenius. "Models for the number of independent samples in reverberation chamber measurements with mechanical, frequency, and combined stirring". In: *IEEE Antennas and Wireless Propagation Letters* 3.1 (2004), pp. 48–51 (cit. on p. 1).

[Mar13] A. C. Marvin, G. Esposito, J. F. Dawson, I. D. Flintoft, L. Dawson, J. A. K. Everard, and G. C. R. Melia. "A wide-band hybrid antenna for use in reverberation chambers". In: *IEEE International Symposium on Electromagnetic Compatibility - EMC*. Denver, USA, Aug. 2013, pp. 222–226 (cit. on p. 64).

[Max65] J. C. Maxwell. “A Dynamical Theory of the Electromagnetic Field”. In: *Philosophical Transactions of the Royal Society of London* 155 (1865), pp. 459–512 (cit. on p. 7).

[Med85] L. Medgyesi-Mitschang and J. Putnam. “Integral equation formulations for imperfectly conducting scatterers”. In: *IEEE Transactions on Antennas and Propagation* 33.2 (1985), pp. 206–214 (cit. on p. 23).

[Mic14] K. A. Michalski and A. A. Kucharski. “On the surface limit in the boundary integral equations of electromagnetics”. In: *IEEE Transactions on Antennas and Propagation* 62.1 (2014), pp. 257–263 (cit. on p. 21).

[Mic90] K. A. Michalski and D. Zheng. “Electromagnetic scattering and radiation by surfaces of arbitrary shape in layered media. I. Theory”. In: *IEEE Transactions on Antennas and Propagation* 38.3 (1990), pp. 335–344 (cit. on p. 109).

[Mog04] F. Moglie. “Convergence of the reverberation chambers to the equilibrium analyzed with the finite-difference time-domain algorithm”. In: *IEEE Transactions on Electromagnetic Compatibility* 46.3 (2004), pp. 469–476 (cit. on p. 2).

[Mog10] F. Moglie and V. M. Primiani. “Evaluation of uncorrelation and statistics inside a reverberation chamber in presence of two independent stirrers”. In: *IEEE International Symposium on Electromagnetic Compatibility - EMC*. Fort Lauderdale, USA, 2010, pp. 515–519 (cit. on pp. 1, 97, 100).

[Mog11] F. Moglie and V. M. Primiani. “Analysis of the independent positions of reverberation chamber stirrers as a function of their operating conditions”. In: *IEEE Transactions on Electromagnetic Compatibility* 53.2 (2011), pp. 288–295 (cit. on pp. 1, 97, 100).

[Mog12] F. Moglie and V. M. Primiani. “Numerical analysis of a new location for the working volume inside a reverberation chamber”. In: *IEEE Transactions on Electromagnetic Compatibility* 54.2 (2012), pp. 238–245 (cit. on pp. 1, 100).

[Mon08] C. Monteverde, G. H. Koepke, C. L. Holloway, J. M. Ladbury, D. A. Hill, V. M. Primiani, and P. Russo. “Source stirring technique for reverberation chambers; experimental investigation”. In: *International Symposium on Electromagnetic Compatibility - EMC Europe*. Hamburg, Germany, 2008, pp. 1–6 (cit. on p. 1).

[Mor53] P. Morse and H. Feshbach. *Methods of Theoretical Physics*. New York: McGraw-Hill, 1953 (cit. on pp. 11, 27, 29).

[Mül57] C. Müller. *Grundprobleme der mathematischen Theorie elektromagnetischer Schwingungen*. Berlin: Springer, 1957 (cit. on p. 8).

[Orj06] G. Orjubin, F. Petit, E. Richalot, S. Mengue, and O. Picon. “Cavity losses modeling using lossless FDTD method”. In: *IEEE Transactions on Electromagnetic Compatibility* 48.2 (2006), pp. 429–431 (cit. on p. 2).

[Par98] M.-J. Park, J. Park, and S. Nam. “Efficient calculation of the Green’s function for the rectangular cavity”. In: *IEEE Microwave and Guided Wave Letters* 8.3 (1998), pp. 124–126 (cit. on pp. 4, 37, 38).

[Pet98] A. F. Peterson, S. L. Ray, and R. Mittra. *Computational Methods for Electromagnetics*. New York and Oxford: IEEE Press and Oxford University Press, 1998 (cit. on p. 2).

[Pfe12] S. Pfennig and H. G. Krauthäuser. “A general method for determining the number of independent stirrer positions in reverberation chambers”. In: *IEEE International Symposium on Electromagnetic Compatibility - EMC Europe*. Rome, Italy, 2012, pp. 1–6 (cit. on pp. 1, 91, 93, 95, 97, 99, 101, 103).

[Pfe13] S. Pfennig and H. G. Krauthäuser. “Comparison of methods for determining the number of independent stirrer positions in reverberation chambers”. In: *IEEE International Symposium on Electromagnetic Compatibility - EMC Europe*. Brugge, Belgium, 2013, pp. 431–436 (cit. on pp. 1, 97, 101).

[Pfe14] S. Pfennig, H. G. Krauthäuser, F. Moglie, and V. M. Primiani. “A continued evaluation of the general method for determining the number of independent stirrer positions in reverberation chambers”. In: *IEEE International Symposium on Electromagnetic Compatibility - EMC Europe*. Gothenburg, Sweden, Sept. 2014, pp. 257–262 (cit. on pp. 1, 97, 101).

[Pfe15] S. Pfennig. “Charakterisierung der Modenverwirbelungskammer der TU Dresden und Untersuchung von Verfahren zur Bestimmung der unabhängigen Rüh- rerstellungen”. Doktorarbeit. Technische Universität Dresden, Apr. 2015 (cit. on pp. 92–94).

[Pre92] W. H. Press. *Numerical recipes in C*. 2nd ed., v2.0. Cambridge England and New York N.Y: Cambridge University Press, 1992 (cit. on p. 60).

[Pri14] V. M. Primiani and F. Moglie. “Reverberation chamber performance varying the position of the stirrer rotation axis”. In: *IEEE Transactions on Electromagnetic Compatibility* 56.2 (2014), pp. 486–489 (cit. on pp. 1, 100).

[Pul06] W. J. Pullan and H. H. Hoos. “Dynamic local search for the maximum clique problem.” In: *Journal of Artificial Intelligence Research* 25 (2006), pp. 159–185 (cit. on pp. 97, 99, 103).

[Råd04] L. Råde and B. Westergren. *Mathematics Handbook for Science and Engineering*. 5th ed. Berlin and New York: Springer, 2004 (cit. on pp. 18, 27, 33, 37, 98, 109).

[Rao82] S. Rao, D. Wilton, and A. Glisson. "Electromagnetic scattering by surfaces of arbitrary shape". In: *IEEE Transactions on Antennas and Propagation* 30.3 (1982), pp. 409–418 (cit. on p. 24).

[Rau12] C. Raum, L. O. Fichte, M. Stiemer, and U. Kaiser. "Numerische Berechnung transienter elektromagnetischer Felder in dreidimensionalen Hohlraumresonatoren mit variabler Geometrie". In: *Kleinheubacher Tagung*. Miltenberg, Germany, Sept. 2012 (cit. on p. 3).

[Ros00] K. Rosengren, P.-S. Kildal, J. Carlsson, and O. Lunden. "A new method to measure radiation efficiency of terminal antennas". In: *IEEE Conference on Antennas and Propagation for Wireless Communications - APS*. Waltham, USA, 2000, pp. 5–8 (cit. on p. 1).

[Ros01] K. Rosengren, P.-S. Kildal, C. Carlsson, and J. Carlsson. "Characterization of antennas for mobile and wireless terminals in reverberation chambers: Improved accuracy by platform stirring". In: *Microwave and Optical Technology Letters* 30.6 (2001), pp. 391–397 (cit. on p. 1).

[Ros05] K. Rosengren and P.-S. Kildal. "Radiation efficiency, correlation, diversity gain and capacity of a six-monopole antenna array for a MIMO system: theory, simulation and measurement in reverberation chamber". In: *IEE Proceedings - Microwaves, Antennas and Propagation* 152.1 (2005), pp. 7–16 (cit. on p. 1).

[Saa93] Y. Saad. "A flexible inner-outer preconditioned GMRES algorithm". In: *SIAM Journal on Scientific Computing* 14.2 (1993), pp. 461–469 (cit. on pp. 63, 87).

[Sen95] T. B. Senior and J. L. Volakis. *Approximate Boundary Conditions in Electromagnetics*. London: Institution of Electrical Engineers, 1995 (cit. on p. 23).

[Sil49] S. Silver. *Microwave Antenna Theory and Design*. Vol. 12. M.I.T. Radiation Laboratory Series. New York: McGraw-Hill, 1949 (cit. on p. 8).

[Slo12] Sloane, N. J. A. *Tables of spherical codes*. 2012. URL: `http://neilsloane.com/packings/` (cit. on pp. 98, 99).

[Son97] J. Song, Cai-Cheng L., and Weng C. C. "Multilevel fast multipole algorithm for electromagnetic scattering by large complex objects". In: *IEEE Transactions on Antennas and Propagation* 45.10 (1997), pp. 1488–1493 (cit. on p. 24).

[Str07] G. Strang. *Computational Science and Engineering*. Wellesley and MA: Wellesley-Cambridge Press, 2007 (cit. on p. 56).

[Str92] J. Strain. "Fast potential theory. II. Layer potentials and discrete sums". In: *Journal of Computational Physics* 99.2 (1992), pp. 251–270 (cit. on p. 5).

[Taf95] A. Taflove. *Computational Electrodynamics: The Finite Difference Time Domain Method*. Boston: Artech House, 1995 (cit. on p. 2).

[Tai76] C.-T. Tai and P. Rozenfeld. “Different representations of dyadic Green’s functions for a rectangular cavity”. In: *IEEE Transactions on Microwave Theory and Techniques* 24.9 (1976), pp. 597–601 (cit. on pp. 5, 30, 31).

[Val07] G. Valerio, P. Baccarelli, P. Burghignoli, and A. Galli. “Comparative analysis of acceleration techniques for 2-D and 3-D Green’s functions in periodic structures along one and two directions”. In: *IEEE Transactions on Antennas and Propagation* 55.6 (2007), pp. 1630–1643 (cit. on p. 35).

[Wan04] Y. J. Wang, W. J. Koh, and C. K. Lee. “Coupling cross section and shielding effectiveness measurements on a coaxial cable by both mode-tuned reverberation chamber and GTEM cell methodologies”. In: *Progress In Electromagnetics Research* 47 (2004), pp. 61–73 (cit. on p. 1).

[Wel07] N. Wellander, O. Lundn, and M. Bäckström. “Experimental investigation and mathematical modeling of design parameters for efficient stirrers in mode stirred reverberation chambers”. In: *IEEE Transactions on Electromagnetic Compatibility* 49.1 (2007), pp. 94–103 (cit. on pp. 1, 2, 65, 100).

[Wu89] D. Wu and D. Chang. “The effect of an electrically large stirrer in a mode-stirred chamber”. In: *IEEE Transactions on Electromagnetic Compatibility* 31.2 (1989), pp. 164–169 (cit. on p. 1).

[Yan14] K. Yang and A. E. Yilmaz. “An FFT-accelerated integral-equation solver for analyzing scattering in rectangular cavities”. In: *IEEE Transactions on Microwave Theory and Techniques* 62.9 (2014), pp. 1930–1942 (cit. on pp. 4, 63, 66, 67, 69, 107).

[Ylä13] P. Ylä-Oijala, S. P. Kiminki, J. Markkanen, and S. Jarvenpaa. “Error controllable and well-conditioned MoM solutions in computational electromagnetics: Ultimate surface integral-equation formulation”. In: *IEEE Antennas and Propagation Magazine* 55.6 (2013), pp. 310–331 (cit. on pp. 21, 23).

[Zha11] H. Zhao and Z. Shen. “Efficient modeling of three-dimensional reverberation chambers using hybrid discrete singular convolution method of moments”. In: *IEEE Transactions on Antennas and Propagation* 59.8 (2011), pp. 2943–2953 (cit. on pp. 3, 63, 66, 67, 107).

[Zha12a] H. Zhao, E. Li, and Z. Shen. “Modeling of reverberation chamber using FMM-Accelerated hybrid integral equation”. In: *IEEE Asia-Pacific Conference on Antennas and Propagation (APCAP)*. Singapore, Singapore, 2012, pp. 213–214 (cit. on p. 3).

[Zha12b] H. Zhao and Z. Shen. “Memory efficient modeling of reverberation chambers using hybrid recursive update discrete singular convolution method of moments”. In: *IEEE Transactions on Antennas and Propagation* 60.6 (2012), pp. 2781–2789 (cit. on p. 3).

[Zha13] H. Zhao. “MLFMM accelerated integral equation modeling of reverberation chambers”. In: *IEEE Antennas and Propagation Magazine* 55.5 (2013), pp. 299–308 (cit. on p. 3).

List of Own Publications

[Eib12] T. F. Eibert, Y. Weitsch, H. Chen, and M. E. Gruber. "Solving periodic eigenproblems by solving corresponding excitation problems in the domain of the eigenvalue". In: *Progress In Electromagnetics Research* 126 (2012), pp. 65–84.

[Gru12] M. E. Gruber and T. F. Eibert. "3-D Simulation of reverberation chambers using the method of moments and the cavity Green's function accelerated by the Ewald method". In: *Kleinheubacher Tagung*. Miltenberg, Germany, Sept. 2012.

[Gru13a] M. E. Gruber, S. B. Adrian, and T. F. Eibert. "A finite element boundary integral formulation using cavity Green's function and spectral domain factorization for simulation of reverberation chambers". In: *International Conference on Electromagnetics in Advanced Applications (ICEAA)*. Torino, Italy, Sept. 2013, pp. 460–463.

[Gru13b] M. E. Gruber and T. F. Eibert. "An accuracy comparison of various surface integral equations for cavity modeling". In: *International Review of Progress in Applied Computational Electromagnetics (ACES)*. Monterey, USA, Mar. 2013, pp. 285–289.

[Gru13c] M. E. Gruber and T. F. Eibert. "Simulation of reverberation chambers using meth- od of moments with cavity Green's function and spectral domain factorization". In: *IEEE International Symposium on Electromagnetic Compatibility - EMC*. Denver, USA, Aug. 2013, pp. 808–812.

[Gru14a] M. E. Gruber and T. F. Eibert. "A cavity Green's function boundary element method with spectral domain acceleration for modeling of reverberation chambers". In: *IEEE Transactions on Electromagnetic Compatibility* 56.6 (2014), pp. 1466–1473.

[Gru14b] M. E. Gruber and T. F. Eibert. "A hybrid Ewald-Spectral representation of the rectangular cavity Green's function". In: *International Symposium on Electromagnetic Compatibility - EMC Europe*. Gothenburg, Sweden, Sept. 2014, pp. 906–909.

[Gru14c] M. E. Gruber, J. Knapp, and T. F. Eibert. "Independent stirrer positions in reverberation chambers: An inner product space approach". In: *Kleinheubacher Tagung*. Miltenberg, Germany, Sept. 2014.

[Gru14d] M. E. Gruber, C. Koenen, and T. F. Eibert. "Rectangular cavity Green's functions with Ewald summation technique and fast Fourier transform acceleration". In: *International Conference on Scientific Computing in Electrical Engineering - SCEE 2014*. Wuppertal, Germany, July 2014.

[Gru15a] M. E. Gruber, T. Dengler, A. Knaak, J. Knapp, and T. F. Eibert. "Analysis of a simultaneously clockwise and counterclockwise rotated mode stirrer in a reverberation chamber". In: *Joint IEEE International Symposium on Electromagnetic Compatibility and EMC Europe*. Dresden, Germany, Aug. 2015, pp. 1–4.

[Gru15b] M. E. Gruber and T. F. Eibert. "A Cavity Green's Function Boundary Element Method for the Modeling of Reverberation Chambers: Validation against Measurements". In: *Joint IEEE International Symposium on Electromagnetic Compatibility and EMC Europe*. Dresden, Germany, Aug. 2015, pp. 1–4.

[Gru15c] M. E. Gruber and T. F. Eibert. "A Hybrid Ewald-Spectral Cavity Green's Function Boundary Element Method With Spectral Domain Acceleration for Modeling of Over-Moded Cavities". In: *IEEE Transactions on Antennas and Propagation* 63.6 (2015), pp. 2627–2635.

[Gru15d] M. E. Gruber and T. F. Eibert. "Numerical modeling of reverberation chambers: The cavity Green's function boundary element method in comparison to other state-of-the-art algorithms". In: *Progress In Electromagnetics Research Symposium Abstracts*. Prague, Czech Republic, July 2015, pp. 1685–1686.

[Gru15e] M. E. Gruber, C. Koenen, and T. F. Eibert. "A fast Fourier transform accelerated Ewald summation technique for the vector electromagnetic rectangular cavity Green's function". In: *Journal of Computational Physics* 280 (2015), pp. 570–578.

[Koe13b] C. Koenen, M. E. Gruber, and T. F. Eibert. "Computation of the rectangular cavity Green's function using the inverse fast Fourier transform and a Lagrange polynomial interpolation". In: *Kleinheubacher Tagung*. Miltenberg, Germany, Sept. 2013.

List of Supervised Student Projects

[Bro14] L. D. Broska. “Numerische Modellierung von Modenverwirbelungskammern: Ein Vergleich von Momentenmethode und Finiter Integrationstechnik”. Bachelorarbeit. Technische Universität München, Sept. 2014.

[Den14] T. Dengler. “Vergleich zweier Methoden zur Bestimmung der unabhängigen Modenrührerpositionen in Modenverwirbelungskammern”. Masterarbeit. Technische Universität München, Dec. 2014.

[Kna14a] A. Knaak. “Mehrstufiger Algorithmus zur Bestimmung der unabhängigen Feldverteilungen in einer Modenverwirbelungskammer”. Forschungspraxis. Technische Universität München, July 2014.

[Kna14b] J. Knapp. “Bewertung der Effektivität von Modenverwirbelungskammern unter besonderer Betrachtung der Güte”. Bachelorarbeit. Technische Universität München, Mar. 2014.

[Kna14c] J. Knapp. “Einfluss des Rührervolumens auf die Effizienz von Modenverwirbelungskammern: Numerische Simulation und Einordnung in die aktuelle Forschung”. Forschungspraxis. Technische Universität München, June 2014.

[Koe13a] C. Koenen. “Computation of the rectangular cavity Green’s function using the inverse fast Fourier transform and a Lagrange polynomial interpolation”. Master’s Thesis. Technische Universität München, July 2013.

[Sun12] Z. Sun. “Untersuchung der Effizienz verschiedener Modenrührer für Modenverwirbelungskammern”. Forschungspraxis. Technische Universität München, Dec. 2012.

[Tro13] S. Trollmann. “Ausarbeitung eines Praktikumsversuches zu Bauelementen der Rechteckhohlleitertechnik”. Bachelorarbeit. Technische Universität München, Aug. 2013.

[Zag15] F. Zaglauer. “Erstellung einer Übungsaufgabe im Bereich der Rechteckhohlleitertechnik”. Bachelorarbeit. Technische Universität München, Feb. 2015.

[Zie15] D. Zielske. “Ausarbeitung einer Übungsaufgabe zum Thema Skin-Effekt”. Bachelorarbeit. Technische Universität München, Feb. 2015.